Rare earth nickelates as cathodes
for
solid oxide fuel cells

Dissertation

Andreas Egger

Montanuniversität Leoben
Mai 2013

Diese Arbeit wurde im Zeitraum von 2008 bis 2013 am Lehrstuhl für Physikalische Chemie der Montanuniversität Leoben im Rahmen der Projekte SOFC600 und RELIVE-CAT unter der Betreuung von Univ. Prof. Dipl.-Ing. Dr. techn. Werner Sitte durchgeführt.

Eidesstattliche Erklärung:
Ich erkläre an Eides statt, dass ich diese Arbeit selbständig verfasst, andere als die angegebenen Quellen und Hilfsmittel nicht benutzt und mich auch sonst keiner unerlaubten Hilfsmittel bedient habe.

Affidavit:
I declare in lieu of oath, that I wrote this thesis and performed the associated research myself, using only literature cited in this volume.

Acknowledgement

I want to thank the Montanuniversität Leoben for giving me the opportunity to complete my doctoral thesis while working as university assistant at the Chair of Physical Chemistry.

I am especially grateful to my thesis advisor Professor Werner Sitte for his patience, support and encouragement over all these years.

I thank Edith Bucher for introducing me in the world of perovskites, conductivity relaxation and the till then unknown existence of Tirolean Zwergspitzmäusen. Her reluctance to repetition combined with an unfailing memory formed the basis of short but unique conversations. Thanks also for performing thermogravimetric measurements, for sending me numerous reminder emails and for many other things I probably forgot to mention.

I am indebted to Wolfgang Preis for sharing his vast and thorough theoretical knowledge and his willingness to give intelligent answers to stupid questions. Many thanks also for performing DSC-measurements and for the calculation of predominance diagrams.

Special thanks go to Peter Gsaxner for sharing office, providing technical and computer support and for his increasingly refined measurement software employed throughout my work.

Competent advice from Karin Stanglauer in chemical, laboratory and experimental affairs as well as her readiness to share also non-technical information with her colleagues is greatly appreciated.

Thanks go to Liane Hackl for her rigorous government over the secretariat and for almost never losing patience with respect to administrative issues.

I thank Peter Waldner for intensive and exhaustive discussions of various sorts and Dietmar Grosse-Eschedor for software management and by achieving the feat of transporting rather heavy gas bottles between four floors, three of which are connected by elevators.

Thanks are due to Emeritus Professor Heinz Gamsjäger for participating in the inter-generational knowledge transfer program “computer support for thermodynamic support”.

I am grateful to Jean-Marc Bassat and his group from the University of Bordeaux for collaboration and for providing nickelate powders and sintered samples.

Financial support from the EC within the integrated project SOFC600 and from the FFG Austria within the project RELIVE-CAT is gratefully acknowledged. I thank all project partners from AVL and Forschungszentrum Jülich for fruitful collaboration and Frank Tietz for support during my three-month stay at FZJ. Many thanks go to Christian Gspan and Sanja Šimić from ZFE-Graz for SEM/TEM-analysis and evaluation as well as to Frederik Klauser and Alexander Menzel from the University of Innsbruck for XPS-measurements. Thanks are also due to Professor Gregor Mori and Thomas Zauchner for pictures recorded on the 3D-surface microscope.

Best regards go to the guys from the institute of electrotechnics for interesting and at times even helpful discussions at the regulars’ table including, but not limited to, technical affairs.

Table of contents

1 Introduction 1
- 1.1 Fuel cells 2
- 1.2 Solid oxide fuel cells 3
- 1.3 Cathodes 7
- 1.4 Nickelates 8

2 Theory 10
- 2.1 Crystal structure of rare earth nickelates 10
- 2.2 Oxygen diffusion in rare earth nickelates 16
- 2.3 Transport equations for mass and charge transport 18
  - 2.3.1 Chemical and ambipolar diffusion 25
  - 2.3.2 Tracer diffusion 35
  - 2.3.3 Conductivity diffusion coefficient 36
  - 2.3.4 Temperature dependence of transport properties 37
- 2.4 Experimental determination of diffusion coefficients in solids 38
- 2.5 Sample geometries 41
  - 2.5.1 Linear four-point geometry 42
  - 2.5.2 Van der Pauw geometry 43
- 2.6 Determination of the electrical conductivity 45
  - 2.6.1 Linear four-point geometry 45
  - 2.6.2 Van der Pauw geometry 45
- 2.7 Conductivity relaxation technique 52
- 2.8 Modeling oxygen exchange 56
  - 2.8.1 Mixed controlled oxygen exchange 56
  - 2.8.2 Diffusion controlled oxygen exchange 64
  - 2.8.3 Surface controlled oxygen exchange 66
- 2.9 Relaxation techniques 68
- 2.10 Correlation between oxygen non-stoichiometry and conductivity 70
  - 2.10.1 Linear four-point geometry 71
  - 2.10.2 Van der Pauw geometry 79
- 2.11 Flush time correction 84

3 Experimental 90
- 3.1 Setup 90
- 3.2 Equipment 93
- 3.3 Sample preparation 94
- 3.4 Particle size distribution 99
- 3.5 Sintering behavior 100
- 3.6 Reactor flush time 101
- 3.7 Oxygen depletion in the gas phase 105
- 3.8 Oxidation vs. reduction measurements 109
- 3.9 Effect of gas flow rates on relaxation behavior 111
- 3.10 Effect of Ag-deposition on the oxygen surface exchange rate 112

4 Results and discussion 115
- 4.1 Sample characterization 115
  - 4.1.1 Composition, density and microstructure 115
  - 4.1.2 X-ray diffraction 116
  - 4.1.3 Thermal expansion 117
  - 4.1.4 Thermogravimetric analysis 118
  - 4.1.5 Differential scanning calorimetry 124
- 4.2 Transport properties 126
  - 4.2.1 Electronic conductivity 126
  - 4.2.2 Chemical surface exchange coefficient of oxygen 131
  - 4.2.3 Chemical diffusion coefficient of oxygen 135
  - 4.2.4 Ionic conductivity 143
- 4.3 Long-term stability and degradation 145
  - 4.3.1 Phase instability of $Pr_2NiO_{4+\delta}$ 145
  - 4.3.2 Humid atmospheres 146
  - 4.3.3 Chemical stability against CO_2 157
  - 4.3.4 Sulfur tolerance of $La_2NiO_{4+\delta}$ 161

5 Summary and conclusions 169

6 References 171

1 Introduction

The current debate about climate change and its possible consequences, the continuous depletion of oil and gas deposits demanding for increasingly complex oil production methods with all its environmental impacts, rising oil prices and the geopolitical implications following from the dependence of developed countries on oil has led to the widely accepted view that a change in energy resources from fossil fuels to sustainable sources such as solar, wind and hydropower is inevitable. While many different kinds of energy sources can be utilized, energy storage and transport – either in electrical or in chemical form – pose major technological and financial challenges. Progress in battery and hydrogen research is constantly advancing but whether the energy systems of the future will be based on these technologies is still an open question. While the transition to sustainable energy sources may still need decades to come, the aim for the near-term future is to utilize available resources in a more efficient way. In all these respects fuel cells may play an important role in that they can be used as highly-efficient chemical-to-electrical conversion devices that may be operated with a variety of energy carriers such as hydrogen or carbon-based fuels.

The aim of this thesis was the characterization and testing of novel cathode materials for solid oxide fuel cells. In the following introduction a brief overview of the different types of fuel cells is given in which solid oxide fuel cells (SOFCs) are covered in more detail. The requirements for state of the art SOFC-cathode materials are given together with a motivation for the promising material class of rare earth nickelates investigated in this work. An in-depth discussion of structure and properties of nickelates and the theoretical background for the characterization techniques employed in this work are provided in chapter 2. Chapter 3 deals with the experimental details and contains results from preliminary testing with respect to the experimental setup, sample preparation and measurement conditions. Results and discussion are presented in chapter 4. A short summary with main conclusions is given in chapter 5. Publications that originated from research activities in connection with nickelate cathodes and other SOFC-related topics are appended.

It should be mentioned that many research efforts are currently devoted to SOFCs operated in reverse mode, that is solid oxide electrolyzer cells (SOECs) working as high-temperature electrolyzers for electrical-to-chemical energy conversion [1,2]. If successfully developed these devices would provide a means to store electrical energy in chemical form such as hydrogen or synthesis gas, which may be reformed to lower hydrocarbons that could be distributed through already existent infrastructure.

1.1 Fuel cells

Fuel cells are devices that convert chemical energy into electrical energy. While this description applies to batteries as well, they differ in the mode of fuel supply. Batteries are ‘batch-devices’ with a fixed amount of chemical energy available, whereas fuel cells are operating in a continuous mode where the reactants are externally supplied and reaction products constantly removed from the cell. Fuel cells offer a clean, highly-efficient and low-noise production of energy without moving parts. When operated with pure hydrogen, water is emitted as exhaust gas.

Several types of fuel cells have been developed which are classified with respect to the kind of electrolyte material employed. All of them have essentially the same underlying operation principle but differ in the operating characteristics and constraints originating mainly from the nature of the electrolyte. In particular, the operating temperature of a fuel cell is essentially adjusted to the domain in which the conductivity of the electrolyte is sufficiently high and predominantly ionic. Tab. 1.1 gives an overview of the five main fuel cell types including some basic operating parameters. Fuel cell types with operating temperatures below 250°C are referred to as low-temperature fuels cells (PEMFC, AFC and PAFC) while high-temperature fuel cells have working temperatures above 500°C (MCFC and SOFC).

Tab. 1.1 Different types of fuel cells with operating characteristics [3].

Type	**Operating temperature / °C**	**Fuel**	**Electrolyte**	**Ionic charge carrier**
Polymer electrolyte membrane fuel cell (PEMFC)	70 – 110	H_2, Methanol	Sulfonated polymers	$H^+(aq)$
Alkaline fuel cell (AFC)	100 – 250	H_2	Aqueous KOH	OH^-
Phosphoric acid fuel cell (PAFC)	150 – 250	H_2	H_3PO_4	H^+
Molten carbonate fuel cell (MCFC)	500 – 700	H_2, hydrocarbons, CO	$(Li,K)_2CO_3$	CO_3^{2-}
Solid oxide fuel cell (SOFC)	600 – 1000	H_2, hydrocarbons, CO, alcohols	$(Zr,Y)O_{2-\delta}$	O^{2-}

The principle of the fuel cell was first described by the English William R. Grove in 1839 and co-discovered by German chemist Christian Friedrich Schönbein, who investigated fuel cell reactions in acidic electrolytes [4]. Nowadays various types of fuel cells exist showing different levels of development and commercialization. The alkaline fuel cell was the first practical fuel cell and was employed by NASA on the Apollo space vehicle and in the Space Shuttle [5]. Much research effort has been devoted to the development of the PEMFC mainly for automotive applications and PEMFCs from Siemens have been installed in German submarines. A variant of the PEMFC is the direct methanol fuel cell (DMFC) which is highly attractive due to its operation with liquid fuel without preceding reforming. PAFCs were the first fuel cells to be commercialized and are mainly used for stationary applications [6]. High-temperature MCFCs have been constructed as stationary power plants and are commercially available in the USA and asia. Much R&D effort has been put into SOFCs which are the focus of this work and are discussed in more detail in the following sections.

1.2 Solid oxide fuel cells

The SOFC is a high-temperature fuel-cell presently operating at temperatures between 800 and 1000°C. Such high temperatures are necessary for a sufficient ionic conductivity of zirconia-based electrolytes first proposed by Baur and Preis in 1937 [7,8]. Contrary to the molten-carbonate fuel cell the SOFC is an all-solid-state device which implies less corrosion issues and provides easier handling. Due to the high temperatures thermally activated electrode processes are sufficiently fast and the use of expensive catalysts is not required. SOFCs offer high fuel flexibility due to internal reforming and can be operated with hydrogen as well as hydrocarbons or alcohols. Furthermore, SOFCs are ideal for combined heat and power applications which utilize both electrical power and high-quality heat. On the other hand, the high operating temperatures implicate long start-up and shut-down times and large thermal stress, which makes requirements for functional materials more stringent than those of low-temperature fuel cells.

Fig. 1.1 shows the working scheme of a single SOFC-cell. While fuel is supplied to the anode side the cathode compartment is flushed with air or oxygen. When using hydrocarbons as energy carrier the fuel is preprocessed by an internal reformer that produces a mixture of H_2, CO, CO_2 and water fed to the cell. During operation, oxygen is diffusing through the porous cathode to the electroactive region near the electrolyte and after dissociation and reduction steps is being incorporated into the electrolyte as oxide ions. The oxide ions migrate through the dense electrolyte to the anode side oxidizing the fuel (e.g. H_2, CO) and the reaction products are continuously removed from the porous anode. Due to the low electronic conductivity of the electrolyte the electronic current generated by the redox-reaction is diverted through the external load performing electrical work.

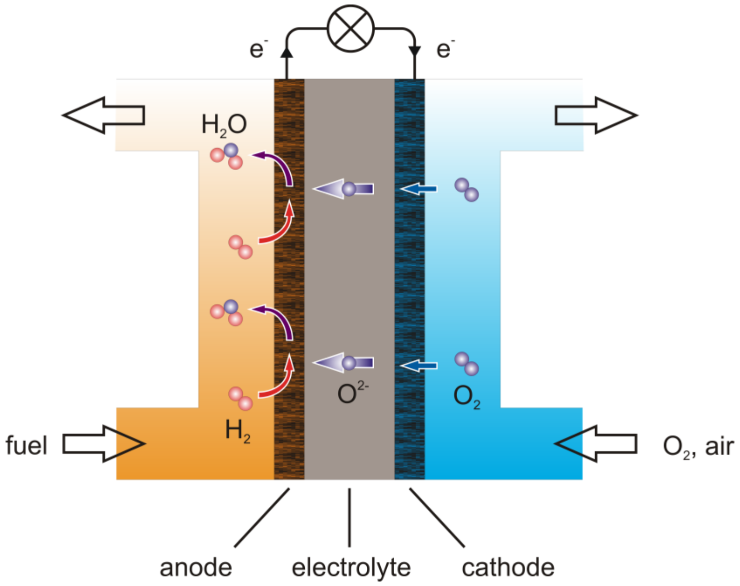

Fig. 1.1 Working scheme of a solid oxide fuel cell.

Each of the cell components must meet several structural and functional requirements offering adequate chemical and structural stability during cell operation and cell fabrication [9]. The electrolyte has to provide a gastight barrier between both gas compartments while featuring low electronic and high oxide ionic conductivity. Electrodes must exhibit high electronic conductivity as well as good catalytic activity for the respective oxygen reactions and possess sufficient porosity to allow for an effective transport of gas species between the gas stream and the electrode-electrolyte interface. Often electrodes are applied as multilayers with optimized microstructure. Moreover, good compatibility and low chemical reactivity between different cell components as well as matching thermal expansion coefficients are necessary. Sustaining such structural and functional requirements at temperatures around 800°C with sufficient stability over the whole lifetime poses a challenge to material development and processing. For mobile applications 5000-10,000 hours of operation are demanded while 40,000-100,000 hours are targeted for stationary applications [10]. Conventional materials employed as SOFC-electrolytes are fluorite-type oxide ceramics usually based on ZrO_2 [11]. Perovskite materials have been widely used as cathode in SOFCs and a typical compound is lanthanum manganite $LaMnO_3$ doped with alkaline earth elements. In almost all cases a nickel-electrolyte cermet is used as anode.

The maximum cell voltage delivered by a SOFC is about 1.2 V depending on temperature, fuel composition and load. Since this is insufficient for most applications, cells are stacked in series and in parallel to build up the necessary voltages and currents. Electrical connections between the single cells are established by interconnects, which were for a long time made of La-chromite ceramics for operating temperatures between 800°C and 1000°C. Interconnects face stringent requirements such as high electronic and low ionic conductivity, low permeability for oxygen and thermal and chemical compatibility with other cell components. Similar to electrolytes, interconnects separate both fuel and air compartments and thus have to be stable in both reducing and oxidizing atmospheres.

The two most common cell designs developed for SOFCs correspond to planar and tubular cell geometries. Both types are depicted in Fig. 1.2 where the cell stacking has been indicated. In the conventional tubular design the cell tube is closed at one end and the oxidant is introduced through a ceramic injector tube inserted into the cell. Other cell designs have been proposed such as the planar segmented design [12], ribbed-tubular design [9] or the SOFCRoll design [13].

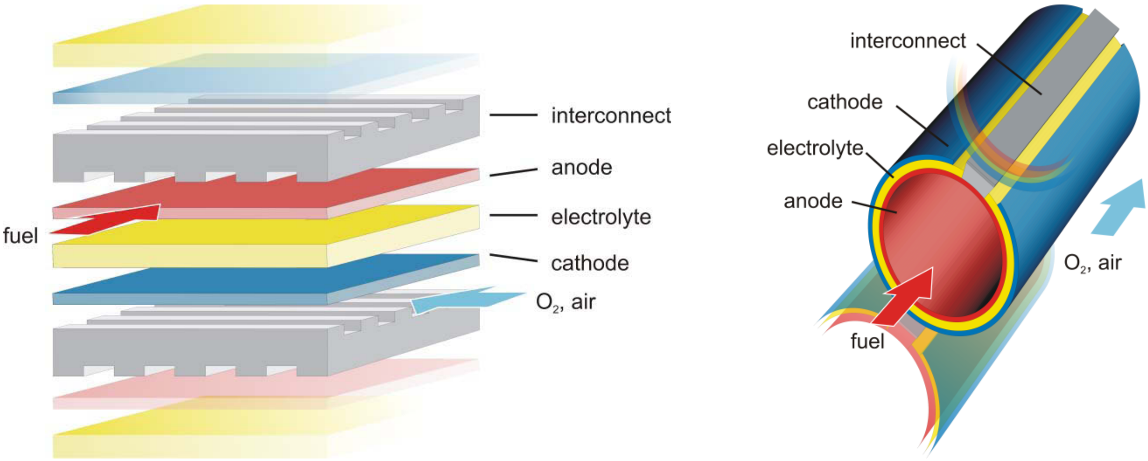

Fig. 1.2 Planar (left) and tubular (right) SOFC-cell designs. Cell stacking is indicated.

Planar cells are easy to manufacture and allow for a compact stacking of single cells with short current paths. The planar cell design offers high power densities but requires high-temperature gas sealings at the edges of the plates to avoid leakage of both fuel and oxidant. The main advantage of the tubular cell design is that it dispenses with the need for high-temperature sealings. Major drawbacks are high manufacturing costs combined with lower power density.

In self-supporting SOFC-cells one of the cell components has to act as the structural support which usually makes it the thickest layer in the cell assembly. Thus, cells can be manufactured as anode-, cathode- or electrolyte supported cells. More recently, metal-supported cell designs have been explored which appear to be promising with respect to power density and robustness.

The current trend in SOFC-research is to lower the operating temperature to the intermediate temperature (IT) region of 500-800°C [14-16]. One advantage arising from the temperature reduction is the use of metallic materials for interconnects with lower material and fabrication costs, easier and more complex shaping and structuring capabilities, better electrical and thermal conductivity and less deformation issues [17]. Furthermore, operating SOFCs in the IT-range permits the use of a broader set of materials, is less demanding for seals and balance-of-plant components, simplifies thermal management, results in faster start-up and cool-down cycles and may afford lower degradation rates of cell and stack components [16]. However, electrode kinetics and internal resistance of the cell are compromised at reduced temperatures. In particular, electrolyte resistance and cathode polarization losses have been identified as major contributions to the overall increase in the internal cell resistance [14,18] which stimulated the development of new materials that show sufficient electrochemical performance at lower temperatures. To decrease the ohmic loss in the electrolyte, new materials based on ceria or La-gallates have been proposed featuring higher oxygen ion conductivity at reduced temperatures than the classical electrolyte material yttria-stabilized zirconia (YSZ). Furthermore, anode or metal supported cell designs allow for an application of thin electrolyte layers [19]. On the cathode side mixed ionic-electronic conducting (MIEC) ceramics have been proposed to overcome the increased polarization loss in IT-SOFC cathodes as discussed in the following section.

1.3 Cathodes

In the course of lowering the operating temperature of SOFCs to the IT-range of 600-800°C, special attention has been drawn to the cathode polarization resistance as a limiting factor for efficiency [20]. The standard cathode material (La,Sr)MnO$_3$ (LSM) cannot be used at such reduced temperatures as it is too inactive for the oxygen reduction reaction due to its low oxygen ion conductivity. One remedy is to use a porous composite consisting of an electronically conducting cathode material and an appropriate amount of ionically conducting electrolyte material such as LSM-YSZ. Another strategy proposed early on by Takeda et al. [21] employs mixed ionically-electronically conducting materials which reduce the cathodic polarization resistance by extending the active zone of the electrode reaction from the immediate triple phase boundary (TPB) to part of the cathode-gas interface. The different types of SOFC-air electrodes are compared in Fig. 1.3 [22]. Using cathodes with pure electronic conduction the oxygen reduction reaction is limited to the triple phase boundaries between cathode, electrolyte and gas phase (Fig. 1.3, left). While electrolyte particles dispersed within the cathode structure increase the length of the TPB-region and thus the number of electrochemically active reaction sites [23] (Fig. 1.3, center), MIEC-ceramics integrate both types of conduction in one material, thus extending the electrochemically active zone into the cathode layer and reducing cathodic polarization effects [24,25] (Fig. 1.3, right).

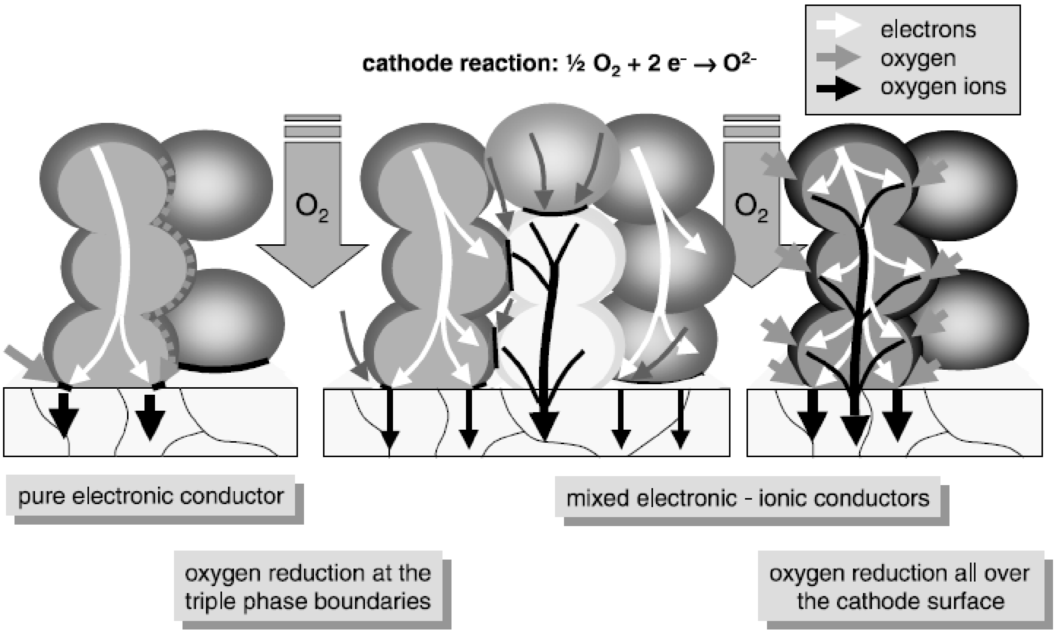

Fig. 1.3 Oxygen reduction mechanisms for different kinds of cathode materials with pure electronic conductivity (left) and with both electronic and ionic conductivity using composite materials (center) or mixed ionic-electronic conductors (right) [22].

So far, the dominating material class for MIEC-cathodes comprises perovskite-type oxide ceramics and a great number of compounds with different compositions and doping levels have been investigated. More recently, mixed conducting rare earth nickelates $Ln_2NiO_{4+\delta}$ have attracted considerable interest as alternative cathode materials for IT-SOFCs.

1.4 Nickelates

Rare earth nickelates adopt the perovskite-related K_2NiF_4-structure and feature fast oxygen surface exchange and diffusion as well as high electrocatalytic activity for oxygen reduction [26-28]. Chemical and thermal expansion are rather low for nickelates and thermal expansion coefficients match reasonably well with those of common electrolytes such as yttria-stabilized zirconia or gadolinia-doped ceria [26,29,30]. The most significant feature of the nickelates is their ability to accommodate additional oxygen on interstitial positions located inside rock salt-type layers (see chapter 2). Since oxygen diffusion in nickelates takes place mainly via interstitials, substitution with strontium or other alkaline earth ions is not required for efficient oxygen transport as it is in the case of perovskite-type materials. The absence of alkaline earths might be beneficial with respect to long-time stability issues since many degradation processes in cathode materials involve alkaline earth metals. Such degradation mechanisms include segregation of Sr to the surface [31,32], formation of low-conducting Sr-zirconates at the cathode-electrolyte interface [33,34], formation of carbonates or hydroxides at exposed surfaces [35,36], poisoning with chromium from stainless steel interconnects [20,37,38], formation of Sr-sulfates from SO_2 in air or other sources [37,39,40] or development of Sr-silicate layers with silicon emanating from sealing materials [41,42]. However, it should be mentioned that reactivity with electrolyte materials have been reported for unsubstituted nickelates at temperatures relevant for cell fabrication [43-49]. Furthermore, sensitivity of $Nd_2NiO_{4+\delta}$ against chromium and silicon have been reported by Schuler et al. [50,51] and detrimental effects of H_2O/Si and sulfur on oxygen transport properties of $Nd_2NiO_{4+\delta}$ and $La_2NiO_{4+\delta}$ have been observed in this work (see chapter 4).

Performance measurements on single cells with electrodes of rare earth nickelates show promising results [43,52-54]. $Pr_2NiO_{4+\delta}$ shows excellent performance for IT-SOFC/SOEC applications [28,55-57] but suffers from limited phase stability (see chapter 4). However, providing conclusive comparisons of cell test results is difficult since cathode performance depends significantly on the microstructural details. For example, the area-specific resistance of $La_2NiO_{4+\delta}$-electrodes on YSZ-electrolyte was lowered more than one order of magnitude by optimizing the electrode microstructure [54].

Rare earth nickelates are frequently doped on the rare earth and/or nickel-site to adjust or modify chemical and physical properties for applications as SOFC-cathodes or ceramic membranes. For example, doping with alkaline earths like Sr or Ca on the lanthanide site increases the rather moderate electronic conductivity of nickelates (~100 Scm^{-1}) [58-66] and improves the phase stability [59,61,67,68] while partial substitution of nickel by Cu enhances sinterability [69-71] and Co-doping yields higher surface exchange rates and diffusivities of oxygen at low temperatures [72-74]. However, since such substitutions may also lead to undesired side effects, this work is focusing on chemically simple systems and hence only undoped rare earth nickelates have been investigated.

2 Theory

2.1 Crystal structure of rare earth nickelates

Undoped rare earth nickelates $La_2NiO_{4+\delta}$, $Pr_2NiO_{4+\delta}$ and $Nd_2NiO_{4+\delta}$ crystallize in the so-called K_2NiF_4-structure type first described by Balz and Plieth for the compound K_2NiF_4 [75]. The K_2NiF_4-structure is considered to be a perovskite-related structure because it can be thought of being constituted on the basis of the building block given in Fig. 2.1 (left), which corresponds to the unit cell of a cubic perovskite (*P*m-3m, SG 221). As is well known, the unit cell of an ideal cubic perovskite oxide ABX_3 in *B*-centered representation (Fig. 2.1, left) consists in *A*-cations residing on the corners of the cell (red), a body-centered *B*-cation (purple) and *X*-anions arranged on the centers of the cell faces (blue). In the perovskite structure *B*-cations are octahedrally coordinated by the *X*-anions while *A*-cations are surrounded by a cuboctahedral arrangement of the anions *X*. Fig. 2.1 (middle) shows the unit cell of the ideal tetragonal K_2NiF_4-structure (*I*4/mmm, SG 139) outlined in yellow. The perovskite building block is apparent in the middle of the K_2NiF_4-unit cell, where each Ni-ion is octahedrally coordinated by 6 fluoride anions (green octahedra). Above and below the center further perovskite blocks are located, but shifted in the (*a*,*b*)-plane with respect to the center block in order to maximize electrostatic attraction between the fluoride anions and potassium cations (red).

Fig. 2.1 (right) displays a stacking plot of the K_2NiF_4 unit cell which illustrates the two-dimensional character of the compound consisting of single perovskite layers stacked along the crystallographic *c*-axis. Adjacent perovskite layers are shifted by (½, ½) in the (*a*,*b*)-plane for closest approach of fluoride anions in one perovskite layer and potassium cations in the next layer. Closer scrutiny of the inter-layer region between adjacent perovskite layers shows that the geometric arrangement of potassium and fluoride ions corresponds to that of rock salt. Hence, K_2NiF_4 can be described as an intergrowth compound between perovskite and rock salt structures.

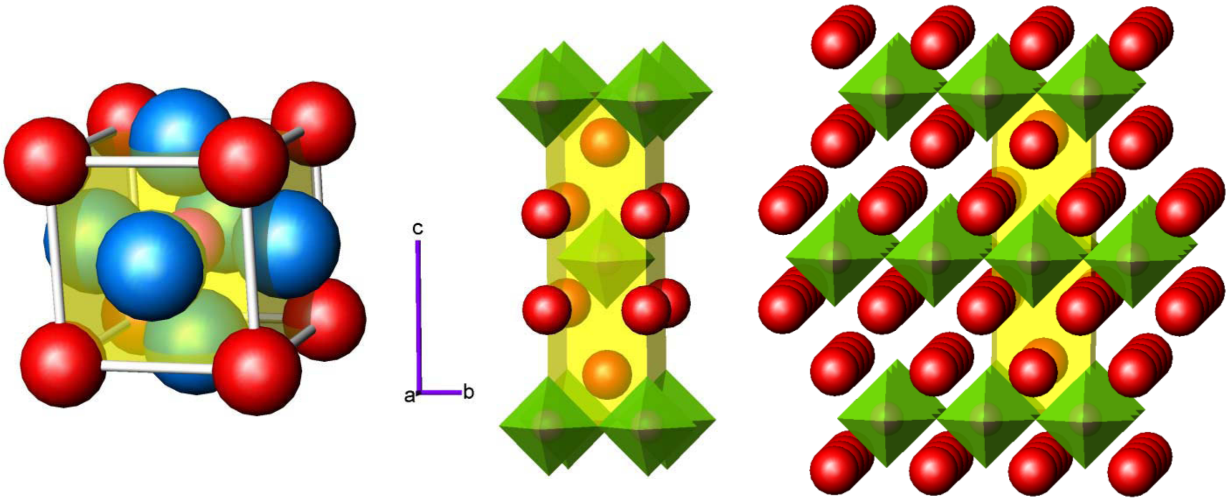

Fig. 2.1 The unit cell of the ideal perovskite structure (left) is the basic building block of the ideal tetragonal K_2NiF_4-structure. Stacking the K_2NiF_4-unit cell (middle) along the (*a*,*b*)-directions displays the two-dimensional character of the K_2NiF_4-structure (right). Unit cells are outlined yellow.

The K_2NiF_4-structure can be considered as the first member of the so-called Ruddlesden-Popper (RP) series differing in the number n of perovskite layers that make up the perovskite slabs of the structure. Fig. 2.2 shows unit cells and stacking plots for $n = 2$ (left) and $n = 3$ (right). Although higher RP-homologues of the K_2NiF_4 compound exist, they have first been reported for Sr_2TiO_4 [76] by Ruddlesden and Popper who published the crystal structures of $Sr_3Ti_2O_7$ ($n = 2$) and $Sr_4Ti_3O_{10}$ ($n = 3$) [77]. Formally, the perovskite structure may be considered as a limiting member of the series corresponding to $n = \infty$. The generic formula of the RP-oxide series is $A_{n+1}B_nO_{3n+1}$ ($= (AO)(ABO_3)_n$) and the highest-symmetric crystallographic space group is $I4/\mathrm{mmm}$ for all members.

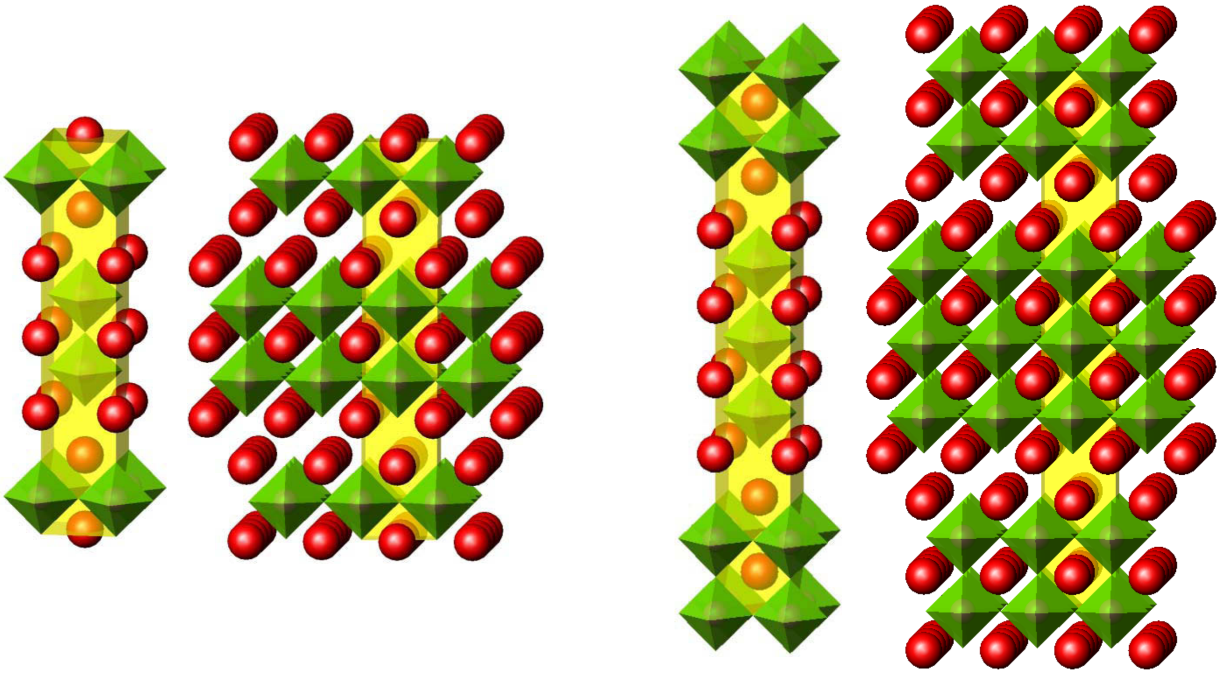

Fig. 2.2 Crystal structures of second-order (*n* = 2, left) and third-order (*n* = 3, right) Ruddlesden-Popper phases for $A_{n+1}B_nO_{3n+1}$. *A*-ions are shown as red spheres, BO_6-units are plotted as green octahedra, unit cells are outlined yellow. Both unit cell and packing plot are depicted for each structure type.

Rare earth nickelates $Ln_2NiO_{4+\delta}$ (*Ln* = La, Pr, and Nd) are often found to crystallize in lower-symmetry space groups caused by tilting of the rigid Ni-O octahedra. Fig. 2.3 (middle) shows a perspective view of the unit cell of stoichiometric La_2NiO_4 (i.e. $La_2NiO_{4+\delta}$ with $\delta = 0$) as determined by neutron diffraction at room temperature [78]. The left and right pictures are projections along the *a*- and *b*-direction, respectively, showing the Ni-oxygen octahedra to be rotated cooperatively around the *a*-axis. Such tilting is a characteristic feature of the nickelates and originates in a slight mismatch in the bond distances of Ni-O and *Ln*-O, where the *Ln*-O distance in the rock salt layer is too small with respect to the NiO_2-layer and the corresponding interlayer strain is partially relieved by a buckling of the octahedra network [79]. Due to the lanthanide contraction, this mismatch increases in the lanthanide series with Sm already being too small to give a stable structure, as undoped $Sm_2NiO_{4+\delta}$ does not exist [72]. Due to the symmetry reduction caused by tilting and distortion of the NiO_6-octahedra a different axes-setting has to be chosen where the (*a*,*b*)-axes are rotated by ca. 45° with respect to axes in the ideal K_2NiF_4-structure, thus doubling the cell volume (Fig. 2.3).

The interlayer strain between *Ln*O- and NiO_2-single layers can be characterized by the Goldschmidt tolerance factor *t* defined in analogy to perovskite compounds [80,81]

$$t = \frac{r_{Ln} + r_O}{\sqrt{2}(r_{Ni} + r_O)} \tag{2.1}$$

where r_{Ln}, r_{Ni} and r_O are the ionic radii of Ln^{3+}, Ni^{2+} and O^{2-}-ions, respectively. A perfect radii match gives $t = 1$ for the ideal tetragonal structure. Based on Shannon's ionic radii [82] tolerance factors for $La_2NiO_{4+\delta}$, $Pr_2NiO_{4+\delta}$ and $Nd_2NiO_{4+\delta}$ are 0.89, 0.88 and 0.87, respectively, which indicates that the NiO_2-layer is under compressive stress resulting from stretched La-O bonds. For more precise calculations of *t* the oxygen non-stoichiometry as well as different valencies and spin-states of nickel ions have to be considered.

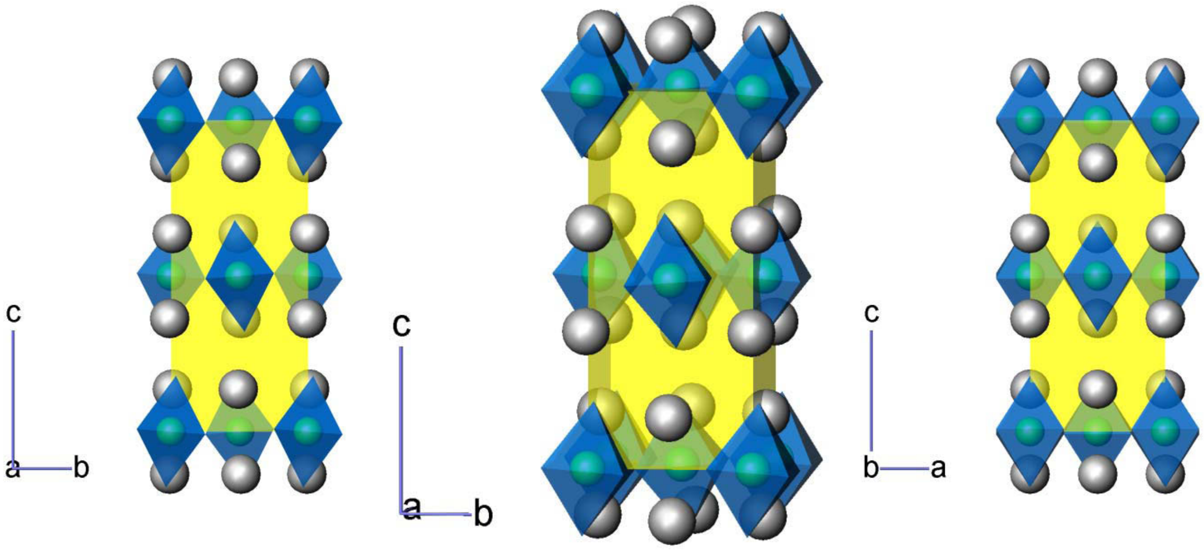

Fig. 2.3 Crystal structure of La_2NiO_4 at 295 K (*B*mab, SG 64). La-ions are plotted in grey, NiO_6-octahedra (blue) are tilted around the *a*-axis by ±4.5° [78].

The most significant feature of the nickelates is their ability to accommodate excess oxygen as has been established on the basis of precise density measurements [83], coulometric titration [84], thermogravimetric analysis [26,85], iodometric titration [26] and neutron diffraction [78,86]. It has been suggested early on that excess oxygen is residing inside the rather open rock salt layers, since the close-packed perovskite structure does not allow for accommodating oxygen interstitials. However, there has been some controversy about the type of oxygen defect and its exact lattice site within the rock salt layer. Several oxygen defect species have been proposed such as O^{2-} (oxide), O^{-}, O_2^{-} (superoxide) and O_2^{2-} (peroxide) but experimental evidence [78,85] as well as results from DFT-calculations [87] point to oxide ion interstitials. Jorgensen et al. established the precise crystallographic position of the oxygen interstitials in $La_2NiO_{4+\delta}$ based on Rietveld refinement of neutron diffraction patterns [78]. Fig. 2.4 (left) outlines the interstitial location for the ideal tetragonal structure in the center of the tetrahedral space made up by four cations of adjacent perovskite slabs. Fig. 2.4 (right) shows the actual oxygen interstitial position for orthorhombic $La_2NiO_{4.18}$ as experimentally determined by Jorgensen et al. [78], where the distortion of the local structure around the interstitial defect is omitted in the figure [78,88,89]. It is interesting to note that oxygen interstitials are also tetrahedrally surrounded by four regular oxygen ions on apical sites.

The amount of oxygen incorporated into the nickelate compound depends on the rare earth element, *A*- and *B*-site doping, temperature and oxygen partial pressure. For example, stoichiometric La_2NiO_4 has been obtained by annealing in hydrogen [78], while La-nickelate with oxygen excess as high as $\delta = 0.25$ has been prepared by electrochemical intercalation of oxygen in aqueous solutions [90-93]. Under normal conditions with respect to temperature and oxygen partial pressure the oxygen overstoichiometry for rare earth nickelates ranges roughly between 0.05 and 0.25. The strong tendency towards oxygen incorporation can be explained by a reduction of the size mismatch between perovskite and rock salt layers due to (i) a decrease of the average Ni-O bond distance caused by partial oxidation of Ni^{2+} to Ni^{3+} and (ii) an increase of the average *Ln*-O distance due to a higher average coordination number of the lanthanide ions [94]. The oxygen hyperstoichiometry in $Pr_2NiO_{4+\delta}$ and $Nd_2NiO_{4+\delta}$ is generally higher than that of $La_2NiO_{4+\delta}$ due to the smaller ionic radii of Pr and Nd, which results in a stronger driving force to relieve the interlayer-strain by oxygen incorporation.

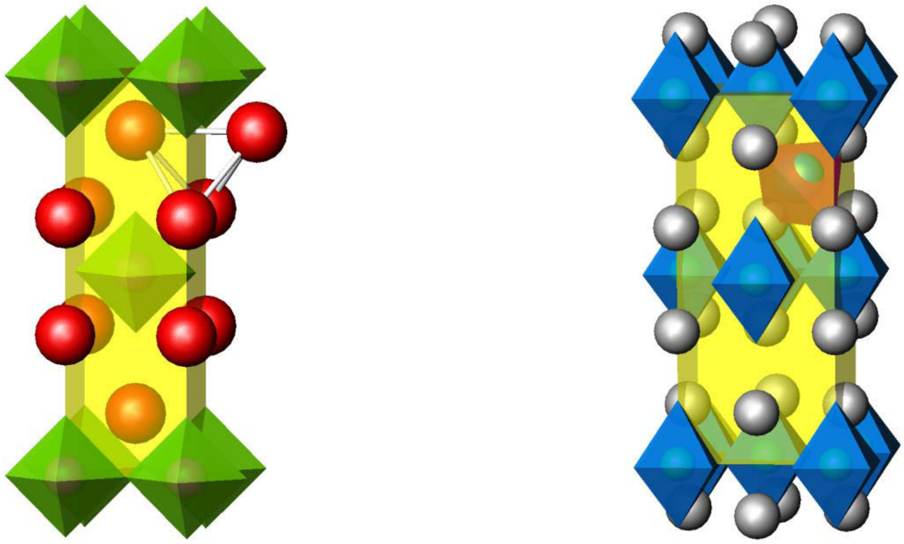

Fig. 2.4 The left picture indicates the interstitial position located in the center of the tetrahedron inside the rock salt layer of the K_2NiF_4-structure. Experimental confirmation was first obtained for $La_2NiO_{4+\delta}$ (right) where the tetrahedral coordination of the interstitial oxide ion by four La-ions is shown in red [78].

Many structural and physical properties of nickelates are very sensitive to the actual oxygen stoichiometry. For example, changes in oxygen content have a strong impact on the electronic conductivity due to electronic charge compensation (see section 4.2.1). $La_2NiO_{4+\delta}$ has been thoroughly investigated due to its structural and electronic similarity to $La_2CuO_{4+\delta}$ which forms the basis for several high-temperature superconducting compounds [95]. Despite the very similar electronic configurations of Ni and Cu, high-temperature superconductivity has not been found in nickelates [96]. It is interesting to note that while $La_2CuO_{4+\delta}$ cystallizes in the K_2NiF_4-structure type, Nd- and Pr-cuprates adopt a different crystal structure [79].

A great many publications about $La_2NiO_{4+\delta}$ deal with the crystallographic aspects as a function of oxygen content, which in turn depends on temperature and oxygen partial pressure [78,86,91,92,94,97-109]. Many structural investigations have also been published for $Pr_2NiO_{4+\delta}$ [88,94,110-114] and $Nd_2NiO_{4+\delta}$ [94,115-117]. The detailed interdependency between structure and oxygen content in the nickelate system is rather intricate, several phase transitions have been described in the literature with some discrepancies between reported space groups, which is further complicated by the occurrence of two-phase regions due to phase segregation caused by miscibility gaps between nickelates of different oxygen content [105,107,108,113].

From a practical viewpoint phase transitions in nickelates appear to be relevant with respect to thermo-mechanical stability and compatibility with other components, for example regarding adhesion to the electrolyte during heat-up or cool-down of an SOFC. While K_2NiF_4-type nickelates of La and Nd appear to be stable at temperatures and oxygen partial pressures of interest for SOFC-application, $Pr_2NiO_{4+\delta}$ suffers from a severe thermodynamic instability at elevated temperatures which is discussed in more detail in section 4.1.4.

Many publications deal with structural, thermodynamic and physical properties of second- and third-order Ruddlesden-Popper phases of rare earth nickelates [72,81,118-137]. Successful preparation of RP-homologues $(La,Pr,Nd)_{n+1}Ni_nO_{3n+1}$ with $n \geq 4$ as bulk compounds has not been reported in the literature, although they have been observed as intergrowth defects in disordered $La_3Ni_2O_7$ and $La_4Ni_3O_{10}$ by HRTEM analysis [118]. Several higher-order RP-nickelates have been investigated with respect to their applicability as SOFC-cathodes [72,127,128,135,136]. Furthermore, a great many studies deal with rare earth nickelates doped on the *A*- and/or *B*-site by alkaline earth and transition metals, respectively, whereby the structural, electronic and oxygen transport properties of the materials can be modified. However, those materials are outside the scope of this work.

2.2 Oxygen diffusion in rare earth nickelates

Due to the layered structure of rare earth nickelates the oxygen transport is expected to be highly anisotropic. This has been confirmed by Bassat et al. [138] for single crystals of $La_2NiO_{4+\delta}$ by using $^{16}O/^{18}O$ isotopic exchange and secondary ion mass spectroscopy (SIMS) for the determination of the oxygen composition profile. Diffusion within the (*a*,*b*)-plane was found to be isotropic with no significant difference between tracer diffusion coefficients along the *a*- and *b*-axes, while diffusion coefficients along the *c*-axis were roughly two orders of magnitudes smaller at 900°C. Surprisingly, activation energies of tracer diffusion coefficients were significantly lower in the *c*-direction [138]. Fast in-plane diffusion has also been reported for oriented thin films of $La_2NiO_{4+\delta}$ prepared by epitaxial deposition on single crystals of $SrTiO_3$ and $NdGaO_3$ [139] and similar findings were obtained for isostructural $(La,Sr)_2CuO_4$ [140]. While in-plane oxygen diffusion is expected to take place through ion hopping between interstitial oxygen sites within in the rock salt layers of the structure, oxygen diffusing along the *c*-axis has to traverse perovskite blocks via oxygen vacancies. Since the vacancy concentration is supposed to be rather low in oxygen hyperstoichiometric compounds such as undoped nickelates a much lower diffusivity in *c*-direction is to be expected. While this picture is in agreement with experimental data, it is difficult to establish the details from experiments alone. Further insight in oxygen diffusion mechanisms has been obtained by atomistic modeling of $La_2NiO_{4+\delta}$ [141-143] and $Pr_2NiO_{4+\delta}$ [144].

Minervini et al. [141] concluded from theoretical calculations that the in-plane diffusion mechanism is not a direct interstitial hopping process but rather an interstitialcy mechanism where an interstitial oxygen ion displaces an apical oxygen ion which in turn moves into an adjacent interstitial site (path *a* in Fig. 2.5, left). Results from molecular dynamics calculations support the interstitialcy migration mechanism for in-plane oxygen diffusion in $La_2NiO_{4+\delta}$ [143] (Fig. 2.5, right) and $Pr_2NiO_{4+\delta}$ [144]. Minervini et al. [141] proposed a cascaded interstitialcy mechanism for cross-plane diffusion along the crystallographic *c*-axis (path *b* in Fig. 2.5, left) while Cleave et al. considered oxygen vacancy pathways for stoichiometric La_2NiO_4 [142].

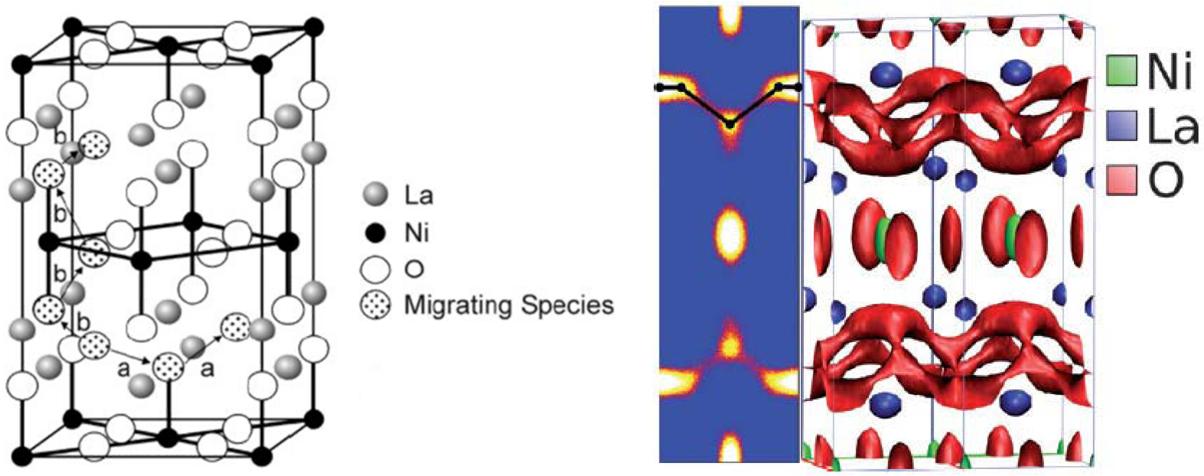

Fig. 2.5 Oxygen diffusion paths in $La_2NiO_{4+\delta}$ based from theoretical calculations. Minervini et al. [141] proposed interstitialcy mechanisms for in-plane and cross-plane oxygen diffusion (left). In-plane interstitialcy diffusion was confirmed by molecular dynamics simulations (right) showing curved oxygen paths within the rock salt layers (red color) [143].

Of course, for polycrystalline materials investigated in this work diffusion is effectively isotropic with the overall diffusion coefficient given as weighted average of the individual diffusion coefficients in the different crystallographic directions.

2.3 Transport equations for mass and charge transport

The starting point for the following treatment of solid-state mass and charge transport is the theory of linear irreversible thermodynamics. This theory supposes a linear relationship between generalized forces X_i and corresponding fluxes (flows) J_i. The flux is defined as the amount of some extensive physical quantity flowing per time through a plane of unit area normal to the direction of flow. Fluxes are assumed to be caused by the presence of some generalized driving forces, usually expressed as negative gradients of corresponding potential functions (intensive scalar physical quantities as a function of space and time). Examples are the negative gradient of electrical potential (electric field), gradients in pressure, temperature or chemical potential. In the realm of linear irreversible thermodynamics these cause-effect relationships are assumed to be linear. However, linearity is not an inherent property of most systems but rather an approximation valid for sufficiently small forces close to equilibrium where the range of validity has to be established separately for each type of system investigated.

In the general case the assumption of linear flux-force equations give rise to the so-called phenomenological equations (Onsager equations)

$$J_i = \sum_{k=1}^{n} L_{ik} X_k \qquad i = 1..n \tag{2.2}$$

or in matrix notation

$$\begin{pmatrix} J_1 \\ \vdots \\ J_n \end{pmatrix} = \begin{pmatrix} L_{11} & \cdots & L_{1n} \\ \vdots & \ddots & \vdots \\ L_{n1} & \cdots & L_{nn} \end{pmatrix} \begin{pmatrix} X_1 \\ \vdots \\ X_n \end{pmatrix} \tag{2.3}$$

where the constants of proportionality L_{ik} are called phenomenological coefficients (transport coefficients, Onsager coefficients). According to the theory of linear irreversible thermodynamics the flux-force pairs have to be chosen in a way that the sum over the corresponding products $J_i X_i$ equals the rate of entropy production per volume $\dot{s}$ [145].

$$\dot{s} = \sum_{k=1}^{n} J_k X_k \tag{2.4}$$

Based on the principle of microscopic reversibility, Onsager [146,147] derived a symmetry relation between the phenomenological coefficients

$$L_{ik} = L_{ki} \tag{2.5}$$

which holds in the absence of magnetic or Coriolis forces. Thus, the coefficient matrix in Eq. (2.3) is symmetric.
It can be seen from Eq. (2.2) that in general a flux J_i of the irreversible process i is depending not only on its corresponding force X_i, but also on forces $X_{k\neq i}$ corresponding to all other fluxes in the system. Examples are the Soret-effect or thermodiffusion due to interference between gradients in temperature and concentration and thermoelectric effects caused by interacting thermal and electrical potential gradients [145].

As a special case J_i and X_i (i = 1...3) may be components of two linearly related vector quantities $\vec{J}$ and $\vec{X}$ and in this case the phenomenological coefficients are the components of a second-rank tensor relating both vector quantities. Examples of well-known transport phenomena that fall into this category are

(i) Ohm's law

$$\vec{j} = -\sigma\nabla\varphi \tag{2.6}$$

where the flux is the current density $\vec{j}$, the 'force' is the negative gradient of the electrical potential φ (electric field) and the transport coefficient is the electrical conductivity tensor σ.

(ii) Fourier's law of heat conduction

$$\vec{h} = -\lambda\nabla T \tag{2.7}$$

where the heat flux $\vec{h}$ is caused by a gradient in temperature T and the transport coefficient λ is the thermal conductivity tensor.

(iii) Ficks first law of diffusion

$$\vec{J} = -D\nabla c \tag{2.8}$$

where the transferred amount of substance $\vec{J}$ is caused by a gradient in concentration c and the transport coefficient D is the diffusion coefficient tensor.

As will be discussed further below the appropriate driving force for the diffusion process is not the gradient in concentration but rather the gradient in chemical potential. Nevertheless, Eq. (2.8) is important as it serves as the definition for the diffusion coefficient.

It follows from the Onsager symmetry principle (2.5) that representation matrices of the tensor quantities σ, λ and D in Eqs. (2.6) to (2.8) are necessarily symmetric.

It is well-known from equilibrium thermodynamics that one way of characterizing the condition of thermodynamic equilibrium inside a phase or between phases is the spatial uniformity of the chemical potential μ_i for each component i

$$\begin{aligned} \mu_i &= constant \qquad &\text{(within phase)} \\ \mu_i^\alpha &= \mu_i^\beta \qquad &\text{(between phases } \alpha \text{ and } \beta\text{)} \end{aligned} \tag{2.9}$$

In the case of charged species, chemical potentials have to include the effect of electrical potential on the charges and the chemical potentials are extended to electrochemical potentials η_i through

$$\eta_i \equiv \mu_i + z_i F \varphi \tag{2.10}$$

where z_i is the charge number of component i and F is Faraday's constant. For charged components in the presence of electrical fields the equilibrium condition can be expressed similar to Eqs. (2.9) as

$$\begin{aligned} \eta_i &= constant \qquad &\text{(within phase)} \\ \eta_i^\alpha &= \eta_i^\beta \qquad &\text{(between phases } \alpha \text{ and } \beta\text{)} \end{aligned} \tag{2.11}$$

For constant chemical or electrochemical potentials no macroscopic transport of components takes place, otherwise the system would not have been in equilibrium. It appears therefore natural to assume that mass transport is caused by a deviation from the equilibrium conditions (2.9) or (2.11). Furthermore, if the system is still sufficiently close to equilibrium it can be assumed that a flux caused by non-uniformity in electrochemical potential depends linearly on the spatial change of the electrochemical potential, i.e. its gradient. Thus, the fundamental equation for mass transport of a charged species in the frame of linear irreversible thermodynamics is

$$\vec{J} = -L\nabla\eta \tag{2.12}$$

or, with Eq. (2.10)

$$\vec{J} = -L\nabla\mu - LzF\nabla\varphi \tag{2.13}$$

For a neutral component or vanishing gradient in electrical potential, Eq. (2.12) simplifies to

$$\vec{J} = -L\nabla\mu \tag{2.14}$$

However, it is important to note that electrochemical potentials may have to be used for charged particles even in the absence of *external* electric fields since the movement of charged particles can generate an *internal* electric field which affects all other mobile charged species in the system as described below for the ambipolar diffusion process.

Considering the physical dimensions of the flux-force pairs in Eqs. (2.6), (2.7), (2.12) and (2.14) it is obvious that they actually do not satisfy Eq. (2.4). The reason is that those flux equations have already been simplified based on additional assumptions with respect to temperature. For example, in Eq. (2.12) the correct thermodynamic force is actually the negative gradient of the electrochemical potential divided by the absolute temperature T [145]

$$\vec{J} = -L'\nabla\frac{\eta}{T} \tag{2.15}$$

but since diffusion measurements are usually conducted in the absence of thermal gradients, T can be incorporated into the Onsager coefficient L'. In the case of heat conduction the general flux equation according to linear irreversible thermodynamics is [145,148]

$$\vec{h} = L\nabla\frac{1}{T} \tag{2.16}$$

which can be transformed to

$$\vec{h} = -\frac{L}{T^2}\nabla T \tag{2.17}$$

where the temperature dependence of the thermal conductivity $\lambda = L/T^2$ may be neglected for small temperature gradients.

Continuing with Eq. (2.12) for a charged component, some important relations between L and other quantities can be established. For the special case of a vanishing gradient in chemical potential, Eq. (2.12) reduces to

$$\vec{J} = -LzF\nabla\varphi \tag{2.18}$$

Taking into account the relation between the molar flux $\vec{J}$ of charged particles and the corresponding charge flux (i.e. current density) $\vec{j}$

$$\vec{j} = zF\vec{J} \tag{2.19}$$

the combination of Eqs. (2.18) and (2.19) yields

$$\vec{j} = -L(zF)^2\nabla\varphi \tag{2.20}$$

Comparing Eq. (2.20) with Eq. (2.6) gives an expression of L in terms of the isotropic electrical conductivity σ

$$L = \frac{\sigma}{(zF)^2} \tag{2.21}$$

Since electrical conductivity can be expressed by the concentration of charge carriers c and their electrical mobility u according to the fundamental equation

$$\sigma = |z|Fcu \tag{2.22}$$

the transport coefficient can be expressed as

$$L = \frac{cu}{|z|F} \tag{2.23}$$

Another important relation for the transport coefficient can be derived by assuming constant electrical potential in Eq. (2.12) and expressing the chemical potential as a function of activity a

$$\mu = \mu^{\circ} + RTln\, a = \mu^{\circ} + RTln\, \gamma + RTln\, c \tag{2.24}$$

where γ is the activity coefficient. If the activity coefficient is independent of position, Eq. (2.14) reduces to

$$\vec{J} = -LRT\nabla ln\, c = -\frac{LRT}{c}\nabla c \tag{2.25}$$

Comparison of Eq. (2.25) with Eq. (2.8) for isotropic diffusion yields

$$L = \frac{cD}{RT} \tag{2.26}$$

where D is called self-diffusion coefficient to distinguish it from other types of diffusion coefficients to be introduced further below.

Therefore, the phenomenological equation for mass transport (2.12) can be equivalently expressed in terms of conductivity, electrical mobility or diffusivity, according to

$$\vec{J} = -\frac{\sigma}{(zF)^2}\nabla\eta \tag{2.27}$$

$$\vec{J} = -\frac{cu}{|z|F}\nabla\eta \tag{2.28}$$

$$\vec{J} = -\frac{cD}{RT}\nabla\eta \tag{2.29}$$

Moreover, Eqs. (2.21), (2.23) and (2.26) give relations between the diffusion coefficient and the electrical quantities, namely the Einstein relation

$$\frac{u}{|z|F} = \frac{D}{RT} \tag{2.30}$$

and the Nernst-Einstein equation

$$\sigma = \frac{(zF)^2 cD}{RT} \tag{2.31}$$

The Einstein relation is a consequence of the assumption that the transport coefficients L in Eqs. (2.18) and (2.25) are actually identical. This follows from Eq. (2.12) and the fact that the electrochemical potential is the appropriate quantity for indicating thermodynamic equilibrium [145].

2.3.1 Chemical and ambipolar diffusion

So far in the discussion mass transfer of a single component has been treated. However, very often mass transport involves more than one component and Eqs. (2.12) or (2.14) have to be extended to the general form of Eq. (2.2). Setting up the phenomenological equations for a system of direct relevance to mixed ionic-electronic conducting oxides investigated in this work gives

$$\begin{aligned} \vec{J}_{O^{2-}} &= -L_{O^{2-}} \nabla \eta_{O^{2-}} - L_{O^{2-}e^-} \nabla \eta_{e^-} \\ \vec{J}_{e^-} &= -L_{e^-O^{2-}} \nabla \eta_{O^{2-}} - L_{e^-} \nabla \eta_{e^-} \end{aligned} \tag{2.32}$$

where $\vec{J}_{O^{2-}}$ and $\vec{J}_{e^-}$ are the fluxes of oxygen ions and electrons, respectively. $L_{O^{2-}}$ and L_{e^-} are the transport coefficients proper and $L_{O^{2-}e^-}$ and $L_{e^-O^{2-}}$ are the so-called cross-coefficients of mass transport. According to the symmetry principle given in Eq. (2.5) $L_{O^{2-}e^-} = L_{e^-O^{2-}}$. Cationic species of the compound are assumed to be immobile and serve as a frame of reference for the movement of the mobile components.

It is often assumed that the cross-coefficients between ions and electrons are practically zero, however, this assumption is not of general validity and has to be verified experimentally for each system under consideration. It is often found to hold for ions with constant valency and moderate electric currents [145]. In this work electron-ion cross-coefficients are neglected for a description of oxygen transport in rare earth nickelates. However, it should be mentioned that Kim and Yoo obtained significant cross-coefficients for $La_2NiO_{4+\delta}$ from ion-blocking polarization experiments at 800°C [149].

Setting $L_{O^{2-}e^-} = L_{e^-O^{2-}} = 0$ in Eq. (2.32) gives two decoupled transport equations for the oxygen ions and the electrons. Rewriting Eq. (2.32) in terms of conductivities

$$\begin{aligned} \vec{J}_{O^{2-}} &= -\frac{\sigma_{O^{2-}}}{4F^2} \nabla \eta_{O^{2-}} \\ \vec{J}_{e^-} &= -\frac{\sigma_{e^-}}{F^2} \nabla \eta_{e^-} \end{aligned} \tag{2.33}$$

where $\sigma_{O^{2-}}$ and σ_{e^-} are the electrical conductivity of oxygen ions and electrons, respectively.

However, the decoupling between ionic and electronic fluxes is not a complete one because of the lower electrical mobility of oxygen ions compared to that of electrons. The difference in the corresponding velocities of the carriers in the initial phase quickly builds up an internal electric field which accelerates the slower moving ions and retards the motion of the electrons until some average velocity is attained. Hence, the electrical term of the electrochemical potential must not be neglected. Eq. (2.33) is restated in the following formulas by expanding the electrochemical potential according to Eq. (2.10)

$$\begin{aligned} \vec{J}_{O^{2-}} &= -\frac{\sigma_{O^{2-}}}{4F^2}\nabla\mu_{O^{2-}} + \frac{\sigma_{O^{2-}}}{2F}\nabla\varphi_{int} \\ \vec{J}_{e^-} &= -\frac{\sigma_{e^-}}{F^2}\nabla\mu_{e^-} + \frac{\sigma_{e^-}}{F}\nabla\varphi_{int} \end{aligned} \tag{2.34}$$

where $-\nabla\varphi_{int}$ is the internally generated electrical field.

In addition, the flows of ions and electrons are coupled to maintain electroneutrality in the bulk. The electroneutrality condition can be treated in the context of the continuity equation as follows. The local version of the continuity equation reads

$$\frac{\partial c}{\partial t} = -\nabla \cdot \vec{J} + \dot{q} \tag{2.35}$$

that is, a change of ‘concentration’ of some physical quantity around a point can be caused by a flow $\vec{J}$ through the closed surface into the point or by the ‘generation’ $\dot{q}$ of the quantity per volume and time at the point.

When applying Eq. (2.35) to electrical charge, the concentration of charge becomes the charge density ρ, the charge flux is the current density $\vec{j}$ and the source term must be zero due to charge conservation

$$\frac{\partial \rho}{\partial t} = -\nabla \cdot \vec{j} \tag{2.36}$$

Contrary to the situation at internal and external interfaces of a sample the electroneutrality condition in the bulk is usually strictly observed, that is $\rho = 0$ in Eq. (2.36). From the vanishing divergence of the current density it follows that the current density is constant within the bulk

$$\vec{j} = const\ (space) \tag{2.37}$$

A constant internal net current can be sustained if balanced by an outer electronic current, i.e. when the sample is part of an electronic circuit. In the case of pure diffusion, there is no external current and the current density in Eq. (2.37) has to be zero. Since the current is the sum of the electronic and ionic partial currents, which in turn are related to the electronic and ionic flows by Eq. (2.19), it follows that the electronic and ionic flows are linked by

$$2\vec{J}_{O^{2-}} + \vec{J}_{e^-} = 0 \tag{2.38}$$

It should be mentioned that, strictly speaking, the existence of an internal electrical potential and perfect electroneutrality are inconsistent, since it is the deviation from electroneutrality that gives rise to internal electric fields. However, since even a very small amount of charge separation can create large fields, the electroneutrality condition can be assumed to hold.

Eliminating the internal potential in Eq. (2.34) and including the electroneutrality condition via Eq. (2.38) leads to an expression for the flux of oxygen ions

$$\vec{J}_{O^{2-}} = -\frac{1}{4F^2}\frac{\sigma_{O^{2-}}\sigma_{e^-}}{\sigma_{O^{2-}}+\sigma_{e^-}}(\nabla\mu_{O^{2-}} - 2\nabla\mu_{e^-}) \tag{2.39}$$

For a further simplification it is assumed that the classical relationships of equilibrium thermodynamics still hold at each point in the system, although the system is clearly not in thermodynamic equilibrium due to non-vanishing gradients of electrochemical potentials. In other words the system is assumed to be in a state of *local equilibrium*, which is not a contradiction to the system as a whole being out of equilibrium [148]. This can be appreciated from the fact that equations in classical thermodynamics do not involve spatial gradients of state variables and is further based on the assumption that, despite of flux divergences, concentrations are still close to their equilibrium values [150].

The external oxygen equilibrium is described by

$$\frac{1}{2}O_2 + 2e^- \leftrightarrows O^{2-} \tag{2.40}$$

and the corresponding equilibrium condition reads

$$\frac{1}{2}\mu_{O_2} + 2\eta_{e^-} = \eta_{O^{2-}} \tag{2.41}$$

Since Eq. (2.40) is balanced with respect to charge, electric terms of the electrochemical potential cancel in Eq. (2.41) with the result

$$\frac{1}{2}\mu_{O_2} + 2\mu_{e^-} = \mu_{O^{2-}} \tag{2.42}$$

Taking the gradient of Eq. (2.42) gives

$$\frac{1}{2}\nabla\mu_{O_2} + 2\nabla\mu_{e^-} = \nabla\mu_{O^{2-}} \tag{2.43}$$

Including the reaction between molecular and atomic oxygen

$$O_2 \leftrightarrows 2O \tag{2.44}$$

with the corresponding equilibrium condition

$$\mu_{O_2} = 2\mu_O \tag{2.45}$$

gives a relation between gradients of oxygen and charged components of the material according to

$$\frac{1}{2}\nabla\mu_{O_2} = \nabla\mu_O = \nabla\mu_{O^{2-}} - 2\nabla\mu_{e^-} \tag{2.46}$$

and plugging Eq. (2.46) into Eq. (2.39) yields the fundamental transport equations for the oxygen flux

$$\vec{J}_{O^{2-}} = \vec{J}_O = 2\vec{J}_{O_2} = -\frac{1}{4F^2}\frac{\sigma_{O^{2-}}\sigma_{e^-}}{\sigma_{O^{2-}}+\sigma_{e^-}}(\nabla\mu_{O^{2-}} - 2\nabla\mu_{e^-})$$

$$= -\frac{1}{4F^2}\frac{\sigma_{O^{2-}}\sigma_{e^-}}{\sigma_{O^{2-}}+\sigma_{e^-}}\nabla\mu_O = -\frac{1}{8F^2}\frac{\sigma_{O^{2-}}\sigma_{e^-}}{\sigma_{O^{2-}}+\sigma_{e^-}}\nabla\mu_{O_2} \qquad (2.47)$$

The conductivity factor in Eq. (2.47) is the so-called ambipolar conductivity σ_{amb}

$$\sigma_{amb} \equiv \frac{\sigma_{O^{2-}}\sigma_{e^-}}{\sigma_{O^{2-}}+\sigma_{e^-}} \qquad (2.48)$$

which corresponds to a series connection of ionic and electronic currents, expressing the fact that both currents are necessary for the transport process [151].

The link to the diffusion coefficient can be established by expressing the gradient in oxygen chemical potential as the corresponding gradient in concentration in Eq. (2.47)

$$\vec{J}_O = -\frac{\sigma_{amb}}{4F^2}\nabla\mu_O = -\frac{\sigma_{amb}}{4F^2}\frac{\partial\mu_O}{\partial c_O}\nabla c_O \qquad (2.49)$$

Comparing Eq. (2.49) with Eq. (2.8) gives

$$D_{chem} = \frac{\sigma_{amb}}{4F^2}\frac{\partial\mu_O}{\partial c_O} = \frac{RT}{4F^2}\frac{\sigma_{amb}}{c_O}\frac{\partial ln\, a_O}{\partial ln\, c_O} \qquad (2.50)$$

where D_{chem} is the chemical or ambipolar diffusion coefficient of oxygen. Alternative notations for D_{chem} are $\widetilde{D}$ and D^{δ}. Chemical diffusion is diffusion as a response to a gradient in chemical composition. Ambipolar diffusion, on the other hand, is the coupled diffusion of at least two different kinds of charged particles or charged defects. Although, strictly speaking, ambipolar diffusion and chemical diffusion describe different processes, this differentiation is usually not observed in the literature and for any process where there is coupling between fluxes, the terms chemical diffusion and chemical diffusion coefficient are used almost exclusively [152].

The derivative $\frac{\partial \ln a_O}{\partial ln c_O}$ in Eqs. (2.49) and (2.50) is the so-called thermodynamic factor Γ_O, which is an important quantity used for converting the chemical diffusion coefficient to the self-diffusion coefficient as is shown further below. The thermodynamic factor can be expressed in various ways

$$\Gamma_O \equiv \frac{c_O}{RT}\frac{\partial \mu_O}{\partial c_O} = \frac{1}{RT}\frac{\partial \mu_O}{\partial ln\, c_O} = \frac{\partial ln\, a_O}{\partial ln\, c_O}$$
$$= \frac{1}{RT}\frac{\partial \frac{1}{2}\mu_{O_2}}{\partial ln\, c_O} = \frac{1}{2}\frac{\partial ln\, a_{O_2}}{\partial ln\, c_O} = \frac{1}{2}\frac{\partial ln\, p_{O_2}}{\partial ln\, c_O} \tag{2.51}$$

The last expression in Eq. (2.51) forms the basis for the experimental determination of the thermodynamic factor by means of thermogravimetric analysis or coulometric titration. Thus, measuring the oxygen concentration of a material in equilibrium with the surrounding gas phase at an oxygen partial pressure pO_2 allows the determination of Γ_O as long as a reference point for the oxygen concentration c_O is known. For example, using thermogravimetric analysis c_O can be obtained by transforming the material to well-known reduction products by exposure to hydrogen-containing atmospheres.

The derivative $\frac{\partial \mu_O}{\partial c_O}$ in Eqs. (2.49) – (2.51) can be separated into contributions of ionic and electronic components according to

$$\frac{1}{RT}\frac{\partial \mu_O}{\partial c_O} = \frac{w_{O^{2-}}}{c_{O^{2-}}} + 4\frac{w_{e^-}}{c_{e^-}} \tag{2.52}$$

where $w_{O^{2-}} \equiv \frac{\partial ln\, a_{O^{2-}}}{\partial ln\, c_{O^{2-}}}$ and $w_{e^-} \equiv \frac{\partial ln\, a_{e^-}}{\partial ln\, c_{e^-}}$ are thermodynamic factors of oxygen ions and electrons, respectively, which differ significantly from unity [151].

The ambipolar conductivity (Eq. (2.48)) can be couched in various ways when introducing transport numbers (transference numbers) t_i, which are defined as the fraction of partial current j_i that a charge carrier i contributes to the total current j_t or, equivalently, as the ratio of the partial conductivity σ_i to the total conductivity σ_t.

The transport number of oxygen ions reads

$$t_{O^{2-}} \equiv \frac{j_{O^{2-}}}{j_t} = \frac{\sigma_{O^{2-}}}{\sigma_t} \tag{2.53}$$

and similar for electronic charge carriers

$$t_{e^-} \equiv \frac{j_{e^-}}{j_t} = \frac{\sigma_{e^-}}{\sigma_t} \tag{2.54}$$

where $j_t = j_{O^{2-}} + j_{e^-}$ and $\sigma_t = \sigma_{O^{2-}} + \sigma_{e^-}$.
Hence, the ambipolar conductivity in Eq. (2.48) can be expressed as

$$\sigma_{amb} = \frac{\sigma_{O^{2-}}\sigma_{e^-}}{\sigma_{O^{2-}} + \sigma_{e^-}} = t_{O^{2-}}\sigma_{e^-} = t_{e^-}\sigma_{O^{2-}} = t_{O^{2-}}t_{e^-}\sigma_t \tag{2.55}$$

In the case of predominantly electronic conductors like SOFC-cathodes, t_{e^-} is ~1 and thus $\sigma_{amb} \approx \sigma_{O^{2-}}$, whereas for ionic conductors like SOFC-electrolytes $t_{O^{2-}}$ is ~1 and $\sigma_{amb} \approx \sigma_{e^-}$.

Hence, for mixed conductors with predominantly electronic conduction, the chemical diffusion coefficient in Eq. (2.50) becomes

$$D_{chem} = \frac{RT\sigma_{O^{2-}}}{4F^2 c_O}\Gamma_O \tag{2.56}$$

and using the Nernst-Einstein equation (2.31) yields

$$D_{chem} = D_O\Gamma_O \tag{2.57}$$

where D_O is called the self-diffusion coefficient or component diffusion coefficient of oxygen. The self-diffusion coefficient describes diffusion in absence of a driving force based solely on statistical and uncorrelated atomic jumps. Thus, for predominantly electronic conductors the thermodynamic factor establishes the connection between chemical diffusion coefficient and self-diffusion coefficient of oxygen if the thermodynamic factor of oxygen at the corresponding temperature and oxygen partial pressure is known.

So far all mobile species have been treated on the component level. However, the transport equations can also be expressed in terms of defects [150] if some knowledge of the defect structure of the material under consideration is available. Relations between chemical potentials of ionic and electronic defects can be established on the basis of local equilibrium for the appropriate defect-chemical equations and the calculation of the flux equations proceeds along the same lines as given above for the components. However, a somewhat different approach is used below without drawing upon the concept of internal electrical potential and instead using electrochemical potentials to express defect equilibria.

The following discussion deals with the rather general case of an oxide ceramics with oxygen vacancies and oxygen interstitials as ionic defects and conduction electrons and holes as electronic defects. The ionic defects are assumed to be in a Frenkel-type defect equilibrium, according to

$$O_O^x + V_i^x \leftrightarrows V_O^{\cdot\cdot} + O_i'' \tag{2.58}$$

where Kröger-Vink notation has been used for structure elements [153].

Rewriting Eq. (2.58) in terms of building elements gives

$$nil \rightleftarrows (V_O^{\cdot\cdot} - O_O^x) + (O_i''-V_i^x) \tag{2.59}$$

Assigning electrochemical potentials to charged building units, the equilibrium condition for Eq. (2.59) reads

$$\eta_{\{V_O^{\cdot\cdot}\}} + \eta_{\{O_i''\}} = 0 \tag{2.60}$$

where $\{V_O^{\cdot\cdot}\} \equiv (V_O^{\cdot\cdot} - O_O^x)$ and $\{O_i''\} \equiv (O_i''-V_i^x)$ are building units of oxygen vacancies and interstitials, respectively.

Electronic defects, which may either be localized on ions in the material or may be accommodated in electron bands, are created or annihilated according to

$$nil \ \rightleftarrows \ e' + h^{\cdot} \tag{2.61}$$

where e' and $h^{\cdot}$ are electronic building units. The equilibrium condition for Eq. (2.61) is

$$\eta_{e'} + \eta_{h^{\cdot}} = 0 \tag{2.62}$$

Moreover, external equilibrium with gaseous oxygen is assumed according to

$$\frac{1}{2}O_2 + V_O^{\cdot\cdot} \ \leftrightarrows \ O_O^x + 2h^{\cdot} \tag{2.63}$$

or in terms of building units

$$\frac{1}{2}O_2 + (V_O^{\cdot\cdot} - O_O^x) \ \leftrightarrows \ 2h^{\cdot} \tag{2.64}$$

In equilibrium the corresponding electrochemical potentials are related by

$$\frac{1}{2}\mu_{O_2} + \eta_{\{V_O^{\cdot\cdot}\}} = 2\eta_{h^{\cdot}} \tag{2.65}$$

The external oxygen reaction equation can be framed in various ways differing from Eqs. (2.63) – (2.65) in the type of ionic or electronic defect species used. However, these equations are all equivalent by virtue of Eqs. (2.58) – (2.62).

The flux equations for the defects are

$$\begin{aligned} \vec{J}_{\{V_O^{\cdot\cdot}\}} &= -\frac{\sigma_{\{V_O^{\cdot\cdot}\}}}{4F^2}\nabla\eta_{\{V_O^{\cdot\cdot}\}} \qquad & \vec{J}_{\{O_i''\}} &= -\frac{\sigma_{\{O_i''\}}}{4F^2}\nabla\eta_{\{O_i''\}} \\ \vec{J}_{e'} &= -\frac{\sigma_{e'}}{F^2}\nabla\eta_{e'} & \vec{J}_{h^{\cdot}} &= -\frac{\sigma_{h^{\cdot}}}{F^2}\nabla\eta_{h^{\cdot}} \end{aligned} \tag{2.66}$$

The electroneutrality condition in the absence of external currents gives

$$2\vec{J}_{\{V_O^{\cdot\cdot}\}} + \vec{J}_{h^{\cdot}} = 2\vec{J}_{\{O_i''\}} + \vec{J}_{e'} \tag{2.67}$$

and the net oxygen flux is given as the difference between oxygen interstitial and vacancy flows as

$$\vec{J}_O = \vec{J}_{\{O_i''\}} - \vec{J}_{\{V_O^{\cdot\cdot}\}} \tag{2.68}$$

Combining Eqs. (2.66) – (2.68) and assuming local equilibrium (Eqs. (2.60), (2.62), (2.65)) gives

$$\vec{J}_O = -\frac{\sigma_{amb}}{4F^2}\nabla\mu_O = -\frac{\sigma_{amb}}{4F^2}\frac{\partial\mu_O}{\partial c_O}\nabla \mathrm{c}_O \tag{2.69}$$

similar to Eq. (2.49). However, the ambipolar conductivity is now

$$\sigma_{amb} \equiv \frac{\sigma_{ion}\sigma_{eon}}{\sigma_{ion}+\sigma_{eon}} = \frac{(\sigma_{\{V_O^{\cdot\cdot}\}} + \sigma_{\{O_i''\}})(\sigma_{h^{\cdot}} + \sigma_{e'})}{\sigma_{\{V_O^{\cdot\cdot}\}} + \sigma_{\{O_i''\}} + \sigma_{h^{\cdot}} + \sigma_{e'}} \tag{2.70}$$

where $\sigma_{ion} \equiv \sigma_{\{V_O^{\cdot\cdot}\}} + \sigma_{\{O_i''\}}$ and $\sigma_{eon} \equiv \sigma_{h^{\cdot}} + \sigma_{e'}$ are the total ionic and electronic conductivity, respectively.

Expressions for the chemical diffusion coefficient and thermodynamic factor are identical to Eqs. (2.50) and (2.51), respectively. An interesting result is obtained when expanding $\frac{\partial\mu_O}{\partial c_O}$ in Eq. (2.69) in terms of defects for dilute conditions. In this case concentrations can be used instead of activities [150] and thus thermodynamic factors of the defects approach unity, yielding

$$\frac{1}{RT}\frac{\partial\mu_O}{\partial c_O} = \frac{1}{c_{\{V_O^{\cdot\cdot}\}} + c_{\{O_i''\}}} + \frac{4}{c_{h^{\cdot}} + c_{e'}} \tag{2.71}$$

Eq. (2.71) is to be compared with the corresponding description on the component level (Eq. (2.52)) where the above simplification does not apply. A more general treatment considers interaction between ionic and electronic defects (trapping) which generates oxygen defects of different valence such as O_i', O_i^x, $V_O^{\cdot}$ and V_O^x [150]. While some of these defect species might be relevant for rare earth nickelates [141] and have to be considered for a correct interpretation of the diffusion coefficient, their presence does not change the essential form of the equations used to model conductivity relaxation transients.

Many oxides can be considered as special cases of the generic description given above. Taking as an example perovskite-type oxides like $La_{1-x}Sr_xCo_yFe_{1-y}O_{3-\delta}$ relevant defect species are oxygen vacancies and electron holes and thus the following simplifications can be applied to the equations given above

$$c_{\{O_i''\}} = 0,\ \sigma_{\{O_i''\}} = 0$$

$$c_{e'} \approx 0,\ \sigma_{e'} \approx 0 \tag{2.72}$$

Considering $Ln_2NiO_{4+\delta}$ (Ln = La, Pr, Nd) as another example and assuming oxygen interstitials, oxygen vacancies and electron holes as relevant defects, the contribution of electron defects can be neglected

$$c_{e'} \approx 0,\ \sigma_{e'} \approx 0 \tag{2.73}$$

2.3.2 Tracer diffusion

Tracer diffusion is a diffusion process that is caused by a concentration gradient while maintaining constant chemical composition. This can be achieved by using different isotopes of an element, for example ^{18}O diffusing into a sample containing mostly ^{16}O

$$\vec{J}_O = D_O^* \nabla c_O = -\frac{c_O D^*}{RT} \nabla \mu_O \tag{2.74}$$

where D_O^* is the tracer diffusion coefficient of oxygen. Since no change in composition takes place and assuming isotopic mass effects to be negligible, activities can be replaced by concentrations. If the atomic jumps are uncorrelated, that is the probability of a single elementary jump does not depend on the previous jumps, as is the case for a dilute interstitial diffusion mechanism, then the tracer diffusion coefficient D_O^* is equal to the self-diffusion coefficient D_O. If the jumps are correlated, e.g. for vacancy-based diffusion mechanisms, both diffusion coefficients are related by a correlation factor f according to

$$D_O^* = f D_O \tag{2.75}$$

In the case of tracer diffusion via vacancies the correlation factor expresses the backwards directed tendency in the diffusion process. The atomistic interpretation of this ‘drag-effect’ is that after a successful jump, where vacancy and tracer atom have changed place, it is more likely for the tracer to jump back into its previous position than the probability that a newly arrived vacancy is available for a next forward jump of the tracer. Correlation factors for several lattice types are given by Philibert [154]. For oxygen diffusion via vacancies in perovskite materials the correlation factor has been estimated as 0.69 [155]. For interstitial oxygen diffusion like rare earth nickelates $f = 1$ [154,156].

2.3.3 Conductivity diffusion coefficient

The Nernst-Equation Eq. (2.31) establishes the connection between the self-diffusion coefficient and the partial electrical conductivity. More accurately, however, it is rather the conductivity diffusion coefficient D^Q (D^σ) which is obtained by measuring the dc-conductivity and converting it to a diffusivity by means of the Nernst-Einstein equation [157]

$$D^Q = \frac{RT\sigma}{(zF)^2 c} \tag{2.76}$$

D^Q is linked to the tracer diffusion coefficient D^* by the Haven ratio H_R, which is defined as the ratio between the two types of diffusion coefficients

$$H_R \equiv \frac{D^*}{D^Q} \tag{2.77}$$

Usually $H_R < 1$ but in special situations H_R can exceed 1 [157]. Typically, Haven ratios lie in the range of 0.6-0.8 [158] and thus are often neglected considering the usually much higher experimental uncertainties.

2.3.4 Temperature dependence of transport properties

Diffusion is a thermally activated process and the temperature dependence of the self-diffusion coefficient of oxygen D_O is described by the Arrhenius equation

$$D_O = D^0 e^{-\frac{E_a^D}{RT}} \tag{2.78}$$

where E_a^D is activation energy for the diffusion process and D^0 is the pre-exponential factor. D^0 may show a slight variation with temperature which is usually neglected due to the dominant contribution of the exponential factor.

Since $D_{chem} = D_O \Gamma_O$ (Eq. (2.57)) the activation energy of the chemical diffusion coefficient D_{chem} contains contributions from both self-diffusion D_O and the thermodynamic factor Γ_O. Empirically, a sufficiently linear $ln\, \Gamma_O\ vs.\ T^{-1}$-relationship is often observed and thus the temperature dependence of D_{chem} is usually modeled by an Arrhenius-type equation of the form of Eq. (2.78). In the case of nickelates and many mixed conducting perovskites Γ_O is found to decrease with increasing temperature and therefore the activation energy of D_{chem} is somewhat smaller than for the corresponding self-diffusion coefficient. Similarly, for oxygen surface exchange coefficients – introduced further below – an Arrhenius-type temperature dependence is usually found.

Inserting Eq. (2.78) into the Nernst-Einstein equation Eq. (2.31) gives the temperature dependence of the ionic conductivity

$$\sigma_i = \frac{\sigma^0}{T} e^{-\frac{E_a^\sigma}{RT}} \tag{2.79}$$

where E_a^σ and σ^0 are the activation energy and the pre-exponential factor, respectively, of the ionic conductivity.

2.4 Experimental determination of diffusion coefficients in solids

Diffusion coefficients can be obtained by direct application of Fick's first law. For example, analyzing the steady state particle flux through an oxygen-conducting ceramic membrane affords the determination of the chemical diffusion coefficient of oxygen. However, more often it is the combination of Fick's first law with the continuity equation whose solutions, under appropriate boundary and initial conditions, form the basis for interpretation of experiments and derivation of diffusivities. The full expression of the continuity equation has already been mentioned above where it has been used to link changes in the charge density with electrical current. Eq. (2.35) can be applied to mass flux as well which yields in the context of oxygen mass transport

$$\frac{\partial c_O}{\partial t} = -\nabla \cdot \vec{J}_O + \dot{q}_O \tag{2.80}$$

and states that the rate of concentration change of oxygen at a certain point in space is the result of oxygen entering or leaving a volume element around that point through its closed surface $(-\nabla \cdot \vec{J}_O)$ or the production or annihilation of the component inside the volume element $(\dot{q}_O)$. The divergence term includes fluxes caused by diffusion, migration and convection. Convection is relevant for fluid systems but is obviously of minor significance in solids. The second term $(\dot{q}_O)$ lumps together sources and sinks for the oxygen species under consideration like defect chemical reactions, electron or hole trapping (i.e. reduction or oxidation of oxygen) or ionic trapping processes such as the immobilization and thus withdrawal of the oxygen species from the transport process by forming vacancy-dopant complexes or clusters.

For example, considering an oxide with Frenkel disorder on the oxygen sublattice (Eqs. (2.58) and (2.59)) the application of the continuity equation (2.80) to both oxygen vacancies and interstitials yields

$$\begin{aligned} \frac{\partial c_{\{V_O^{\cdot\cdot}\}}}{\partial t} &= -\nabla \cdot \vec{J}_{\{V_O^{\cdot\cdot}\}} + \dot{q}_{\{V_O^{\cdot\cdot}\}} \\ \frac{\partial c_{\{O_i''\}}}{\partial t} &= -\nabla \cdot \vec{J}_{\{O_i''\}} + \dot{q}_{\{O_i''\}} \end{aligned} \tag{2.81}$$

where neither $\dot{q}_{\{V_O^{\bullet\bullet}\}}$ nor $\dot{q}_{\{O_i''\}}$ are zero due to internal Frenkel-type defect reaction (despite the assumption of local equilibrium [150]). However, it was shown by Maier and Schwitzgebel [159] that for certain linear combinations of defect concentrations (conservative ensembles) the source term in the continuity equation can be dropped. For Frenkel-type defect equilibria the appropriate choice of the conservative ensemble of oxygen is $c_O \equiv c_{\{O_i''\}} - c_{\{V_O^{\bullet\bullet}\}}$ (and similarly for the oxygen flux $\vec{J}_O \equiv \vec{J}_{\{O_i''\}} - \vec{J}_{\{V_O^{\bullet\bullet}\}}$) and it is easily seen from Eq. (2.59) that the source term $\dot{q}_O = \dot{q}_{\{O_i''\}} - \dot{q}_{\{V_O^{\bullet\bullet}\}}$ vanishes. A comprehensive treatment of conservative ensembles with respect to oxygen transport processes in oxides including oxygen defects of various charge and the correct interpretation of results from electrochemical transport measurements has been given by Maier [150,160-162].

Assuming that defect reactions and trapping mechanisms are either inactive or have been accounted for by introducing conservative ensembles of oxygen, Eq. (2.80) reduces to

$$\frac{\partial c_O}{\partial t} = -\nabla \cdot \vec{J}_O \tag{2.82}$$

Plugging in Fick's first law for the flux $\vec{J}_O$ yields

$$\frac{\partial c_O}{\partial t} = \nabla \cdot (D \nabla c_O) = \nabla D \nabla c_O + D \nabla^2 c_O \tag{2.83}$$

where the actual type of diffusion coefficient is left unspecified in Eq. (2.83) and depends on the kind of experiment conducted (e.g. tracer or chemical diffusion). Eq. (2.83) is called Fick's second law or diffusion equation. It is a partial differential equation of first order in time and second order in space and its solution – based on the appropriate boundary and initial conditions – gives the concentration of oxygen as a function of space and time. If the diffusion coefficient is considered independent of the spatial coordinates or at least $|\nabla D \nabla c_O| \ll |D \nabla^2 c_O|$, Eq. (2.83) is considerably simplified to

$$\frac{\partial c_O}{\partial t} = D \nabla^2 c_O \tag{2.84}$$

which in Cartesian coordinates can be explicitly written as

$$\frac{\partial c_O}{\partial t} = D(\frac{\partial^2 c_O}{\partial x^2} + \frac{\partial^2 c_O}{\partial y^2} + \frac{\partial^2 c_O}{\partial z^2}) \tag{2.85}$$

Finally, if the experimental arrangement or the sample dimensions are chosen so that diffusion is taking place in one dimension only, one arrives at

$$\frac{\partial c_O}{\partial t} = D\frac{\partial^2 c_O}{\partial x^2} \tag{2.86}$$

which is Fick's second law in its most simplified form. Eq. (2.86) is the starting point for the development of solutions used in this work for the determination of chemical diffusion coefficients and – introduced through corresponding boundary conditions – for chemical surface exchange coefficients, as discussed below. Starting from the one-dimensional solutions extensions to higher dimension are straightforward in rectangular systems.

2.5 Sample geometries

Electrochemical measurements have been performed on densely sintered samples using the four point technique in galvanostatic mode. With this method an electrical connection to the sample is accomplished by four different electronic contacts. Two contacts serve as constant current source and sink and the other two as voltage probes that carry practically no current, provided a high-impedance voltmeter is used for measurement. This separation eliminates the contributions of non-ohmic contact and polarization resistances, which affect only the current-carrying contacts but not the probes.

Two sample geometries with different contact arrangements and sample geometries have been employed in this work (Fig. 2.6). In the linear four-point geometry the sample is cut as an elongated rectangular parallelepiped where the two current contacts cover the front faces and the voltage probes are wound around the sample with some distance from the current contacts (Fig. 2.6, right). The distance between the voltage probes should be as large as possible to give maximum voltage signals. However, the probes should also be located at some distance from the current-carrying contacts to allow for homogenization of the current paths, which are assumed to be parallel to the sample axis when traversing the sample cross sections where the probes are located. Taking into considering the two opposing trends mentioned above, the probes were symmetrically placed at a distance of one third of the bar length [163].

In the van der Pauw geometry the sample is shaped as a thin slab with the four contacts located at the circumference of the sample (Fig. 2.6, left). In principle, sample shape as well as contact positions at the sample boundary are arbitrary, the only requirements from theory being a constant sample thickness and point-like contacts. For practical reasons, samples prepared in van der Pauw geometry were usually more or less square slabs with roughly equally spaced contacts at their four corners.

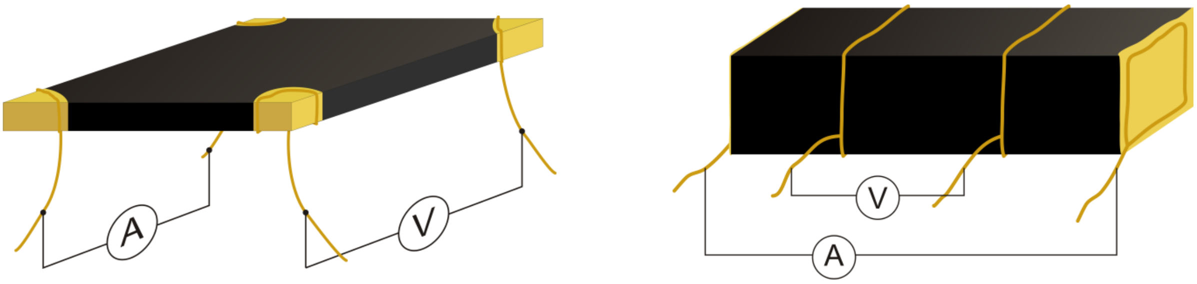

Fig. 2.6 Four-point contact arrangements used in this work; van der Pauw geometry (left) and linear four-point geometry (right).

The following discussion summarizes the advantages and disadvantages of both sample geometries from a practical point of view as well as the requirements to be fulfilled for a correct determination of electrical and transport parameters from the measurements. The theoretical treatment of the transport processes for both sample geometries is given in detail further below.

As mentioned above the application of the four-contact technique eliminates errors introduced by both polarization effects and contact resistances at the interfaces of current-carrying electrodes.

2.5.1 Linear four-point geometry

For the determination of the electrical conductivity the sample should have a constant cross-section over the entire sample length and the lateral dimensions of the bar as well as the distance of the voltage probes have to be known. This puts a somewhat higher demand on sample preparation when compared to samples in van der Pauw geometry. The main drawback is the difficulty in attaching the voltage probes at a constant distance along the sample axis. This is complicated by the application of contact paste necessary to establish a good electronic contact to the ceramic material, where the paste may be difficult to apply as a thin band along the probe wires which makes the probe distance somewhat ill-defined. In this work, a precise positioning of the voltage probes was facilitated by cutting small grooves into the sample surface by a diamond wire saw before attaching the probe wires. However, applying a thin line of contact paste still remains an issue.

For the determination of oxygen transport properties by the conductivity relaxation technique it is important to limit the diffusion process to two-dimensional diffusion normal to the sample axis, while oxygen diffusion must not take place parallel to the axis. Although analytical solutions to the diffusion equation for three-dimensional diffusion are readily obtained, the simple relation between mass relaxation and conductivity relaxation is lost when the above mentioned limitation is not satisfied. This restriction may be lifted if the distance between current-carrying contacts and voltage probes is significantly larger that the diffusion length of oxygen along the sample axis during a relaxation measurement. It can then be assumed that the current lines perturbed by the non-homogeneous oxygen distribution along the sample axis have been homogenized at the position of the voltage probes. For bar-shaped samples prepared in this work the entire sample fronts were covered by thin gold foils, thus preventing oxygen exchange at the two front faces. Contrary to the thin sample necessary for van der Pauw measurements, bar-shaped specimens can be made rather thick, which is advantageous for measuring diffusion coefficients of materials that tend to have predominantly surface controlled oxygen exchange kinetics.

2.5.2 Van der Pauw geometry

The van der Pauw technique was originally developed for precise measurements of electronic conductivity and Hall-coefficients of semiconductors [164]. Later on, its use has been extended to the determination of the electrical conductivity for mixed ionic-electronic conductors [165-167]. The main advantage is its independence from the precise locations of the electronic contacts as long as they are positioned at the circumference of the sample and are designed sufficiently small. The sample geometry is limited to slabs of a constant thickness but otherwise no constraints have to be imposed on the sample shape. The measurement itself is more complicated than for linear samples because current and voltage probes have to be switched at least once by 90 degree which makes more advanced electronic equipment or switching devices necessary for automated measurements.

It has been shown by Preis et al. [168] that measurements on MIECs in van der Pauw geometry can be used for conductivity relaxation measurements as well. Similar to the linear four-point geometry given above, the direction of diffusion has to be restricted in order to maintain the equivalence between transients in the relaxation of mass and conductivity. For samples in van der Pauw geometry the diffusion flow is to be limited normal to the plane of the disk and must not take place parallel to it. This can be ensured by blocking the lateral faces by some material that is electronically insulating and impervious to oxygen. For samples with a side length-to-thickness ratio around 10:1 or above lateral diffusion can be neglected [169].

As a general rule it can be established that in conductivity relaxation measurements diffusion may only take place *normal* to lines or planes of current flow, but *not parallel* to them in order to transfer the analytical solutions derived for mass exchange to the transients in electrical conductivity. An illustration of this rule is given in Fig. 2.7 for the two geometries under consideration.

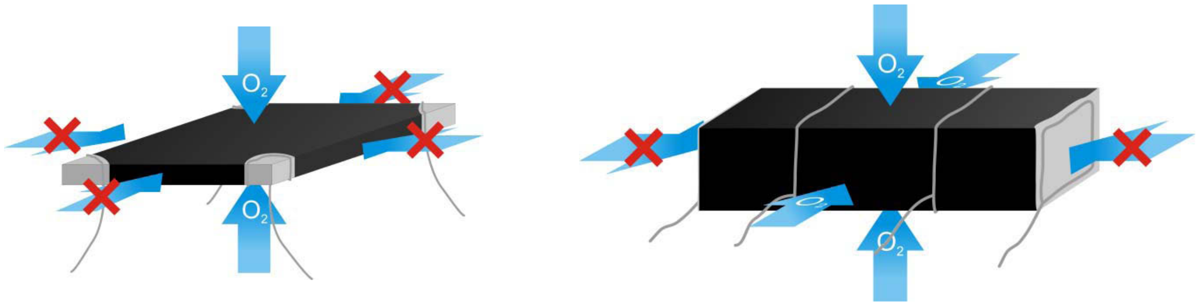

Fig. 2.7 Restrictions that have to be placed on diffusion flows for allowing to apply analytical expressions derived for mass relaxation equally for conductivity transients; specimens are shown in van der Pauw (left) and bar-shape geometry (right).

2.6 Determination of the electrical conductivity

2.6.1 Linear four-point geometry

The calculation of the electrical conductivity is simple due to the defined geometry of the sample and the contacts

$$\sigma = \frac{1}{R}\frac{d}{A} \tag{2.87}$$

where R is the measured resistance of the sample, A is the cross section of the bar and d the distance of the voltage probes. The resistance can in principle be determined from a single current-voltage measurement according to Ohm's law

$$R = \frac{V_d}{I} \tag{2.88}$$

where I is the applied current and V_d is the potential difference measured between the voltage probes (see Fig. 2.6, right). However, for increased accuracy and to eliminate voltage offsets from e.g. thermo-voltages it is preferred to perform several measurements at various current strengths and determine R from the slope of the regression line to the $V_d - I$ data points.

2.6.2 Van der Pauw geometry

For samples in van der Pauw geometry the theoretical treatment for the determination of the electrical conductivity from $V - I$ measurements is more complicated. The approach put forward by van der Pauw [164] was to first solve the problem for a particularly simple geometry that allows a rather straightforward derivation of the corresponding equations and then to demonstrate that the obtained results apply equally well to samples with arbitrary shape.

The sample geometry adopted for the first step is that of a flat sheet of constant thickness with semi-infinity extent (Fig. 2.8, left). If the four electrodes are assumed to be vertical line contacts at arbitrary positions along the boundary of the sample, the potential distribution is constant over the sample thickness and from a mathematical point of view the problem can be treated as two-dimensional (Fig. 2.8, right).

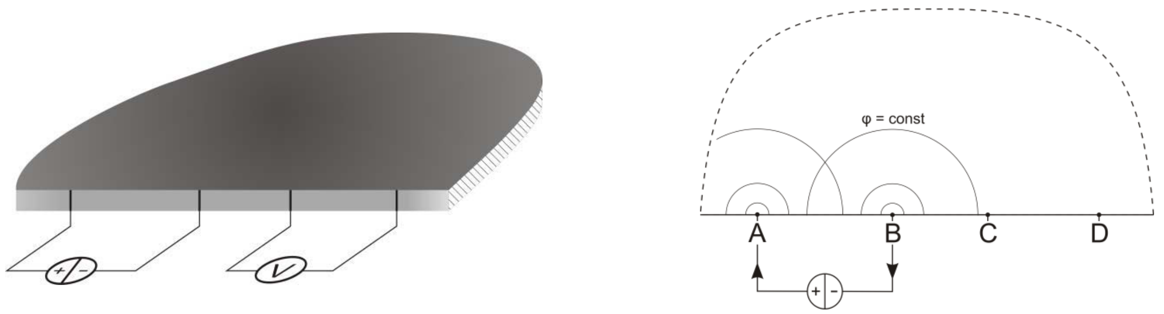

Fig. 2.8 Section of a hypothetical semi-infinite slab of conducting material with 4 vertical line electrodes at the sample boundary; constant current is applied via two adjacent contacts and the voltage is measured between the remaining electrodes; perspective view (left), top view and two-dimensional mathematical representation with equipotential lines (right).

In the following it is assumed that current is applied through contacts A and B in the polarity given in Fig. 2.8 (right). Since electroneutrality is maintained in the bulk, the continuity equation for charge flow in Eq. (2.36) reads

$$\nabla \cdot \vec{j} = 0 \tag{2.89}$$

If electrical conduction in the material is ohmic, the relation between the electrical potential and the current flow is given by Ohm’s law

$$\vec{j} = -\sigma \nabla \varphi \tag{2.90}$$

where the conductivity σ is assumed to be isotropic, either because the solid has a cubic crystal structure or is a polycrystalline material, in which case σ can be considered as some kind of average over the conductivities in different crystallographic directions.

Plugging Eq. (2.90) into Eq. (2.89) gives

$$\nabla(\sigma\nabla\varphi) = 0 \tag{2.91}$$

and assuming that the conductivity is independent of position the Laplace-equation

$$\nabla^2\varphi = 0 \tag{2.92}$$

is obtained as a starting point for the derivation of the potential distribution.

Focusing on contact A in Fig. 2.8, where a current I is injected into the sample, the potential distribution around A can be assumed to be of cylindrical symmetry for semi-infinite geometry. Expressing Eq. (2.92) in polar coordinates gives

$$\frac{d^2\varphi}{dr^2} + \frac{1}{r}\frac{d\varphi}{dr} = 0 \tag{2.93}$$

where r is the radial distance from contact A. Solving Eq. (2.93) gives

$$\varphi = K_1 ln\, r + K_2 \tag{2.94}$$

with two integration constants K_1 and K_2.

K_2 depends on the reference value chosen for the potential and – since only differences in potential are of interest – can be set to zero. K_1 is determined from the condition that, in order to be preserve electroneutrality, the current that flows through each surface surrounding A equals the injected current I. Calculating the current flow through an arbitrary equipotential surface around A and considering that no current flow takes place through the sample boundary, yields

$$I = r\pi dj = -r\pi d\sigma\nabla\varphi = -\pi d\sigma K_1 \tag{2.95}$$

where d is the sample thickness.

Thus, the potential distribution developed around point A is given by

$$\varphi_A = -\frac{I}{\pi d\sigma} \ln r_A \tag{2.96}$$

Similarly, when a current I is leaving the sample through contact B the potential distribution around B is

$$\varphi_B = \frac{I}{\pi d\sigma} \ln r_B \tag{2.97}$$

According to the superposition principle the potential at an arbitrary point inside the sample after applying a current between electrodes A and B can be calculated from the sum of Eqs. (2.96) and (2.97)

$$\varphi = \varphi_A + \varphi_B = \frac{I}{\pi d\sigma} \ln \frac{r_B}{r_A} \tag{2.98}$$

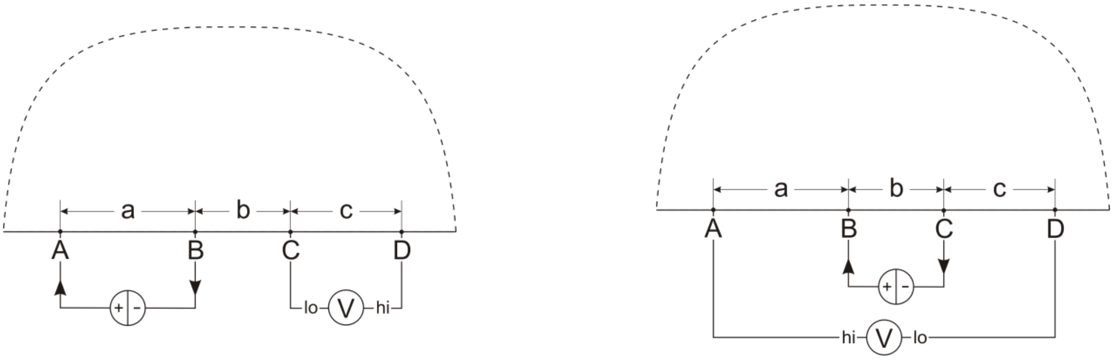

Fig. 2.9 Van der Pauw wiring scheme of both current-source and voltmeter to four contacts A-D at the boundary of a flat sample of semi-infinite extension. Small letters denote inter-electrode distances.

Applying Eq. (2.98) to the configuration in Fig. 2.9 (left) yields an expression for the voltage measured between D and C

$$\begin{aligned} \mathrm{V}_{DC} = \varphi_D - \varphi_C &= \frac{I_{AB}}{\pi d\sigma} ln \frac{b+c}{a+b+c} - \frac{I_{AB}}{\pi d\sigma} ln \frac{b}{a+b} \\ &= \frac{I_{AB}}{\pi d\sigma} ln \, \frac{(a+b)(b+c)}{b(a+b+c)} \end{aligned} \tag{2.99}$$

where a, b and c are the distances between the contacts as shown in Fig. 2.9.

Repeating the calculation after all contacts have been shifted one position to the right, where connection at D wraps around to A (Fig. 2.9, right), yields a similar expression for the voltage measured between A and D when applying a current at B and C

$$\begin{aligned} \mathrm{V}_{AD} = \varphi_A - \varphi_D &= \frac{I_{BC}}{\pi d\sigma} ln \frac{a+b}{a} - \frac{I_{BC}}{\pi d\sigma} ln \frac{c}{b+c} \\ &= \frac{I_{BC}}{\pi d\sigma} ln \, \frac{(a+b)(b+c)}{ac} \end{aligned} \tag{2.100}$$

Finally, when Eqs. (2.99) and (2.100) are combined according to the following equation, electrode distances cancel yielding the so-called van der Pauw equation

$$e^{-\pi d\sigma R_{AB,DC}} + e^{-\pi d\sigma R_{BC,AD}} = 1 \tag{2.101}$$

where $R_{AB,DC} \equiv V_{DC}/I_{AB}$ and $R_{BC,AD} \equiv V_{AD}/I_{BC}$.

It has been shown by van der Pauw [164] that Eq. (2.101) is equally valid for a flat sample of arbitrary shape with line contacts at the circumference. This can be established on the basis of the Riemann mapping theorem, which states that for every singly connected domain there exists an analytic mapping which maps the region one-to-one and conformally (i.e. angle-preserving) onto the unit disk [170]. Thus, there exists a bijective and conformal mapping for any arbitrary pair of singly connected domains in the complex plane. Since conformal mapping necessarily maps boundaries onto boundaries and preserves both the validity of the

Laplace-equation (2.92) and the boundary conditions (Eqs. (2.99) and (2.100)), the van der Pauw equation (2.101) holds for any other sample shape as well. The only qualification is that the sample may not contain isolated holes, corresponding to the mathematical assumption of singly connected domains.

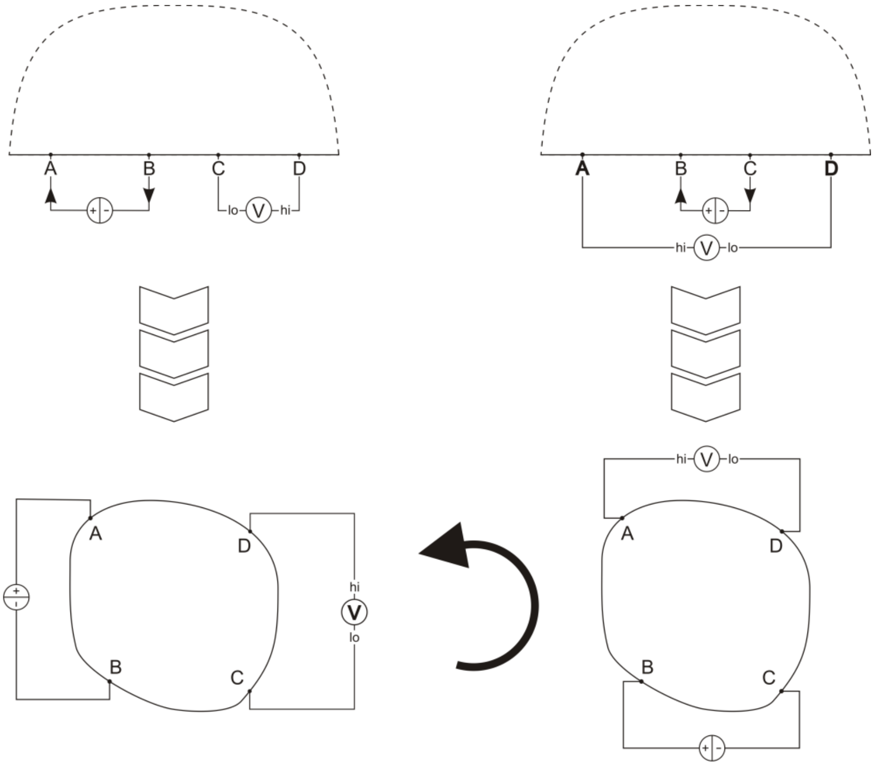

Fig. 2.10 Application of the van der Pauw theory derived for semi-infinite flat sample (top row) to real samples of arbitrary shape (bottom row). The connection is established by means of conformal mapping between the two sample geometries.

Fig. 2.10 summarizes the relationship between the two contacting schemes of a hypothetical semi-infinity sample (top row) and their corresponding counterparts for a finite-sized specimen (bottom row), correlated by conformal mapping. The circular arrow in Fig. 2.10 denotes the 90° rotation of current and voltage leads.

The van der Pauw equation cannot be analytically solved for σ, unless $R_{AB,DC} = R_{BC,AD} \equiv R$. For this special case Eq. (2.101) can be rewritten as

$$\sigma = \frac{\ln 2}{\pi d R} \tag{2.102}$$

In general the van der Pauw equation has to be solved numerically for σ by iterative methods and Eq. (2.102) can be used to calculate a starting value for the conductivity by setting $R = (R_{AB,DC} + R_{BC,AD})/2$.

As already described for the linear four-point geometry, voltages have to be corrected for thermal offsets. In van der Pauw measurements this is achieved by repeating each measurement after current reversal and averaging resistances for each value of $R_{AB,DC}$ and $R_{BC,AD}$.

The technique can be further improved by switching contacts in full-circle, that is 4 × 90°, whereby four resistances $R_{AB,DC}$, $R_{BC,AD}$, $R_{CD,BA}$ and $R_{DA,CB}$ are obtained. According to the reciprocity theorem of passive multipoles [164], resistances measured after interchanging current and voltage leads, i.e. after a 180° rotation of contacts, are supposed to be equal

$$\begin{aligned} R_{AB,DC} &= R_{CD,BA} \\ R_{BC,AD} &= R_{DA,CB} \end{aligned} \tag{2.103}$$

Of course, the identities in Eq. (2.103) are not perfectly satisfied for experimentally determined values, but they may help to discover gross measuring errors. Moreover, by averaging the corresponding resistances accuracy may be increased.

The derivation of the van der Pauw equation assumes infinitely thin line electrodes located at the perimeter. In his seminal paper van der Pauw states several relations for estimating relative errors introduced by different types of non-ideal contacts [164]. An in-depth investigation of the contact size effects on the accuracy was given by Chwang et al. for semiconductors [171] and by Grientschnig and Sitte for mixed conductors [165]. Based on their results a relative error in conductivity of around 5% is expected for a square-shaped sample with four triangular electrodes (Fig. 2.6, left) covering ~15% of the sample surface.

It should be mentioned that the van der Pauw method can also be employed for electrodes pressed on top of a flat sample provided that the contacts are sufficiently close to the boundary and the sample thickness is much smaller than the distances between the contacts.

2.7 Conductivity relaxation technique

In this work oxygen transport parameters were determined by the conductivity relaxation technique [168,172-188], first proposed by Dünwald and Wagner [189]. In this method the sample is brought to equilibrium with the surrounding atmosphere with respect to temperature and oxygen partial pressure. During the measurement the electrical conductivity of the sample is recorded as a function of time. After a conductivity baseline of the equilibrated sample has been established, the oxygen partial pressure pO_2 in the gas phase is abruptly changed. Oxygen is incorporated or released from the MIEC, depending on whether the pO_2 of the gas phase has been increased or decreased, respectively, and the material relaxes to a new equilibrium state (Fig. 2.11). According to defect-chemical equations given further below, variations in oxygen content also change the concentration of electronic charge carriers in the sample, which affects the electronic conductivity of the material. Nonlinear regression of the corresponding diffusion equations to the conductivity transient of the relaxation process allows to extract D_{chem} and k_{chem} as adjustable fitting parameters. Both the van der Pauw and linear four-point contacting schemes can be employed to obtain transport properties such as chemical diffusion coefficients D_{chem} and chemical surface exchange coefficients of oxygen k_{chem}, provided the restrictions with respect to diffusion flow are observed, as detailed above.

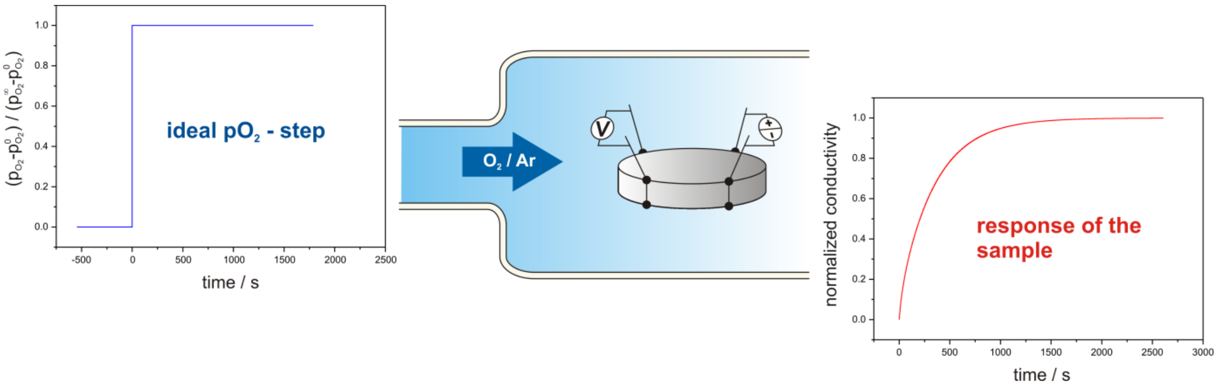

Fig. 2.11 Illustration of the conductivity relaxation method. The change in oxygen partial pressure around an equilibrated sample can be considered as the system input while the sample response is the change in electrical conductivity caused by oxygen incorporation or release.

Modeling of the relaxation process is based on several assumptions. Oxygen incorporation and release proceeds by two serially connected processes: one is the oxygen exchange between the gas phase and the immediate sample surface, the other is the diffusion of atomic oxygen within the sample. Oxygen diffusion proceeds via defects such as oxygen vacancies and interstitials, depending on the defect chemistry of the material, and is quite well understood. Its contribution is usually derived from Eq. (2.84), applied to the case of chemical diffusion of oxygen

$$\frac{\partial c}{\partial t} = D_{chem} \nabla^2 c \tag{2.104}$$

where it is assumed that the chemical diffusion coefficient is practically constant during the relaxation process.

The oxygen exchange process comprises several elementary steps such as adsorption of molecular oxygen from the gas phase at the sample surface, dissociation, reduction and incorporation into the material [190]. The details of the mechanism are less well known than for diffusion, as is the rate determining step, which may be different for different materials and may even change for the same material with temperature or oxygen partial pressure [191]. As a result the surface exchange process is usually modeled by a simple linear rate law

$$J = k_{chem}(c_s(t) - c_\infty) \tag{2.105}$$

where c_s is the time-dependent concentration of oxygen in the immediate surface layer of the sample and c_∞ is the oxygen concentration in the sample after relaxation has been completed and the new equilibrium state has been attained. Eq. (2.105) is more motivated by mathematical convenience rather than being supported by the underlying reaction mechanism, since it allows for an analytic solution of the mathematical problem. However, even though the correct expression of the surface exchange flux may differ from Eq. (2.105), it can be assumed that for sufficiently small $p\mathrm{O}_2$-steps Eq. (2.105) represents the 'small-signal' limit.

Therefore, $p\mathrm{O}_2$-steps should be as small as possible in order that Eqs. (2.104) and (2.105) hold and both k_{chem} and D_{chem} can be considered as characteristic values rather than some kind of average over the $p\mathrm{O}_2$-range employed. Further reduction of the oxygen partial pressure swings will result in too low signal-to-noise ratio of the voltage signals. While this can be partially compensated by increasing the applied current, the concomitant increase in Joule-heating of the sample as well as the necessity to keep the burden voltage of the current source below the material's decomposition voltage places a limit to that.

It is obvious that for a precise determination of D_{chem} and k_{chem} from a single relaxation measurement both diffusion and surface exchange must contribute to the relaxation transient. Since both processes are connected in series, a reduction of the kinetics of one process results in the fact that this process will increasingly dominate the overall kinetics up to the point where it becomes 'rate-determining' and no information about the faster process can be obtained from the measurement. Thus, the overall relaxation process can take place in three different regimes, called *surface controlled*, *diffusion controlled* and *mixed controlled* regime. Only in the latter case it is possible to extract both transport parameters from a single measurement, while the former two regimes allow the determination of only one quantity k_{chem} or D_{chem}, respectively.

Bouwmeester et al. [192] introduced the notion of a characteristic thickness L_c for a steady state flux of oxygen through ceramic membranes

$$L_c = \frac{D}{k} \tag{2.106}$$

where D is the self-diffusion coefficient of oxygen and k the surface exchange coefficient of oxygen. For predominantly electronically conducting ceramics and in the limit of small pO_2-gradients across a membrane, L_c can be used as a measure to distinguish between surface controlled and diffusion controlled oxygen permeation, depending on whether the membrane thickness is below or above L_c, respectively.

This parameter has been transferred to oxygen relaxation measurements [178], where the characteristic length is defined in accordance with Eq. (2.106) using the chemical diffusion and exchange coefficient

$$L_c = \frac{D_{chem}}{k_{chem}} \tag{2.107}$$

and quantitative criteria for the transition between the different control regimes can be based on the ratio

$$\frac{a}{L_c} = \frac{k_{chem}a}{D_{chem}} \tag{2.108}$$

where a is the total sample thickness L or half the sample thickness $L/2$, depending on whether oxygen exchange takes place from only one side of the sample or through two opposite sides, respectively.

According to den Otter et al. [178], a/L_c should be between 0.03 and 30 to allow for a simultaneous determination of k_{chem} and D_{chem} while Song et al. [183] stated boundaries of 0.1 and 10 of a/L_c to obtain reliable values for both transport parameters. In case that data on both D_{chem} and k_{chem} are available, Eq. (2.107) can be used to calculate the sample thickness necessary for relaxation measurements to be in the mixed regime, but it should be noted that the characteristic thickness depends on the temperature and oxygen partial pressure, since the activation energy of k_{chem} is usually larger than that of D_{chem} and the surface exchange coefficient is also more sensitive to changes in pO_2.

The above criterion is often applied ‘in reverse’, that is if a relaxation measurement is evaluated assuming mixed controlled oxygen exchange and the corresponding value of a/L_c satisfies the criteria given above, the assumption of mixed control is – somewhat ‘after the fact’ – retrospectively justified.

2.8 Modeling oxygen exchange

2.8.1 Mixed controlled oxygen exchange

In the following the analytical solution for the concentration relaxation of oxygen for one-dimensional two-sided diffusion is derived in the time-domain. An alternative approach is to take the Laplace-transform of the corresponding equations and solve them in the Laplace-domain. While the calculations are usually much easier in the Laplace-domain, back-transformation to the time domain is often rather difficult and may not pay off unless the experiment itself is performed in the frequency domain. However, the Laplace-transform technique is used below as a convenient tool to convert the solution of the relaxation transients following an ideal pO_2-step to more general pO_2-'inputs'.

Analytical expressions for many diffusion problems have been given by Crank [193] and by Carslaw and Jaeger [194]. The latter book actually deals with heat conduction but the solutions can be easily transcribed to diffusion due to the isomorphic nature of the governing differential equations.

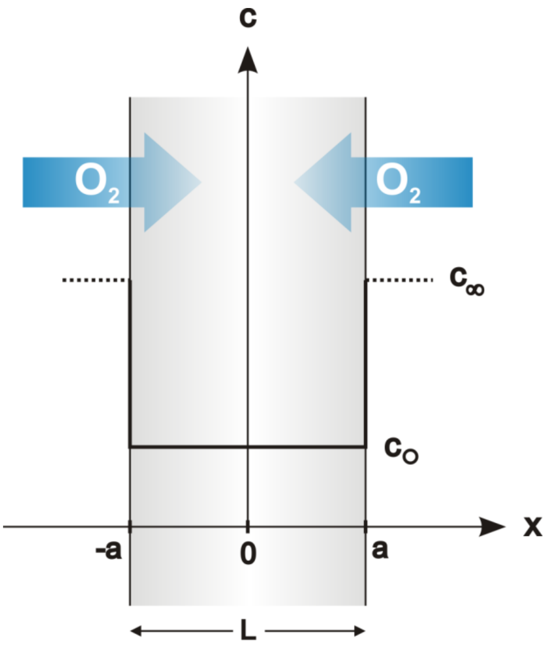

Fig. 2.12 Oxygen concentration vs. position inside a sample of thickness L, where c_0 denotes the concentration at t = 0 and c_∞ the concentration at the end of the relaxation experiment. The graphical overlay illustrates the case of oxygen incorporation from the gas phase into the sample due to a stepwise change to higher pO_2.

Fig. 2.12 shows a two-dimensional section of a sample of thickness L where oxygen can be transferred across opposite surfaces, located at $x = a$ and $x = -a$. The oxygen exchange process is modeled based on the one-dimensional diffusion equation (2.86)

$$\frac{\partial c}{\partial t} = D_{chem} \frac{\partial^2 c}{\partial x^2} \tag{2.109}$$

where $c = c(x, t)$ is the concentration of oxygen ions in the material as a function of position and time. The oxygen surface exchange flux between the sample and the gas phase form the boundaries conditions (BCs) of the problem and are accounted for by Eqs. (2.8) and (2.105)

$$\left.\begin{aligned} J(a,t) = -D_{chem} \left.\frac{\partial c}{\partial x}\right|_{x=a} &= k_{chem}(c(a,t) - c_\infty) \\ J(-a,t) = -D_{chem} \left.\frac{\partial c}{\partial x}\right|_{x=-a} &= -k_{chem}(c(-a,t) - c_\infty) \end{aligned}\right\} BC \tag{2.110}$$

If the sample is in equilibrium with the gas phase the concentration of oxygen ions is uniform throughout the sample, which yields the initial condition (IC) of the problem

$$c(x,0) = c_0 \qquad -a < x < a \quad \} \; IC \tag{2.111}$$

c_∞ and c_0 in Eqs. (2.110) and (2.111) are constants denoting the initial oxygen concentration in the sample and the (asymptotically approached) final oxygen concentration corresponding to the new oxygen partial pressure in the atmosphere, respectively.

It is possible to simplify calculations by taking full advantage of the symmetry of the system and setting up a somewhat more restricted set of BCs than those given in Eq. (2.110). Since for symmetry reasons there can be no oxygen flow through the central plane in the sample at $x = 0$ (Fig. 2.12) the BCs can be simplified to

$$\left.\begin{aligned} J(a,t) = -D_{chem} \left.\frac{\partial c}{\partial x}\right|_{x=a} &= k_{chem}(c(a,t) - c_\infty) \\ J(0,t) = -D_{chem} \left.\frac{\partial c}{\partial x}\right|_{x=0} &= 0 \end{aligned}\right\} BC \tag{2.112}$$

It is interesting to note that Eqs. (2.112) are also the boundary conditions for the related problem of a sample of thickness a where the surface at $x = 0$ is impervious to oxygen. Therefore, the solutions derived for two-sided diffusion for a sample of thickness L and uniform initial oxygen concentration can be applied to one-sided diffusion by substituting L by $L/2$ in the analytic solutions.

Before starting to solve the problem it is expedient to get rid of the c_∞-term in the BCs, which can be achieved by the substitution $\tilde{c}(x,t) \equiv c(x,t) - c_\infty$. The transformed diffusion equation with BCs and IC expressed in terms of $\tilde{c}(x,t)$ is thus

$$\frac{\partial \tilde{c}}{\partial t} = D \frac{\partial^2 \tilde{c}}{\partial x^2} \tag{2.113}$$

$$\left.\begin{aligned} -D \left.\frac{\partial \tilde{c}}{\partial x}\right|_{x=a} &= k\tilde{c}(a,t) \\ \left.\frac{\partial \tilde{c}}{\partial x}\right|_{x=0} &= 0 \end{aligned}\right\} BC \tag{2.114}$$

$$\tilde{c}(x,0) = c_0 - c_\infty \qquad -a < x < a \quad \} \; IC \tag{2.115}$$

where from now on the $chem$-index is being omitted from the transport parameters to simplify notation.

As a first step a particular solution to Eq. (2.113) is determined through separation of variables, assuming that $\tilde{c}$ can be expressed as the product of two factors, one being a function of time and the other being a function of space

$$\tilde{c}(x,t) = X(x)\,T(t) \tag{2.116}$$

Plugging Eq. (2.116) into Eq. (2.113) and dividing by $DX(x)T(t)$ gives

$$\frac{1}{D}\frac{1}{T}\frac{dT}{dt} = \frac{1}{X}\frac{d^2X}{dx^2} \tag{2.117}$$

where each side in the equation must equal a constant. This constant has to be negative in order that Eq. (2.116) will satisfy the BCs for $k, D, a > 0$ and non-vanishing $\tilde{c}$ and can therefore be written as $-\lambda^2$ ($\lambda \in \mathbb{R}$)

$$\frac{1}{D}\frac{1}{T}\frac{dT}{dt} = -\lambda^2 \qquad \frac{1}{X}\frac{d^2X}{dx^2} = -\lambda^2 \tag{2.118}$$

Thus, the partial differential equation (2.113) has been reduced to two ordinary differential equations

$$\frac{dT}{dt} = -\lambda^2 DT \tag{2.119}$$

$$\frac{d^2X}{dx^2} + \lambda^2 X = 0 \tag{2.120}$$

which can be easily solved as

$$T(t) = e^{-\lambda^2 Dt} \tag{2.121}$$

$$X(x) = Acos(\lambda x) + Bsin(\lambda x) \tag{2.122}$$

where A and B are constants of integration to be determined by the initial and boundary conditions.

Plugging Eq. (2.116) into the BCs (2.114) the time function $T(t)$ cancels, yielding

$$\left.\begin{aligned} -D\left.\frac{dX}{dx}\right|_{x=a} &= kX(a) \\ \left.\frac{dX}{dx}\right|_{x=0} &= 0 \end{aligned}\right\} BC \tag{2.123}$$

Eqs. (2.120) and (2.123) together constitute a so-called Sturm-Liouville problem and according to Sturm-Liouville theory there is a countable infinite number of solutions which form an orthogonal and complete set on the interval $[0, a]$.

Solving Eq. (2.120) along with Eq. (2.123) gives the eigenfunctions of the problem

$$X(x) = Acos(\lambda_n x) \tag{2.124}$$

where λ_n is the n-th eigenvalue satisfying the condition

$$\lambda_n \tan(\lambda_n a) = \frac{k}{D} \tag{2.125}$$

To remove the parameter a from the l.h.s. of Eq. (2.125) the eigenvalue λ_n is substituted according to $\beta_n \equiv \lambda_n a$ and Eqs. (2.124) and (2.125) are rewritten as

$$X(x) = Acos(\beta_n \frac{x}{a}) \tag{2.126}$$

$$\beta_n \tan(\beta_n) = \frac{ka}{D} \equiv L_\beta \tag{2.127}$$

where L_β is just the a/L_c-ratio discussed above.
Thus, one solution to Eq. (2.113) is

$$\tilde{c}(x,t) = Acos(\beta_n \frac{x}{a})\, e^{-\frac{\beta_n^2}{a^2}Dt} \tag{2.128}$$

which does satisfy the BCs, but not the initial condition Eq. (2.115). However, due to the linearity of the diffusion equation (2.113) a more general expression can be used

$$\tilde{c}(x,t) = \sum_{n=1}^{\infty} A_n cos(\beta_n \frac{x}{a})\, e^{-\frac{\beta_n^2}{a^2}Dt} \tag{2.129}$$

where the sum runs over the infinite number of positive eigenvalues β_n defined by Eq. (2.127) and numbered by $n \in \mathbb{N}$.

Since the eigenfunctions form a complete set, the initial condition can be expanded in terms of the eigenfunctions

$$\tilde{c}(x,0) = \sum_{n=1}^{\infty} A_n cos\left(\beta_n \frac{x}{a}\right) = c_0 - c_\infty \qquad -a < x < a \tag{2.130}$$

where the coefficients A_n are determined by means of the orthogonality property of the eigenfunctions

$$\int_0^a \cos(\beta_m \frac{x}{a})\cos(\beta_n \frac{x}{a})\, dx = \begin{cases} 0 & m \neq n \\ \frac{a}{2}\frac{L_\beta^2 + L_\beta + \beta_m^2}{\beta_m L_\beta} & m = n \end{cases} \tag{2.131}$$

as can be confirmed by direct calculation. Applying Eq. (2.131) to Eq. (2.130) gives

$$A_n = (c_0 - c_\infty)\frac{2L_\beta}{(L_\beta^2 + L_\beta + \beta_n^2)\cos(\beta_n)} \tag{2.132}$$

and inserting Eq. (2.132) into Eq. (2.129), considering $c(x,t) = \tilde{c}(x,t) + c_\infty$, yields the final expression

$$c(x,t) = c_\infty + (c_0 - c_\infty)\sum_{n=1}^{\infty}\frac{2L_\beta cos(\beta_n \frac{x}{a})}{(L_\beta^2 + L_\beta + \beta_n^2)\cos(\beta_n)}\, e^{-\frac{\beta_n^2}{a^2}Dt} \tag{2.133}$$

Eq. (2.133) is commonly stated by using the normalized concentration $\bar{c}(x,t)$

$$\bar{c}(x,t) \equiv \frac{c(x,t) - c_0}{c_\infty - c_0} = 1 - \sum_{n=1}^{\infty}\frac{2L_\beta cos(\beta_n \frac{x}{a})}{(L_\beta^2 + L_\beta + \beta_n^2)\cos(\beta_n)}\, e^{-\frac{\beta_n^2}{a^2}Dt} \tag{2.134}$$

$$\beta_n \tan(\beta_n) = L_\beta \qquad L_\beta \equiv \frac{ka}{D}$$

The eigenvalues β_n have to be numerically calculated from the transcendental equation (2.127) with high precision to avoid systematic errors for k and D obtained through curve fitting [195]. An iterative algorithm used for calculating eigenvalues was given by den Otter et al. [195]. Fig. 2.13 shows the distribution of the first eight eigenvalues corresponding to the zeros of the plotted function. It is interesting to note that the eigenvalues β_n approach $(n-1)\pi$ for large values of n. For the numerical evaluation of the infinite series an abort criterion for the summation has to be defined. In this work the breaking condition was based on the absolute value of the added values with limits set to 10^{-7} for single sums and 10^{-5} for non-separable double sums (in case of two-dimensional mixed or diffusion controlled oxygen exchange with flush time correction applied).

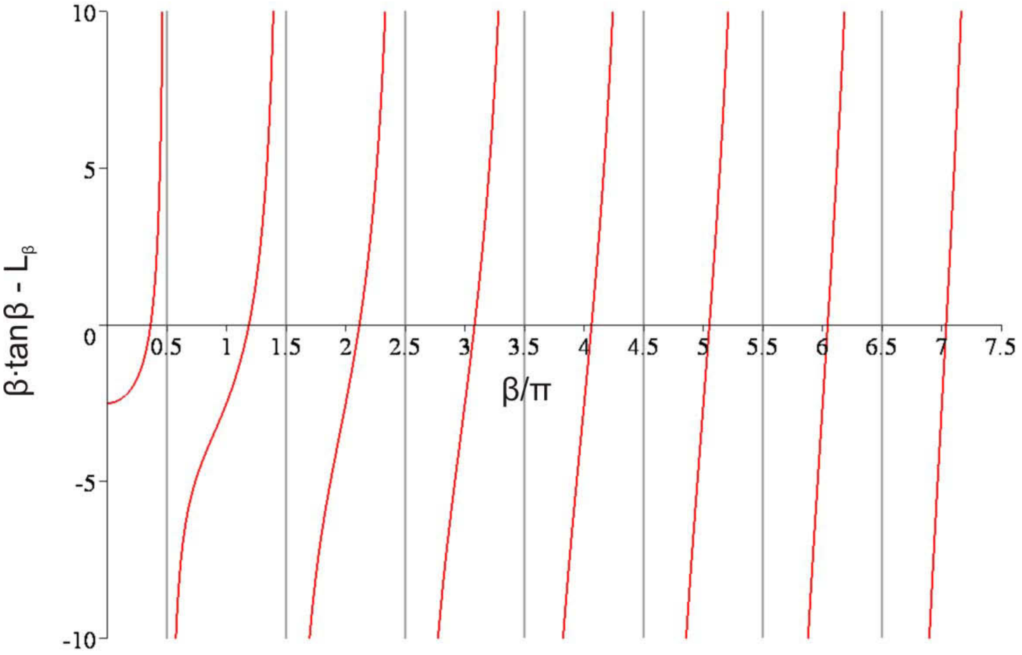

Fig. 2.13 Illustration of the distribution of the first eight eigenvalues β ($L_\beta = 2.5$, see Eq. (2.127)) in units of π corresponding to the zeros of the plotted function (red); gray vertical lines are asymptotes.

The above derivation can be easily extended to two-dimensional mass transport. The spatial part in the corresponding diffusion equation can be factored into two one-dimensional differential equations and solved along the same lines as given above. The result for mixed controlled oxygen exchange in perpendicular directions along the x- and y-axis is

$$\begin{aligned} \bar{c}(x,y,t) &\equiv \frac{c(x,y,t)-c_0}{c_\infty - c_0} \\ &= 1 - \sum_{n=1}^{\infty}\sum_{m=1}^{\infty} \frac{2L_\beta cos(\beta_n \frac{x}{a})}{(L_\beta^2 + L_\beta + \beta_n^2)\cos(\beta_n)} \, \frac{2L_\gamma cos(\gamma_m \frac{y}{b})}{(L_\gamma^2 + L_\gamma + \gamma_m^2)\cos(\gamma_m)} \; e^{-(\frac{\beta_n^2}{a^2}+\frac{\gamma_m^2}{b^2})Dt} \\ &= 1 - \sum_{n=1}^{\infty} \frac{2L_\beta cos(\beta_n \frac{x}{a})}{(L_\beta^2 + L_\beta + \beta_n^2)\cos(\beta_n)} \; e^{-\frac{\beta_n^2}{a^2}Dt} \sum_{m=1}^{\infty} \frac{2L_\gamma cos(\gamma_m \frac{y}{b})}{(L_\gamma^2 + L_\gamma + \gamma_m^2)\cos(\gamma_m)} \; e^{-\frac{\gamma_m^2}{b^2}Dt} \end{aligned} \tag{2.135}$$

$$\beta_n \tan(\beta_n) = L_\beta \ , \quad \gamma_m \tan(\gamma_m) = L_\gamma \qquad\qquad L_\beta \equiv \frac{ka}{D} \ , \quad L_\gamma \equiv \frac{kb}{D}$$

where for each spatial dimension a separate set of eigenvalues β_n and γ_m has to be calculated. a and b denote the lateral dimensions of the sample in the x- and y-direction, respectively, and correspond to either the full side length or half that value depending on whether diffusion is one-sided or two-sided in the corresponding direction.

2.8.2 Diffusion controlled oxygen exchange

Pure diffusion control occurs if the actual sample thickness is well above its characteristic length or $a/L_c \gg 1$. In this case diffusion is the rate determining process and the sample surface can be assumed to attain its final oxygen concentration c_∞ immediately after the gas switch. The mathematical description of the process is similar to that give above for mixed control but with more simple boundary conditions, due to the absence of the surface exchange process.

$$\frac{\partial c}{\partial t} = D\frac{\partial^2 c}{\partial x^2} \tag{2.136}$$

$$\left.\begin{array}{r} c(a,t) = c_\infty \\ \left.\dfrac{\partial c}{\partial x}\right|_{x=0} = 0 \end{array}\right\} BC \tag{2.137}$$

$$c(x,0) = c_0 \qquad -a < x < a \quad \} \; IC \tag{2.138}$$

The solution to Eqs. (2.136) – (2.138) proceeds in a similar manner as given above for the mixed controlled case. However, the calculation of the eigenvalues simplifies to

$$\lambda_n = (2n+1)\frac{\pi}{2a} \tag{2.139}$$

and the eigenfunction development of the initial condition reduces to a Fourier series expansion. Thus, the analytical expression for one-dimensional diffusion is

$$\bar{c}(x,t) \equiv \frac{c(x,t) - c_0}{c_\infty - c_0} = 1 - \frac{4}{\pi}\sum_{n=0}^{\infty}\frac{(-1)^n}{2n+1}\cos[(2n+1)\frac{\pi}{2a}x]\, e^{-(2n+1)^2\frac{\pi^2}{4a^2}Dt} \tag{2.140}$$

The analytical expression for two-dimensional diffusion corresponds to a straightforward extension of Eq. (2.140) and is given by the double Fourier-series

$$\bar{c}(x,y,t) \equiv \frac{c(x,y,t)-c_0}{c_\infty - c_0}$$

$$= 1 - \frac{16}{\pi^2}\sum_{n=0}^{\infty}\sum_{m=0}^{\infty}\frac{(-1)^n}{2n+1}\frac{(-1)^m}{2m+1}\cos\left[(2n+1)\frac{\pi}{2a}x\right]\cos\left[(2m+1)\frac{\pi}{2b}y\right] \times$$

$$e^{-\frac{\pi^2}{4}\left(\frac{(2n+1)^2}{a^2}+\frac{(2m+1)^2}{b^2}\right)Dt} \tag{2.141}$$

$$= 1 - \frac{16}{\pi^2}\sum_{n=0}^{\infty}\frac{(-1)^n}{2n+1}\cos\left[(2n+1)\frac{\pi}{2a}x\right]\ e^{-(2n+1)^2\frac{\pi^2}{4a^2}Dt} \times$$

$$\sum_{m=0}^{\infty}\frac{(-1)^m}{2m+1}\cos\left[(2m+1)\frac{\pi}{2b}y\right]\ e^{-(2m+1)^2\frac{\pi^2}{4b^2}Dt}$$

As discussed above, a is either the sample thickness L or $L/2$ along the x-axis, depending on whether two- or one-sided diffusion is considered, respectively. A similar condition holds for b.

It is interesting to note that Eqs. (2.140) and (2.141) can also be directly derived from Eqs. (2.134) and (2.135), respectively, by taking the limit for $k \rightarrow \infty$.

Experimentally, the oxygen exchange process can be rendered diffusion controlled by either preparing sufficiently thick samples or by increasing the surface exchange process through surface modification.

2.8.3 Surface controlled oxygen exchange

When the surface exchange process of oxygen determines overall oxygen exchange there is no diffusion involved and the exchange process is governed solely by Eq. (2.105). Concentration gradients cannot build up because the concentration of oxygen inside the sample is infinitely fast homogenized when oxygen is entering or leaving the material.

Thus, oxygen exchange is described by

$$J = k(c(t) - c_\infty) \tag{2.142}$$

where J is the oxygen flux (positive for oxygen leaving the sample) and c and c_∞ are the homogeneous concentration of atomic oxygen inside the sample at time t and after relaxation is finished, respectively. Combining Eq. (2.142) with the continuity equation (2.82) and integrating over the sample volume V yields

$$\iiint_V \frac{\partial c}{\partial t} dV = -\iiint_V \nabla \cdot \vec{J}\, dV = -\oint\!\!\oint_A \vec{J} d\vec{A} = -k(c - c_\infty)\, A \tag{2.143}$$

where A denotes the total sample surface. Since c is a function of time only, Eq. (2.143) gives

$$\frac{dc}{dt} V = -k(c - c_\infty)A \tag{2.144}$$

which upon integration and considering the initial condition $c(0) = c_0$ yields

$$\bar{c}(t) \equiv \frac{c(t) - c_0}{c_\infty - c_0} = 1 - e^{-k\frac{A}{V}t} \tag{2.145}$$

In the case of a flat sample oxygen is transferred mainly through two opposite sides (see Fig. 2.7, left) and Eq. (2.145) becomes

$$\bar{c}(t) = 1 - e^{-k\frac{2}{L}t} \tag{2.146}$$

Eq. (2.146) can also be derived by taking the limit for $D \longrightarrow \infty$ in Eq. (2.134).

It should be mentioned that in the case of surface exchange control there exists an analytical equation for the more general situation where k depends linearly on the oxygen concentration. Indeed, when performing the appropriate substitution in Eq. (2.144)

$$\frac{dc}{dt}V = -(qc + p)(c - c_\infty)A \tag{2.147}$$

where $k = qc + p$ and q, p are constants that establish the linear dependence of k on the concentration. Integration of Eq. (2.147) and including $c(0) = c_0$ gives

$$\begin{gathered} \bar{c}(t) = 1 - \frac{k_\infty}{(k_\infty - k_0) + k_0 e^{k_\infty \frac{A}{V} t}} \\ k_0 \equiv qc_0 + p \qquad\qquad k_\infty \equiv qc_\infty + p \end{gathered} \tag{2.148}$$

where k_0 and k_∞ correspond to the exchange coefficient at the beginning and after conclusion of the relaxation process, respectively. For $k_\infty = k_0$, Eq. (2.148) simplifies to Eq. (2.145).

2.9 Relaxation techniques

Different experimental techniques have been applied to follow the temporal evolution of the relaxation process. However, these techniques do not measure the oxygen concentration directly but rather some physical property depending on the concentration. Furthermore, it is difficult to measure the concentration simultaneously as a function of both time and space and only a few cases are reported in the literature where spatially resolved concentration profiles have been recorded [196]. In most cases the physical quantity measured in a relaxation experiment is an integral property that averages over the concentration distribution in the sample. This latter category includes weight [197-199] and conductivity relaxation techniques [168,172-188] as well as those based on following changes in pO_2 in the gas phase like coulometric titration and carrier gas coulometry [200-202]. Hence, the equations derived above have to be integrated over the sample volume in a way that is consistent with the kind of averaging inherent in the applied relaxation technique.

Probably the most straightforward calculation is required for weight relaxation. In this case changes in mass can be easily linked to changes in oxygen concentration according to the general relation

$$\bar{m}(t) \equiv \frac{m(t) - m_0}{m_\infty - m_0} = \frac{\iiint_V M_O(c(\vec{r},t) - c_0)\, dV}{V M_O(c_\infty - c_0)} = \frac{1}{V} \iiint_V \bar{c}(\vec{r},t)\, dV \qquad (2.149)$$

where M_O is the atomic mass of oxygen and V is the sample volume. The weight relaxation technic itself puts no restrictions on the sample geometry, but of course the geometry has to be chosen in a way that is amenable to modeling the relaxation transient.

In the case of conductivity relaxation the relationship between oxygen concentration and bulk conductivity is more complicated. Firstly, some additional assumptions regarding the relation between oxygen concentration and electronic conductivity have to be made, which depends on the defect chemistry of the material. Secondly, the overall resistance (or conductance) of the sample has to be derived from the conductivity profile. To obtain analytical solutions, the current flow in the sample must be restricted to patterns that permit analytical integration of the corresponding resistance-conductivity relationship. This is shown in the following section for both the linear and the van der Pauw geometry.

It might appear from the above-said that methods like weight relaxation or carrier gas coulometry are to be preferred in relaxation measurements since they dispense with the additional assumptions that are required for the application of the conductivity relaxation technique. However, there are several experimental issues that prevent straightforward application of the weight relaxation technique like more complicated setup, difficulties with low-noise measurement of masses in a reactor permanently flushed with gas and in particular the large flush-times of the inherently larger reactor volumes that complicate or may even prohibit relaxation measurements [178]. Coulometric titration techniques suffer from inaccuracies through oxygen leakage through glass sealings and permeation through the electrolyte membrane due to finite electronic conductivity. Furthermore, the temperature range is limited to 600-800 °C due to the low oxygen conductivity of solid electrolytes below 600°C and the high oxygen permeation and reactivity of glasses above 800°C [202]. However, it should me mentioned that both methods allow a simultaneous determination of changes in the oxygen stoichiometry of the material which cannot be achieved by conductivity-based techniques.

2.10 Correlation between oxygen non-stoichiometry and conductivity

For a correct modeling of conductivity relaxation transients in mixed ionic-electronic conductors the relationship between oxygen content and electronic conductivity has to be established. Conductivity relaxation experiments are usually performed in galvanostatic mode and it is assumed that the applied current does not interfere with the diffusion process of oxygen. The latter assumption is permissible for predominantly electronically conducting mixed conductors.

Due to local electroneutrality, the concentration of charged particles balance according to

$$[e'] + 2[O_i''] + acceptor = [h^{\cdot}] + 2[V_O^{\cdot\cdot}] + donor \tag{2.150}$$

where brackets denote concentrations, and *acceptor* and *donor* subsume contributions from aliovalent acceptor and donor dopants, respectively.

In the case of unsubstituted rare earth nickelates in the high-pO_2 region the major ionic and electronic defects are oxygen interstitials (O_i'') and defect electrons $(h^{\cdot})$ and electrical conduction is carried by electron holes. Thus, changes in the concentration of electron holes are linearly coupled to changes in the concentration of oxygen interstitials

$$\Delta c_{h^{\cdot}} \propto \Delta c_{O_i''} \tag{2.151}$$

where in this case the constant of proportionality is 2. Considering predominantly electronically conducting MIEC materials for which a detailed knowledge of the defect structure is not available, a relation of the general form

$$\Delta c_{el} \propto \Delta c_O \tag{2.152}$$

may often be assumed on the basis of local electroneutrality, where c_{el} is the concentration of either conduction electrons or holes and c_O denote oxygen defects such as vacancies or interstitials. The simple proportionality (2.152) fails in the mixed p/n-regime and the correlation between oxygen non-stoichiometry and electronic defect concentration becomes more complex [183,203]. It should be noted that Eq. (2.152) is not affected by the presence of immobile aliovalent acceptor or donator dopants with fixed valence.

The relation between concentration and electronic conductivity is established by the fundamental equation

$$\sigma_{el} = ec_{el}u_{el} \tag{2.153}$$

where e is the elementary charge and u_{el} is electrical mobility of the electronic defect. If the mobility of the electronic carriers does not depend on oxygen non-stoichiometry (i.e. u_{el} is independent of carrier concentration) the relationship between oxygen concentration and electronic conductivity can be established by combining $\Delta\sigma_{el} \propto \Delta c_{el}$ and $\Delta c_{el} \propto \Delta c_O$ to

$$\Delta\sigma_{el} \propto \Delta c_O \tag{2.154}$$

During a relaxation experiment $\Delta\sigma_{el}$ as well as $\Delta\sigma_O$ are to be considered time dependent local properties $\Delta\sigma_{el}(\vec{r},t)$ and $\Delta\sigma_O(\vec{r},t)$.

2.10.1 Linear four-point geometry

For the sample geometry shown in Fig. 2.6 (right), the calculation of the total conductance of the sample from the conductivity distribution is straightforward, provided that the direction oxygen diffusion has no component parallel to that of the current flow (see section 2.8.2). In this case the current is flowing along straight lines between the two opposite current-carrying electrodes. Fig. 2.14 (left) shows such a current path of infinitesimal thickness. Its contribution dG to the total conductance G is

$$dG = \sigma(x,y,t)\frac{dxdy}{L_z} \tag{2.155}$$

$\sigma(x,y,t)$ is constant along the infinitesimal volume because the oxygen concentration is constant due to the diffusion pattern shown in Fig. 2.7 (right).

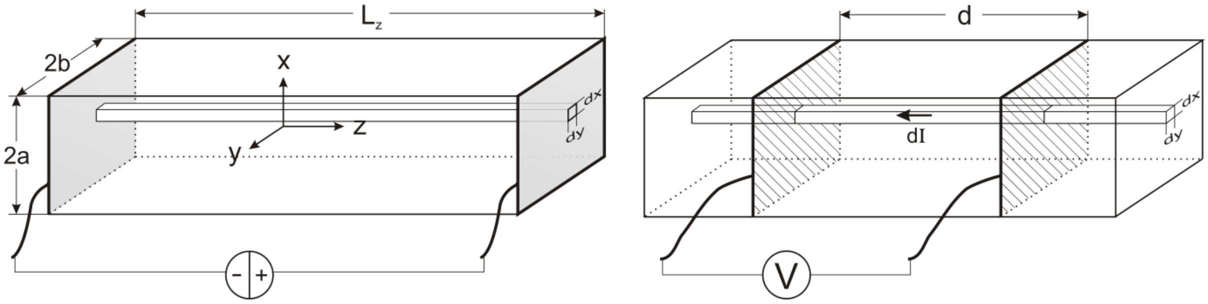

Fig. 2.14 Bar-shaped sample contacted with planar electrodes at both ends for applying current (left) and two wires wound around the specimen used as voltage probes (right). A linear current path is sketched within the sample bulk.

Since the total current is made up of such infinitesimal current lines connected in parallel, the total conductance is the sum of the individual contributions according to

$$G = \iint_A dG = \frac{1}{L_z} \int_{x=-a}^{a} \int_{y=-b}^{b} \sigma(x, y, t) dx dy \tag{2.156}$$

However, if the voltage is measured between separate voltage probes, as is usually done (Fig. 2.14, right), the probe distance *d* is used instead of L_z

$$G(t) = \frac{I}{V_d} = \iint_A dG = \frac{1}{d} \int_{x=-a}^{a} \int_{y=-b}^{b} \sigma(x, y, t) dx dy \tag{2.157}$$

where I is the current applied between the outer electrodes and V_d is the voltage measured between the probes.

It is expedient to introduce the normalized conductance $\bar{G}$, which is identical to the normalized conductivity σ_n, since the geometric factor relating conductance and conductivity cancels on normalization

$$\bar{G}(t) \equiv \frac{G(t) - G_0}{G_\infty - G_0} \tag{2.158}$$

Commonly, the so-called normalized conductivity σ_n is used instead of the normalized conductance $\bar{G}$. This may be motivated by formally defining σ_n as

$$\sigma_n \equiv \frac{\tilde{\sigma}(t) - \tilde{\sigma}_0}{\tilde{\sigma}_\infty - \tilde{\sigma}_0} \tag{2.159}$$

where the tilde denotes spatial averages over the sample volume. When evaluating Eq. (2.159) it turns out that in all cases of practical importance σ_n is indeed identical to $\bar{G}$.

Plugging Eq. (2.157) into Eq. (2.158) yields

$$\sigma_n(t) \equiv \frac{G(t) - G_0}{G_\infty - G_0} = \frac{1}{4ab} \int\limits_{x=-a}^{a} \int\limits_{y=-b}^{b} \frac{\sigma(x,y,t) - \sigma_0}{\sigma_\infty - \sigma_0} dxdy \tag{2.160}$$

which – by means of Eq. (2.154) – can be converted into a relation between the normalized conductivity and the oxygen concentration profile

$$\sigma_n(t) = \frac{1}{4ab} \int\limits_{x=-a}^{a} \int\limits_{y=-b}^{b} \bar{c}(x,y,t) dxdy \tag{2.161}$$

Through Eq. (2.161) the oxygen profiles derived above for different rate-determining processes can be transformed into an equation describing the relaxation transients of the normalized conductivity.

It can be seen that the integral in Eq. (2.161) is actually a special case of the mass transient given in Eq. (2.149) for $\bar{c} \neq f(z)$ and thus in this case

$$\sigma_n(t) = \bar{m}(t) \tag{2.162}$$

However, it is important to note that this identity is by no means obvious or self-evident and requires separate justification as was presented above. For example, Eq. (2.162) does not hold if the oxygen flux has a component parallel to the *z*-axis in Fig. 2.14.

Applying Eq. (2.161) to the concentration profiles derived above for the linear configuration yields for the conductivity transient under mixed control

$$\sigma_n(t) = 1 - \sum_{n=1}^{\infty}\sum_{m=1}^{\infty} \frac{2L_\beta^2}{(L_\beta^2 + L_\beta + \beta_n^2)\beta_n^2} \frac{2L_\gamma^2}{(L_\gamma^2 + L_\gamma + \gamma_m^2)\gamma_m^2}\, e^{-(\frac{\beta_n^2}{a^2}+\frac{\gamma_m^2}{b^2})Dt}$$

$$= 1 - \sum_{n=1}^{\infty} \frac{2L_\beta^2}{(L_\beta^2 + L_\beta + \beta_n^2)\beta_n^2}\, e^{-\frac{\beta_n^2}{a^2}Dt} \sum_{m=1}^{\infty} \frac{2L_\gamma^2}{(L_\gamma^2 + L_\gamma + \gamma_m^2)\gamma_m^2}\, e^{-\frac{\gamma_m^2}{b^2}Dt} \tag{2.163}$$

$$\beta_n \tan(\beta_n) = L_\beta \;\; , \;\; \gamma_m \tan(\gamma_m) = L_\gamma \qquad\qquad L_\beta \equiv \frac{ka}{D} \;\; , \;\; L_\gamma \equiv \frac{kb}{D}$$

while in the case of diffusion controlled oxygen exchange Eq. (2.163) simplifies to

$$\sigma_n(t) = 1 - \frac{64}{\pi^4}\sum_{n=0}^{\infty}\sum_{m=0}^{\infty} \frac{1}{(2n+1)^2}\frac{1}{(2m+1)^2}\, e^{-\frac{\pi^2}{4}(\frac{(2n+1)^2}{a^2}+\frac{(2m+1)^2}{b^2})Dt}$$

$$= 1 - \frac{64}{\pi^4}\sum_{n=0}^{\infty} \frac{1}{(2n+1)^2}\, e^{-(2n+1)^2\frac{\pi^2}{4a^2}Dt} \sum_{m=0}^{\infty} \frac{1}{(2m+1)^2}\, e^{-(2m+1)^2\frac{\pi^2}{4b^2}Dt} \tag{2.164}$$

If the relaxation process is dominated by the surface exchange of oxygen the transient is described by Eq. (2.165)

$$\sigma_n(t) = 1 - e^{-k\frac{A}{V}t} = 1 - e^{-k(\frac{1}{a}+\frac{1}{b})t} \tag{2.165}$$

and in the more general case where the surface exchange coefficient is a linear function of the oxygen concentration, Eq. (2.166) holds

$$\begin{aligned}\sigma_n(t) &= 1 - \frac{k_\infty}{(k_\infty - k_0) + k_0 e^{k_\infty \frac{A}{V}t}} \\ &= 1 - \frac{k_\infty}{(k_\infty - k_0) + k_0 e^{k_\infty (\frac{1}{a}+\frac{1}{b})t}}\end{aligned} \tag{2.166}$$

In Fig. 2.15 relaxation transients are plotted as normalized conductivity σ_n vs. time for the three major models for two-dimensional oxygen exchange. Using linear axes the curve shapes are quite similar and good data quality is necessary to identify the correct model (Fig. 2.15, left). A very useful representation is obtained when plotting $ln(1 - \sigma_n)$ against time ('semi-logarithmic plot') shown in Fig. 2.15 (right). At large times all transients become linear in the semi-logarithmic representation while showing different characteristics in the short-time region (inset in Fig. 2.15, right). This demonstrates the importance of accurate data right after the pO$_2$-switch for a correct identification of the control mechanism. While ideal k-controlled oxygen exchange gives a straight line in the semi-logarithmic plot, diffusion controlled relaxation processes show a pronounced convex shape (downward-bending) at the beginning of the relaxation experiment. For oxygen exchange processes under mixed control the curvature in the short-time region ranges between these limiting cases and the curvature depends on the relative contribution of the surface- and diffusion-process to the overall exchange kinetics.

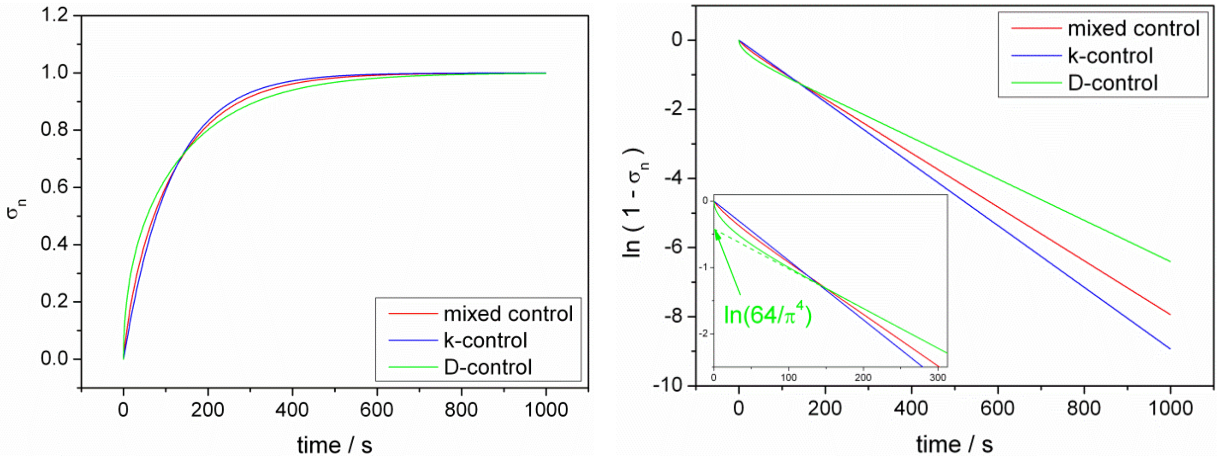

Fig. 2.15 Conductivity relaxation transients for different relaxation models for two-dimensional oxygen exchange. σ_n is plotted on linear axes (left) and in semi-logarithmic representation (right).

Slopes and intercepts of linear sections in the semi-logarithmic representation can be easily derived from the corresponding relaxation equations. For example, from Eq. (2.165) for pure surface exchange control

$$ln(1-\sigma_n) = k\frac{A}{V}t = k(\frac{1}{a}+\frac{1}{b})t \tag{2.167}$$

is obtained, which holds during the whole relaxation period.

For two-dimensional diffusion controlled oxygen exchange only the first exponential term in Eq. (2.164) remains relevant at large times, giving

$$ln(1-\sigma_n) \approx ln\left(\frac{64}{\pi^4}\right) - \frac{\pi^2}{4}\left(\frac{1}{a^2}+\frac{1}{b^2}\right)Dt \tag{2.168}$$

in the limit of $t \to \infty$. Thus, a y-axis intercept of the asymptote of -0.42 ≈ $\ln(64/\pi^4)$ indicates diffusion controlled oxygen exchange and the diffusion coefficient can be calculated from the corresponding slope. A similar expression can be derived from Eq. (2.163) for the model of mixed controlled oxygen exchange but may be of less importance since it does not allow calculating k_{chem} and D_{chem} from the slope in the long-time region. However, the intercept at the y-axis must lie within the interval of $-0.42 \ldots 0$ for the mixed control model to apply.

For the case of surface controlled oxygen exchange with variable k_{chem} three relaxation curves are shown in Fig. 2.16 (left) corresponding to $k_0 < k_\infty$, $k_0 > k_\infty$ and $k_0 = k_\infty$ (k-control). Characteristic differences can be better appreciated from transients in semi-logarithmic representation (Fig. 2.16, right) which show upward- or downward-bending in the short-time range, depending on whether k_0 is above or below k_∞, respectively. For $k_0 = k_\infty$ a straight line is obtained.

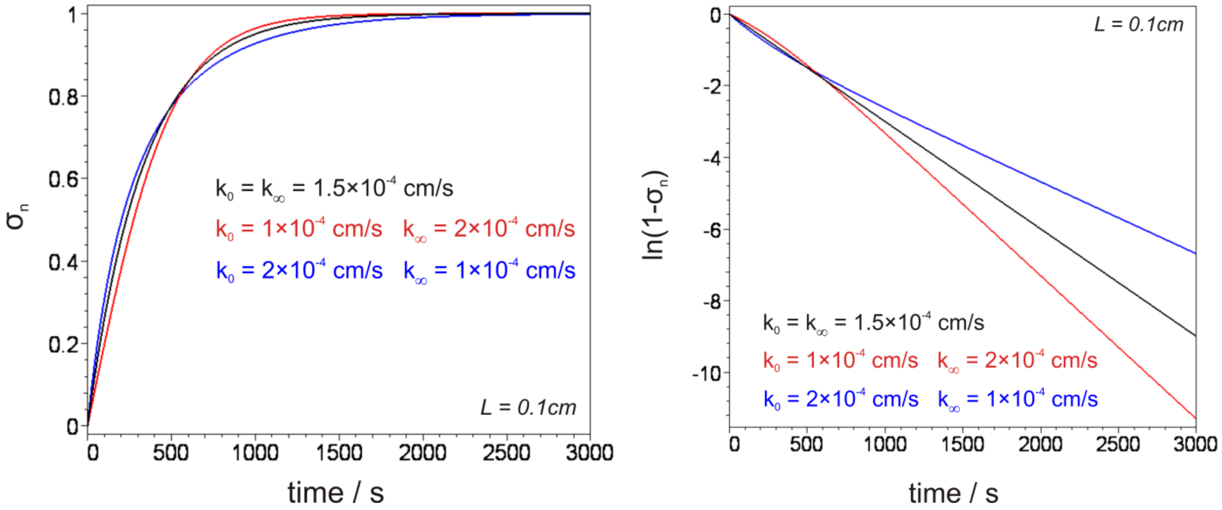

Fig. 2.16 Conductivity relaxation transients for surface controlled oxygen exchange where k_{chem} is a linear function of the oxygen concentration and runs from k_0 to k_∞ during the relaxation process. The curves are plotted on linear axes (left) and in semi-logarithmic representation (right) for $k_0 = k_\infty$ (i.e. ideal k-control), $k_0 < k_\infty$ and $k_0 > k_\infty$.

The link between the characteristic bending of the variable-k exchange model in semi-logarithmic representation and the exchange parameter k_0 and k_∞ is illustrated in Fig. 2.17 for one-dimensional two-sided oxygen exchange. As can be derived from Eq. (2.166) the slopes of the tangent at $t = 0$ and for $t \to \infty$ are proportional to k_0 and k_∞, respectively.

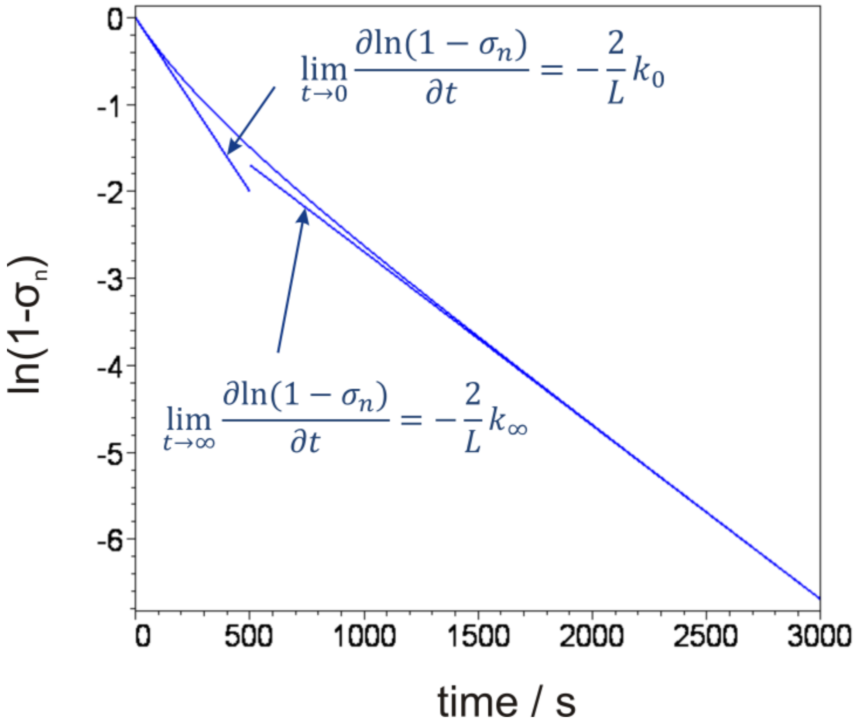

Fig. 2.17 Conductivity relaxation transient for surface controlled oxygen exchange with k_{chem} depending linearly on the oxygen concentration. k_{chem} changes from k_0 to k_∞ during the relaxation measurement with k_0 and k_∞ being proportional to the slopes in the short- and long-time regions, respectively. The convex shape of the relaxation transient is due to $k_0 > k_\infty$.

2.10.2 Van der Pauw geometry

It has been shown by Preis et al. [168] that the van der Pauw-type electrode arrangement can be employed for conductivity relaxation measurements as well, provided the current is flowing perpendicular to the direction of oxygen diffusion (see section 2.8.2).

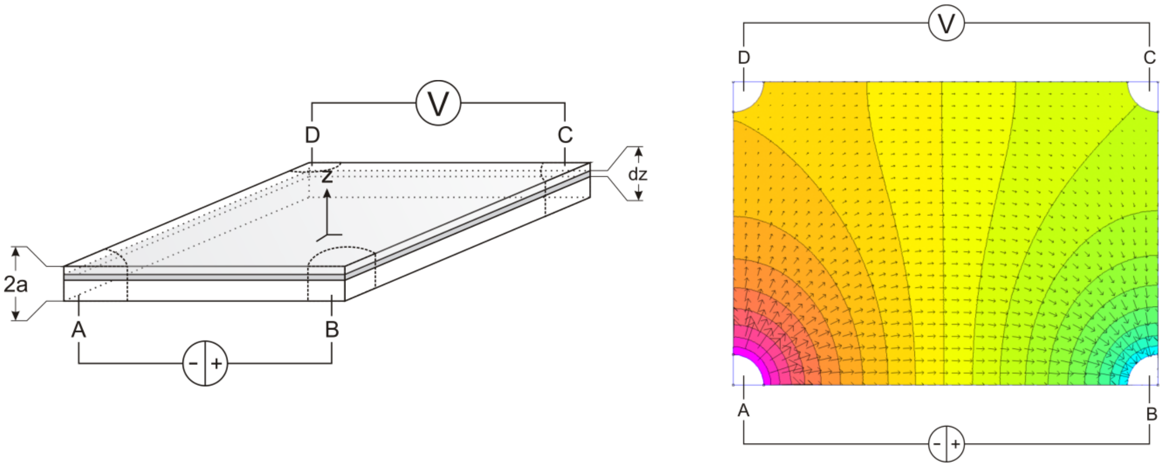

Fig. 2.18 Rectangular flat sample of thickness $2a$ contacted in van der Pauw geometry. A layer of infinitesimal thickness dz is shown in the perspective view (left). The right diagram gives a top view showing equipotential lines (boundaries between colored regions) as well as current density vectors [204].

This can be shown on the basis of Eq. (2.99), which was derived for a flat sample of thickness d but can equally well be applied to a sheet of infinitesimal thickness dz (Fig. 2.18, left), since the conductivity is constant within the layer when oxygen flow is restricted parallel to the z-axis in Fig. 2.18 (see also Fig. 2.7, left)

$$\mathrm{V}_{DC}(t) = \frac{1}{\pi} ln \frac{(a+b)(b+c)}{b(a+b+c)} \frac{1}{\sigma(z,t)} \frac{dI_{AB}(z)}{dz} = K \frac{1}{\sigma(z,t)} \frac{dI_{AB}(z)}{dz} \qquad (2.169)$$

In Eq. (2.169) K includes all factors that are constant over the sample thickness, including the logarithmic term containing the geometric arrangement of the electrodes. The effect of the finite size of the electrodes – as indicated in Fig. 2.18 – is neglected in the theoretical treatment where infinitely thin line contacts are assumed. Errors in conductivity caused by extended contacts have been discussed in section 2.6.2.

Thus, the conductance of a layer of thickness *dz* is

$$dG = \frac{dI_{AB}(z)}{V_{DC}(t)} = K^{-1}\sigma(z,t)dz \tag{2.170}$$

and since the sample slab can be assembled by stacking such layers electrically connected in parallel, the infinitesimal conductances add up according to

$$G(t) = K^{-1} \int\limits_{z=-a}^{a} \sigma(z,t)dz \tag{2.171}$$

Inserting Eq. (2.171) into the definition of σ_n gives

$$\sigma_n(t) \equiv \frac{G(t) - G_0}{G_\infty - G_0} = \frac{1}{2a} \int\limits_{z=-a}^{a} \frac{\sigma(z,t) - \sigma_0}{\sigma_\infty - \sigma_0} dz \tag{2.172}$$

and taking into account the relationship between electrical conductivity and oxygen concentration (Eq. (2.154)) yields

$$\sigma_n(t) = \frac{1}{2a} \int\limits_{z=-a}^{a} \bar{c}(z,t)dz \tag{2.173}$$

Similar to the linear sample geometry, the integral in Eq. (2.173) can be considered as a special case of the weight relaxation transient given in Eq. (2.149) for $\bar{c} \neq f(x,y)$. Thus

$$\sigma_n(t) = \overline{m}(t) \tag{2.174}$$

but it is again emphasized that Eq. (2.174) cannot be taken for granted but has to be derived separately based on the local current-voltage relationship within the sample. Indeed, if oxygen is flowing normal to the z-axis in Fig. 2.18, Eqs. (2.173) and (2.174) become invalid.

Applying Eq. (2.173) to the various expressions of $\bar{c}$ derived for one-dimensional oxygen transport (i.e. Eqs. (2.134), (2.140), (2.146) and (2.148)) yields equations of the corresponding transients to be applied to conductivity relaxation measurements on van der Pauw contacted samples.

For the case of mixed controlled oxygen exchange Eq. (2.175) is obtained

$$\sigma_n(t) = 1 - \sum_{n=1}^{\infty} \frac{2L_\beta^2}{(L_\beta^2 + L_\beta + \beta_n^2)\beta_n^2} \, e^{-\frac{\beta_n^2}{a^2}Dt}$$

$$\beta_n \tan(\beta_n) = L_\beta \qquad\qquad L_\beta \equiv \frac{ka}{D} \tag{2.175}$$

which in the case of pure diffusion control simplifies to

$$\sigma_n(t) = 1 - \frac{8}{\pi^2} \sum_{n=0}^{\infty} \frac{1}{(2n+1)^2} \, e^{-(2n+1)^2 \frac{\pi^2}{4a^2}Dt} \tag{2.176}$$

For surface controlled oxygen exchange with constant k_{chem} Eq. (2.177) holds

$$\sigma_n(t) = 1 - e^{-k\frac{1}{a}t} \tag{2.177}$$

while for the more general case of a *k*-controlled exchange where the surface exchange coefficient linearly depends on the oxygen concentration, Eq. (2.178) is obtained

$$\sigma_n(t) = 1 - \frac{k_\infty}{(k_\infty - k_0) + k_0 e^{k_\infty \frac{1}{a}t}} \tag{2.178}$$

In the above relaxation models *a* is identical to the sample thickness *L* for one-sided oxygen exchange but has to be substituted by *L/2* in case of two-sided oxygen flux.

Fig. 2.19 shows transients for different types of exchange control in linear and semi-logarithmic representation. The characteristic features are similar to those discussed above for the linear electrode arrangement.

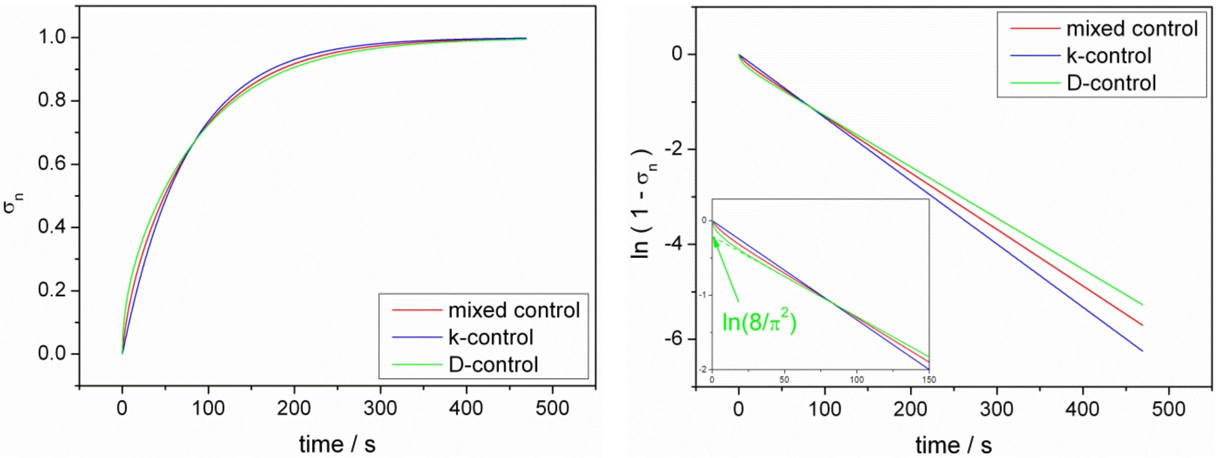

Fig. 2.19 Conductivity relaxation transients of relaxation models for one-dimensional oxygen exchange. σ_n is plotted on linear axes (left) and in semi-logarithmic representation (right).

At large times relaxation transients become linear in a semi-logarithmic representation. For *k*-controlled oxygen exchange

$$ln(1-\sigma_n) = \frac{k}{a}t \tag{2.179}$$

while for the model of diffusion controlled exchange the long-time approximation yields

$$ln(1-\sigma_n) \approx ln\left(\frac{8}{\pi^2}\right) - \frac{\pi^2}{4a^2}Dt \qquad \text{for } t \to \infty \tag{2.180}$$

with an *y*-axis intercept of -0.21 ≈ $\ln(8/\pi^2)$. For mixed controlled oxygen exchange the intercept at the *y*-axis is between 0 and -0.21.

It is interesting to note that for the model of diffusion controlled oxygen exchange a short-time approximation is available

$$\sigma_n \approx \frac{2}{a\sqrt{\pi}}\sqrt{Dt} \qquad \text{for } \sqrt{Dt} \ll a \tag{2.181}$$

which holds in the initial stage of the diffusion process where the diffusion length $\sqrt{Dt}$ is significantly below the sample thickness and the system does not yet perceive the impenetrable boundary at the far end.

2.11 Flush time correction

In the case of conductivity relaxation measurements the reactor volume necessary to accommodate the sample, wirings, thermocouples and possibly an oxygen sensor can be made rather small. Therefore, the pO_2-change inside the reactor after a gas switch can usually be assumed to follow an ideal step function (Fig. 2.20, right).

However, such an approximation is becoming inaccurate for specimens showing fast relaxation behavior as observed for thin samples or at high temperatures. In this case corrections should be applied to the models to take into account the flush time of the reactor. This is achieved by considering the flushing behavior of a continuous ideally stirred tank reactor (CISTR) as illustrated in Fig. 2.20.

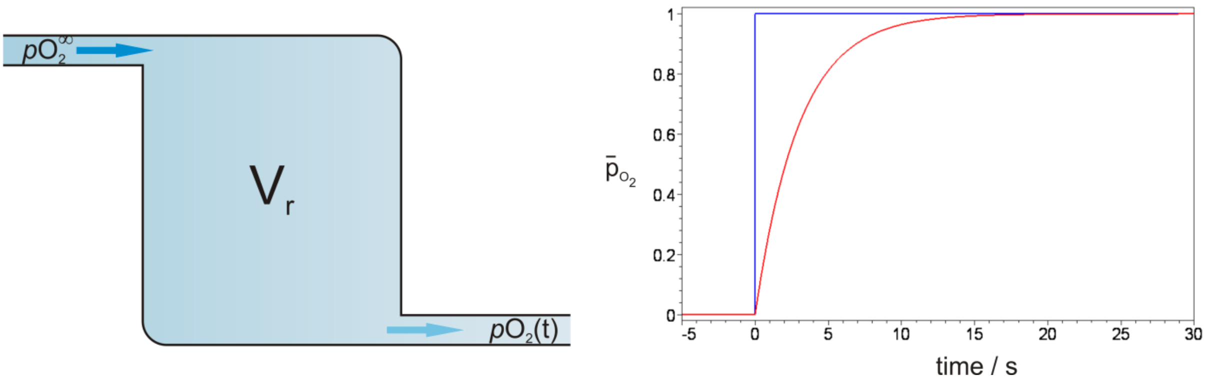

Fig. 2.20 Illustration of the flushing process inside a reactor of volume V_r where the oxygen partial pressure of the inflow is pO_2^∞ and the O_2-pressure of the gas leaving the reactor relaxes from the initial value pO_2^0 to pO_2^∞ (left). The right diagram compares the ideal pO_2-step (blue line) with that of a reactor with a time-constant $\tau_r = 3$ s (red line), showing the normalized oxygen partial pressure $\bar{p}_{O_2} \equiv (pO_2(t) - pO_2^0)/(pO_2^\infty - pO_2^0)$ as a function of time.

Setting up the mass balance of oxygen for the empty reactor and converting amounts to partial pressures via the ideal gas equation gives

$$V_r \frac{dp_{O_2}(t)}{dt} = \dot{V} p_{O_2}^\infty - \dot{V} p_{O_2}(t) \tag{2.182}$$

where $\dot{V}$ is the total volumetric gas flow into and out of the reactor.

Solving Eq. (2.182) with the initial condition $pO_2(0) = pO_2^0$ yields

$$p_{O_2}(t) = p_{O_2}^{\infty} + (p_{O_2}^{0} - p_{O_2}^{\infty})e^{-\frac{\dot{V}}{V_r}t} \tag{2.183}$$

and normalizing the oxygen partial pressure in Eq. (2.183) in analogy with $\bar{c}(t)$ and $\bar{G}(t)$ leads to

$$\bar{p}_{O_2}(t) \equiv \frac{p_{O_2}(t) - p_{O_2}^{0}}{p_{O_2}^{\infty} - p_{O_2}^{0}} = 1 - e^{-\frac{t}{\tau_r}} \tag{2.184}$$

where $\tau_r \equiv \frac{V_r}{\dot{V}}$ is the so-called reactor flush time, i.e. the time constant of the reactor. The larger the reactor volume and the smaller the gas flow through the reactor are, the longer it takes to replace the gas inside the reactor. It should be noted that $\dot{V}$ is not identical to the flow adjusted by means of flow controllers outside the furnace, because the volumetric gas flow is a function of temperature according to

$$\dot{V} = \dot{V}_{FC}\frac{T_r}{T_{FC}} \tag{2.185}$$

where $\dot{V}_{FC}$ is the total gas flow through the flow controllers at temperature T_{FC} and T_r is the reactor temperature (both in Kelvin). Thus, the time constant of the reactor can be estimated from

$$\tau_r = \frac{V_r}{\dot{V}_{FC}}\frac{T_{FC}}{T_r} \tag{2.186}$$

if the reactor volume is known [178]. Conversely, Eq. (2.186) allows to estimate the reactor volume after the time-constant of the reactor has been determined by fitting Eq. (2.184) to an experimental pO_2-transient of the empty reactor recorded with an oxygen sensor. Fig. 2.20 (right) shows the normalized pO_2-transient of a CISTR compared with an ideal pO_2-step.

It should be mentioned that the assumption of a certain pO_2-transient of the empty reactor, be it unit step, exponential or any other, neglects the contribution of the sample which itself absorbs or releases oxygen after a change of the gas composition. Hence, it is assumed that the gas flows and/or the reactor volumes are large enough to buffer or to quickly purge or replenish the oxygen released or absorbed by the sample and thus oxygen starvation or accumulation effects around the sample surface do not occur.

To take into account the non-ideal gas change around the sample the analytical equations of all conductivity transients given above could be recalculated from scratch after incorporating Eq. (2.183) into the boundary conditions. However, den Otter et al. provided an elegant way by which the updated equations can be derived on the basis of the existing ones using linear response theory [178]. This theory applies to all different types of transients given above, except for the case of surface controlled oxygen exchange with variable k_{chem} in Eq. (2.166), because of the non-linearity of the corresponding differential equation (2.147).

Thus, the sample can be viewed as a linear system that takes a (normalized) $p\text{O}_2$-profile as input and whose response or output is a change in (normalized) conductivity. According to linear response theory this interrelation between input and output can be described by a simple expression when transformed to Laplace-space

$$\mathcal{L}_{(s)}\left(\sigma_{n_{(t)}}\right) = H(s)\,\mathcal{L}_{(s)}\left(\bar{p}_{O_2(t)}\right) \tag{2.187}$$

where $H(s)$ is the so-called transfer function of the linear system which establishes the relation between the Laplace transforms of an arbitrary input $\mathcal{L}(\bar{p}_{O_2})$ and the corresponding output $\mathcal{L}(\bar{G})$. s and t denote the independent variables in the Laplace-domain and time-domain, respectively, and will be omitted in the following. Once Eq. (2.187) is established for a single input-output pair, the transfer function of the system can be obtained and the response to any other input function can be calculated.

Applying Eq. (2.187) to the relaxation curves derived above, which are the response to the normalized ideal $p\text{O}_2$-step, gives

$$\mathcal{L}(\sigma_n) = H(s)\,\frac{1}{s} \tag{2.188}$$

where $1/s$ is the Laplace-transform of the unit-step function.

Thus, the transfer function is

$$H(s) = s\mathcal{L}\left(\sigma_n^{id}\right) \tag{2.189}$$

where $\mathcal{L}\left(\sigma_n^{id}\right)$ is the Laplace-transform of the conductivity transient obtained for an ideal pO$_2$-step. The response to the pO$_2$-input of the CISTR can now be determined as

$$\mathcal{L}(\sigma_n^{CISTR}) = H(s)\frac{1}{\tau_r}\frac{1}{s(s+\tau_r{}^{-1})} \tag{2.190}$$

where $[\tau_r s(s+\tau_r{}^{-1})]^{-1}$ is the Laplace-transform of $\bar{p}_{O_2}$ for the CISTR (Eq. (2.184)). Plugging Eq. (2.189) into Eq. (2.190) gives

$$\mathcal{L}(\sigma_n^{CISTR}) = \frac{1}{\tau_r}\frac{1}{(s+\tau_r{}^{-1})}\mathcal{L}\left(\sigma_n^{id}\right) \tag{2.191}$$

Finally, considering that multiplication in Laplace-domain corresponds to convolution in the time domain, Eq. (2.191) can be transformed back to the time domain, yielding

$$\sigma_n^{CISTR} = \int_0^t \frac{1}{\tau_r} e^{-\frac{t-\tau}{\tau_r}}\,\sigma_n^{id}(\tau)d\tau = \frac{1}{\tau_r}e^{-\frac{t}{\tau_r}}\int_0^t e^{\frac{\tau}{\tau_r}}\,\sigma_n^{id}(\tau)d\tau \tag{2.192}$$

Thus, any of the Eqs. (2.163), (2.164), (2.165), (2.175), (2.176) and (2.177) can be converted to include the reactor flush time correction by calculating the convolution integral given in Eq. (2.192).

The generic form of the relaxation equations for bar-shaped samples contacted in linear four-point geometry including flush time correction is

$$\sigma_n^{CISTR} = 1 - e^{-\frac{t}{\tau_r}} - \sum_m\sum_n A_{m,n}\frac{\tau_{m,n}}{\tau_{m,n}-\tau_r}\left(e^{-\frac{t}{\tau_{m,n}}} - e^{-\frac{t}{\tau_r}}\right) \tag{2.193}$$

and a similar expression is obtained for flat samples in van der Pauw geometry

$$\sigma_n^{CISTR} = 1 - e^{-\frac{t}{\tau_r}} - \sum_n A_n \frac{\tau_n}{\tau_n - \tau_r} \left(e^{-\frac{t}{\tau_n}} - e^{-\frac{t}{\tau_r}} \right) \tag{2.194}$$

where $A_{m,n}$ and A_n are the pre-exponential factors in the corresponding series, $\tau_{m,n}$ and τ_n are time constants in the exponential terms of the model function and τ_r is the flush time of the reactor. Eqs. (2.193) and (2.194) include k-controlled transients as well, in which case the sums can be considered to consist of a single term. It should be mentioned that the double sum in Eq. (2.193) cannot be factored into single sums for $\tau_r > 0$ which makes the numerical evaluation more cumbersome and slows down computation.

Fig. 2.21 shows conductivity relaxation transients with a reactor flush time of 3 s calculated according to Eq. (2.194). The flushing process of the reactor manifests itself in a slight inflection of the transients at the beginning of the experiment [181].

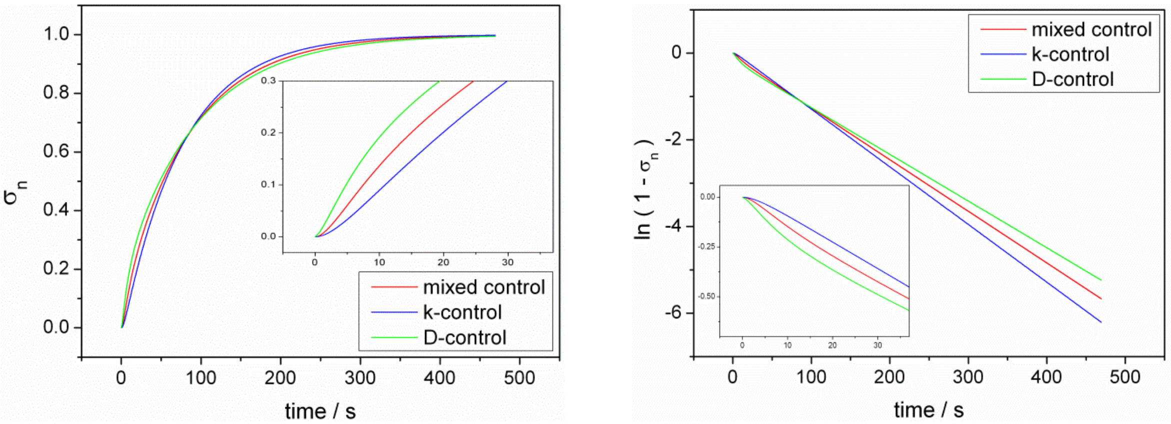

Fig. 2.21 Calculated conductivity transients of relaxation models for one-dimensional oxygen exchange and a reactor flush time τ_r = 3s. σ_n is plotted on linear axes (left) and in semi-logarithmic representation (right). Insets give magnified views of short-time data showing the characteristic curvature caused by reactor flushing.

It is important to note that flush time corrections cannot be adopted to correct for arbitrarily large reactor volumes. If the time constant of the reactor is too large compared to the relaxation time of the sample itself, crucial information contained in the short time range of the conductivity transient is lost which makes results obtained from non-linear fitting ambiguous. This point is further elaborated in the experimental chapter. According to an estimation given by den Otter et al. flush time correction can be neglected if the duration of the experiment is at least 500 or 5000 times larger than τ_r for diffusion and surface controlled oxygen exchange, respectively [178]. Moreover, the authors present criteria when flush-time correction can and should be performed and when it becomes impossible to obtain both k_{chem} and D_{chem} from a single experiment [178].

3 Experimental

3.1 Setup

Fig. 3.1 gives an illustration of the setup used for electrical conductivity and conductivity relaxation measurements. Experiments were performed in a quartz reactor placed in a horizontal tube furnace equipped with a temperature controller (Eurotherm Mod. 2416). During each measurement the reactor was flushed with appropriate oxygen-argon gas mixtures at total flow rates of 2-8 L/h (STP). Gas mixtures were either taken directly from the gas bottle as delivered by the gas supplier or were established by means of mass flow controllers (MFCs) mixing oxygen and argon in the appropriate ratio. Sample temperature and oxygen partial pressure (pO_2) were measured with a potentiometric oxygen sensor with integrated S-thermocouple (MicroPoas, Setnag) placed close to the sample. The oxygen sensor has an internal oxygen reference (Ir/IrO_2 solid state buffer) with linear temperature-voltage characteristics in the operating range between 700 and 900°C. For measuring the sensor signal a high-impedance voltmeter (Keithley Mod. 2000) was used since a minimum internal resistance of 1 GΩ is specified by the sensor manufacturer. A National Instruments device (NI 9211 with 9162 USB-Carrier) was used for converting the thermocouple signal into temperature and interfacing with the computer. In some cases sample holders without oxygen sensors (S-thermocouple only) as well as ball-flowmeters with needle valves were employed when using pre-mixed gases from the supplier.

The dc conductivity was measured using the four-point method in either van der Pauw or linear electrode geometry. Van der Pauw measurements were performed using a source-meter (Keithley Mod. 2400) acting both as current source and voltmeter. Automated I/U-switching between contacts was performed by changing between front and rear panel linked by wires in 90° rotational displacement. In some cases a voltmeter (Keithley Mod. 2000) with plug-in scanner card was used to allow for a complete 4×90° scan for increased accuracy and to check the quality of the electronic contacts. Currents of 100-500 mA were applied, depending on the sample resistance, and each I-U measurement was repeated in reversed current direction to eliminate thermal offsets by subsequent averaging.

Four-point dc conductivity relaxation measurements were conducted by oxygen partial pressure steps of factor 2 or smaller while recording the transient voltage signal as a function of time. Currents were applied using a current source (Keithley Mod. 2400 or Knick J 152) and the voltage was measured with a nano-voltmeter (Keithley Mod. 182 or 2182). Using a sensitive digital voltmeter in conductivity relaxation measurements is important for obtaining stable and low-noise voltage transients, considering that the changes in voltage are usually below 1 mV, sometimes as low as 50 μV.

A four-way valve was used for manually switching between different gas streams, feeding one gas flow into the reactor while venting the other. For degradation investigations in humid atmospheres the gas streams were passed through water flasks before entering the reactor. The flasks were filled with deionized water and thermostatted at a temperature corresponding to the desired pH_2O under equilibrium conditions.

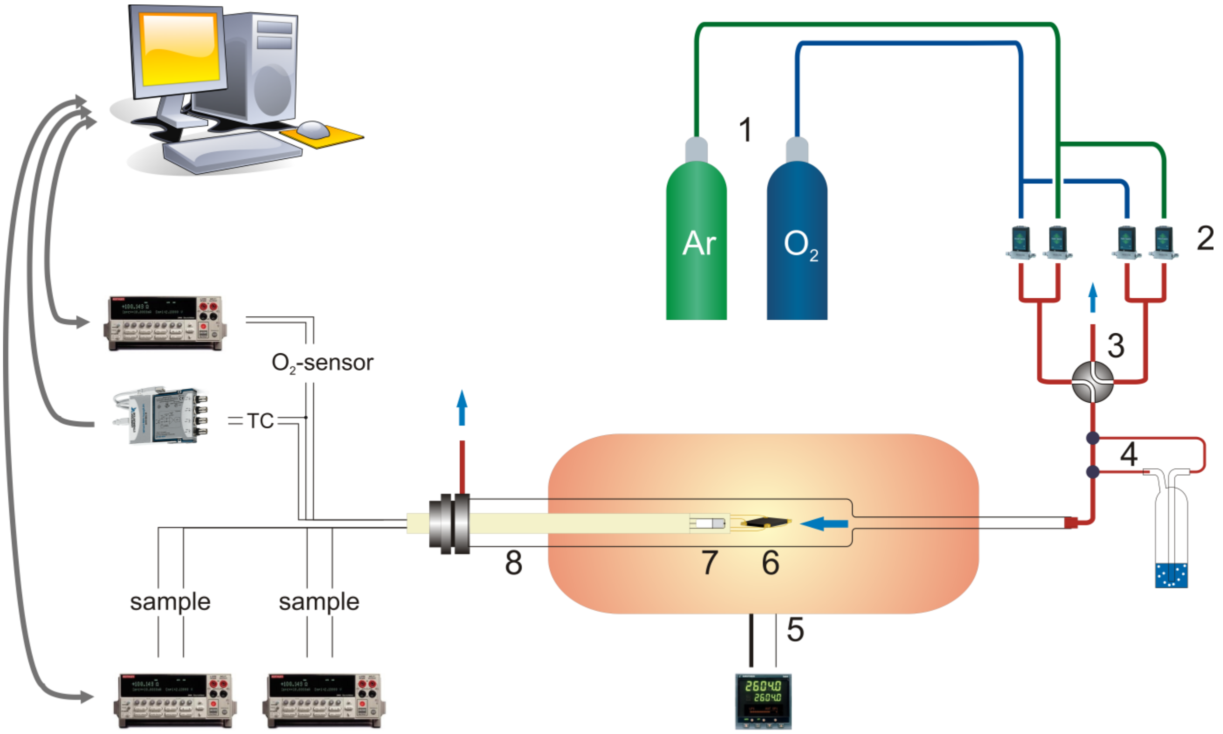

Fig. 3.1 Setup used for conductivity and conductivity relaxation measurements: 1 – gas supply, 2 – mass flow controllers (MFCs), 3 – manual four-way valve, 4 – gas bypass through thermostatted water flask used for humidification, 5 – furnace with temperature controller, 6 – sample, 7 – oxygen sensor with integrated S-type thermocouple (TC), 8 – quartz reactor with flange and mounted sample holder. Blue arrows denote gas flows. Components are not to scale.

Materials for piping, fittings, flanges and valves in the gas supply were Cu or Cu-alloys except when using SO_2-containing gases, where stainless steel components had to be employed due to the reactivity of sulfur with Cu. Sample and oxygen sensor were mounted on an alumina rod inserted in the quartz reactor and sealed by a flange with centering ring and O-ring gasket. The alumina rod contains 8 capillaries used for inserting leads to the sample and O_2-sensor. Gold wires were used to establish contacts to the sample while the leads of oxygen sensor and thermocouples were Pt-based. All measuring devices were interfaced to a computer via GPIB or USB. Data acquisition was performed with software developed in-house using LabView ®.

3.2 Equipment

Density measurements of the raw powder were performed by helium-pycnometry (Quantachrome Ultrapycnometer 1000). Particle size distribution of the raw powder was determined by laser-diffractometry using a particle size analyzer (CILAS 1064). Powders were milled in a planetary ball mill (Fritsch, Pulverisette 7) using zirconia-lined milling cups with zirconia balls (Ø 2mm) in ethanol. Sintering curves and thermal expansion coefficients of the compounds were measured with a dilatometer (Netzsch DIL 402 PC) using Al_2O_3 as reference material. Thin silver layers were deposited onto the sample surface using a sputtering machine (Baltek MED 020).

Chemical composition and microstructure were determined by scanning electron microscopy (SEM; Cambridge Stereoscan 250 MK3) with energy dispersive X-ray spectroscopy (EDX; Oxford Instruments 6272). Crystal structure and phase purity was investigated by X-ray diffraction (XRD; Bruker AXS D8 Advance) using Cu-Kα radiation in the range $10° \leq 2\theta \leq 100°$ with a step size of 0.020° and acquisition time of 2-3 s per step.

The chemical composition of the sample surface was quantified by X-ray photoelectron spectroscopy (XPS). The measurements were carried out at room temperature in ultrahigh vacuum at a base pressure of $2 \cdot 10^{-10}$ mbar utilizing a Thermo MultiLab 2000 spectrometer equipped with an alpha 110 hemispherical analyzer from Thermo Electron, operated in the constant analyzer energy mode at a pass energy of 100 eV corresponding to 2.5 eV overall resolution. The analysis spot size was set to 500-600 µm. XPS-spectra were collected using Al Kα (1486.6 eV) or Mg Kα radiation (1253.6 eV) The chemical composition was obtained from peak areas in survey scans, performing a linear background subtraction and taking into account Scofield sensitivity factors for each constituent [205]. Depth profiles were obtained by an EX05 Ion Gun from Thermo Electron providing a 3 keV argon ion beam, irradiating a ca. 2×2 mm² surface area at an ion current of 1.0-2.5 µA.

3.3 Sample preparation

Powders as well as sintered pellets of $La_2NiO_{4+\delta}$, $Pr_2NiO_{4+\delta}$ and $Nd_2NiO_{4+\delta}$ were obtained from different commercial and non-commercial sources.

Applications of mixed-conducting ceramics may require densely sintered components, as in the case of oxygen-separating membranes, or rather porous structures, as for SOFC- and SOEC-electrodes. However, regardless of the structural features of the final product, it is important to use densely sintered bodies for the investigation of basic materials properties or otherwise some kind of average quantity of both material and pores will be obtained. For example, using porous samples for materials characterization will give too low electrical conductivities, since pores are non-conducting, and may yield too high oxygen diffusion coefficients, since gas phase diffusion is faster than solid state diffusion. While in the case of electrical conductivity correction formulas have been proposed in the literature to account for sample porosity [66,206,207], such formulas are not available for diffusivities.

A convenient measure to specify the amount of porosity in a sintered body is the relative density, which is the ratio of the actual density and the theoretical density as calculated from the crystal structure. While densities of arbitrarily shaped bodies can be determined by different techniques such as Archimedes method or helium-pycnometry, care should be taken to choose a technique that does not exclude parts of the porosity from the result as, for example, helium penetrating into open pores. In this respect the most reliable way to determine the density is probably using the sample mass and dimensions and calculating a geometric density, which of course requires rather regularly shaped bodies. Samples with relative densities above 95% are usually considered to be sufficient since they can be assumed to possess no open porosity [208] and are expected to yield reliable results in diffusion measurements [70].

In the case of unsubstituted nickelates samples with relative densities of above 95% were obtained after isostatic pressing at 200-300 MPa and sintering at 1350°C for 4-10 hours with heating and cooling rates of 2 K/min. From the sintered tablets slabs or bars were cut with a diamond wire saw, ground with a diamond grinding disk and polished on polymer-embedded diamond lapping films with 30, 6, and 1 μm particle size. After the final polishing step the sample was cleaned for 10 min in acetone in an ultrasonic bath.

Electrical contacts were established by attaching four gold wires (Ø 0.1mm, twisted) to the sample with gold paste (Metalor T-10112). The gold paste was burned in for 15 min at 850°C after a drying step at 150°C for 10 min, with heating and cooling rates of 2°C/min. The contact quality can be assessed by measuring the resistance between each pair of gold wires at room temperature with a multimeter. Well established contacts show a resistance below 1 Ω.

XRF-analysis of the gold paste showed Bi, Cd and Pb as additives. Bi was regularly detected by post-test XPS-analyses on the surface of samples contacted with the gold paste. No traces of Cd or Pb were detected by XPS-analysis on the sample surfaces, either due to the higher volatility of Cd- and Pb-oxides or because of a possibly higher reactivity of Bi with the nickelate compounds. However, an impact of Bi on the electronic conductivity or oxygen transport parameters was not observed.

In the case of $Pr_2NiO_{4+\delta}$ it was necessary to keep the temperature below 700°C during sample preparation due to a phase decomposition process observed above that temperature. Contacts were initially prepared by using silver paste (dmc^2, Degussa) as a contact paste, burned in at 600°C for 1 hour with heating and cooling rates of 2°C/min. However, results from thermogravimetric investigations suggested that the phase decomposition might be suppressed in the absence of oxygen in the gas phase. Thus, an alternative contacting method was tested for $Pr_2NiO_{4+\delta}$ where the gold paste was burned in under flowing argon according to the temperature profile stated above. This was done in two steps, where the gold paste was first burned in at 600°C under air, the sample mounted in the reactor and heated in-situ to 850°C while flushing the reactor with pure Ar. No increase of the compound's electronic conductivity was observed after such heat treatment, indicating the absence of decomposition products in the material. A detailed discussion of the phase stability of $Pr_2NiO_{4+\delta}$ and its dependence on temperature and pO_2 is given in chapter 4.

Two different sample geometries have been employed to determine the electronic conductivity and perform conductivity relaxation experiments. One sample design was a flat slab contacted in van der Pauw electrode configuration. In this configuration the sample can be polished to a rather small thickness and samples as thin as 100 μm have been successfully prepared. Contacts have been established by attaching a twisted gold wire with a loop at its closed end to each corner of the sample using gold paste (Fig. 3.2, top left). The contacted sample was mounted in a hand-made quartz holder to fix the position and orientation of the sample since the thin gold wires tend to deform at higher temperatures. The quartz holder was used to accommodate additional pieces of the material for subsequent analytical investigations (Fig. 3.2, top right). For thicker samples wire loop contacts became impracticable and an alternative contacting scheme consisted in cutting vertical grooves along the thin edges (Fig. 3.2, bottom left and right).

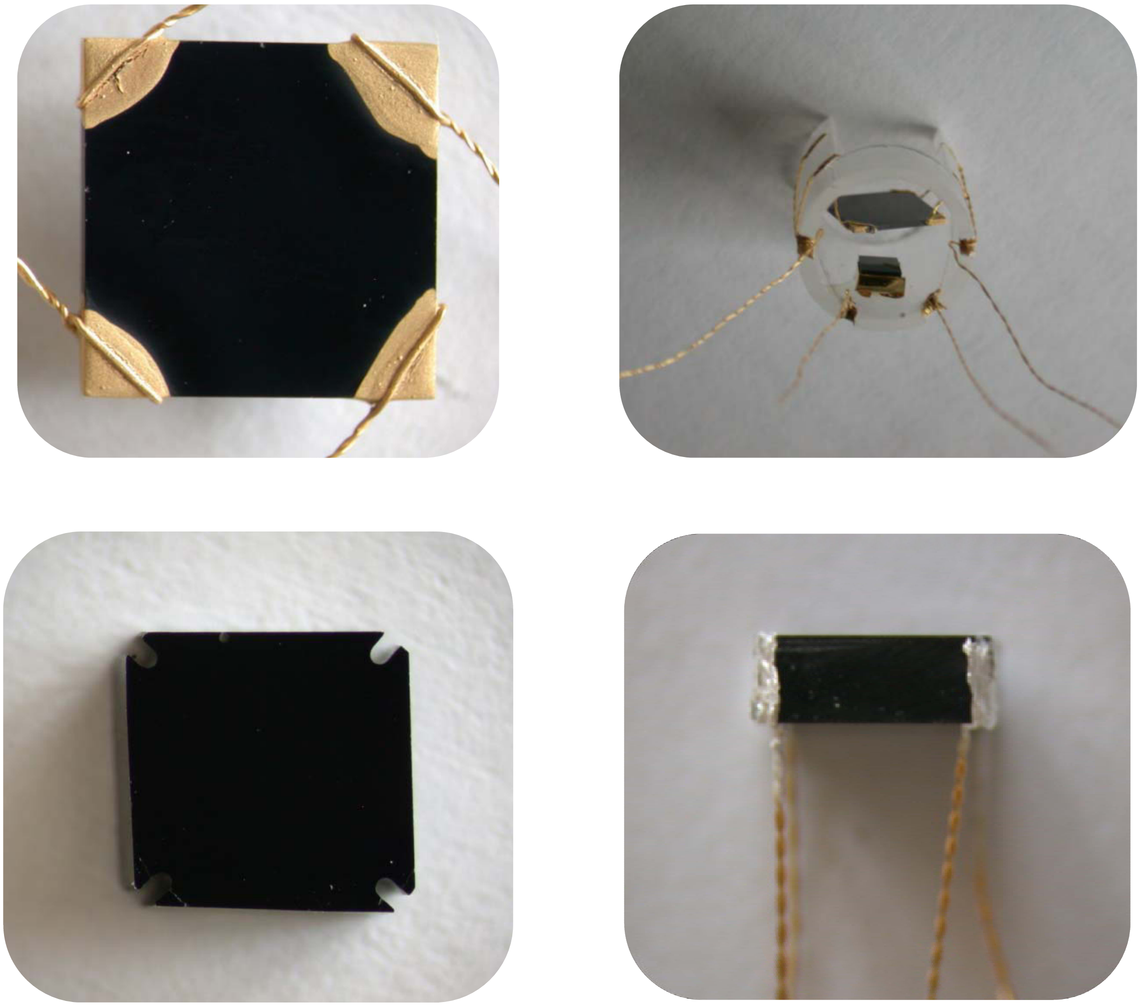

Fig. 3.2 Contacting schemes for a flat sample design. For very thin samples gold wires were attached via gold loops to the sample corners (top left) with gold paste. Usually the sample was mounted in a quartz holder, which – if required – can be equipped with additional pieces of sample material for later investigation (top right). For thicker samples, vertical grooves are cut along the sample edges (bottom left) where silver paste was used in this case as contacting paste (bottom right).

The flat sample design was mainly used to obtain surface exchange coefficients of oxygen especially in connection with long-term investigations of degradation phenomena, which are usually limited to the sample surface and thus mainly affect the surface exchange process of oxygen. For a reliable determination of diffusion coefficients the preparation of thick samples was required. However, in the flat design the sample sheets cannot be made arbitrarily thick without violating the assumption of one-dimensional diffusion necessary in the evaluation of conductivity relaxation measurements (see section 2.5.2). Thus, bar-shaped samples were used to improve the accuracy for diffusion coefficients obtained by relaxation experiments.

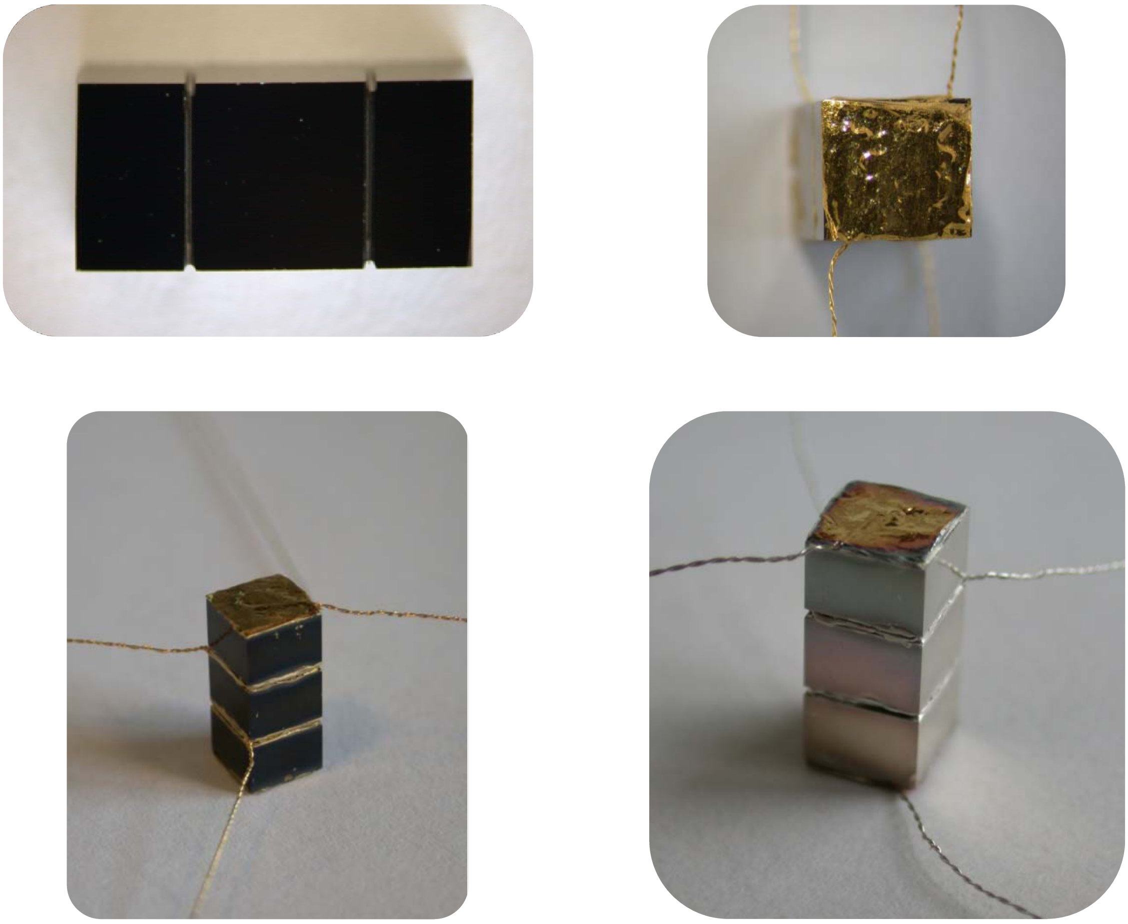

Fig. 3.3 Contacting scheme for bar-shaped samples. The dimension of the sample shown is roughly 4×4×10 mm^3. Thin groves have been cut around the sample to improve positioning of wires used as voltage probes (top left). Large-area current-carrying contacts were established at the front faces of the sample using gold foils (top right). The finished sample is shown in the bottom left picture. To improve the oxygen surface exchange rate a thin silver layer was sputtered onto the sample surfaces (bottom right).

Bar-shaped samples were contacted at both front faces with gold wires and two layers of gold foil fixed with gold paste (Fig. 3.3, top right). The gold foils serve as large-area contacts for applying the current. Furthermore, they impede oxygen incorporation from the gas phase into the sample, thus precluding any diffusion along the sample axis along the current lines (see sections 2.5 and 2.10.1). Two thin grooves have been cut along the sample circumference for easier attachment of the voltage probes (Fig. 3.3, top left). The grooves were symmetrically positioned with a spacing of roughly one third of the bar length [163]. Gold wires were wound around the grooves and fixed with gold paste (Fig. 3.3, bottom left). In some cases silver was sputtered on the sample surface to improve the surface exchange rate of oxygen (Fig. 3.3, bottom right).

3.4 Particle size distribution

Sample powders were characterized with respect to particle size distribution before sintering. To achieve a stable particle suspension 0.2 g of powder (or few drops of suspension from the milling cup) were mixed with 0.2 g NPA as dispersant (Na-polyacrylate, molecular mass 2100) in 20 ml deionized water and treated with an ultrasonic rod for several minutes. 1 g NPA was dissolved in the circulating water flow of the particle analyzer before adding the nickelate suspension. The ultrasonic unit of the analyzer was turned on during the measurement.

Fig. 3.4 (left) shows the particle size distribution of $La_2NiO_{4+\delta}$ as-delivered. The large-diameter fraction of the bimodal distribution is most likely due to hard agglomerates which are detrimental for obtaining high sinter densities. The powder was milled in a planetary ball mill 6 times for 10 min at 900 rpm with intermittent cooling intervals of 30 min. This procedure effectively destroys large agglomerates and affords a unimodal size distribution with an average particle size of 1 µm (Fig. 3.4, right).

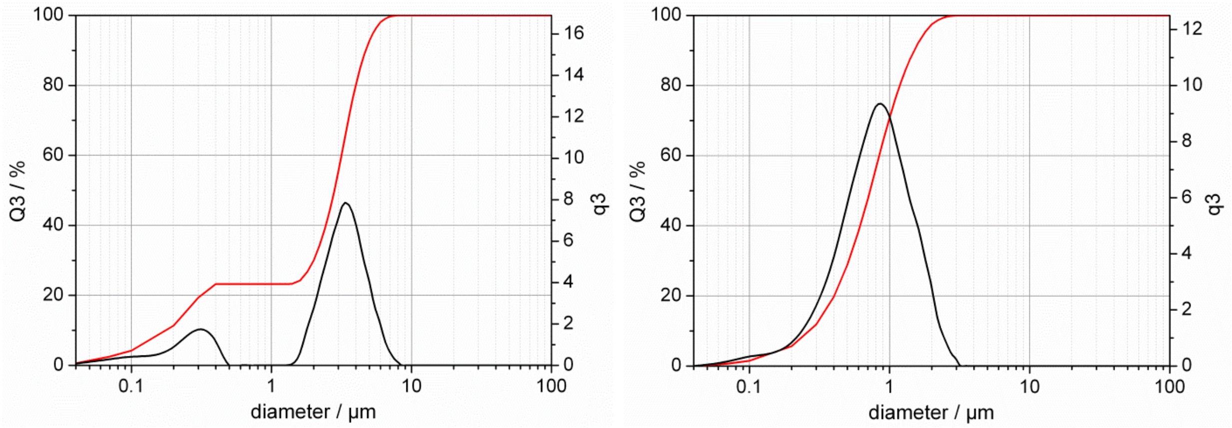

Fig. 3.4 Particle size distribution of $La_2NiO_{4+\delta}$ before (left) and after milling (right). Hard agglomerates are destroyed by milling and an approximate log-normal distribution with a mean particle size around 1 µm is achieved. Black curves denote volume density functions (q3), red lines are the corresponding cumulative distributions (Q3).

3.5 Sintering behavior

To determine optimal sintering conditions for dense samples, sintering curves have been recorded by dilatometry. The sintering behavior of $La_2NiO_{4+\delta}$ was investigated by recording the shrinkage of a powder compact up to 1400°C (3 h dwell) with heating and cooling rates of 1 K/min (Fig. 3.5). From the first derivative of the sintering curve the temperature of maximum densification is found at 1330°C. Based on this result a sintering temperature slightly above that maximum of 1350°C appears appropriate for obtaining highly dense samples [209], which coincides with the sintering temperature frequently reported in the literature for rare earth nickelates.

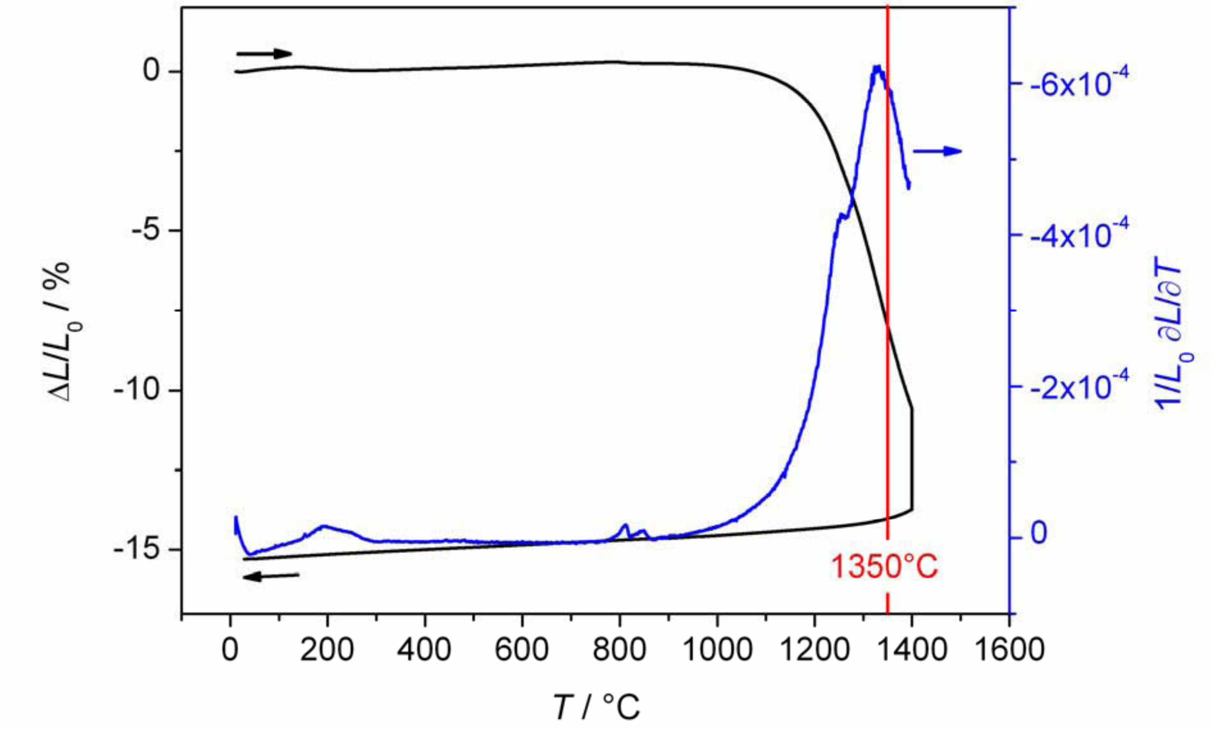

Fig. 3.5 Sintering curve of a green compact of $La_2NiO_{4+\delta}$ in air (black line) and its first derivative (blue line). On the basis of the derivative curve a sintering temperature of 1350°C was chosen for the preparation of densely sintered samples.

3.6 Reactor flush time

Flush times of an empty reactor used for conductivity relaxation measurements were determined at 725°C for different oxygen partial pressures and flow rates. Fig. 3.6 shows results after pO_2-steps for both increasing and decreasing oxygen partial pressures. Time constants τ_r of the reactor have been obtained by fitting Eq. (2.184) to the data.

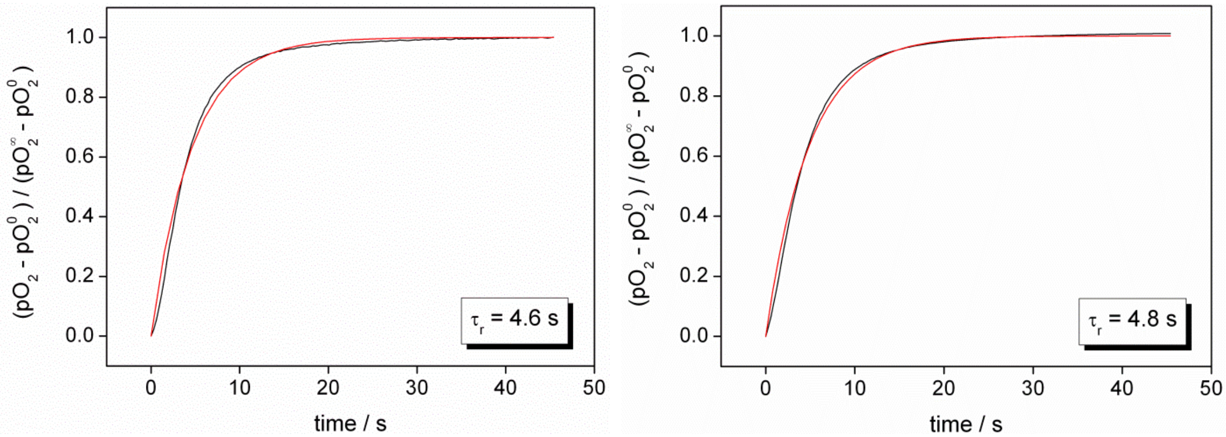

Fig. 3.6 Flushing transients of a quartz reactor used for conductivity relaxation measurements in oxidizing (1%O_2/Ar ⟶ O_2, left) and reducing (O_2 ⟶ 1%O_2/Ar , right) directions at 725°C and a total gas flow of 1 L/h. Normalized oxygen partial pressures are shown as black lines while red lines correspond to fitting curves.

Flushing experiments have been repeated at 725°C for several gas mixtures at total gas flows of 1 L/h and 2 L/h (Fig. 3.7). As a rule, flush times obtained for gas switches to lower pO_2 were slightly larger than those in the opposite direction.

It can be seen from Fig. 3.7 that the average reactor flush time for 1 L/h gas flow was around 4.75 s and is reduced to half of that value when the gas flow is doubled. Reactor volumes calculated from τ_r according to Eq. (2.186) are around 4 cm^3 which is in good agreement with the volume estimated from the reactor geometry. Of course, for real measurements the effective volume is somewhat lower due the presence of the sample and sample holder.

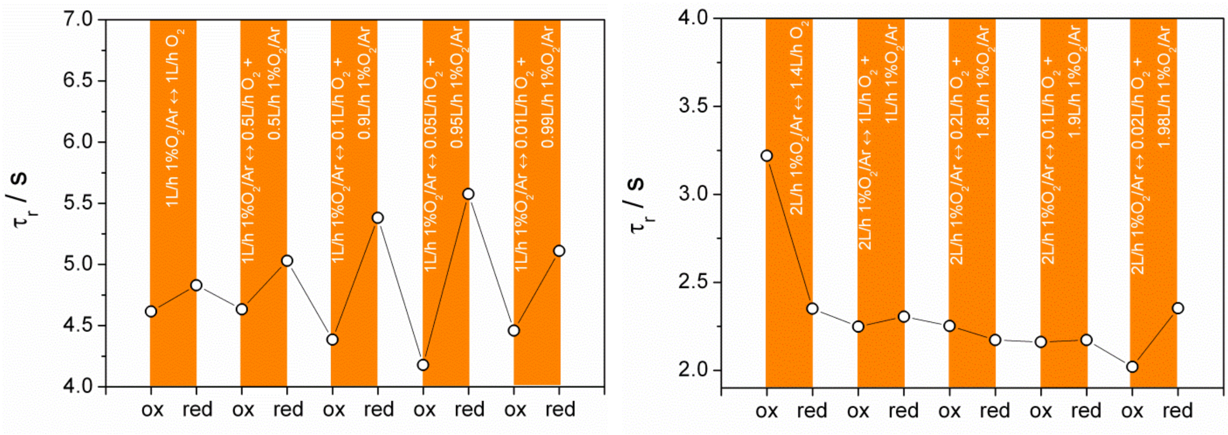

Fig. 3.7 Time constants τ_r of the quartz reactor used for conductivity relaxation measurements at 725°C and a gas flow of 1 L/h (left) and 2 L/h (right). Gas mixtures stated in the diagrams were switched in both directions from low-to-high (ox) and high-to-low (red) oxygen partial pressures.

The effective reactor flush time during a relaxation measurement is not solely a function of reactor volume, gas flow and temperature but is also influenced by the positioning and orientation of the sample. Two different arrangements have been investigated for a flat sample of $La_2NiO_{4+\delta}$ contacted in van der Pauw geometry (Fig. 3.8). The parallel-flow orientation (Fig. 3.8, left) obviously offers less resistance to the gas flow but the perpendicular-flow arrangement (Fig. 3.8, right) allows for a simpler connection to the leads.

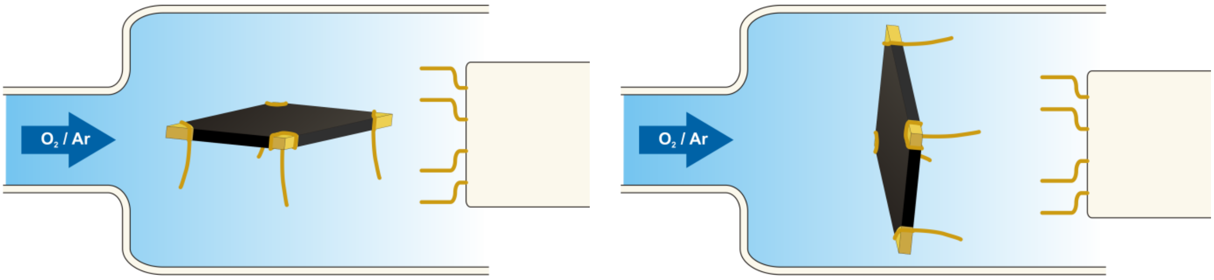

Fig. 3.8 Two different sample orientation tested for conductivity relaxation measurements: parallel-flow (left) and perpendicular-flow (right). Gold leads and the tip of the alumina rod are displayed.

Fig. 3.9 (left) shows conductivity relaxation curves at 700°C corresponding to parallel-flow and perpendicular-flow arrangements of the sample. Perpendicular-flow orientation causes larger effective reactor flush times as evidenced by differences in curvature in the short-time region of the transients. This is illustrated more clearly in the semi-logarithmic plots of the first 500 s of the relaxation experiment as shown in Fig. 3.9 (right).

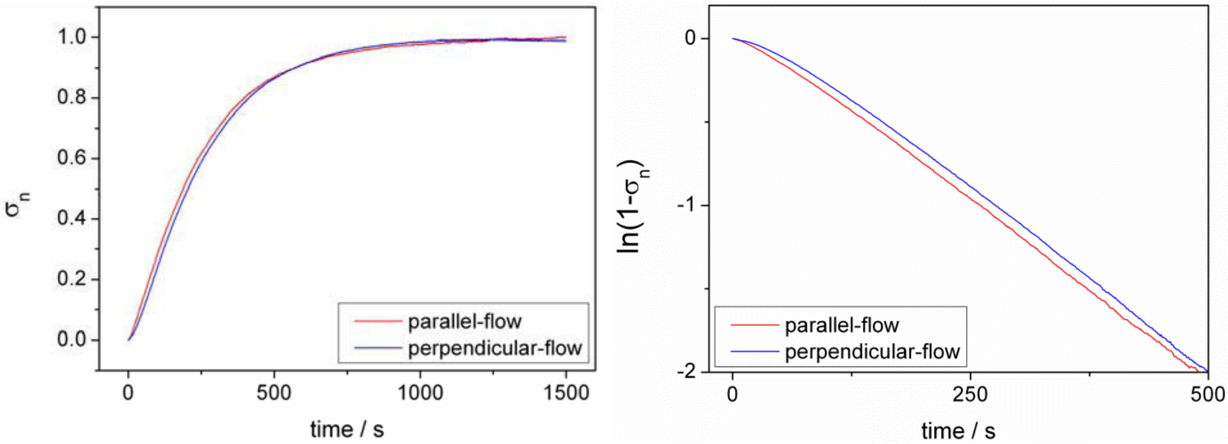

Fig. 3.9 Conductivity relaxation transients of $La_2NiO_{4+\delta}$ 700°C and a pO_2-step of 0.01 ⟶ 0.015 bar for two different sample orientation inside the reactor (see Fig. 3.8). Total gas flow was set to 2 L/h.

Large reactor flush times may impede or even prevent an accurate determination of transport parameters by non-linear curve fitting. However, if the type of exchange control has already been established to be either diffusion or surface controlled, reliable values of the transport parameters may still be obtained since they are essentially determined by the slope in the linear region of the semi-logarithmic representation.

However, special care must be taken when using such measurements to determine the type of control based solely on the fitting quality of the different models to the data. This is because large reactor flush times obscure the curve shape in the short time range, which contains the essential information regarding the dominating contribution to the exchange process. Since in the long-term range all relaxation models become linear in a semi-logarithmic representation (i.e. they all converge to an exponential form of type $1-e^{-const\cdot t}$ at large times), that range cannot be used to determine the exchange control mechanism and by choosing the wrong model transport parameter mays be determined that are actually not contained in the data.

This is demonstrated in Fig. 3.10 (left) where the conductivity transient of a sample mounted perpendicular to the gas flow was fitted by a diffusion controlled model while the reactor flush time was treated as an additional fitting parameter. The quality of the fit is excellent, however the oxygen exchange is definitely not dominated by diffusion as has been established through separate relaxation measurements. Repeating regression analysis with the correct model, that is assuming surface controlled oxygen exchange, yields an equally good match with the data and the obtained surface exchange coefficient is in fairly good agreement with results from independent relaxation measurements (Fig. 3.10, right).

In the case of mixed controlled relaxation the information contained in the short-time data is indispensable since k_{chem} and D_{chem} cannot be unambiguously obtained from the linear slope in the semi-logarithmic plot.

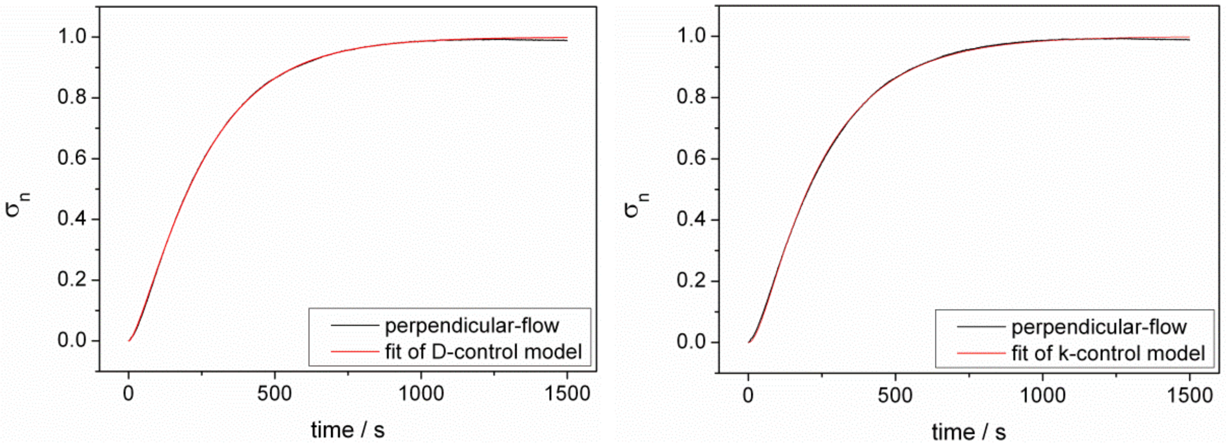

Fig. 3.10 Relaxation curve of a sample of La$_2$NiO$_{4+\delta}$ mounted perpendicular to the flow (see Fig. 3.8). The left diagram shows results assuming diffusion controlled oxygen exchange ($D_{\text{chem}} = 8.8\cdot10^{-6}$ cm^{2}s^{-1}, τ_r = 89 s), the right plot gives results using the fitting model for surface control ($k_{\text{chem}} = 3.0\cdot10^{-4}$ cm s^{-1}, τ_r = 39 s). The fitting quality is excellent in both cases, however, diffusion controlled oxygen exchange is the wrong model.

3.7 Oxygen depletion in the gas phase

Problems may arise with conductivity relaxation measurements performed at low oxygen partial pressures because the oxygen uptake of the specimen may be actually limited by the amount of oxygen supplied by the gas flow rather than being controlled by the oxygen exchange kinetics between the gas phase and the sample. A relaxation experiment of $La_{0.6}Sr_{0.4}CoO_{3-\delta}$ at 700°C and around $1\cdot10^{-3}$ bar pO_2 was investigated in more detail to check whether oxygen exchange may be limited by the oxygen capacity of the gas. According to oxygen stoichiometry data given by Bucher [210] the non-stoichiometry of the sample decreases by $\Delta\delta = -5.2\cdot10^{-3}$ when switching from $1.0\cdot10^{-3}$ to $1.5\cdot10^{-3}$ bar pO_2 at 700°C (Fig. 3.11).

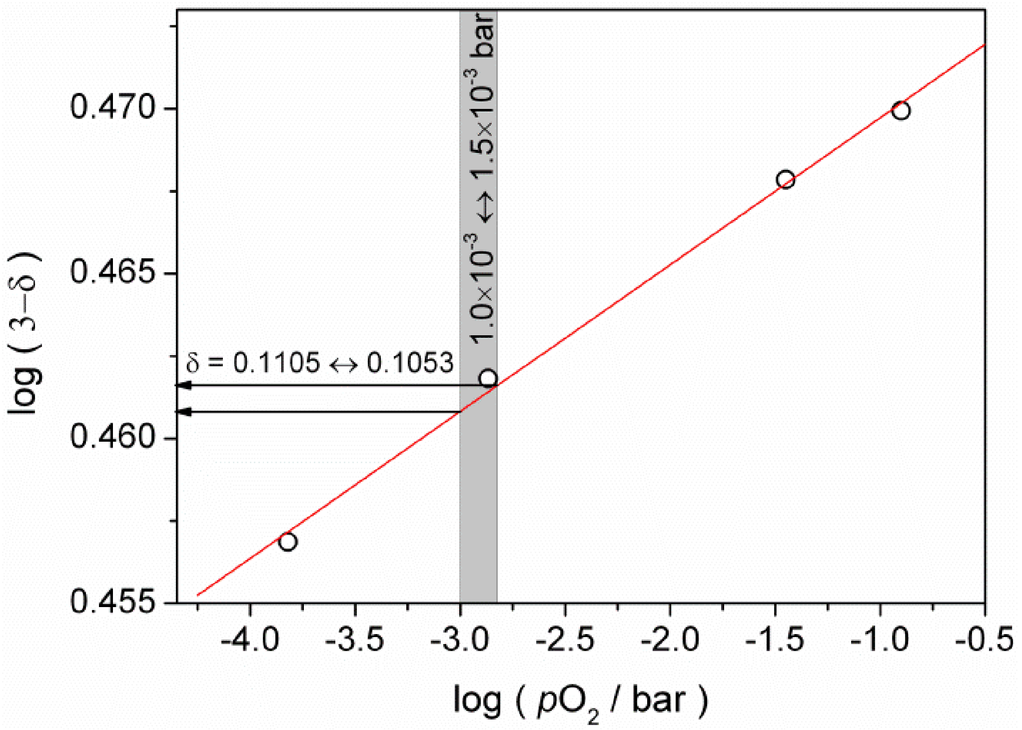

Fig. 3.11 Calculated change in oxygen stoichiometry of $La_{0.6}Sr_{0.4}CoO_{3-\delta}$ as response to a pO_2 switch between $1.0\cdot10^{-3}$ and $1.5\cdot10^{-3}$ bar at 700°C [210].

For a surface exchange controlled relaxation process of $La_{0.6}Sr_{0.4}CoO_{3-\delta}$ at 700°C and $pO_2 = 1\cdot10^{-3}$ bar a chemical surface exchange coefficient of $4.1\cdot10^{-5}$ cm s^{-1} has been obtained (Fig. 3.12).

The electrical conductivity σ of $La_{0.6}Sr_{0.4}CoO_{3-\delta}$ is dominated by electronic conduction via holes $h^{\cdot}$ [211,212]

$$\sigma = \sigma_{h^{\cdot}} = e c_{h^{\cdot}} u_{h^{\cdot}} \tag{3.1}$$

where e is the elementary charge, $u_{h^{\cdot}}$ the hole mobility and $c_{h^{\cdot}}$ the concentration of defect electrons. Applying the local electroneutrality condition gives

$$c_{Sr'_{La}} = c_{h^{\cdot}} + 2c_{V_O^{\cdot\cdot}} \tag{3.2}$$

and as $c_{Sr'_{La}}$ is constant, a linear relationship between $c_{h^{\cdot}}$ and $c_{V_O^{\cdot\cdot}}$ ($\propto \delta$) can be established. Assuming that the electronic mobility is independent of hole concentration, Eqs. (3.1) and (3.2) entail a linear correspondence between σ and δ [211].

Thus, the normalized conductivity σ_n is equal to the normalized oxygen non-stoichiometry δ_n

$$\sigma_n(t) \equiv \frac{\sigma(t) - \sigma_0}{\sigma_\infty - \sigma_0} = \frac{\delta(t) - \delta_0}{\delta_\infty - \delta_0} \equiv \delta_n(t) \tag{3.3}$$

and therefore

$$\frac{\partial \sigma_n}{\partial t} = \frac{\partial \delta_n}{\partial t} \tag{3.4}$$

The oxygen flux through the sample surface corresponds to the rate of change of δ_n according to

$$J(O^{2-}) = \frac{1}{A_S}\frac{V_S}{V_m}\frac{\partial \delta}{\partial t} = \frac{1}{A_S}\frac{V_S}{V_m}(\delta_\infty - \delta_0)\frac{\partial \delta_n}{\partial t} = 2\,J(O_2) \tag{3.5}$$

where A_s and V_S are the sample surface and volume, respectively and V_m is the molar volume of the compound.

The molar flow of oxygen through the sample surface $\dot{n}_{surf}$ is obtained by combining Eqs. (3.3) and (3.5)

$$\dot{n}_{surf} = |A_s\, J(O_2)| = \left|\frac{1}{2}\frac{V_S}{V_m}(\delta_\infty - \delta_0)\frac{\partial \sigma_n}{\partial t}\right| \tag{3.6}$$

and the time dependence of σ_n is modeled by *k*-controlled oxygen exchange

$$\sigma_n(t) = 1 - e^{-k_{chem}\frac{2}{L}t} \tag{3.7}$$

Inserting Eq. (3.7) into Eq. (3.6) gives the total oxygen flow into the sample. With $V_m \approx 60\,\text{Å}^3$, $V_S \approx 32\, mm^3$, $(\delta_\infty - \delta_0) = -0.0052$ and $L = 0.02$ cm the surface exchange coefficients results as $k_{\text{chem}} = 4.1\cdot10^{-5}$ cm s^{-1}.

Such an oxygen demand is to be compared with what can be supplied by the gas stream through the reactor, which is calculated by

$$\dot{n}_{gas}(O_2) = \frac{p_{O_2}\dot{V}}{RT_{FC}} \tag{3.8}$$

where $pO_2 = 1\cdot10^{-3}$ bar, $\dot{V} = 2\, L/h$ (gas flow as measured by flow controllers) and the temperature $T_{FC} = 298\, K$.

Fig. 3.12 (right) illustrates that for an oxygen partial pressure of 10^{-3} bar and a total gas flow of 2 L/h the oxygen supply is by a factor of 10 larger than the oxygen demand of the sample during the initial phase of the sample oxidation, where the oxygen influx rate is at its maximum.

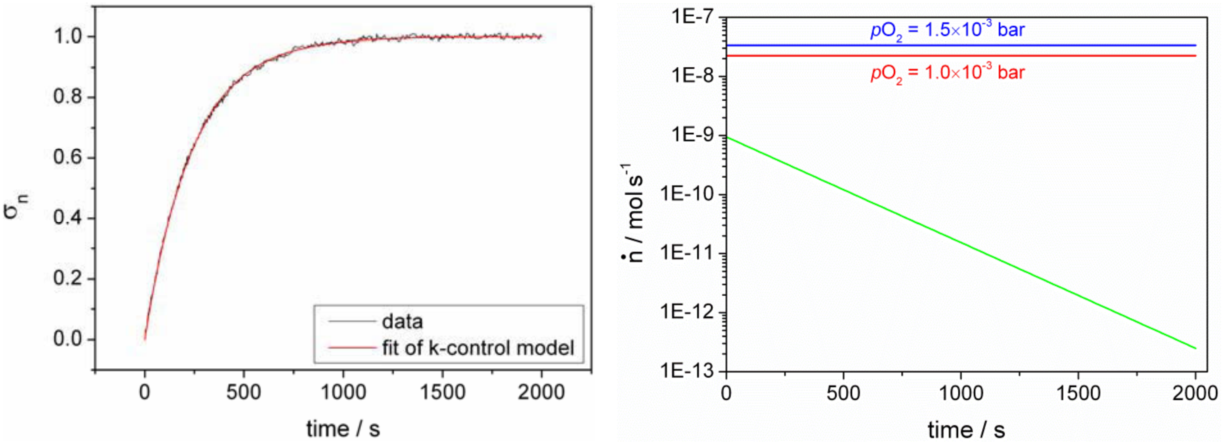

Fig. 3.12 Relaxation transient of $La_{0.6}Sr_{0.4}CoO_{3-\delta}$ at 700°C and pO_2 $1.0\cdot10^{-3} \longrightarrow 1.5\cdot10^{-3}$ bar is plotted in the left diagram including a fitting curve for surface controlled exchange ($k_{\mathrm{chem}} = 4.1\cdot10^{-5}$ cm s^{-1}). The right diagram shows the calculated molar flux of oxygen through the sample surface (green line) as well as oxygen flow rates in the gas supply at different pO_2 for a total gas flow of 2 L/h (red and blue lines).

3.8 Oxidation vs. reduction measurements

It is a common observation that relaxation processes for oxidizing steps are found to be faster than those in the reducing direction. Systematically faster oxidation kinetics have been reported by several authors [173,174,181,200,213,214] who proposed various explanations, such as experimental difficulties or a non-linear pO_2-dependence of k_{chem} and D_{chem}. This effect has also been observed for the nickelates investigated in this work and the dependence of the oxygen surface exchange rate on the magnitude of the pO_2-step as well as on the gas flow rate has been studied in more detail.

Fig. 3.13 (left) shows relaxation curves of oxidation and reduction experiments for a thin sample of $Nd_2NiO_{4+\delta}$ for both the largest and smallest pO_2-steps performed. The results clearly demonstrate the influence of the magnitude of the pO_2-jump on the oxygen exchange kinetics. While for a large pO_2-step of factor 100 the reduction experiment is significantly slower, the transients are almost congruent for a rather small pO_2-step of factor 1.3. Additional oxidation-reduction experiments using intermediate step-sizes in pO_2 confirm the trend. Results are given in Fig. 3.13 (right) where ratios between the oxidation curves and the corresponding reductions transients are given as a function of time. As can be seen, $\sigma_n(ox)/\sigma_n(red)$-curves are consistently larger than 1 and decrease with decreasing magnitude of the pO_2-step.

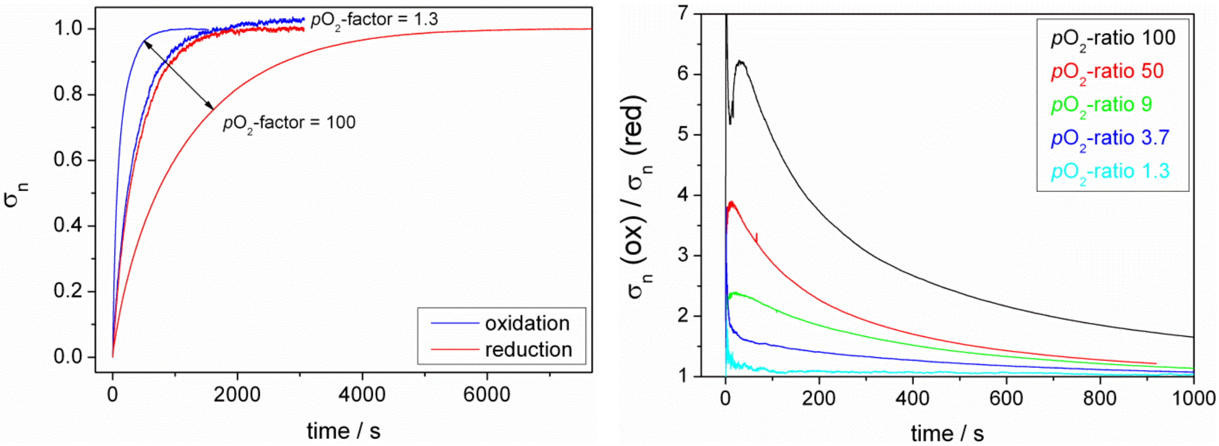

Fig. 3.13 Relaxation curve of $Nd_2NiO_{4+\delta}$ for pO_2-steps of $1\cdot10^{-2}$ ↔ 1 bar and $1\cdot10^{-2}$ ↔ $1.3\cdot10^{-2}$ bar (left). The right diagram shows differences between oxidation and reduction experiments by means of ratios of the corresponding relaxation transients. The lower pO_2 was 10^{-2} bar in all cases. All measurements were performed at 725°C and a total gas flow of 2 L/h.

While a definitive explanation of this effect is still lacking, it may be tentatively ascribed to the $p\mathrm{O}_2$-dependence of the oxygen surface exchange coefficient and possibly, albeit to a lesser degree, of the oxygen diffusion coefficient. Data reported by Wang et al. [174] show that values of k_{chem} and D_{chem} determined for $\mathrm{La}_{0.5}\mathrm{Sr}_{0.5}\mathrm{CoO}_{3-\delta}$ by conductivity relaxation measurements are strongly dependent on the final oxygen partial pressure and less influenced by the starting $p\mathrm{O}_2$. The same finding has also been established in the case of $\mathrm{La}_2\mathrm{NiO}_{4+\delta}$ [186]. This, together with the general observation that k_{chem} (and in some cases D_{chem} as well) increase for increasing oxygen partial pressures may account for the observed dependence of the exchange kinetics on the direction of the $p\mathrm{O}_2$-switch.

It may be desirable to avoid the above-mentioned complications altogether by simply making the $p\mathrm{O}_2$-steps sufficiently small. However, there is some lower limit to the magnitude of the $p\mathrm{O}_2$-steps since smaller changes in conductivity result in an increasingly poor signal-to-noise ratio, as can be seen from the different noise levels of the experimental curves in Fig. 3.13 (left).

3.9 Effect of gas flow rates on relaxation behavior

Changing the gas flow rate is a simple way to check for oxygen starvation in the gas phase or detect insufficient oxygen removal during oxidation and reduction runs. However, no such effects could be observed when varying the flow rates between 2 and 8 L/h. Fig. 3.14 (left) compares relaxation curves of $Nd_2NiO_{4+\delta}$ for oxidation and reduction at 725°C. Virtually no difference could be observed between results for gas flow rates of 2 and 5 L/h. The same finding was obtained for measurements of $La_2NiO_{4+\delta}$ at 700°C and 800°C and flow rates of 2 and 8 L/h (Fig. 3.14, right). After changing the gas flow rates care should be taken to re-adjust the temperature set-point of the furnace because variations of the gas flow result in shifts of the sample temperature up to several degrees centigrade due to changes in heat removal by the gas phase. Finally, it should be pointed out that the systematic difference in relaxation kinetics between oxidation and reduction experiments remains unaffected by changes in the gas flow rates as well, thus excluding mass transfer limitations of oxygen by the gas phase as the origin for the observed discrepancy between oxidation and reduction runs. Rather, this discrepancy appears to be related to the magnitude of the oxygen pressure swings as discussed in section 3.8.

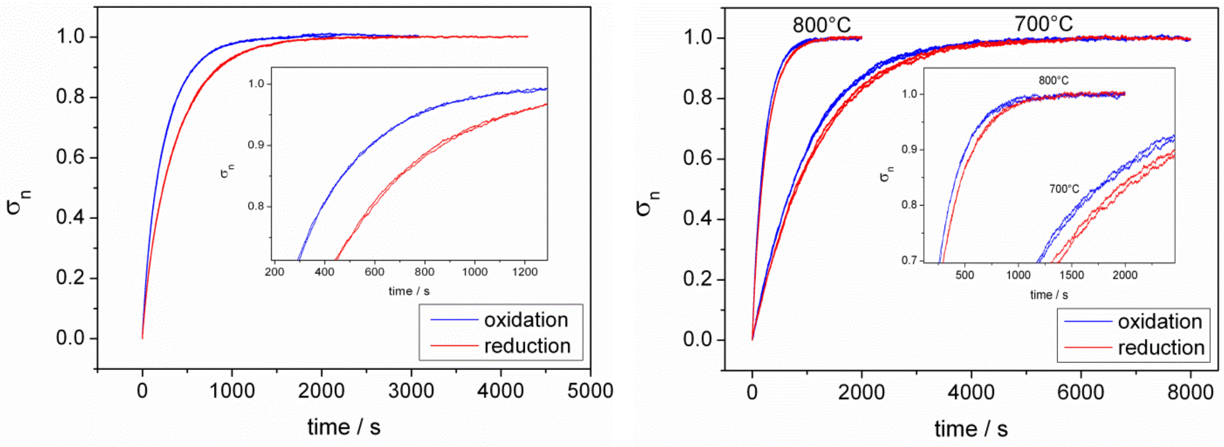

Fig. 3.14 Effects of variations of the gas flow rate on the oxygen exchange kinetics. The left diagram shows relaxation curves of $Nd_2NiO_{4+\delta}$ at 725°C and 0.01 ⟷ 0.02/0.025 bar pO_2 for 2 and 5 L/h gas flow rates. The right diagram compares results for $La_2NiO_{4+\delta}$ between flow rates of 2 and 8 L/h at 700°C and 800°C with 0.01 ⟷ 0.015 bar pO_2. Insets show magnified parts of relaxation curves.

3.10 Effect of Ag-deposition on the oxygen surface exchange rate

Even though surface exchange is rather fast for nickelates it dominates the overall oxygen exchange between gas phase and bulk at lower temperatures. This makes the surface exchange the bottleneck in the overall oxygen transport process and presents an obstacle to the reliable determination of chemical diffusion coefficients. One way to enhance the contribution of diffusion to the overall oxygen exchange process is to increase the thickness of the sample. However, there may be limits to the sample size given by the volume or diameter of the reactor used for relaxation experiments. Another way to render the diffusion process more dominant is by improving the surface exchange kinetics for oxygen. This has been reported by Li and Haugsrud [186], who used a $La_2NiO_{4+\delta}$-sample coated with nano-powder of the same material. A similar method is employed in this work where the surface exchange rate is increased by covering the surface with a thin layer of silver [215].

Silver layers of roughly 200 nm were sputtered on the surface of bar-shaped nickelate samples. After applying 100 nm the sample was turned around by 180° to avoid shadowing effects by the sample and to guarantee a uniform deposition of the Ag-layer. The layer thickness was monitored in-situ during the sputtering process by a quartz crystal microbalance. The accelerating effect of silver deposition can be observed most directly when comparing the normalized relaxation transient with and without applied Ag-layer (Fig. 3.15). It is interesting to note that not only is the surface exchange kinetics considerably enhanced by Ag-deposition but also the discrepancy between oxidation and reduction transients vanishes almost completely.

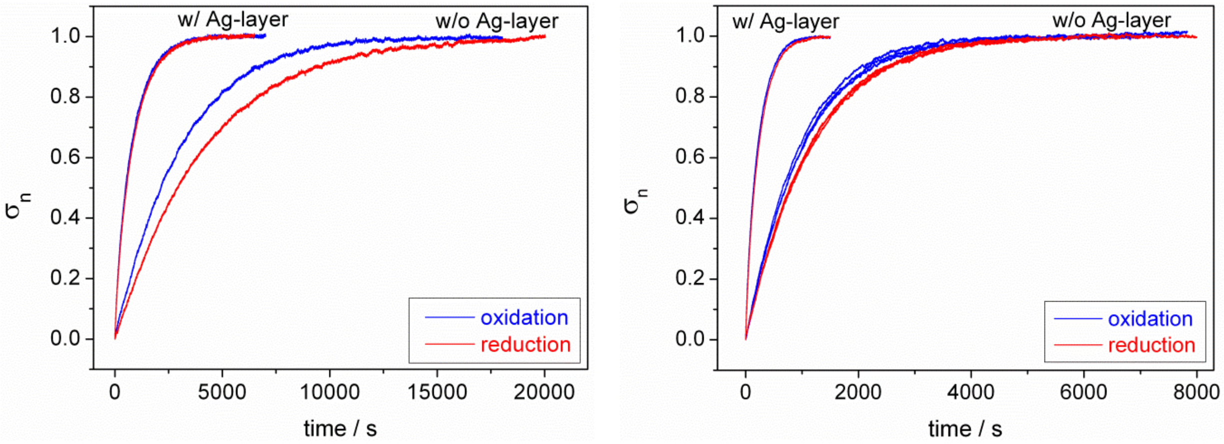

Fig. 3.15 Comparison of relaxation curves for samples with and without Ag-surface layers for $Nd_2NiO_{4+\delta}$ at 600°C / 0.1 bar pO_2 (left) and $La_2NiO_{4+\delta}$ at 700°C / 0.01 bar pO_2 (right).

Fig. 3.16 compares surface exchange coefficients of $La_2NiO_{4+\delta}$ and $Pr_2NiO_{4+\delta}$ with and without Ag-layer. At 600°C the exchange coefficients are increased by roughly one order of magnitude due to silver deposition. The enhancing effect of silver is reduced at higher temperatures and a pronounced hysteresis effect is observed which is caused by the removal of silver at higher temperatures via volatile Ag_2O-species [216]. For $La_2NiO_{4+\delta}$ a good agreement between oxygen exchange coefficients of uncoated nickelate and a silver-coated sample are observed in the cooling run (Fig. 3.16, left). For the Pr-compound the agreement is rather poor, most likely because of different stages of degradation due to the phase instability of $Pr_2NiO_{4+\delta}$ at higher temperatures (see chapter 4).

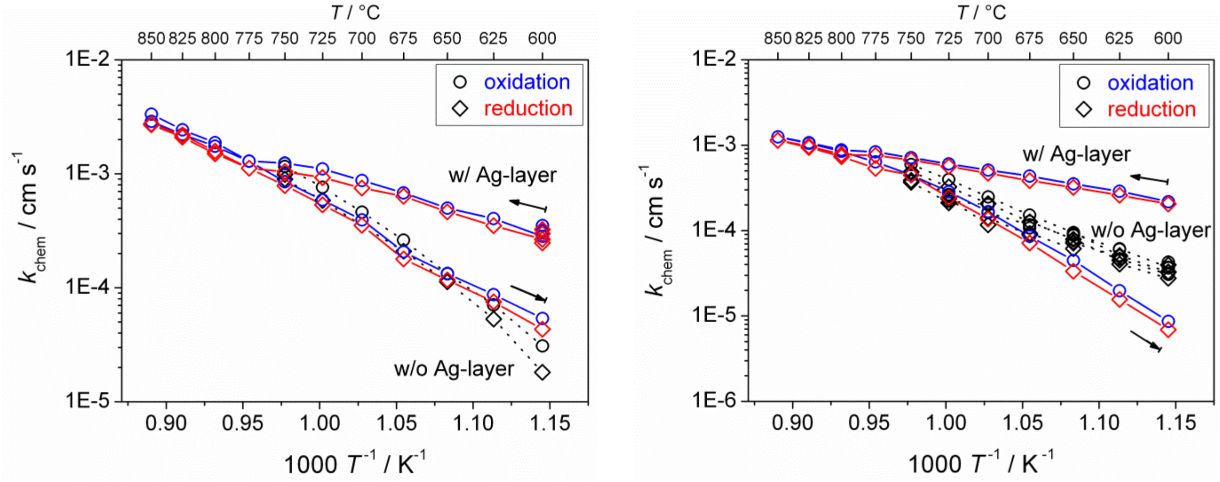

Fig. 3.16 Effect of Ag-deposition on the chemical surface exchange coefficient of $La_2NiO_{4+\delta}$ (left) at $pO_2 = 0.1$ bar and $Pr_2NiO_{4+\delta}$ (right) at $pO_2 = 0.01$ bar. Arrows denote directions of heating and cooling, lines are guides for the eye.

Visual inspection of the nickelate specimens after testing showed no traces of silver on the surface. XPS-depth profiles of $La_2NiO_{4+\delta}$ have been recorded in order to examine whether Ag diffuses into the bulk, thereby affecting the diffusivity of the material under investigation (Fig. 3.17, right). Depth profiles of a reference sample kept at 700°C in dry 1% O_2 / Ar for 1000 hours are presented for comparison in the left diagram of Fig. 3.17. Both samples show contaminations with bismuth originating from the contact paste and with ubiquitous carbon. Contaminations are more pronounced and extend to greater depths for the tested sample which is probably due to exposure to higher temperatures up to 850°C. Most importantly, however, XPS-depth profiles of the Ag-coated $La_2NiO_{4+\delta}$-sample after experiments between

600 and 850°C show no indication of silver within the first 500 nm of the surface (Fig. 3.17, right).

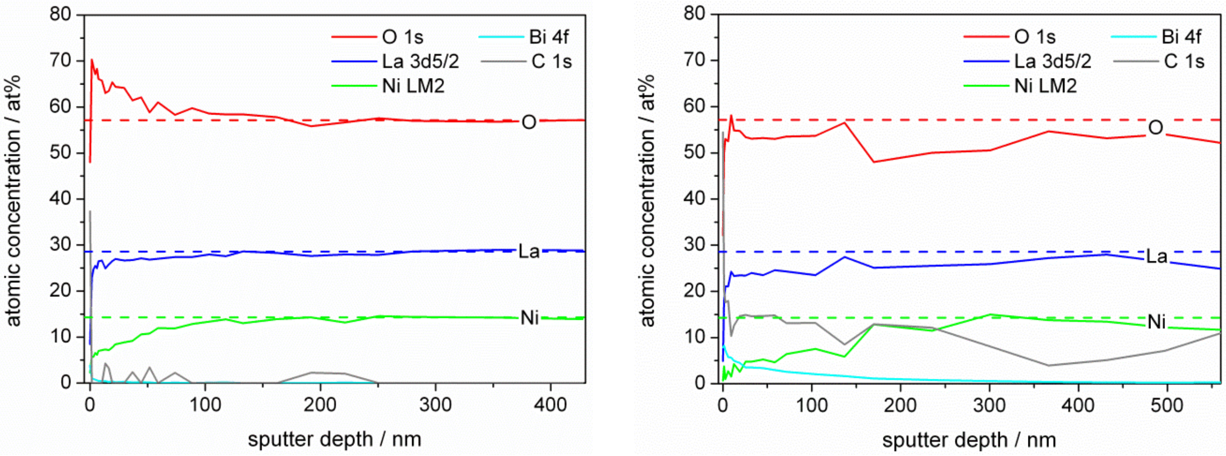

Fig. 3.17 XPS-depth profiles of $La_2NiO_{4+\delta}$-surfaces of a silver-coated sample after testing between 600 and 850°C (right) and a reference sample after exposure to 700°C for 1000 hours (left). The oxygen partial pressure was 0.01 bar in both cases. Dashed lines mark nominal compositions.

4 Results and discussion

4.1 Sample characterization

4.1.1 Composition, density and microstructure

The chemical composition of sintered pellets was checked by SEM/EDX for all nickelates with respect to their cation ratio. Results are collected in Tab. 4.1 together with density data. All relative densities were above 95% based on literature values of theoretical densities obtained from XRD-measurements.

Tab. 4.1 Cation ratio and density data for sintered samples of $Ln_2NiO_{4+\delta}$ (Ln = La, Pr, Nd).

	***Ln* : Ni**	**geometric density / g cm^{-3}**	**theoretical density / g cm^{-3}**	**relative density / %**
$La_2NiO_{4+\delta}$	1.95 : 1	6.76	7.08	95.5
$Pr_2NiO_{4+\delta}$	2.01 : 1	7.07	7.34	96.3
$Nd_2NiO_{4+\delta}$	1.97 : 1	7.33	7.53	97.3

The microstructure of sintered nickelate samples was examined after thermal etching of polished cross sections (Fig. 4.1). Some inter-granular porosity is visible with pores mainly located at triple junctions of grain boundaries. $La_2NiO_{4+\delta}$ has been resintered several times at 1350°C to increase the density and thus shows larger average grain sizes than the other nickelate samples.

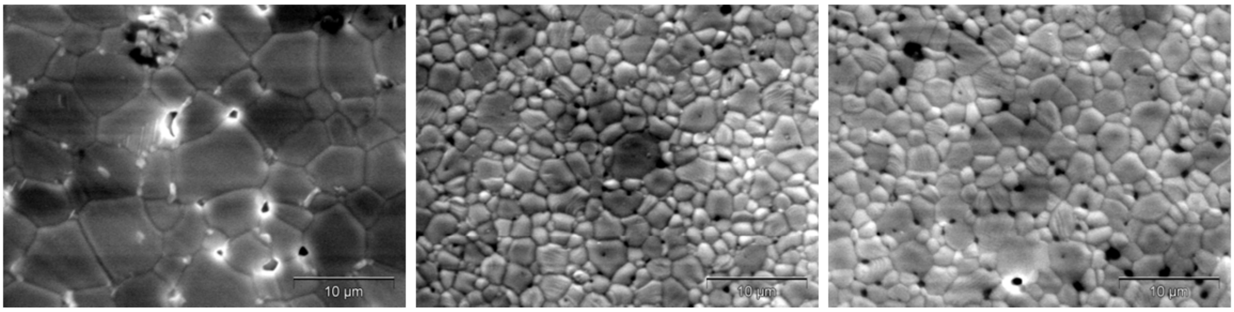

Fig. 4.1 Micrographs of polished cross sections of sintered $La_2NiO_{4+\delta}$ (left), $Pr_2NiO_{4+\delta}$ (center) and $Nd_2NiO_{4+\delta}$ (right) after thermal etching (SEM 3000×).

4.1.2 X-ray diffraction

Room temperature X-ray diffraction (XRD) patterns of the investigated nickelates confirm the K_2NiF_4-structure. Phase purity was verified for $La_2NiO_{4+\delta}$ and $Pr_2NiO_{4+\delta}$ while in the case of $Nd_2NiO_{4+\delta}$ a small amount of Nd_2O_3 was detected as secondary phase (Fig. 4.2). $Nd_2NiO_{4+\delta}$ and $Pr_2NiO_{4+\delta}$ crystallize in an orthogonally distorted crystal structure as can be seen from a characteristic splitting of the reflection at $2\theta \approx 33°$ (separation of (200) / (020) reflections). Since a single (200)-reflection is observed for $La_2NiO_{4+\delta}$ this compound is either crystallizing in the ideal K_2NiF_4-structure at room temperature or the splitting of the reflection at $2\theta \approx 33°$ may be below the resolution of the XRD-pattern. A slight shift of the reflections to higher diffraction angles corresponds to a decrease in unit cell dimensions caused by a decrease in ionic radii due to the lanthanide contraction ($r(La^{3+})$ = 1.216 Å, $r(Pr^{3+})$ = 1.179 Å, $r(Nd^{3+})$ = 1.163 Å for coordination number 9 [82]).

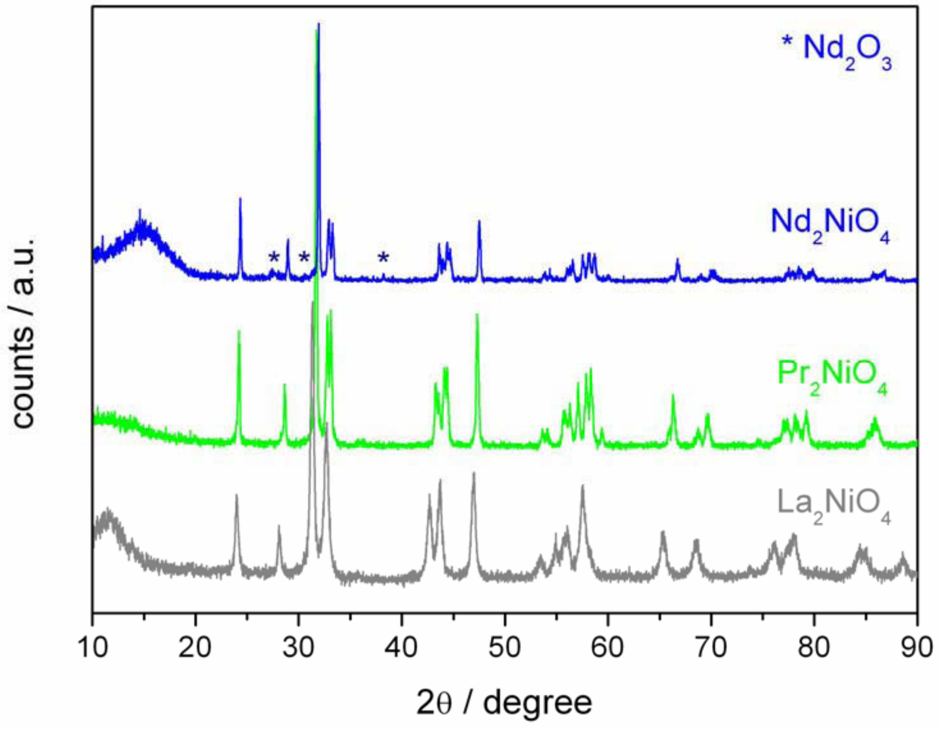

Fig. 4.2 Room temperature XRD-patterns of the investigated nickelates.

4.1.3 Thermal expansion

Dilatometric analyses of unsubstituted nickelates have been performed in air between room temperature and 1250°C with a heating rate of 1 K/min (Fig. 4.3). Calibration was performed using an Al_2O_3-standard. Thermal expansion is found to be quite linear up to 800-1000°C, above which resintering becomes increasingly evident. Thermal expansion coefficients of around $15 \cdot 10^{-6}$ K^{-1} were determined from linear regression to heating curves between 100°C and 900°C. Results are somewhat higher than values reported in the literature for rare earth nickelates [26] but still match reasonably well those of common solid electrolytes such as yttria-stabilized zirconia or gadolinia-doped ceria with TECs between $10 \cdot 10^{-6}$ and $13 \cdot 10^{-6}$ K^{-1} [217]. No appreciable effect of the oxygen release on the TEC could be observed. It is surprising that the phase instability of $Pr_2NiO_{4+\delta}$ does not manifest itself in the expansion curve of Fig. 4.3, whereas dilatometric analyses reported by Kovalevsky et al. [218] show clear signs of the decomposition process above 800°C in air. This effect might have been obscured by the shrinkage caused by resintering above 800°C in this study or may require several thermal cycles in order to be observed by dilatometry. Such irregular behavior of thermal expansion is expected to be detrimental for an application as SOFC-cathode and may result in delamination from the electrolyte.

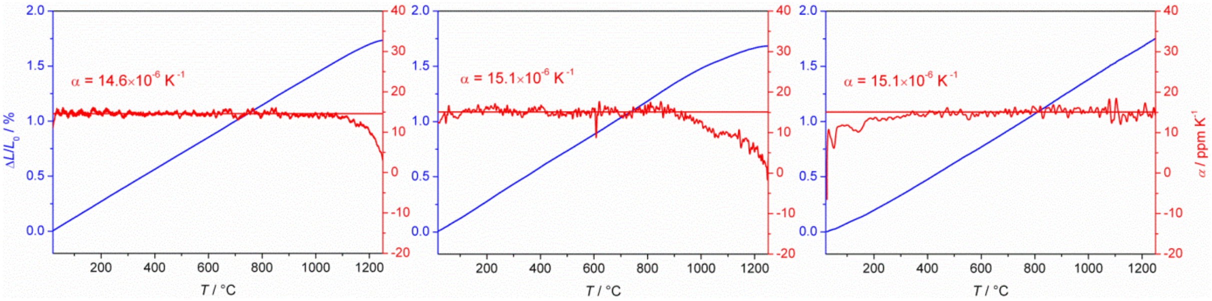

Fig. 4.3 Thermal expansion of $La_2NiO_{4+\delta}$ (left), $Pr_2NiO_{4+\delta}$ (middle) and $Nd_2NiO_{4+\delta}$ (right) in air with heating rates of 1 K/min. Thermal expansion coefficients (red lines) are calculated as first derivatives of relative length changes (blue lines).

4.1.4 Thermogravimetric analysis

Fig. 4.4 shows the relative mass change of nickelates between room temperature and 900°C in dry oxygen-argon mixtures (20 vol% O_2) as determined by thermogravimetry (TG). Since the first heating cycle usually contains anomalies due to non-equilibrium oxygen stoichiometry and adsorbed gas species, only the second or third thermal cycles are interpreted. Good agreement between heating and cooling runs for $La_2NiO_{4+\delta}$ and $Nd_2NiO_{4+\delta}$ imply that true equilibrium data have been obtained. An irreversible mass increase was found for $Pr_2NiO_{4+\delta}$ which is discussed further below. Since oxygen incorporation in nickelates is an exothermic reaction [68,89,141], increasing temperatures cause oxygen to be excorporated from the material if exchange kinetics is sufficiently fast. Onset temperatures of oxygen release are found to be quite different for the investigated compounds. For $Nd_2NiO_{4+\delta}$ oxygen excorporation starts around 350°C, for $Pr_2NiO_{4+\delta}$ at 250°C, while for $La_2NiO_{4+\delta}$ an onset temperature as low as 200°C is observed. This is most likely caused by differences in particle size since planetary-ball milled $La_2NiO_{4+\delta}$-powder was used for TG-measurements while powders of $Pr_2NiO_{4+\delta}$ and $Nd_2NiO_{4+\delta}$ were ground by pestle and mortar.

For $Nd_2NiO_{4+\delta}$ a kink in the TG-curve at 550°C is caused by a reversible phase transition (low-temperature orthorhombic (LTO) to high-temperature tetragonal (HTT) structure), which has been reported in the literature based on XRD- and thermogravimetric investigations [26,116,219]. The precise transition temperature depends on the Nd-stoichiometry [26], oxygen partial pressure [116] and the thermal history of the sample [219]. Phase transition temperatures of $Nd_2NiO_{4+\delta}$, as determined by thermogravimetry in this work and by Egger et al. [220] were 550 and 500°C in 20% O_2 / Ar and pure Ar, respectively, 550°C in Boehm et al. [26] (TG in air), 570°C in Ishikawa et al. [219] (TG-DTA in air), 610°C in Toyosumi et al. [116] (XRD in air) and 620°C in Boehm et al. [26] (XRD in air). It is interesting to note that XRD-measurements consistently yield transition temperatures higher than those obtained from TG-analysis. Nd-deficient compounds $Nd_2NiO_{4+\delta}$ were investigated by Boehm et al. [26], where TG-data gave transition temperatures of 550°C for x=0, 555°C for x=0.05 and 600°C for x=0.1 in air. Such phase transition might be detrimental during run-up and cool-down phases in applications, however, it was shown that changes in lattice parameters leave the unit cell volume virtually constant [116].

For $Pr_2NiO_{4+\delta}$ a similar phase transition takes place around 450°C. There is no indication of an analogous transition for $La_2NiO_{4+\delta}$ confirming a tetragonal structure at room temperature consistent with findings from XRD-analysis given above.

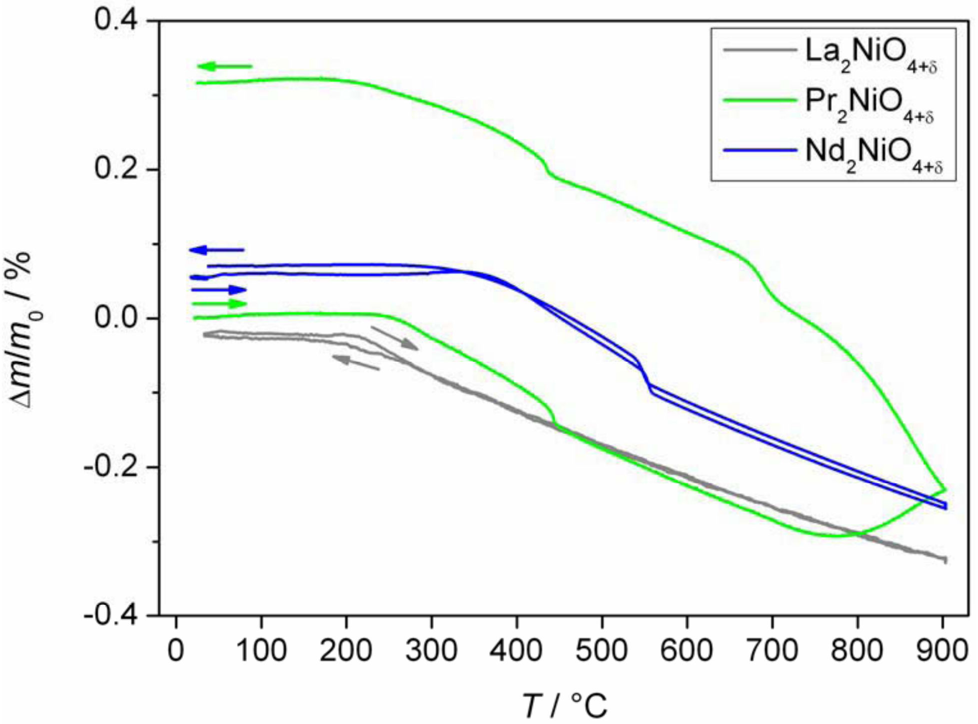

Fig. 4.4 Thermogravimetric analyses of nickelates in dry Ar / 20 vol% O_2 with temperature ramps of 5 K/min. Arrows denote directions of heating and cooling. Curves have been shifted along the ordinate for reasons of clarity.

The TG-curve of $Pr_2NiO_{4+\delta}$ clearly shows an irreversible mass increase starting at temperatures above 700°C. For a more detailed analysis three consecutive runs of $Pr_2NiO_{4+\delta}$ powder in 20 vol% O_2 / Ar with heating and cooling rates of 1 K/min between room temperature and 900°C have been performed (Fig. 4.5).

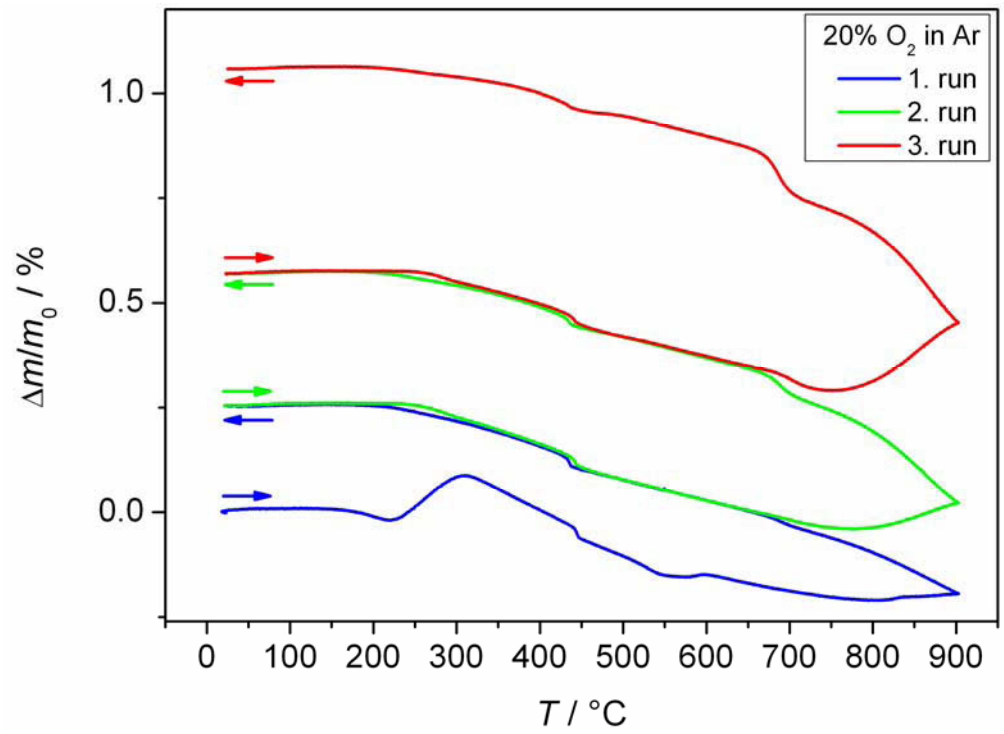

Fig. 4.5 Thermogravimetric profiles of three consecutive TG-cycles of $Pr_2NiO_{4+\delta}$ in 20 vol% O_2 (rest Ar) with 1 K/min heating and cooling rates. Arrows denote directions of heating and cooling.

In the first TG-run (blue curve in Fig. 4.5) a slight decrease in mass can be observed around 200°C, probably due to desorption of adsorbed species like H_2O or CO_2, after which a strong increase in weight takes place due to incorporation of oxygen. This indicates that the sample was not in its equilibrium state with respect to oxygen content, either due to fast cooling after sintering or due to sintering in reducing atmospheres. Both features mentioned above are not visible in the two subsequent temperature runs.

Continuous oxygen release takes place upon further heating until around 450°C a reversible phase transition (LTO ⟶ HTT) [88,114] can be discerned in the TG-curves due to a concomitant oxygen release when transforming to the high-temperature phase.

Between 550°C and 600°C a slight increase in mass is observed in the first run. This effect is ascribed to carbonate decomposition as was evidenced by a separate TG-analysis with coupled mass spectrometry (MS) under pure Ar (Fig. 4.6). The MS-signal of CO_2 in Fig. 4.6 clearly shows a peak between 500°C and 550°C, corresponding to the feature in the TG-profile around 600°C. Carbonate decomposition might be taking place at lower temperatures in the TG-MS-run due to the pure argon atmosphere. The slight increase in mass despite a loss of CO_2 could result from an accompanying uptake of oxygen due to the removal of blocking carbonates from the sample surface. This is substantiated by the TG profile in pure Ar (Fig. 4.6) which indeed shows a mass decrease upon carbonate decomposition when no oxygen is available in the surrounding atmosphere. As expected no carbonate decomposition is observed in the following TG-runs.

Finally, a mass increase started above 800°C, which was less drastic in the first run but became more and more pronounced for subsequent temperature cycles. This effect is due to a decomposition of the nickelate as has been observed by several authors before [88,113,218,221-223]. The decomposition reaction has been proposed by Sullivan et al. [113] as

$$3\,Pr_2NiO_{4+\delta} + x\,O_2 \rightleftarrows Pr_4Ni_3O_{10-\delta'} + 2\,PrO_{1.83-\delta''} \qquad (4.1)$$

where the K_2NiF_4-type nickelate phase transforms to its third-order Ruddlesden-Popper (RP) homologue $Pr_4Ni_3O_{10-\delta}$ and Pr-oxide is expelled from the parent phase due to a decrease in Pr : Ni ratio for higher-order RP-phases. Decomposition products of $Pr_2NiO_{4+\delta}$ were reported by several groups [88,113,218,221,222] and are consistent with the chemical reaction given above. At elevated temperatures in air δ, δ' and δ'' in Eq. (4.1) are estimated as 0.15 [88,221], 0.25 [221] and 0 [224], respectively, so that x in Eq. (4.1) is around 0.5, i.e. the observed phase decomposition is accompanied by oxygen uptake as confirmed by the TG-results.

It is evident from Fig. 4.5 that the decomposition process is not reversible within the investigated temperature range. Furthermore, the decomposition rate seems to be increasing for each subsequent TG-run, which may be due to nucleation at $Pr_4Ni_3O_{10-\delta}$ and/or $PrO_{1.83-\delta}$ precipitates formed in the previous TG-cycles. However, at temperatures well above 1000°C it is to be expected that the K_2NiF_4-type phase $Pr_2NiO_{4+\delta}$ is thermodynamically stable [113] in analogy to La-nickelate [129]. In order to obtain phase pure $Pr_2NiO_{4+\delta}$ this suggests calcination and sintering at correspondingly high temperatures – typically at 1350°C in air – and quenching to room temperature to minimize phase decomposition during cooling.

It is interesting to note that under pure Ar no mass increase is visible up to 900°C (Fig. 4.6). This is of course expected since only a very small amount of oxygen is available in the surrounding atmosphere. However, the TG-results cannot elucidate whether the decomposition process still takes place or the phase decomposition is prevented altogether. Suppressing the phase decomposition of $Pr_2NiO_{4+\delta}$ by employing reducing atmospheres (e.g. N_2 or Ar) would be relevant for sintering or for applying electrical contacts.

This question was explored in more detail by monitoring the electronic conductivity of $Pr_2NiO_{4+\delta}$ at 600°C and 0.01 bar pO_2 with intermittent heating steps to 750°C and 850°C in pure Ar-flow. As discussed in section 4.2.1 the electronic conductivity serves as a sensitive indicator to detect phase decomposition in $Pr_2NiO_{4+\delta}$ due to the higher conductivity of the decomposition products. No change in conductivity could be observed at 600°C before and after the heating cycle, confirming that phase decomposition of $Pr_2NiO_{4+\delta}$ can indeed be suppressed in reducing atmospheres. This observation was used for applying the gold contacts since heating to 850°C is necessary to burn in the gold paste (see section 3.3)

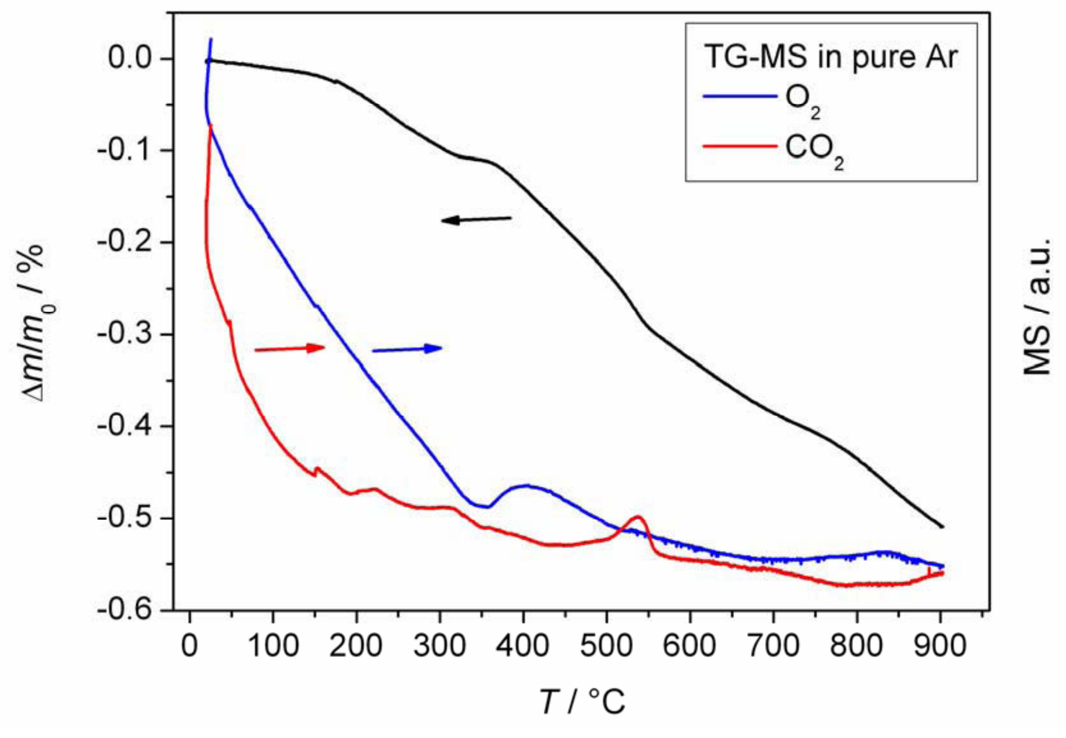

Fig. 4.6 Coupled TG-MS analysis of $Pr_2NiO_{4+\delta}$ in pure Ar with 1 K/min heating rate. The black line is the relative mass change, blue and red curves correspond to MS-signals for O_2 and CO_2, respectively.

The above findings regarding the phase stability of $Pr_2NiO_{4+\delta}$ are consistent with results given by Sullivan et al. [113] who presented a stability plot for Pr-nickelate as a function of temperature and oxygen fugacity (Fig. 4.7). In pure Ar (5.0 purity) a pO_2 of roughly 10^{-5} bar is established which is inside the $Pr_2NiO_{4+\delta}$ single phase field throughout the temperature region of interest. The van't Hoff-type oxidation boundary given by Sullivan et al. has been extrapolated to temperatures below 880°C to estimate the decomposition temperature of Pr-nickelate in ambient air, which is expected to be around 780°C and shifts to higher temperatures at higher pO_2-values. Of course, at temperatures significantly below the decomposition temperature the nickelate phase will be kinetically stabilized. With electronic conductivity measurements, the decomposition reaction was observed around 675-700°C at $pO_2 = 0.1 / 0.01$ bar when heating the sample from 600°C (see section 4.2.1). The low-pO_2 boundary of the single phase region is close to the Ni/NiO-reduction boundary where $Pr_2NiO_{4+\delta}$ is reduced to metallic nickel and Pr_2O_3. This reaction is often used to establish a reference point for the determination of absolute values of oxygen stoichiometry for $Pr_2NiO_{4+\delta}$ in thermogravimetric measurements.

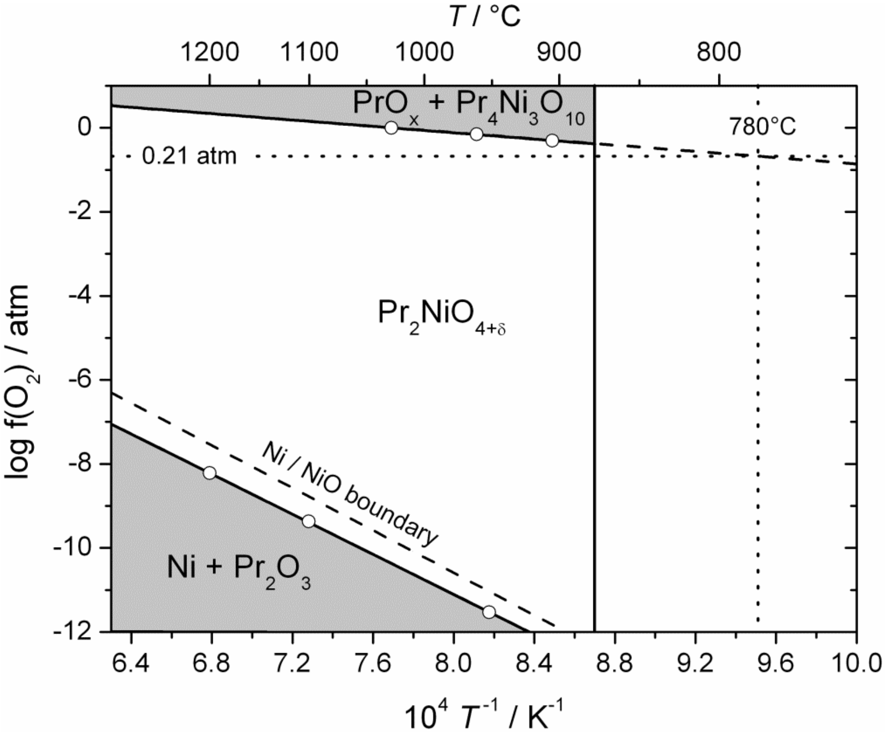

Fig. 4.7 Stability field of $Pr_2NiO_{4+\delta}$ with respect to temperature and oxygen partial pressure (oxygen fugacity). The plot is based on a figure given by Sullivan et al. [113] in which the oxidation boundary has been extrapolated to temperatures below 880°C to estimate the decomposition temperature in air (see dotted lines).

4.1.5 Differential scanning calorimetry

A qualitative thermal analysis of the nickelates has been carried out by differential scanning calorimetry (DSC) in air (Fig. 4.8). Since no temperature calibration has been performed, temperatures are only approximate. In agreement with TG-results presented above, the reversible phase transition for $Nd_2NiO_{4+\delta}$ is reproduced around 540°C in air, showing to be first-order with a slight temperature hysteresis effect. Since the LTO ⟶ HTT-transition is accompanied by a decrease in oxygen content (Fig. 4.4), the endothermic peak in the DSC-curve during heating is consistent with the endothermicity of oxygen release. The same observation is made for $Pr_2NiO_{4+\delta}$, where the first-order phase transition is taking place around 450°C with a small temperature hysteresis effect [114]. In the case of $La_2NiO_{4+\delta}$ no thermal signal is observed in agreement with TG-results.

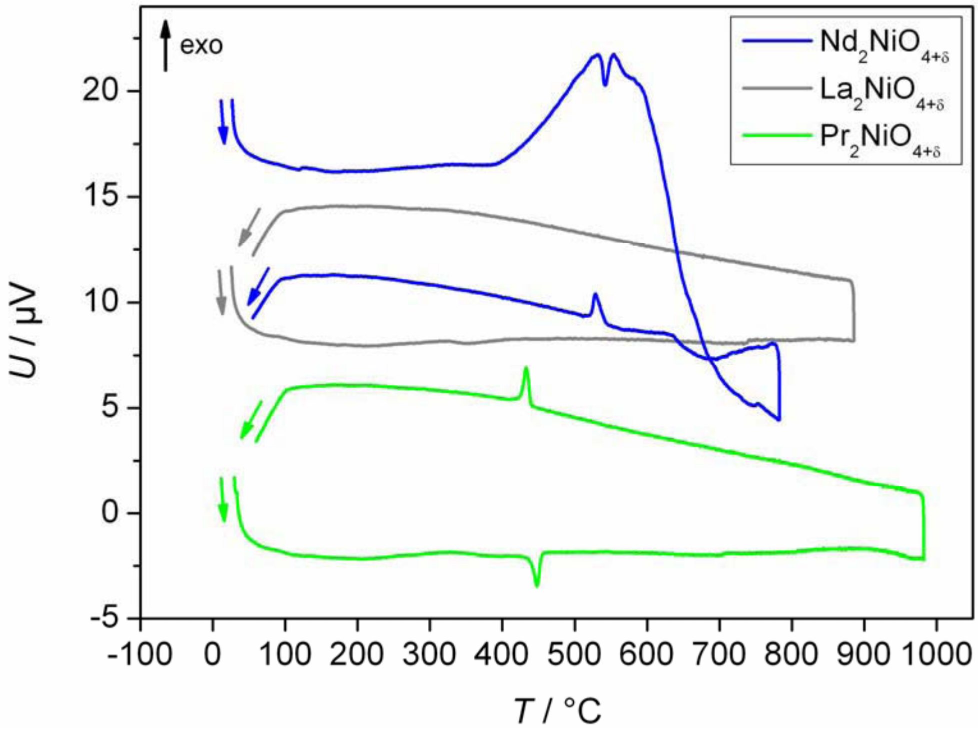

Fig. 4.8 DSC-curves of nickelates in air with heating and cooling rates of 5 K/min. The unsteady background signal observed for $Nd_2NiO_{4+\delta}$ is an artifact of the DSC-instrument. Arrows mark directions of heating and cooling.

Between 800 and 1000°C a broad exothermic peak can be observed for $Pr_2NiO_{4+\delta}$ in air (Fig. 4.8), probably corresponding to the phase decomposition discussed above. To corroborate this speculation, the DSC-analysis of Pr-nickelate has been repeated in pure Ar as shown in Fig. 4.9 in comparison with the profile obtained in air. It is evident that no exothermic signal is observed when heating in an argon atmosphere, confirming that the thermal signal originates in a sluggish phase decomposition of $Pr_2NiO_{4+\delta}$. Since the decomposition reaction in air involves uptake of oxygen (see Fig. 4.5 and Eq. (4.1)), an exothermic peak is to be expected. Similar to TG-measurements, the decomposition reaction was observed to become increasingly apparent in the DSC-curves after repeated temperature cycles (not shown in Fig. 4.9). Moreover, heating in pure Ar shifts the phase transition to lower temperatures [114] and no thermal signal can be observed upon cooling, indicating that the HTT → LTO phase transformation is suppressed in the absence of oxygen.

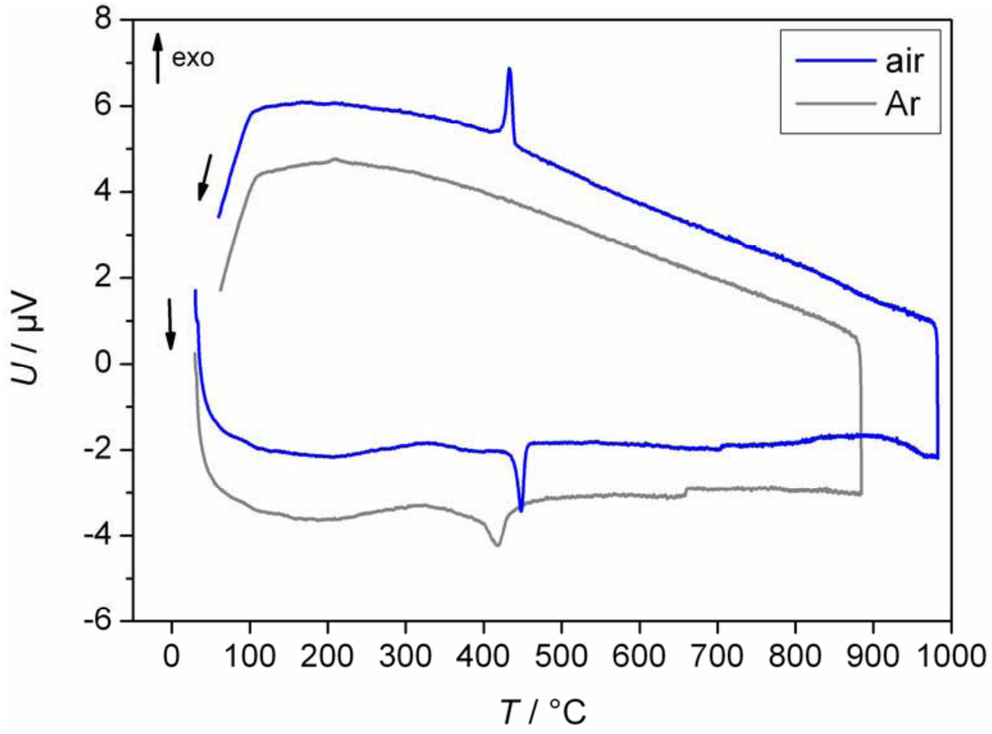

Fig. 4.9 DSC-profiles of $Pr_2NiO_{4+\delta}$ with 5 K/min heating and cooling rate in air (blue) and Ar (gray). Arrows mark directions of heating and cooling. Small steps observed in heating curves around 700°C are artifacts of the calorimeter.

4.2 Transport properties

$La_2NiO_{4+\delta}$, $Pr_2NiO_{4+\delta}$ and $Nd_2NiO_{4+\delta}$ were investigated with respect to electronic conductivity, surface exchange and diffusion of oxygen as a function of temperature and oxygen partial pressure. Special emphasis was put on the applicability of these compounds as IT-SOFC cathode materials and the conditions expected during SOFC-operation. Experimental studies were performed at temperatures between 600° and 850°C and oxygen partial pressures of 0.1 and 0.01 bar. The chosen pO_2-range represents the expected condition in an SOFC-cathode operated with air, where the actual oxygen partial pressure decreases from the cathode-air interface to the cathode-solid electrolyte interface due to polarization under electrical load [225].

4.2.1 Electronic conductivity

Fig. 4.10 (left) shows the electronic conductivity of $Nd_2NiO_{4+\delta}$ in the intermediate temperature regime at oxygen partial pressures between 0.01 and 0.2 bar. For $Nd_2NiO_{4+\delta}$ additional measurements in air and pure oxygen were performed at 725°C to demonstrate the effect of pO_2-variation on the conductivity more clearly. Within the investigated ranges of temperature and pO_2, the following trends can be observed: (i) the conductivity decreases for increasing temperature and (ii) the conductivity increases for higher oxygen partial pressures. Both effects are a consequence of the *p*-type electronic conduction in $Nd_2NiO_{4+\delta}$ [65,226]. Since the electric current in nickelates is predominantly electronic, a discussion of the observed changes in conductivity is based on the fundamental equation

$$\sigma \approx \sigma_{el} = e c_{h^\cdot} u_{h^\cdot} \tag{4.2}$$

where σ is the total electrical conductivity, σ_{el} the electronic conductivity, e the elementary charge, $c_{h^\cdot}$ the number density of electron holes and $u_{h^\cdot}$ their mobility. Thus, any change in σ is a consequence of changes in $c_{h^\cdot}$, $u_{h^\cdot}$ or both.

The observed decrease in conductivity at lower pO_2 is a direct consequence of the decrease in hole concentration due to the removal of oxygen from the structure, according to the defect chemical equation

$$O_i'' + 2h^{\cdot} \leftrightarrows \frac{1}{2}O_2 + V_i^x \tag{4.3}$$

It has been established by Nakamura et al. [65] that the hole mobility $u_{h^{\cdot}}$ of $Nd_2NiO_{4+\delta}$ does not appreciably change with oxygen partial pressure between $1{\cdot}10^{-4}$ and 1 bar in the temperature range 600-900°C. Hence, the pO_2-dependence of σ can be assumed to be solely a result of the change in the hole concentration. Raising the oxygen partial pressure leads to interstitial incorporation of oxygen into the material coupled with the creation of electron holes in accordance with Eq. (4.3).

Rationalizing the temperature dependence of σ is somewhat more complicated, since a change in temperature affects hole concentration and hole mobility simultaneously. Firstly, as reported by Nakamura et al. [65] for undoped Nd-nickelate, $u_{h^{\cdot}}$ increases with temperature between 300 and 600°C and starts to decrease at temperatures above 600°C. Secondly, raising the temperature also leads to oxygen being released from the sample, which lowers the concentration of electron holes according to Eq. (4.3). However, such changes in oxygen stoichiometry are only relevant for temperatures where kinetics permits oxygen exchange with the gas phase. Since the oxygen exchange kinetics of nickelates is frozen in at low temperatures (see Fig. 4.4), σ initially increases with increasing temperature as expected for a semiconductor. Once the rate of oxygen exchange becomes significant upon heating, the conductivity is increasingly affected by the decrease in the number of holes due to oxygen release and σ starts to decrease. Considering these competing contributions a maximum is to be expected when plotting conductivity vs. temperature.

Boehm et al. [26] have measured electronic conductivities of $Nd_{2-x}NiO_{4+\delta}$ (x = 0, 0.05, and 0.1) between 100 and 800°C in air and indeed found an increase in conductivity below 400°C, broad maxima between 400 and 550°C and a decrease in conductivity above 550°C (Fig. 4.10, right). This temperature dependence is consistent with results from thermogravimetric analysis presented in section 4.1.4.

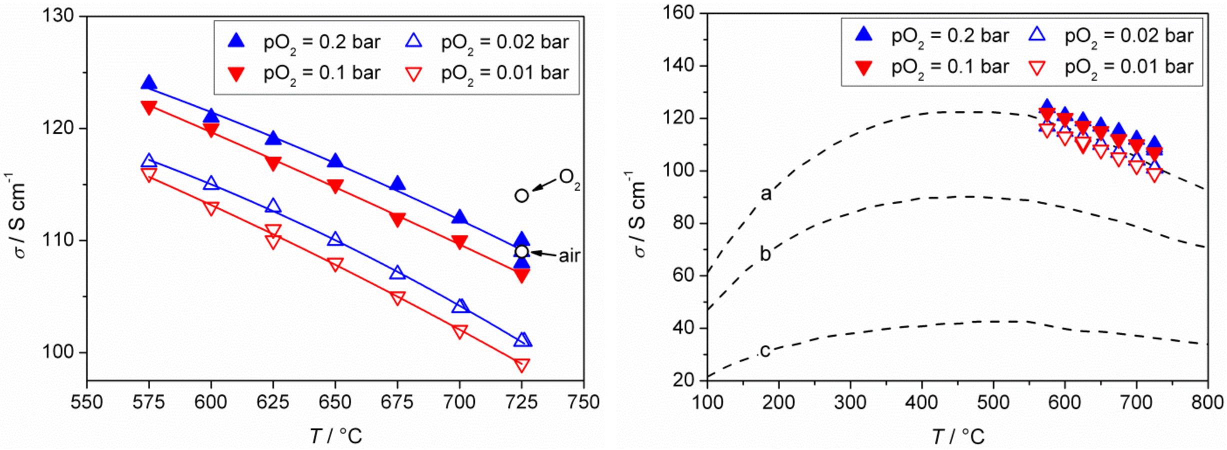

Fig. 4.10 Temperature dependence of the electronic conductivity of $Nd_2NiO_{4+\delta}$ obtained from van der Pauw measurements (left). Data have been replicated in the right diagram, dashed lines represent results from Boehm et al. [26] for (a) $Nd_{1.95}NiO_{4+\delta}$, (b) $Nd_{1.90}NiO_{4+\delta}$ and (c) $Nd_2NiO_{4+\delta}$ in air.

A significant difference is observed between the absolute values of electronic conductivities of $Nd_2NiO_{4+\delta}$ determined in this work and in Boehm et al. [26] (Fig. 4.10, right). Differences in oxygen partial pressures can be excluded as a source of the discrepancy, because the effect of pO_2-variation on the conductivity is not sufficiently pronounced to explain such a large deviation (see Fig. 4.10, left). However, Boehm et al. [26] showed in their work that a small amount of oxygen deficiency of Nd on the *A*-site has a strong impact on conductivity. For instance, changing *A*-site sub-stoichiometry x in $Nd_{2-x}NiO_{4+\delta}$ from 0 to 0.05 increases the conductivity by a factor of ~3 (Fig. 4.10, right). This is most likely due to an electronic charge compensation of Nd-vacancies, which increases the electron hole concentration in the bulk (another compensation mechanism being the decrease of oxygen stoichiometry in the sample). A similar increase in the electronic conductivity for small deviations from the stoichiometric *A*:*B*-ratio was also reported by Ullmann et al. [227] for various perovskite oxides. It is likely that the difference between electronic conductivities given in Boehm et al. [26] and this work is due to a small Nd-deficiency in the nickelate, resulting from either the use of a Nd-substoichiometric starting mixture for synthesis or from the presence of a small amount of Nd_2O_3 secondary phase and the corresponding formation of a Nd-deficient main phase $Nd_{2-x}NiO_{4+\delta}$ (see Fig. 4.2).

The electronic conductivity of $La_2NiO_{4+\delta}$ as a function of temperature and pressure (Fig. 4.11, left) shows the same characteristics as observed for the Nd-analogue and can be discussed along the same lines as above. Fig. 4.11 (right) gives a comparison with data obtained from linear four-point measurements of a bar-shaped $La_2NiO_{4+\delta}$-sample at $pO_2 = 0.01$ bar. Both measurements agree within ~10 Scm^{-1}, hysteresis between heating and cooling run indicates non-equilibrium of oxygen content. Boehm et al. [26] reported somewhat lower values for the conductivity of $La_2NiO_{4+\delta}$ (dashed line in Fig. 4.11, right).

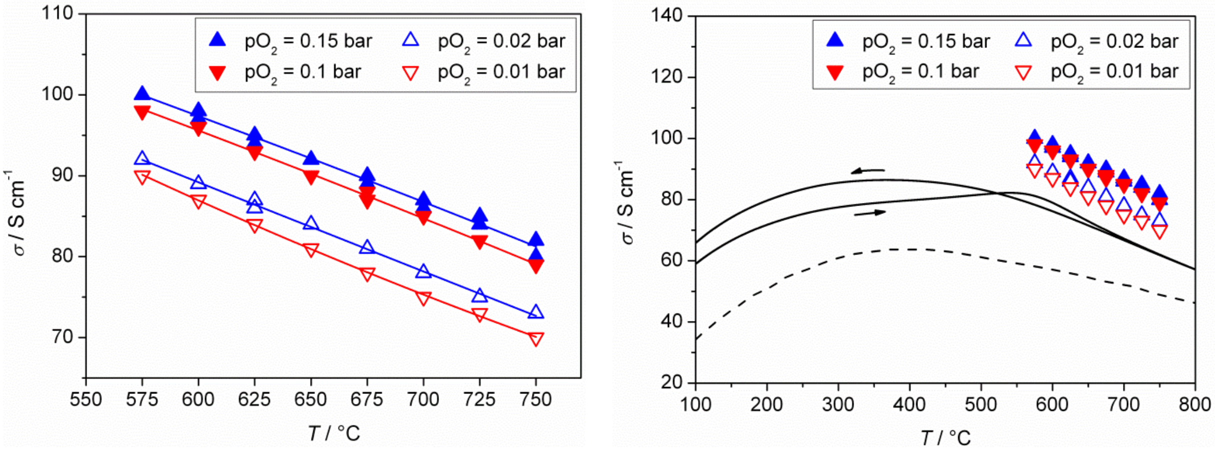

Fig. 4.11 Temperature dependence of the electronic conductivity of $La_2NiO_{4+\delta}$ obtained from van der Pauw measurements (left). In the right diagram data are replotted together with results obtained from a bar-shaped sample of $La_2NiO_{4+\delta}$ (solid line, $pO_2 = 0.01$ bar) and data reported by Boehm et al. [26] (dashed line, in air).

The electronic conductivity of $Pr_2NiO_{4+\delta}$ was measured by the van der Pauw method between 600°C and 750°C at oxygen partial pressures around 0.1 and 0.01 bar (Fig. 4.12). Measurements were started at 600°C and temperature cycles to higher temperatures and back to 600°C were performed. The electronic conductivity turned out to be a very sensitive parameter with respect to the phase decomposition process detailed in section 4.1.4. The decomposition is accompanied by an increase in the electrical conductivity, as has been already observed by Odier et al. [221]. Similar to its La- and Nd-analogues, the electronic conductivity of single-phase $Pr_2NiO_{4+\delta}$ is around 100 S/cm under the conditions investigated. The conductivity of single-phase $Pr_2NiO_{4+\delta}$ decreases for increasing temperature and decreasing oxygen partial pressure within the investigated T- and pO_2-range [214].

At pO_2 = 0.1 bar a slight increase in σ is observed at 650°C, which becomes more pronounced upon further heating. Keeping the sample at 700°C over a period of one week raised the conductivity to 200 S/cm, which is twice its initial value (Fig. 4.12). The origin of the enhanced conductivity is the formation of $Pr_4Ni_3O_{10-\delta}$ with high metallic-type conductivity [123], following the general trend of decreasing resistivity with increasing n in $Ln_{n+1}Ni_nO_{3n+1}$ (Ln = La, Pr and Nd) [72,118,128]. While the electronic conductivity of $PrO_{1.83-\delta}$ is below that of $Pr_2NiO_{4+\delta}$ [228,229], a rather high ionic conductivity of oxygen has been reported for Pr_6O_{11} in air [229]. Thus, with respect to electrical conductivity the limited phase stability of Pr-nickelate may not pose a real obstacle for application as IT-SOFC cathode.

Reducing the oxygen partial pressure lowers the rate of the decomposition reaction as can be seen in Fig. 4.12 from the less pronounced increase in the electronic conductivity at pO_2 = 0.01 bar. This is probably due to slower decomposition kinetics of reaction (4.1) in atmospheres with lower oxygen content. In agreement with TG-results the decomposition is found to be irreversible.

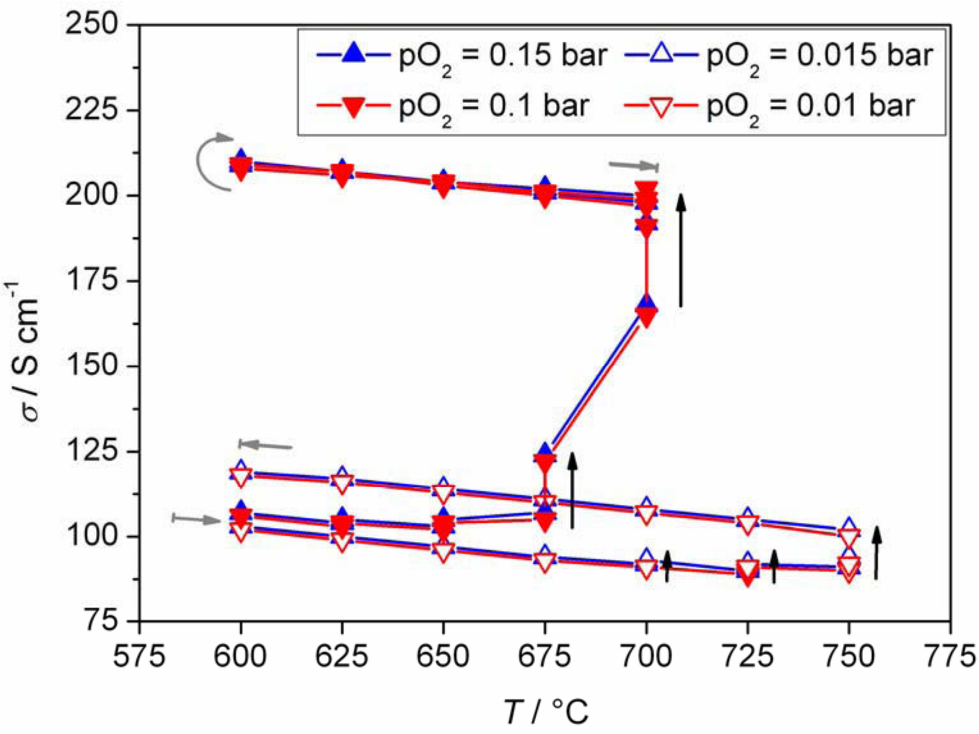

Fig. 4.12 Temperature dependence of the electronic conductivity of $Pr_2NiO_{4+\delta}$ between pO_2-values of 0.01 and 0.15 bar. An increase in the conductivity due to phase decomposition is illustrated by black arrows, gray arrows indicate the chronological order of measurements. Lines are for visual guidance.

4.2.2 Chemical surface exchange coefficient of oxygen

The chemical surface exchange coefficient k_{chem} of oxygen was measured at pO_2-values of 0.1 and 0.01 bar for both flat specimens contacted in van der Pauw geometry and for bar-shaped samples with linear four-point electrode arrangement. Arrhenius plots of k_{chem} for $La_2NiO_{4+\delta}$, $Pr_2NiO_{4+\delta}$ and $Nd_2NiO_{4+\delta}$ are given in Fig. 4.13. Measurements of samples in van der Pauw geometry were performed between ~600°C and 750°C within a full thermal cycle to assess the reproducibility of the kinetic parameters. Results presented for bar-shaped geometry were obtained from measurements in the cooling-run of Ag-coated samples from 850°C down to 600°C, where the silver layer has been removed during the preceding heat treatment (see section 3.10). Relaxation processes for oxidizing steps were consistently found to be faster than those in the reducing direction, the effect being more pronounced for thin samples and less significant for the bar-shaped specimens. As can be seen from Fig. 4.13 exchange coefficients decrease at lower oxygen partial pressures. Slightly slower oxygen surface exchange kinetics at lower oxygen partial pressures have also been found by Li and Haugsrud for $La_2NiO_{4+\delta}$ [186].

Activation energies of k_{chem} determined by regression analysis of linear regions in the Arrhenius plots are listed in Tab. 4.2. As a rule, activation energies obtained from bar-shaped samples are smaller than those of thin samples, except for the case of $Pr_2NiO_{4+\delta}$, which is probably due to different stages of degradation caused by the phase instability of this compound.

Little to no thermal hysteresis was found between cooling and heating runs except for Pr-nickelate. Above 700°C a positive deviation from linearity in the Arrhenius plot was observed for $Pr_2NiO_{4+\delta}$, most likely caused by the decomposition process which was also observed to start at 700°C for EC measurements (Fig. 4.12). When cooling the sample from 750°C at $pO_2 = 0.01$ bar, k_{chem}-values were similar to those of the heating run but an increase in activation energy was observed. At $pO_2 = 0.1$ bar, the phase instability of $Pr_2NiO_{4+\delta}$ made an accurate determination of the exchange coefficients from thin samples impossible.

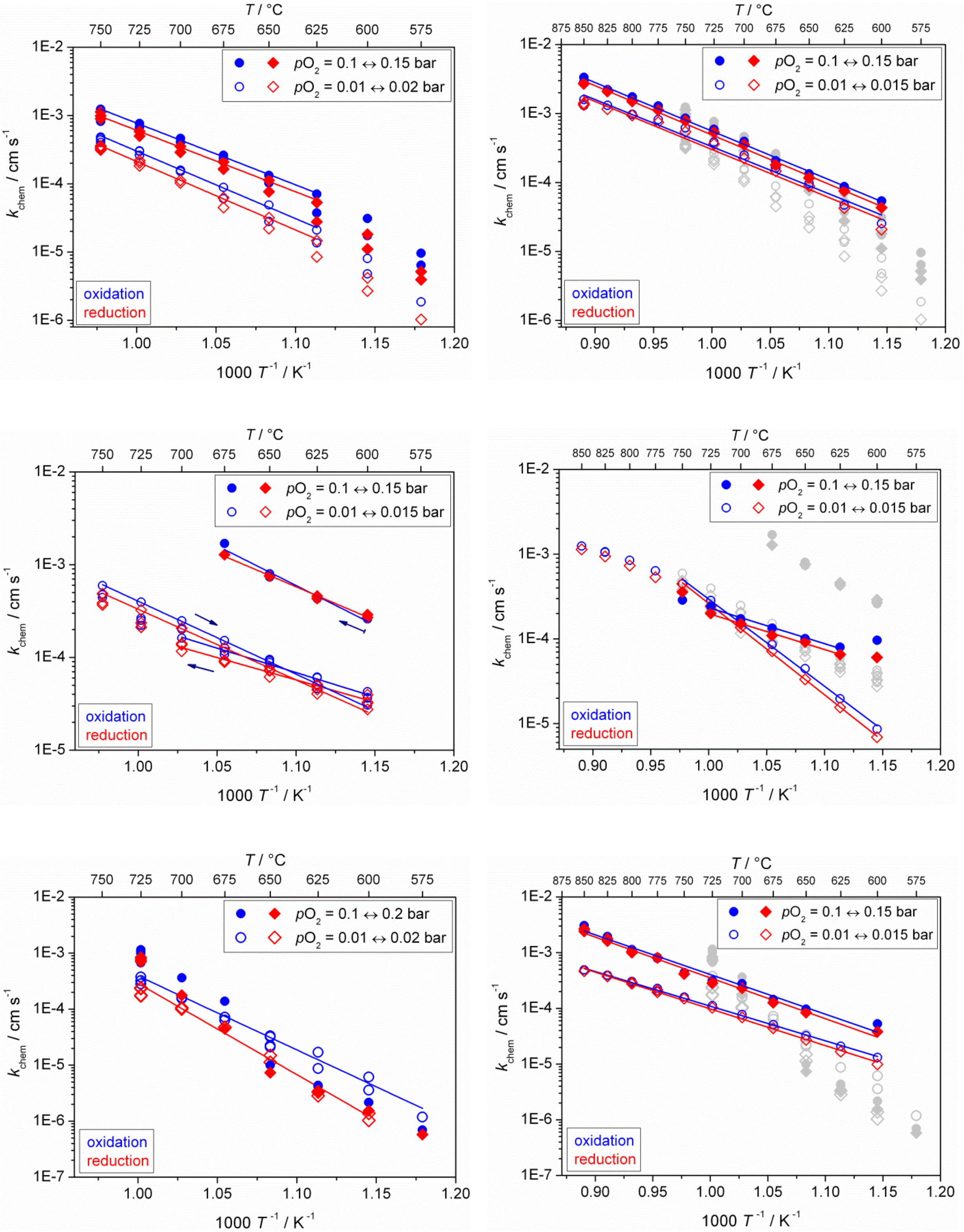

Fig. 4.13 Arrhenius plots of the chemical surface exchange coefficients of oxygen of $La_2NiO_{4+\delta}$ (top), $Pr_2NiO_{4+\delta}$ (middle) and $Nd_2NiO_{4+\delta}$ (bottom). The left column shows results obtained from thin samples measured in van der Pauw geometry, the right diagram displays data of bar-shaped samples including data points from the left diagram in gray color. Lines are linear fits to the data, activation energies calculated from the slopes are given in Tab. 4.2.

Tab. 4.2 Activation energies E_a (in kJmol^{-1}) of k_{chem} of $Ln_2NiO_{4+\delta}$ (Ln = La, Pr, Nd) in the intermediate temperature regime for oxidation (ox) and reduction (red) measurements and different sample geometries.

	pO_2 = 0.1 bar				**pO_2 = 0.01 bar**			
	van der Pauw		**linear four-point**		**van der Pauw**		**linear four-point**	
	ox	red	ox	red	ox	red	ox	red
$La_2NiO_{4+\delta}$	173	172	135	137	189	192	131	133
$Pr_2NiO_{4+\delta}$	164	139	82[a]	81[a]	151[a]	146[a]	197[a]	207[a]
$Nd_2NiO_{4+\delta}$	283[b]	283[b]	136	140	253	312	119	126

[a] secondary phases $Pr_4Ni_3O_{10-\delta}$ and $PrO_{1.83-\delta}$ present due to phase instability

[b] assuming k-controlled oxygen exchange over the whole temperature range

Data reported by Li and Haugsrud [186] for k_{chem} of $La_2NiO_{4+\delta}$ are in good agreement with those obtained in this work (Fig. 4.14). In particular, the surface exchange coefficient determined by pO_2-steps from 1.0 to 0.2 bar is almost congruent with results in this work for relaxation measurements with pO_2-steps between 0.1 and 0.15 bar.

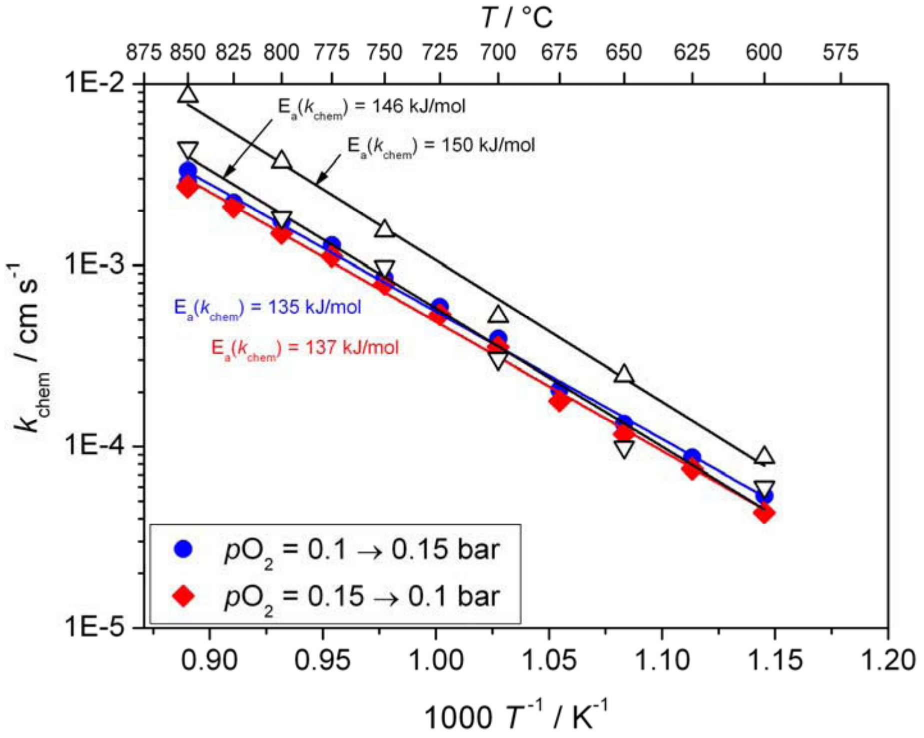

Fig. 4.14 Comparison of k_{chem} of bar-shaped $La_2NiO_{4+\delta}$ in this work with k_{chem} from Li and Haugsrud [186] for pO_2-steps 1.0 ⟶ 1.9 atm (triangles, tip up) and 1.0 ⟶ 0.2 atm (triangles, tip down). Activation energies are plotted in the diagram.

Chemical surface exchange coefficients of $Nd_2NiO_{4+\delta}$ have been calculated from results of tracer experiments by Boehm et al. [26] according to $k_{chem} \approx \Gamma_O k_O$ [158,230]. Values of k_{chem} are similar to results in this work, however, activation energies differ by a factor of ~2 (Fig. 4.15).

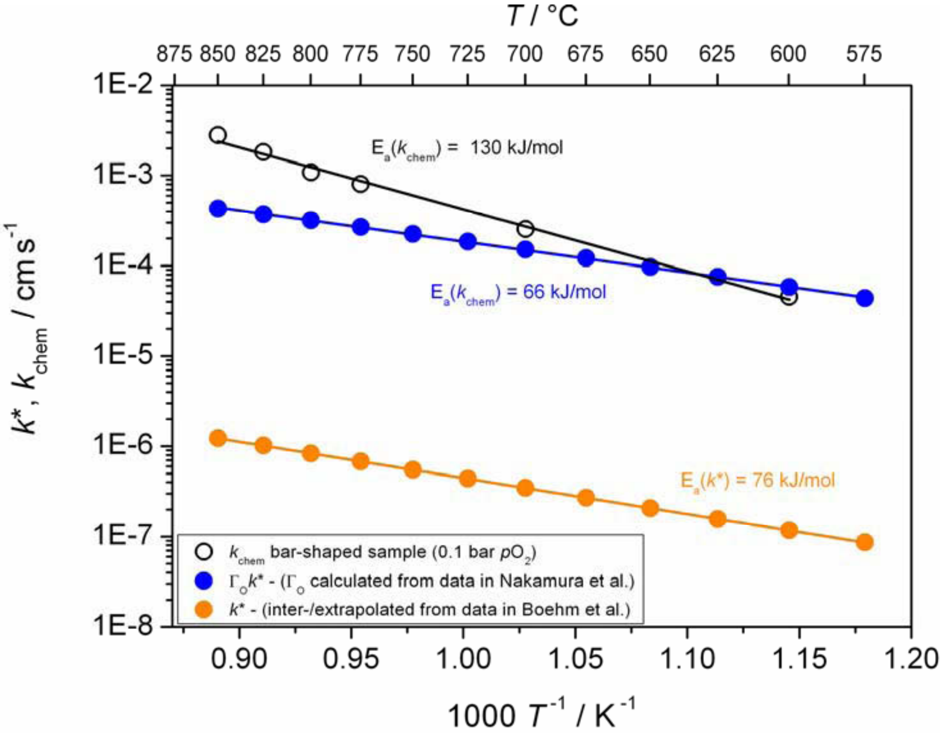

Fig. 4.15 Comparison of k_{chem} of $Nd_2NiO_{4+\delta}$ in this work with k_{chem} converted from tracer surface exchange coefficients k^* (Boehm et al. [26]) by means of the thermodynamic factor Γ_O calculated from oxygen non-stoichiometry data given by Nakamura et al. [231]. Activation energies are shown in the diagram.

4.2.3 Chemical diffusion coefficient of oxygen

Fig. 4.16 shows chemical diffusion coefficients of oxygen D_{chem} of $La_2NiO_{4+\delta}$ at $pO_2 = 0.01$ and 0.1 bar determined from a bar-shaped sample. A reliable determination of D_{chem} was possible only after deposition of a 200 nm Ag-layer on the sample surface, thereby increasing the surface exchange rate [20]. No diffusion coefficients could be determined from flat samples in van der Pauw geometry. Fig. 4.16 (right) includes data at $pO_2 = 1$ atm reported by Li and Haugsrud [186], who employed a similar strategy of enhancing the surface exchange rate by covering the sample surface with nano-powder of $La_2NiO_{4+\delta}$. Their results differ considerably both in absolute values as well as in activation energy from results in this work. An activation energy of 98 kJmol^{-1} was given by Li and Haugsrud [186] which is roughly twice as large as determined in this work (see Tab. 4.3).

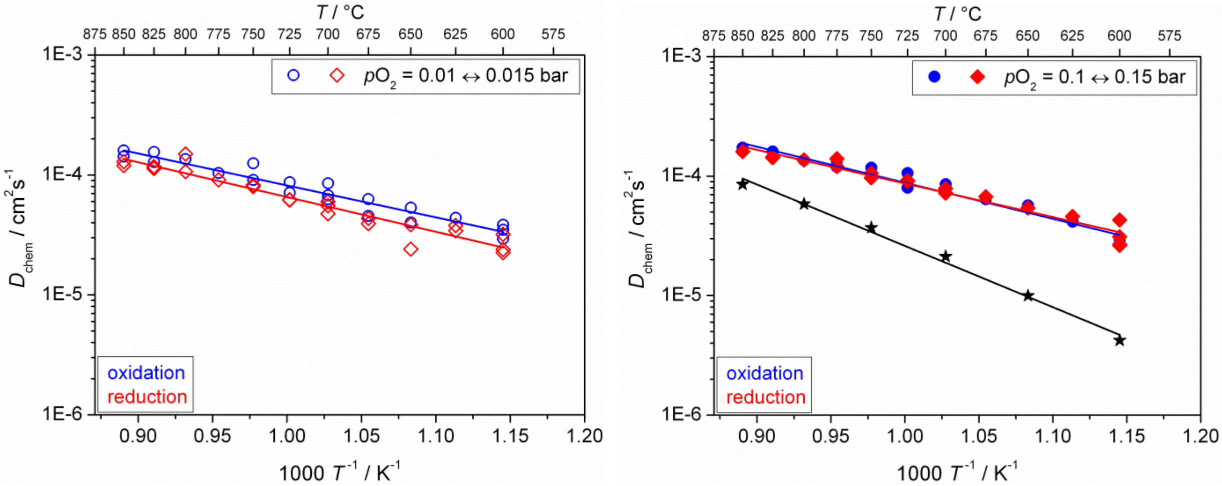

Fig. 4.16 Arrhenius plots of the chemical diffusion coefficient of oxygen of $La_2NiO_{4+\delta}$ at $pO_2 = 0.01$ bar (left) and $pO_2 = 0.1$ bar (right) obtained from a bar-shaped sample after Ag-deposition. Star symbols denote data by Li and Haugsrud [186] of $La_2NiO_{4+\delta}$ coated with nano-$La_2NiO_{4+\delta}$ at $pO_2 = 1$ atm ($E_a = 98$ kJmol^{-1}).

Values of D_{chem} for $Pr_2NiO_{4+\delta}$ were obtained at $pO_2 = 0.1$ bar between 600 and 675°C (Fig. 4.17). Above 675°C the phase decomposition process became dominant resulting in a strong drift and a high noise level in the voltage signal, thus preventing any sensible evaluation of conductivity relaxation experiments. In the cooling run a decrease of D_{chem} by approximately one order of magnitude was found resulting from phase decomposition, where the relaxation process appeared to be limited by the diffusion kinetics (Fig. 4.17). However, it should be mentioned that in an advanced state of decomposition the application of the conductivity relaxation technique becomes problematic since the equations used to model the relaxation process are not adequate to describe oxygen exchange and transport in multiphase materials. Moreover, some caution with the interpretation of diffusivities in Fig. 4.17 is appropriate since relaxation measurements were performed on thin samples which are subject to the same considerations as discussed below for $Nd_2NiO_{4+\delta}$. A bar-shaped sample of $Pr_2NiO_{4+\delta}$ was prepared to obtain reliable diffusion coefficients but even after Ag-deposition the oxygen exchange kinetics was still found to be dominated by the oxygen surface exchange process, indicating very high diffusivities of this material.

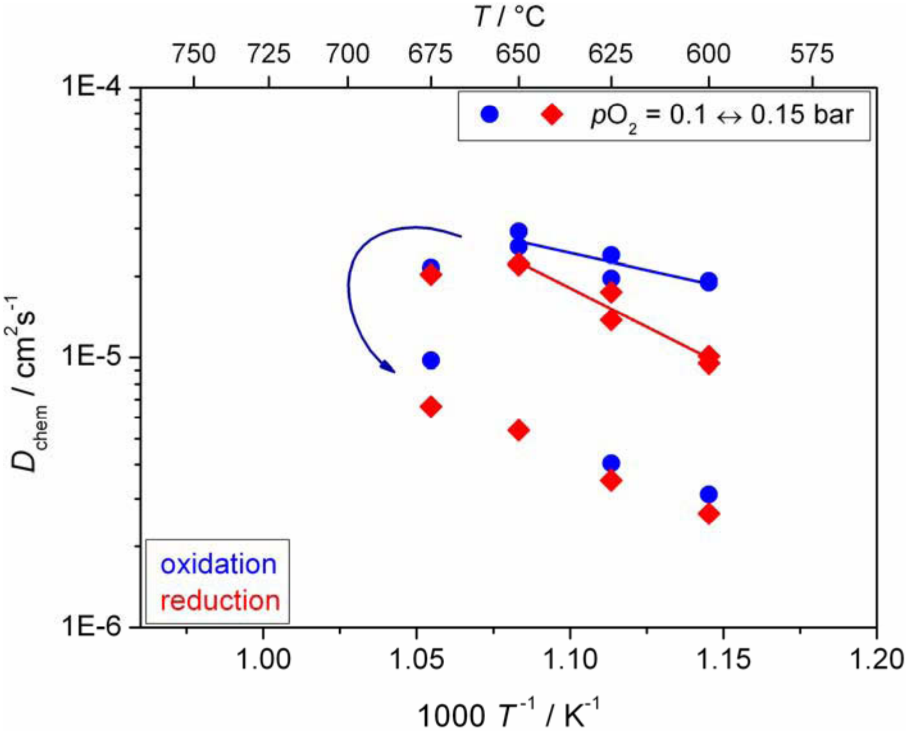

Fig. 4.17 Arrhenius plot of the chemical diffusion coefficient of oxygen of $Pr_2NiO_{4+\delta}$ at $pO_2 = 0.1$ bar, obtained from a flat sample contacted in van der Pauw geometry. The arrow symbolizes a decrease in diffusivity due to the decomposition reaction. Lines are linear fits to data points between 600 and 650°C, calculated activation energies are given in Tab. 4.3.

Fig. 4.18 shows Arrhenius plots of D_{chem} obtained from measurements of flat samples with van der Pauw electrode arrangement (left) and linear-four-point contact geometry of bar-shaped samples of $Nd_2NiO_{4+\delta}$. Limited data at $pO_2 = 0.1$ bar are available in the left diagram due to an apparent change of the oxygen exchange mechanism from mixed controlled to *k*-

controlled oxygen exchange below 675°C. The discrepancy between data from van der Pauw-type relaxation measurements and those from bar-shaped samples is enormous, both with respect to absolute value and activation energies (Fig. 4.18, right).

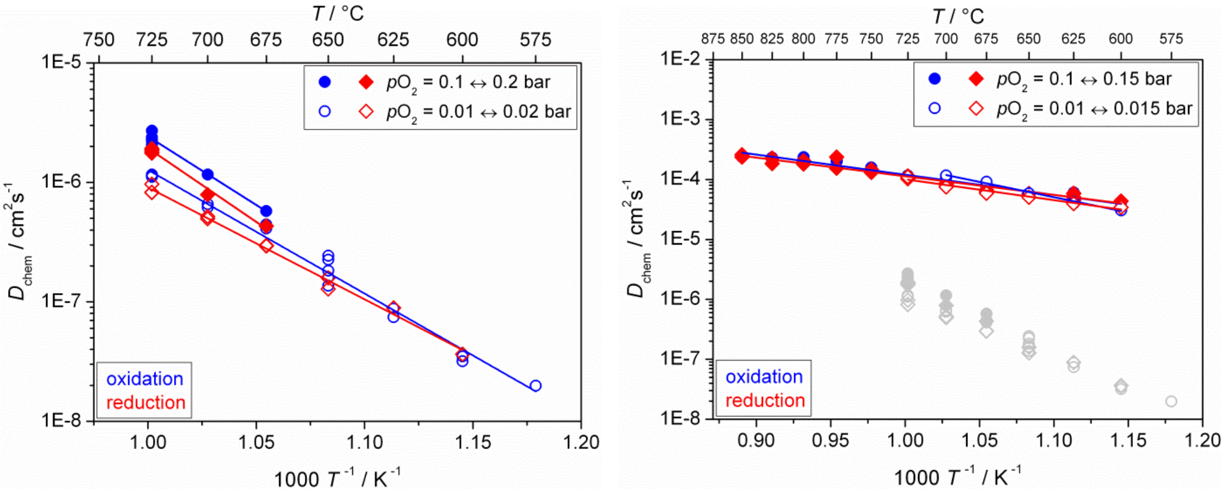

Fig. 4.18 Arrhenius plots of the chemical diffusion coefficients of oxygen of $Nd_2NiO_{4+\delta}$. The left diagram shows results obtained from a thin sample measured in van der Pauw geometry, the right diagram displays data of a bar-shaped Ag-coated sample including data points from the left diagram plotted in gray color. Lines are linear fits to the data, calculated activation energies are listed in Tab. 4.3.

Results for Ag-coated bar-shaped samples appear to be much more reliable than those of flat samples in van der Pauw geometry due to the pronounced contribution of diffusion to the total oxygen exchange process. Fig. 4.19 shows an example of a relaxation transient derived from bar-shaped $Nd_2NiO_{4+\delta}$ at 750°C which can be fitted with a diffusion controlled exchange model, thus leaving little doubt that real diffusion coefficients were determined. Furthermore, values of D_{chem} obtained from bar-shaped samples appear to be closer to results obtained from literature data and have much more reasonable activation energies (see Fig. 4.21 and Tab. 4.3).

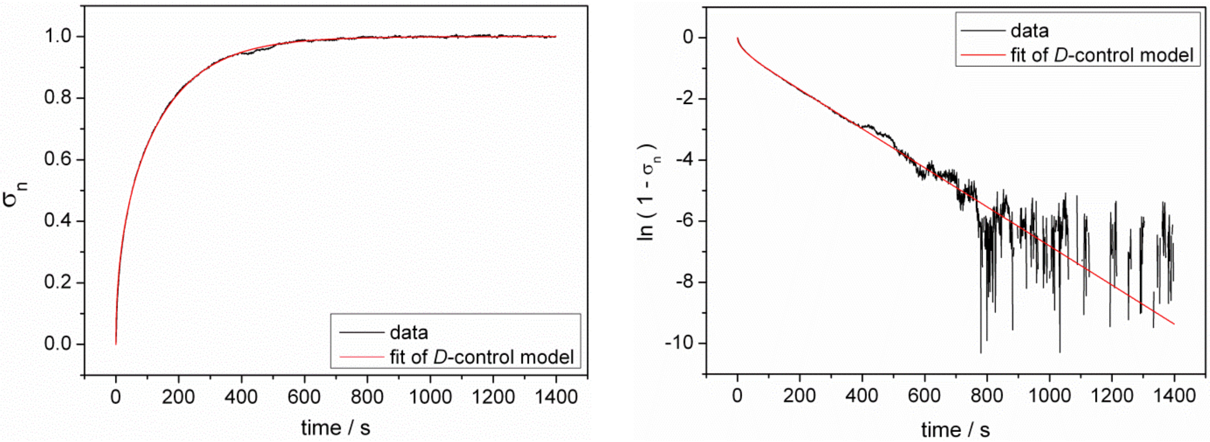

Fig. 4.19 Conductivity relaxation transient of a bar-shaped $Nd_2NiO_{4+\delta}$-sample with Ag-layer at 750°C after a pO_2-step of 0.15 ⟶ 0.1 bar (black lines). Red lines represent fitting curves for two-dimensional oxygen exchange under pure diffusion control.

It is likely that spurious diffusion coefficients were determined from relaxation measurements performed on thin samples. An upwards-curved transient in the semi-logarithmic plot is usually interpreted as a clear indication of a diffusion contribution to the overall oxygen exchange. However, it was discovered at a later phase in this work that such ‘bending’ of the relaxation curve in semi-logarithmic plot might also be caused by a surface controlled oxygen exchange, where the surface exchange coefficient is not constant during the relaxation process but is rather decreasing in the course of the relaxation process (see chapter 2). Indeed, re-examining the data for $Nd_2NiO_{4+\delta}$ showed that the relaxation curves could in many cases be fitted with the variable-k model equally well or even better than with the mixed control exchange model and thus such non-constant k_{chem} may have been mistaken for mixed controlled oxygen exchange. An extreme example is given in Fig. 4.20 for a van der Pauw contacted thin sample of $Nd_2NiO_{4+\delta}$ at the beginning of the measurement series. The convex shape of the transient in semi-logarithmic representation is evident and can be perfectly modeled with the variable-k model, while the mixed control model gives less good agreement with the data. It should be mentioned that for this particular measurement mixed oxygen exchange control can be excluded solely on the basis of the y-axis intercept of the regression line to the linear part of the semi-logarithmic plot, which gives -0.46 and is therefore far below the limit of $ln(8/\pi^2) \approx -0.21$ for 1D-diffusion (see section 2.10.2). However, in cases with less pronounced curvature such a straightforward criterion will not be available.

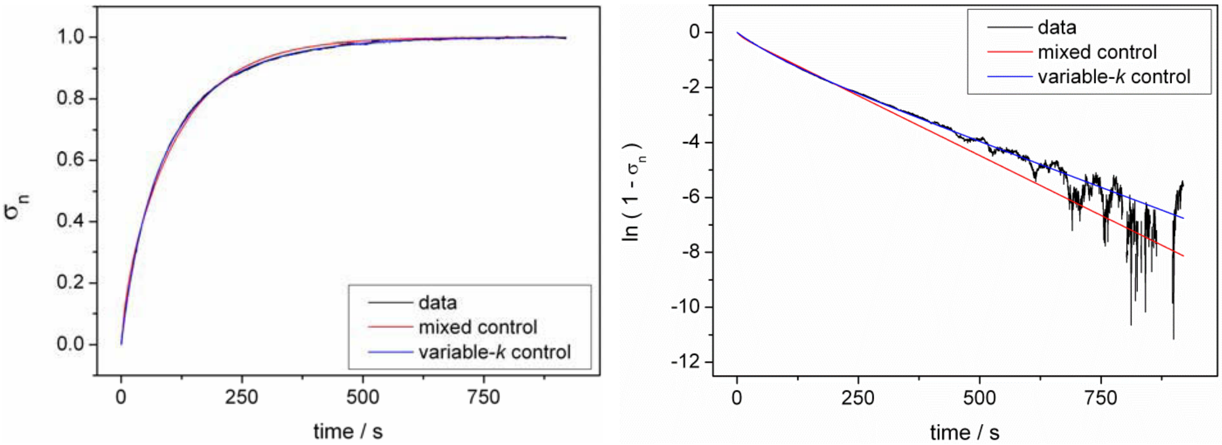

Fig. 4.20 Different representations of the conductivity relaxation transient of a thin sample of $Nd_2NiO_{4+\delta}$ at 725°C after a pO_2-step of 0.1 ⟶ 0.2 bar (black lines). Red lines represent fitting curves for mixed controlled oxygen exchange, blue lines show fitting results for the variable-*k* model. Fitting parameters were $k_{chem} = 1.0\cdot10^{-3}$ cm s^{-1}, $D_{chem} = 2.3\cdot10^{-6}$ cm^{2}s^{-1} for the mixed control model and $k_0 = 3.0\cdot10^{-4}$ cm s^{-1}, $k_\infty = 1.5\cdot10^{-4}$ cm s^{-1} for the variable-*k* model, the sample thickness was 0.467 mm.

It has to be emphasized that at this stage the above discussion is just a speculation solely derived from the quality of the fit and no concrete microscopic mechanism can be proposed for explaining such a variation in k_{chem}. Moreover, no clear trend has been observed for the parameters of the variable-*k* fitting model (i.e. k_0 and k_∞, see chapter 2). In particular, in almost all cases k_0 was found to be higher than k_∞ and no reversal between k_0 and k_∞ between oxidation/reduction measurements under otherwise identical experimental conditions has been observed, as might be expected when based on some underlying physical mechanism. Thus, it remains unclear if there is some real significance to the variable-*k* model or if it just happens to more closely reproduce the relaxation curves whose deviation from the ideal mixed control / *k*-control model is due to experimental issues or other causes.

It is interesting to note, however, that superior fitting quality of the variable-*k* model was also observed during long-term measurements of $La_2NiO_{4+\delta}$ at 700°C when exposing the sample to humidified air. This might be an indication that the applicability of the variable-*k* model may be linked to degradation/reconstruction processes of the sample surface, but again this is solely based on the fitting results to relaxation data and no further experimental evidence or physical models are available to support this claim.

Tab. 4.3 Activation energies E_a (in kJmol^{-1}) of D_{chem} for $Ln_2NiO_{4+\delta}$ (Ln = La, Pr, Nd) in the intermediate temperature regime for oxidation (ox) and reduction (red) measurements and different sample geometries.

	pO_2 = 0.1 bar				**pO_2 = 0.01 bar**			
	van der Pauw		**linear four-point**		**van der Pauw**		**linear four-point**	
	ox	red	ox	red	ox	red	ox	red
$La_2NiO_{4+\delta}$	–	–	58[a]	54[a]	–	–	51[a]	55[a]
$Pr_2NiO_{4+\delta}$	48[b]	110[b]	–	–	–	–	–	–
$Nd_2NiO_{4+\delta}$	220[c]	236[c]	64[a]	59[a]	198	179	97[a,d]	67[a,d]

[a] Ag-coated sample

[b] calculated from limited data at $675 \leq T/°C \leq 600$

[c] calculated from limited data at $725 \leq T/°C \leq 675$

[d] calculated from limited data at $700 \leq T/°C \leq 600$

Fig. 4.21 shows chemical diffusion coefficients of $La_2NiO_{4+\delta}$ obtained from bar-shaped samples after Ag-deposition. The results are compared with data obtained by converting tracer diffusion coefficients D^* by means of the thermodynamic factor Γ_O. Diffusion coefficients determined in this study are systematically above those derived from tracer data by a factor of 2-4, while the agreement between activation energies can be considered acceptable.

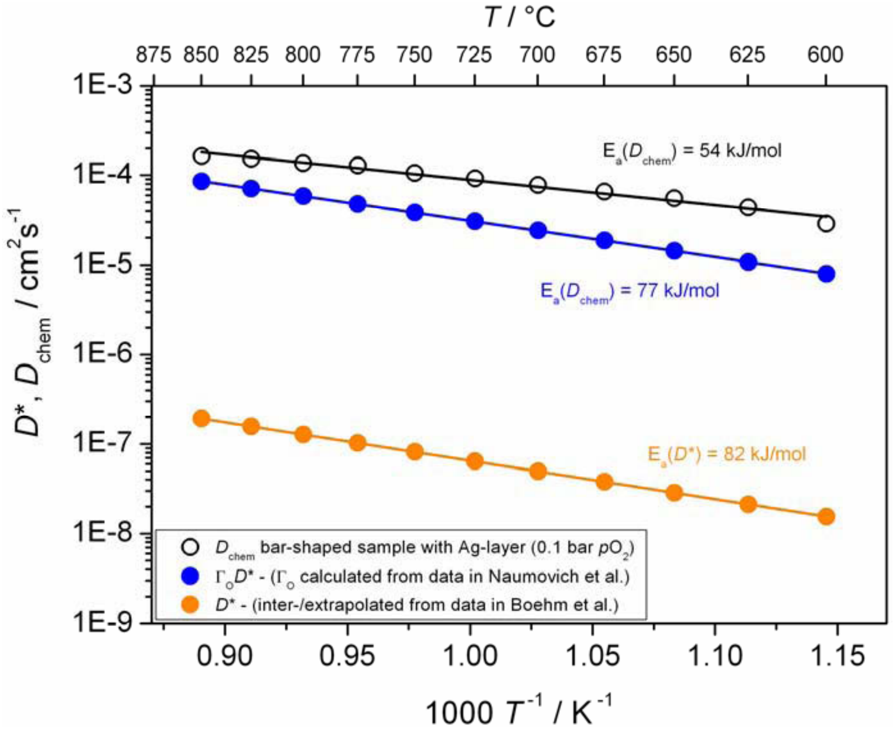

Fig. 4.21 Comparison of D_{chem} of $La_2NiO_{4+\delta}$ from this work with D_{chem} obtained from tracer surface exchange coefficients D^* (Boehm et al. [26]) and the thermodynamic factor Γ_O calculated from oxygen non-stoichiometry data given by Naumovich et al. [84]. Activation energies are plotted in the diagram.

A comparison of D_{chem} for $Nd_2NiO_{4+\delta}$ with chemical diffusion coefficients derived from tracer experiments is shown in Fig. 4.22. Values of D_{chem} differ by roughly one order of magnitude while activation energies are quite close. It is interesting to note that the discrepancy of D_{chem} determined in this work with literature data is similar to that found for $La_2NiO_{4+\delta}$ (see Fig. 4.21) insofar as values for D_{chem} are larger than those from literature by roughly one order of magnitude and feature somewhat lower activation energies. The reason for this systematic deviation is unclear, a diffusion of silver into the bulk of the specimens can be excluded on the basis of surface depth-profiles of a $La_2NiO_{4+\delta}$-sample obtained by XPS-analysis after testing (see section 3.10).

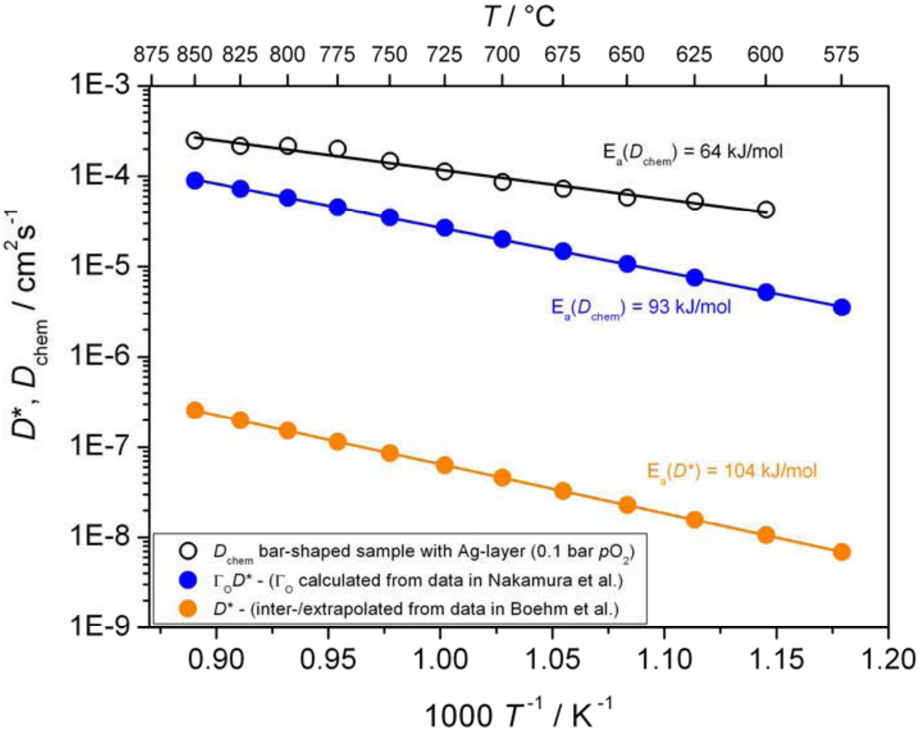

Fig. 4.22 Comparison of D_{chem} of $Nd_2NiO_{4+\delta}$ from this work with D_{chem} obtained from tracer diffusion coefficients D^* (Boehm et al. [26]) and the thermodynamic factor Γ_O calculated from oxygen non-stoichiometry data given by Nakamura et al. [231]. Activation energies are plotted in the diagram.

4.2.4 Ionic conductivity

The oxygen ionic conductivities of $La_2NiO_{4+\delta}$ and $Nd_2NiO_{4+\delta}$ were calculated by means of the Nernst-Einstein equation

$$\sigma_{ionic} = \frac{4F^2 c_O D_O}{RT} \tag{4.4}$$

where c_O and D_O are the concentration and self-diffusion coefficient of oxygen, respectively. D_{chem} was converted to the self-diffusion coefficient of oxygen via thermodynamic factors obtained from oxygen non-stoichiometry data by Naumovich et al. [84] and by Nakamura et al. [231] for $La_2NiO_{4+\delta}$ and $Nd_2NiO_{4+\delta}$, respectively.

The ionic conductivity of $La_2NiO_{4+\delta}$ is shown in Fig. 4.23 as a function of temperature at oxygen partial pressures of 0.1 and 0.01 bar. A comparison with results from Shaula et al. [232] given in Fig. 4.23 (left) shows good agreement at 850°C, but increasingly large deviation at lower temperatures due to lower activation energies found in this work (Fig. 4.23, right).

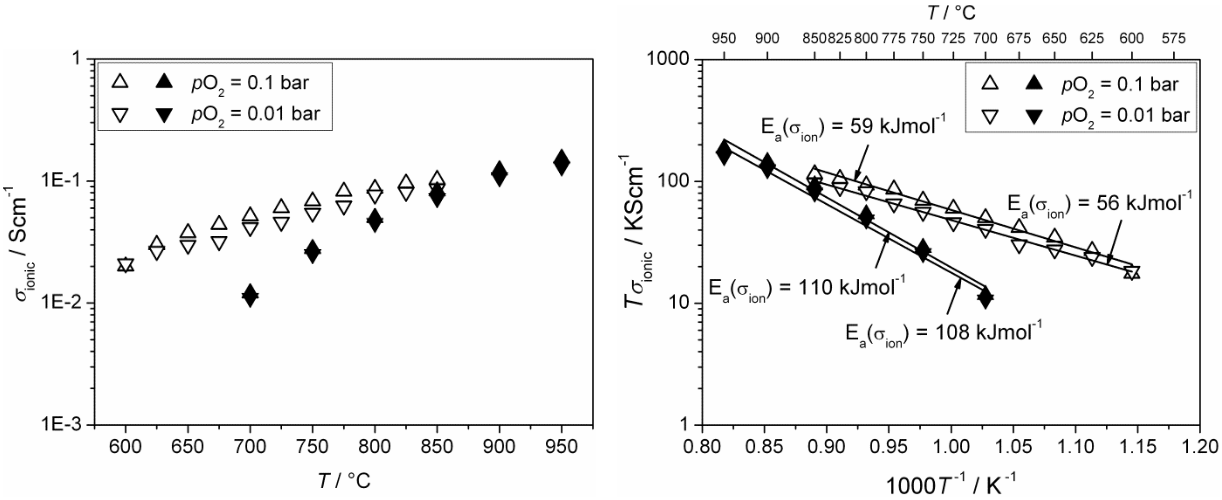

Fig. 4.23 Ionic conductivity of $La_2NiO_{4+\delta}$ from this work (open triangles) compared with data from Shaula et al. [232] (solid triangles). Activation energies were calculated from slopes as shown in the right diagram.

A comparison with results from Mauvy et al. [233] given in Fig. 4.24 (left) for $Nd_2NiO_{4+\delta}$ shows a discrepancy by somewhat less than one order of magnitude, but similar activation energies between 600 and 725°C (Fig. 4.24, right). Comparison of the ionic conductivities of both nickelates with the corresponding total conductivities (Fig. 4.10 and Fig. 4.11) shows the ionic contribution to be below 1%.

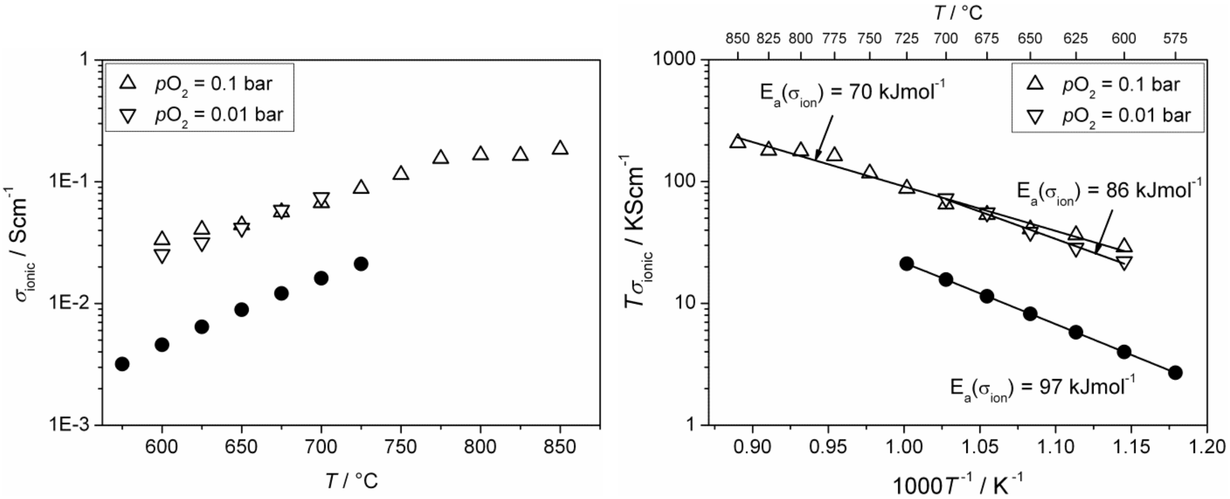

Fig. 4.24 Ionic conductivity of $Nd_2NiO_{4+\delta}$ from this work (open triangles) compared with data from Mauvy et al. [233] (solid circles). Activation energies were calculated from the slopes as shown in the right diagram.

4.3 Long-term stability and degradation

Long-term measurements have been performed on undoped rare earth nickelates for various gas compositions at temperatures and oxygen partial pressures that correspond to real operating conditions at the cathode side of an IT-SOFC. Since the surface exchange rate of oxygen is known to be quite sensitive to changes in the surface composition or morphology [23,24], the chemical surface exchange coefficient of oxygen was selected as a surface sensitive parameter and monitored over periods of thousand hours to characterize changes in the material surface. Moreover, the oxygen exchange coefficient is an important property in itself for assessing the performance of a mixed ionic-electronic conductor as cathode material for IT-SOFCs. The electrical conductivity was periodically measured to detect changes in the bulk of the material. At various stages during the testing period, XPS-depth profiles of the sample surface were determined over several hundred nanometers. Whenever gold contacts were applied to the samples using Metalor® T-10112 gold paste, small amounts of bismuth were identified by XPS or SEM/EDX in surface near regions after long-term measurements. For reasons of clarity the Bi-line has been removed from all XPS-depth profiles as shown below. Likewise, carbon was detected on most sample surfaces by XPS and has been omitted from depth profiles except for cases where high carbon levels were found to extend further into the sample.

4.3.1 Phase instability of $Pr_2NiO_{4+\delta}$

The issue of limited phase stability of $Pr_2NiO_{4+\delta}$ has been treated in section 4.1.4. Fig. 4.25 shows the XRD-pattern of a $Pr_2NiO_{4+\delta}$-sample after experimental investigations at $pO_2 = 0.01$ bar between 600 and 750°C. Additional reflections emerging after the test series are consistent with decomposition products of $Pr_2NiO_{4+\delta}$ proposed in the literature [88,113,218,221,222], namely $Pr_4Ni_3O_{10-\delta}$ and $PrO_{1.83}$ (i.e. Pr_6O_{11}). For a thorough investigation of the decomposition products with respect to their identity and relative amounts in the material, e.g. by Rietveld analysis, prolonged exposure to air at elevated temperatures would be necessary. Due to the limited phase stability of $Pr_2NiO_{4+\delta}$ under conditions relevant for the application as IT-SOFC cathode material, this compound was not included in the long-term testing discussed further below. It should be mentioned that from an electrochemical point of view the phase instability may not exclude $Pr_2NiO_{4+\delta}$ from SOFC applications because $Pr_4Ni_3O_{10-\delta}$ itself is a mixed conductor featuring an electronic conductivity that is higher than that of $Pr_2NiO_{4+\delta}$ [218,221] and a significant ionic conductivity has been suggested based on results from permeation measurements [218]. Moreover, praseodymium oxides are known to be catalytically active for the oxygen reduction reaction [62,71]. However, with respect to thermo-mechanical compatibility with other cell components the phase decomposition is expected to be highly detrimental since it is accompanied by pronounced changes in volume [218].

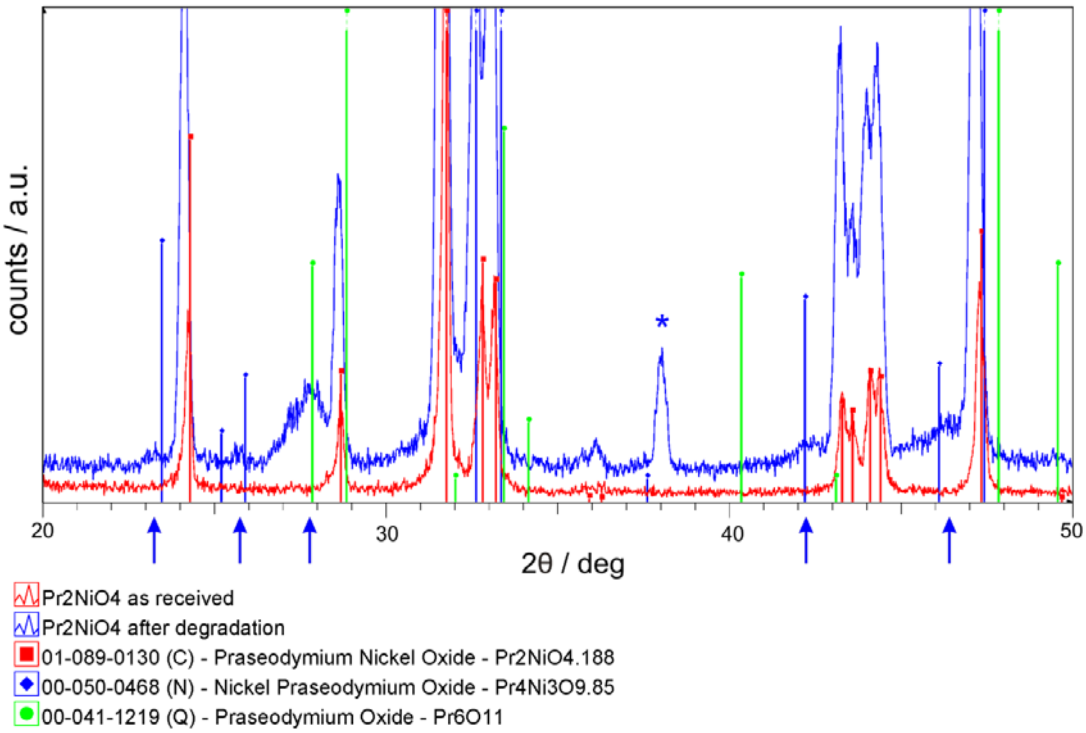

Fig. 4.25 XRD-pattern of a Pr$_2$NiO$_{4+\delta}$-sample after long-term measurements at pO_2 = 0.01 bar. Arrows indicate positions of additional reflections from decomposition products. The reflection marked with an asterisk is due to gold residues from electrical contacts.

4.3.2 Humid atmospheres

The chemical stability of La$_2$NiO$_{4+\delta}$ and Nd$_2$NiO$_{4+\delta}$ against humidity was investigated by periodically measuring the electronic conductivity σ and the chemical surface exchange coefficient of oxygen at 700°C over a period of 1000 h in dry atmospheres, after which the gas streams were enriched with water vapor and monitoring was continued for another 1000 hours. The surface exchange coefficient of La$_2$NiO$_{4+\delta}$ at 700°C is around $2 \cdot 10^{-4}$ cm s^{-1} and no decrease in k_{chem} was observed under dry conditions over a period of 1000 hours (Fig. 4.26, right). Results for Nd$_2$NiO$_{4+\delta}$ show stable oxygen exchange kinetics for 1000 hours under dry conditions. This is in contrast to other promising cathode materials like $La_{0.6}Sr_{0.4}CoO_{3-\delta}$ and $La_{0.58}Sr_{0.4}Co_{0.2}Fe_{0.8}O_{3-\delta}$ where a decrease in k_{chem} was observed even in dry atmospheres at 600°C [36,42].

After humidification of the gas stream the surface exchange rate of both compounds starts to decline (Fig. 4.26, right). The degradation process levels off within the investigated period and a total decrease of the oxygen exchange rate by factor of ~3 was found for $La_2NiO_{4+\delta}$. The decrease in k_{chem} of $La_2NiO_{4+\delta}$ is slower and less pronounced as in the case of $Nd_2NiO_{4+\delta}$, where the exchange coefficient drops by one order of magnitude in humid atmospheres. For the perovskite-type cathode materials $La_{0.6}Sr_{0.4}CoO_{3-\delta}$ and $La_{0.58}Sr_{0.4}Co_{0.2}Fe_{0.8}O_{3-\delta}$ a similar detrimental effect of water on the oxygen surface exchange is reported [36,42,234], though drawing quantitative comparisons is difficult due to different conditions in these studies with respect to temperature or pH_2O. It is interesting to note that for thin films of $La_{0.6}Sr_{0.4}CoO_{3-\delta}$ a short-time effect of water leading to an increase of the oxygen surface exchange rate was reported [235]. However, no such effect has been observed in this study after switching from dry to humid atmospheres.

The electronic conductivity was not affected by long-term operation or humidity (Fig. 4.26, left) indicating that the degradation process is limited to the sample surface in contact with the gas phase.

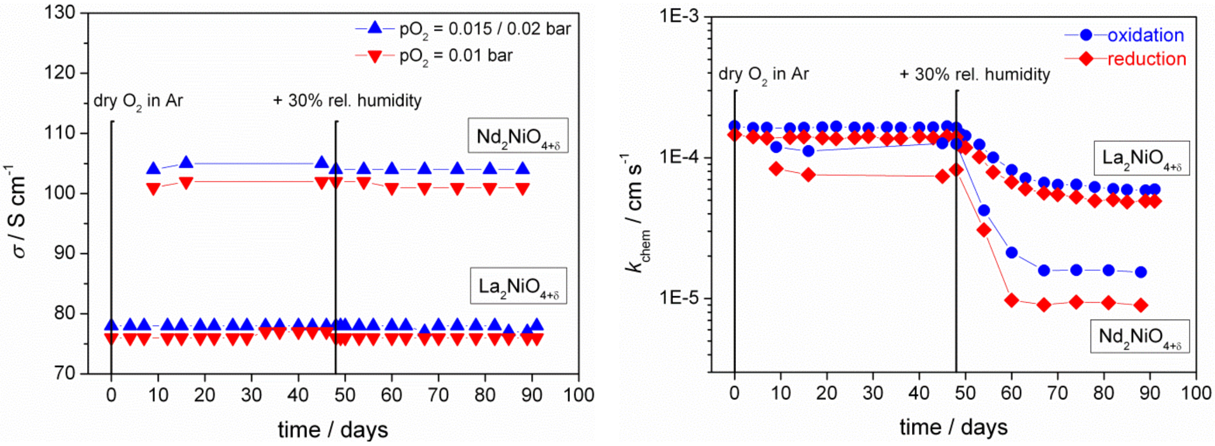

Fig. 4.26 Long-term behavior of the electronic conductivity (left) and the chemical surface exchange coefficient of oxygen (right) of $La_2NiO_{4+\delta}$ and $Nd_2NiO_{4+\delta}$ at 700°C and $pO_2 = 0.01$ bar in dry and humid atmospheres (30% relative humidity).

To gain some insight into the surface degradation mechanism, XPS-depth profiles have been recorded at different stages along the period of investigation. Reference measurements were performed on freshly sintered samples and after 1000 hours in dry conditions. The effect of water on the material surface was determined after another 1000 hours in humid atmospheres. For the recording of each XPS-depth profile sputtering was continued until the elemental composition was found to be fairly constant, indicating that the sample bulk has been reached. Depth profiles were then calibrated using the compositions at higher sputtering depths where the nominal composition of the material can be assumed.

Fig. 4.27 (top row) shows the results from XPS-analysis of $La_2NiO_{4+\delta}$. The elemental distribution of La, Ni and O in an as-sintered sample is maintained throughout the topmost 700 nm of the sample and shows a fairly constant La:Ni-ratio over the whole depth range. After 1000 hours in a dry Ar-O_2 gas flow significant changes in composition within the first 100 nm of the surface layer are observed (Fig. 4.27, middle row). An increase in the La:Ni-ratio is evident from the profiles. A similar finding has also been reported by other authors [236] and may be caused by a formation of La_2O_3 at the gas-solid interface [89]. Interestingly, the surface exchange rate of oxygen appears to be not affected by such modification of the surface composition (Fig. 4.26, right).

XPS-depth profiles were determined after exposing $La_2NiO_{4+\delta}$ to humid atmospheres over 1000 hours (Fig. 4.27, bottom row). Despite the observed decrease in k_{chem} no distinct differences between XPS-profiles from samples in dry and humid atmospheres are evident. Upon closer inspection, La-enrichment and nickel depletion appears to be somewhat more pronounced and reaches to greater depths of approx. 200 nm when compared with samples kept under dry conditions. Apart from this finding there seems to be no principal difference between depth profiles in dry and humid atmospheres and a clear-cut rationale for the detrimental effect of humidity on the oxygen exchange of $La_2NiO_{4+\delta}$ cannot be established. Results from prolonged exposure to humid atmospheres – as given further below – indicate that the drop in the oxygen exchange rate is reversible at least to some extent, since a partial recovery could be observed after switching back to dry atmospheres.

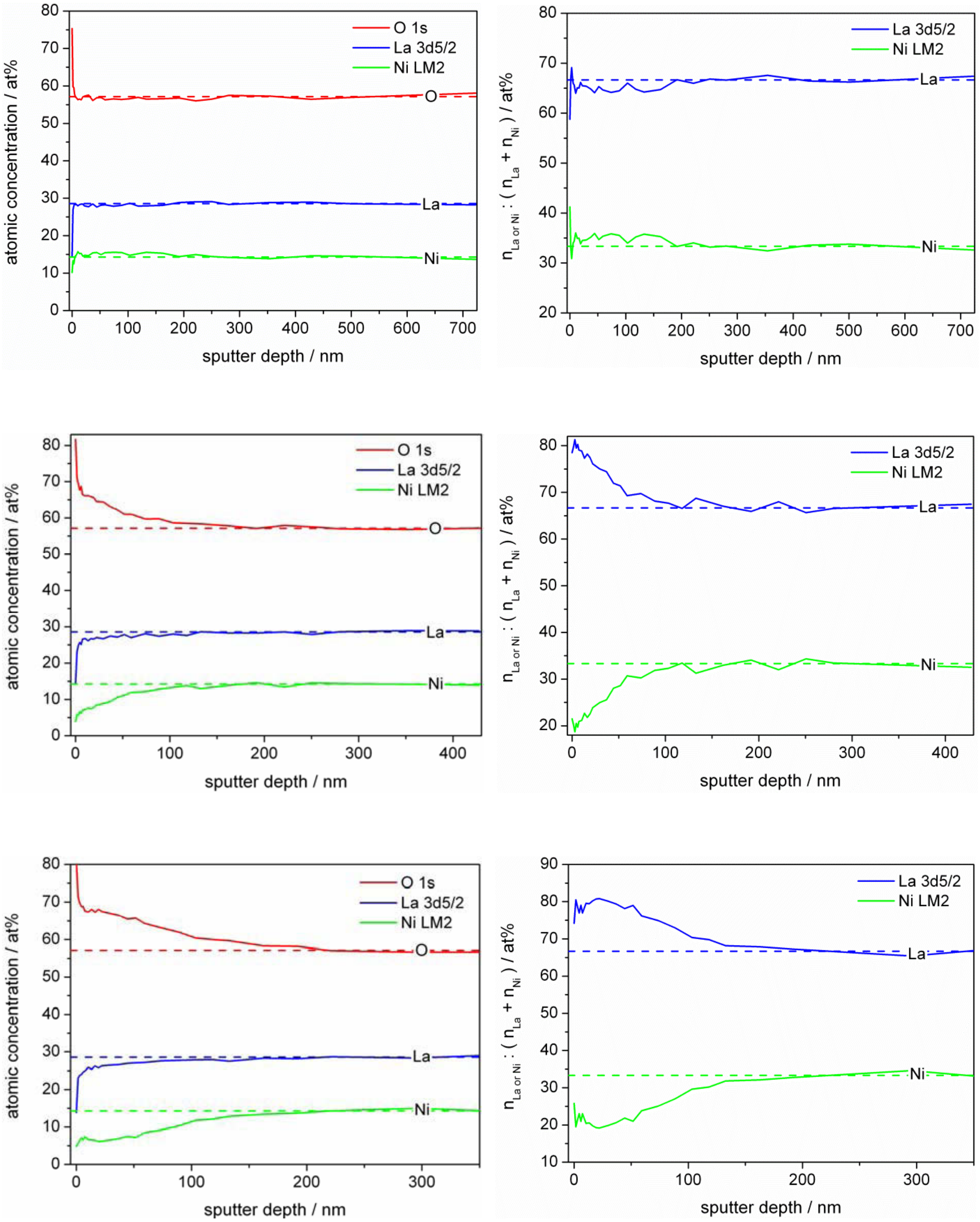

Fig. 4.27 XPS-depth profiles of $La_2NiO_{4+\delta}$: main components (left column) and distribution of the cations (right column) of the as-sintered sample (top row), after 1000 hours in dry atmosphere (middle row) and after 1000 additional hours in humid atmosphere (30% rel. humidity, bottom row) at 700°C and $pO_2 = 0.01$ bar. Dashed lines mark nominal compositions.

Similar observations have been made by a long-term study of $Nd_2NiO_{4+\delta}$ under dry conditions. The composition of the as-sintered Nd-nickelate is quite homogeneous throughout the profile except for the top 20 nm to the surface, where strong oxygen enrichment is observed which may originate from adsorption of H_2O in the ambient atmosphere before testing (Fig. 4.28, top row). After 1000 hours in a dry gas flow a 50 nm wide region below the surface has formed where Nd is enriched with respect to Ni (Fig. 4.28, middle row), similar to the results given above for $La_2NiO_{4+\delta}$. The chemically driven rare earth enrichment is expected to result from the higher thermodynamic stability of the corresponding oxides ($\Delta_f H^{\ominus}(Nd_2O_3) = -1808\ kJmol^{-1}$, $\Delta_f H^{\ominus}(La_2O_3) = -1794\ kJmol^{-1}$) in comparison to NiO ($\Delta_f H^{\ominus}(NiO) = -240\ kJmol^{-1}$) [237].

Despite such similar changes in surface composition at 700°C in dry Ar-O_2-mixtures, there are pronounced differences in the distributions of the cations between both nickelate compounds after annealing in humid atmospheres. While cation distributions in $La_2NiO_{4+\delta}$ under both dry and humid conditions show La-enrichment at the surface, a strong decrease in Nd-content was observed for $Nd_2NiO_{4+\delta}$ in humid atmospheres (Fig. 4.28, bottom row). The most striking feature is a dramatic decrease in the Nd:Ni ratio from 2:1 in non-degraded $Nd_2NiO_{4+\delta}$ to 1:1 in the near-surface region of the degraded sample. Beyond 300 nm depth, the nominal bulk composition is found. When approaching the sample surface, a Ni-depleted zone is crossed between 300 and 100 nm depth, while in the top 50 nm the Nd:Ni ratio approaches unity. This substantial surface reconstruction of $Nd_2NiO_{4+\delta}$ goes parallel with a strong decrease of k_{chem} in humid atmospheres (Fig. 4.26, right). Such discrepancy in the degradation behavior toward humidity is rather surprising considering the similarity of the investigated compounds. A detailed discussion of a possible degradation mechanism was presented by Egger et al. [238].

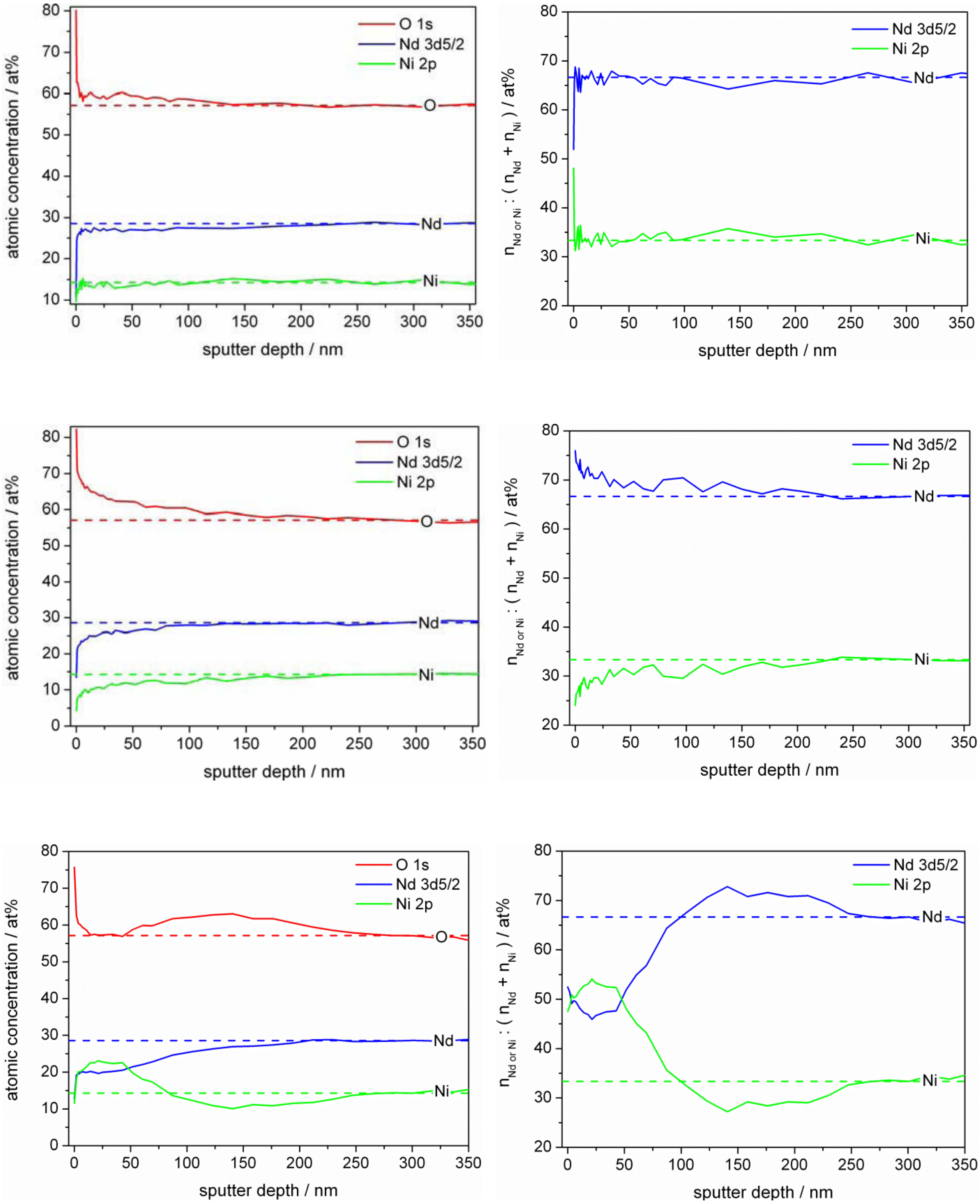

Fig. 4.28 XPS-depth profiles of $Nd_2NiO_{4+\delta}$: main components (left column) and distribution of the cations (right column) of the as-sintered sample (top row), after 1000 hours in dry atmospheres (middle row) and after 1000 additional hours in humid atmosphere (30% rel. humidity, bottom row) at 700°C and $pO_2 = 0.01$ bar. Dashed lines mark nominal compositions.

To obtain further insight into the degradation mechanisms in humid atmospheres, a $La_2NiO_{4+\delta}$-sample was subjected to a prolonged exposure to humid gas flows at an elevated humidity level of 75% over a period of 5000 hours. Fig. 4.29 shows the trend in the oxygen surface exchange rate over the whole testing period where data of the first 100 days are identical with those given in Fig. 4.26 (right). At the beginning the increase in water content of the gas phase caused a further reduction of k_{chem} but shortly afterwards the surface exchange activity started to recover. This was, however, caused by some experimental problems since the water level in the thermostatted bubbler flask, which was used to establish a defined pH_2O, was substantially lowered due to a high evaporation rate. Soon after replenishing distilled water in the bubbler k_{chem} started to decrease again and continued in such a way without reaching a plateau. Before concluding the long-term study dry O_2-Ar gas mixture was fed into the reactor which resulted in a strong increase in k_{chem}, thus showing the degradation to be at least partially reversible. After switching back to 75% rel. humidity degradation continued.

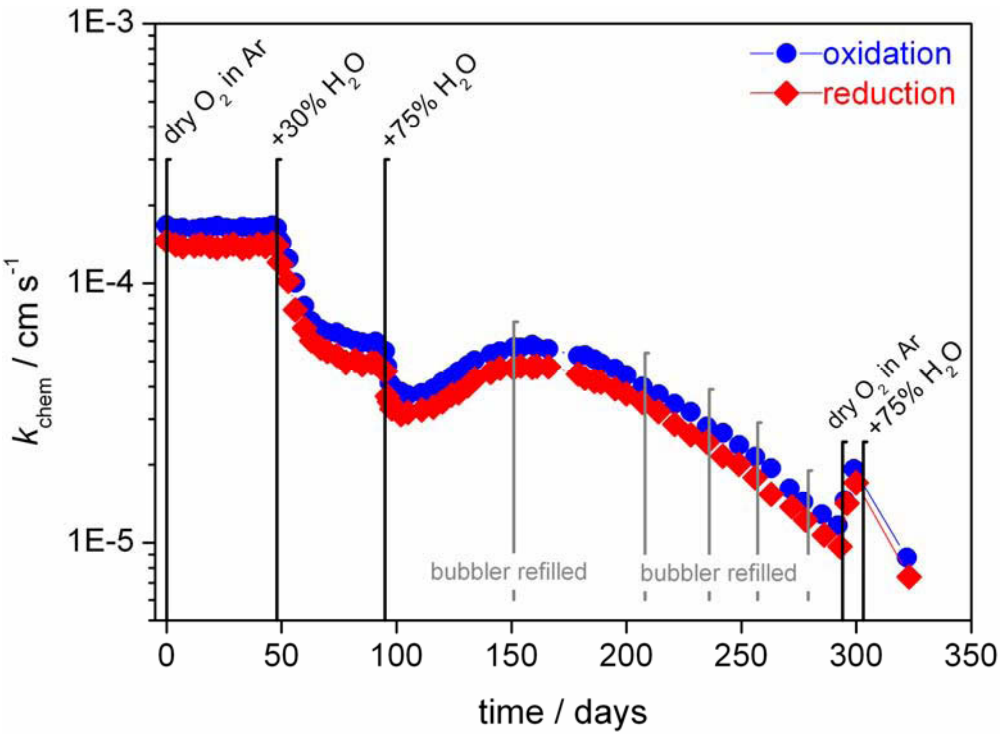

Fig. 4.29 Long-term measurements of $La_2NiO_{4+\delta}$ at 700°C and $pO_2 = 0.01$ bar in dry and humid atmospheres (30 and 75% humidity). For details see text.

After degradation under such harsh conditions the $La_2NiO_{4+\delta}$-sample was found to be covered by an opalescent layer (Fig. 4.30, left). The right picture of Fig. 4.30 was recorded with an optical 3D-surface microscope (Alicona InfiniteFocus), showing the peculiar surface pattern more clearly.

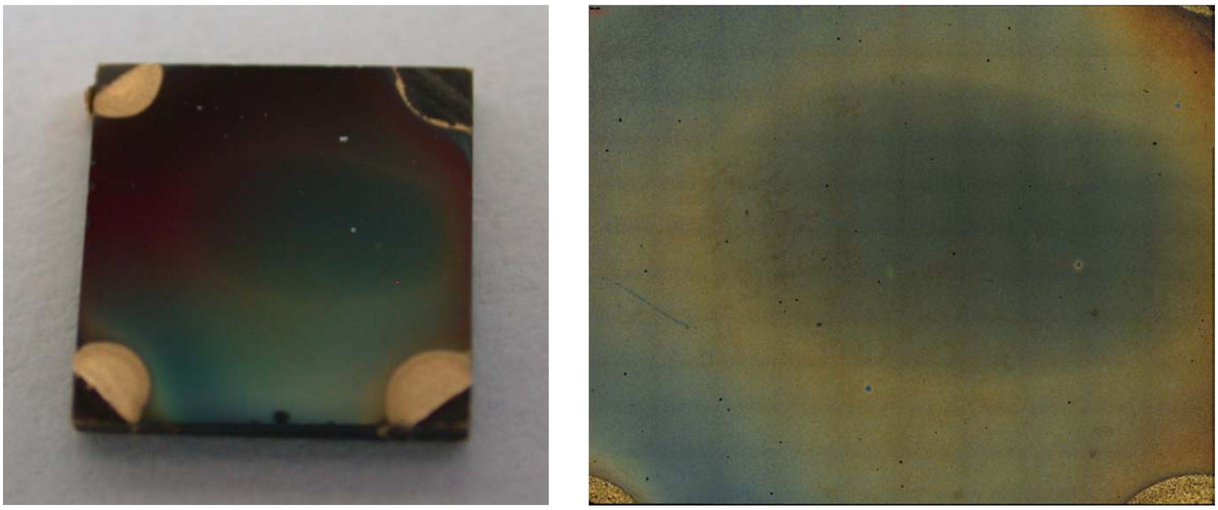

Fig. 4.30 Sample pictures of $La_2NiO_{4+\delta}$ after annealing for 5000 hours at 700°C in atmospheres with 75% relative humidity at $pO_2 = 0.01$ bar. The right picture was recorded with a 3D-surface microscope (Alicona InfiniteFocus).

The XPS-depth profile of the strongly degraded specimen shows essentially the same features as discussed above for a sample in 35% rel. humidity (Fig. 4.31). However, La-enrichment has progressed to such an extent that practically no nickel is present within the first 50 nm of the sample (Fig. 4.31, right). Furthermore, high amounts of carbon have been detected by XPS over the whole depth range. Apart from small amounts of Bi and Cd (not shown in Fig. 4.31) originating from the gold paste no further elements were detected in XPS-scans.

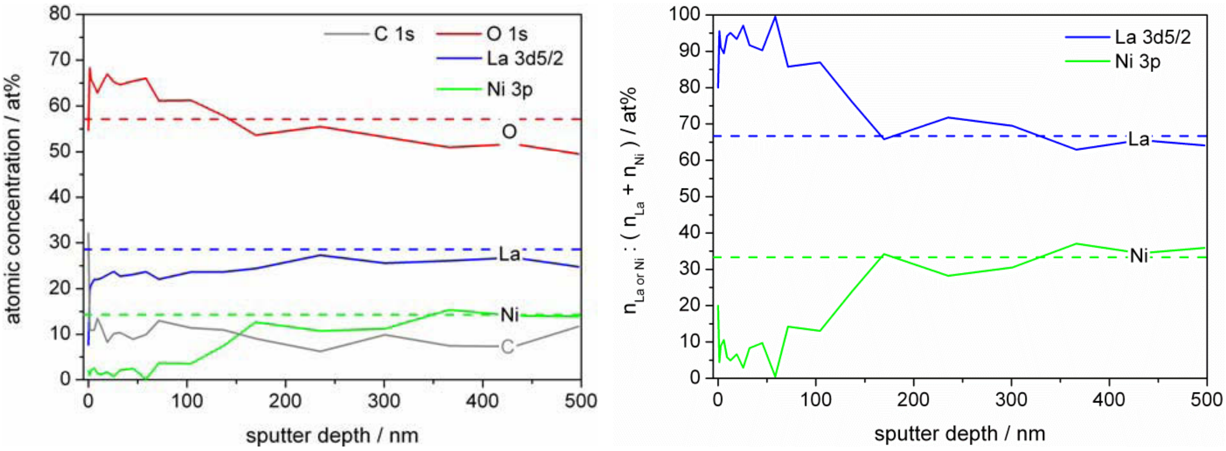

Fig. 4.31 XPS-depth profiles of $La_2NiO_{4+\delta}$ after annealing for 5000 hours in humid atmospheres (75% rel. humidity) at 700°C and pO_2 = 0.01 bar. Dashed lines mark nominal compositions.

The origin of the high amount of carbon determined by XPS is unclear. However, due to the excellent resistance against carbonate-formation (see below) it is rather unlikely that the carbon contamination is the source for the strong decrease in surface exchange kinetics. Rather, the pronounced La-enrichment and the concomitant Ni-depletion of the surface may account for the surface exchange deactivation. Obviously water plays an important role in the degradation mechanism but it is difficult to conclude from the XPS-results whether water is involved in the formation of secondary phases or if it acts as a catalyst for transport processes as was proposed by Egger et al. for $Nd_2NiO_{4+\delta}$ [238]. From a thermodynamic perspective it seems unlikely that oxides or oxy-hydroxides of Ni or La should form at temperatures as high as 700°C.

Further information was obtained from SEM/EDX-investigation and elemental distribution maps of a surface region of degraded $La_2NiO_{4+\delta}$. As shown in Fig. 4.32 besides the bulk elements and bismuth, Na and Si have been identified as surface contaminants. There appears to be some difficulty in determining Si from XPS-spectra which is due to the rather low detection sensitivity for silicon and the overlap of Si-peaks with those of Bi and La.

The presence of silicon on the sample is rather problematic and its detrimental effect on the cathode performance is well known [41,239-241]. The formation of a thin SiO_2-layer may well account for the decrease in oxygen exchange activity by blocking parts of the surface area. However, considering the high amount of La on the surface, the formation of Lasilicates such as $La_4(SiO_4)_3$ or $La_2Si_2O_7$ should be taken into account as well. Such mechanism was reported by Schuler et al. [50,51] for $Nd_2NiO_{4+\delta}$, where decline in cathode performance was caused by the formation of $Nd_4Si_3O_{12}$.

The silicon source is most likely the quartz reactor used for performing the conductivity relaxation measurements. The critical role of water is shown by the fact that the surface exchange rate of the nickelates remains perfectly stable in dry gas flows (see Fig. 4.26). Hence, water affects surface degradation rather indirectly by forming volatile gas species with Si such as $Si(OH)_4$ [242-244], thus permitting Si-poisoning of the material via gas phase transport and subsequent deposition on the sample surface. However, it is rather surprising to find the effect of Si-poisoning being reversible, which was observed for $La_2NiO_{4+\delta}$ when reverting to dry atmospheres (see Fig. 4.29).

Despite Si-poisoning being a rather unintended side effect in this study the results are still of relevance for fuel cell applications since there is a number of potential Si-sources in an SOFC-system like glass sealings [37], high temperature alloys [245] or other components [246].

It should be mentioned that an equally detailed investigation as given above for $La_2NiO_{4+\delta}$ was not performed for $Nd_2NiO_{4+\delta}$. Thus, no conclusive mechanism can be given for the degradation of $Nd_2NiO_{4+\delta}$ in humid atmospheres. Though it has not been confirmed in this work, it appears likely that Si-poisoning might account for the decrease in oxygen exchange activity for $Nd_2NiO_{4+\delta}$ as well. However, the observed surface composition of $Nd_2NiO_{4+\delta}$ with a Nd:Ni ratio close to unity is in strong contrast to findings for $La_2NiO_{4+\delta}$ under similar conditions and it is unclear whether this can be rationalized by the thermodynamic stability of silicate compounds of La, Nd and Ni.

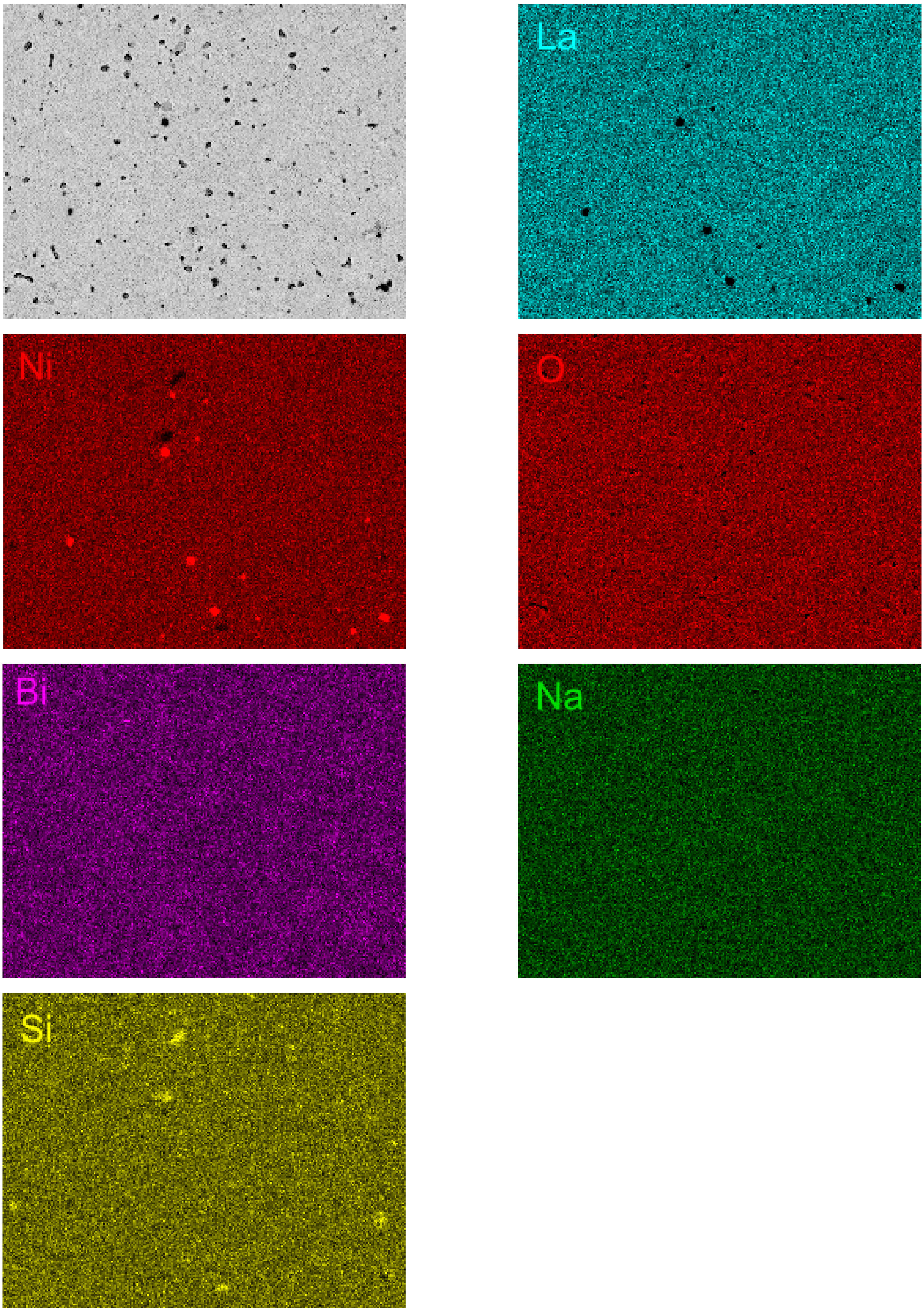

Fig. 4.32 EDX-elemental distribution maps of strongly degraded $La_2NiO_{4+\delta}$ kept at 700°C and an oxygen partial pressure of 0.01 bar for 5000 hours in atmospheres with 75% rel. humidity. The top left picture shows a SEM-image of the selected surface region (width 108.8 µm, magnification 1000×).

4.3.3 Chemical stability against CO_2

Stability of $La_2NiO_{4+\delta}$ and $Nd_2NiO_{4+\delta}$ against carbonate formation was examined by exposing the material to an Ar-O_2-mixture containing 5 vol% CO_2. For measuring the electronic conductivity and the oxygen surface exchange coefficient, the gas flows were switched between oxygen partial pressures of 0.01 and 0.015 bar in argon. Electronic conductivities of both nickelates at 700°C are close to those measured during degradation in humid atmospheres (Fig. 4.26, left) and remain virtually constant during the entire period of investigation (Fig. 4.33, left). Likewise, no effect of CO_2 on the oxygen surface exchange coefficient of $La_2NiO_{4+\delta}$ is observed and a similar investigation for $Nd_2NiO_{4+\delta}$ also shows only a very small impact of CO_2 on the surface exchange process (Fig. 4.33, right).

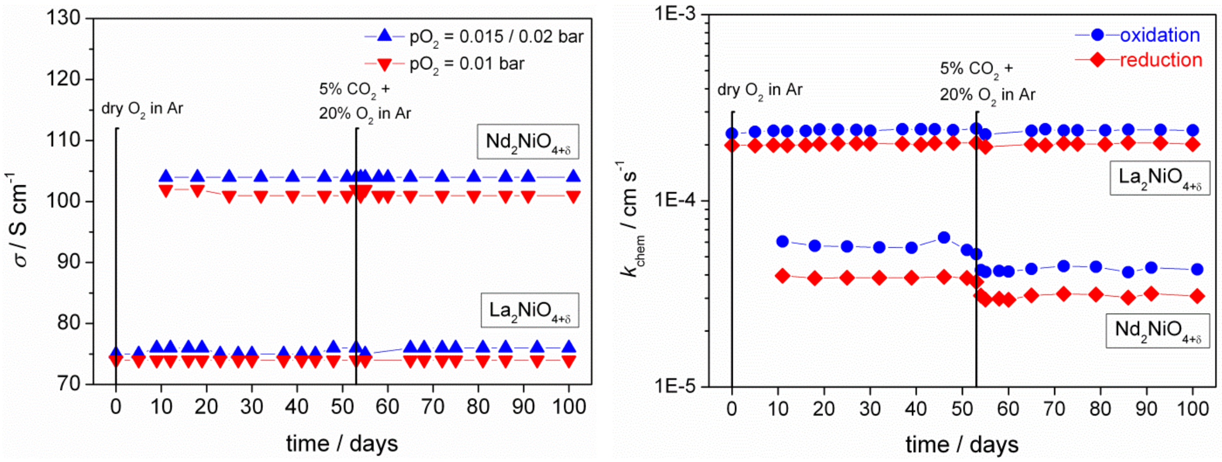

Fig. 4.33 Electronic conductivity (left) and chemical surface exchange coefficients of oxygen (right) of $La_2NiO_{4+\delta}$ and $Nd_2NiO_{4+\delta}$ at 700°C and $pO_2 = 0.01$ bar in CO_2-free and CO_2-enriched atmospheres (5 vol% CO_2).

XPS-depth profiles determined for $La_2NiO_{4+\delta}$ after 1000 hours in CO_2-rich atmosphere are very similar to those under dry conditions (Fig. 4.34) which confirms the excellent resistance against carbonate formation resulting from the absence of alkaline earths in the materials. High CO_2-tolerance of $La_2NiO_{4+\delta}$ has also been reported by other authors [247,248].

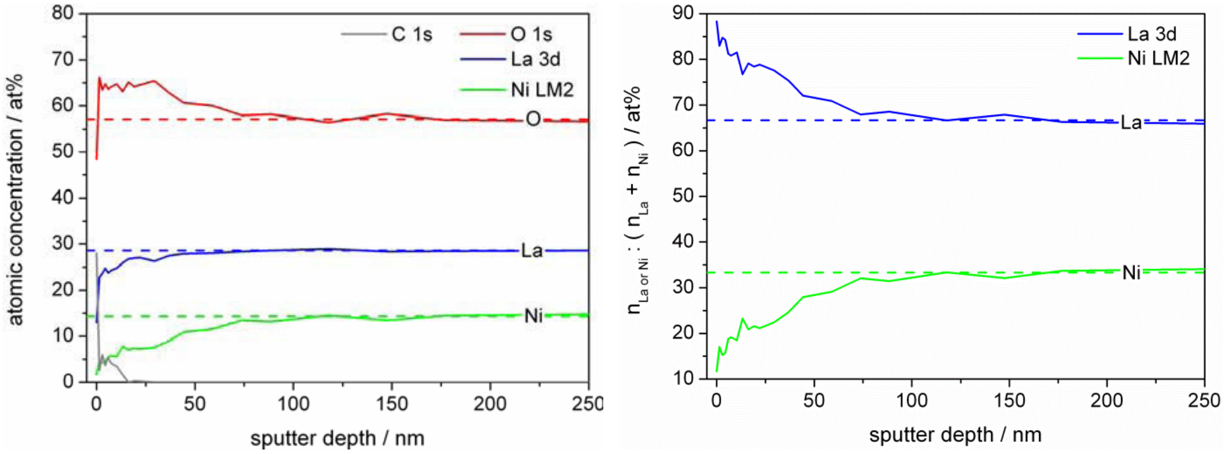

Fig. 4.34 XPS-depth profiles of $La_2NiO_{4+\delta}$ of the main components (left) and cation fractions (right) after 1000 hours in CO_2-containing atmosphere (5 vol% CO_2) at 700°C and $pO_2 = 0.2$ bar. Dashed lines mark nominal compositions.

Post-test XPS-surface investigations of CO_2-treated $Nd_2NiO_{4+\delta}$ evidence a rather small influence of CO_2 on the elemental distribution in the top 200 nm zone (Fig. 4.35). However, in the immediate surface layer there appears to be a slight local enrichment of Ni which is contrary to the trend for the oxygen-exposed specimen (Fig. 4.28). The small variation in composition is not directly related to a reaction with CO_2 because the carbon level drops below the detection limit within the first few nanometer of the surface. Since the surface exchange rate was hardly affected by CO_2-enriched atmospheres in the investigated time interval no further investigations were performed. It is, however, interesting to find again that the change in surface composition of $Nd_2NiO_{4+\delta}$ after long-term degradation measurements is significantly different from its La-analogue, though less pronounced as in the case of degradation in humid atmospheres and with much less effect on the surface exchange kinetics.

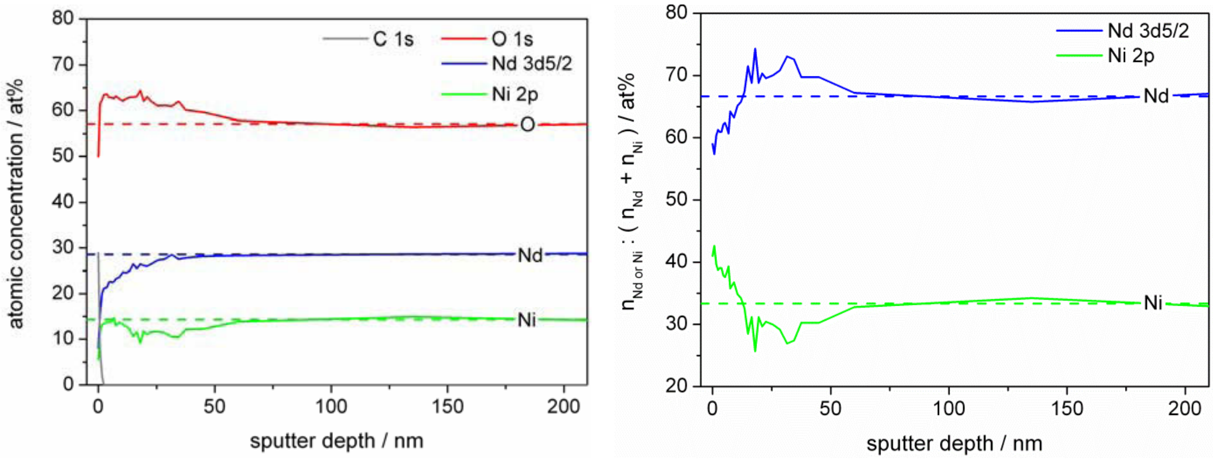

Fig. 4.35 XPS-depth profiles of $Nd_2NiO_{4+\delta}$ of the main components (left) and cation fractions (right) after 1000 hours in CO_2-containing atmosphere (5 vol% CO_2) at 700°C and pO_2 = 0.2 bar. Dashed lines mark nominal compositions.

A good stability of undoped nickelates against carbon formation is not surprising due to the absence of alkaline earth ions since alkaline earths are well known to readily form carbonates. A prominent example is $(Ba,Sr)(Co,Fe)O_{3-\delta}$ which has been proposed as cathode material for IT-SOFCs [249] but features, among other disadvantages, a strong tendency for carbonate formation below 800°C [35,250].

To assess the thermodynamic stability of unsubstituted nickelates against CO_2, experimental results of $La_2NiO_{4+\delta}$ were complemented by thermodynamic modeling. Predominance diagrams for gas atmospheres containing varying amounts of O_2 and CO_2 at 600 and 700°C and $pH_2O \approx 30$ mbar have been calculated using FactSage v6.2 [251]. Thermodynamic values for $La_2NiO_{4+\delta}$ were taken from Zinkevich et al. [129,132], data for La-oxycarbonate was obtained from Shirsat et al. [252]. Results from thermodynamic modeling show that $La_2NiO_{4+\delta}$ is expected to react with CO_2 above a pCO_2 of ≈ 0.01 bar at 600°C (Fig. 4.36, left) forming $La_2O_2(CO_3)_2$ and NiO. The equilibrium pCO_2 is slightly shifted to a higher value when increasing the temperature to 700°C (Fig. 4.36, right). Thus, a concentration of 5 vol% CO_2 in gas mixtures as used for degradation measurements appears to be close to the stability limit of $La_2NiO_{4+\delta}$ at 700°C. However, such high concentrations of carbon dioxide are not to be expected at the cathode side of a SOFC under real operating conditions since the CO_2-content of ambient air ranges between 0.03 and 0.04 vol% (300-400 ppmv). Hence, sufficient stability of $La_2NiO_{4+\delta}$ against CO_2 is confirmed from a thermodynamic point of view for SOFC-applications. The situation might be different when using nickelates as oxygen-conducting membranes in oxyfuel and oxycoal processes where recirculated gas streams contain high amounts of CO_2.

In the case of Nd-nickelate a similar thermodynamic analysis was not possible due to the lack of thermodynamic data for carbonate compounds.

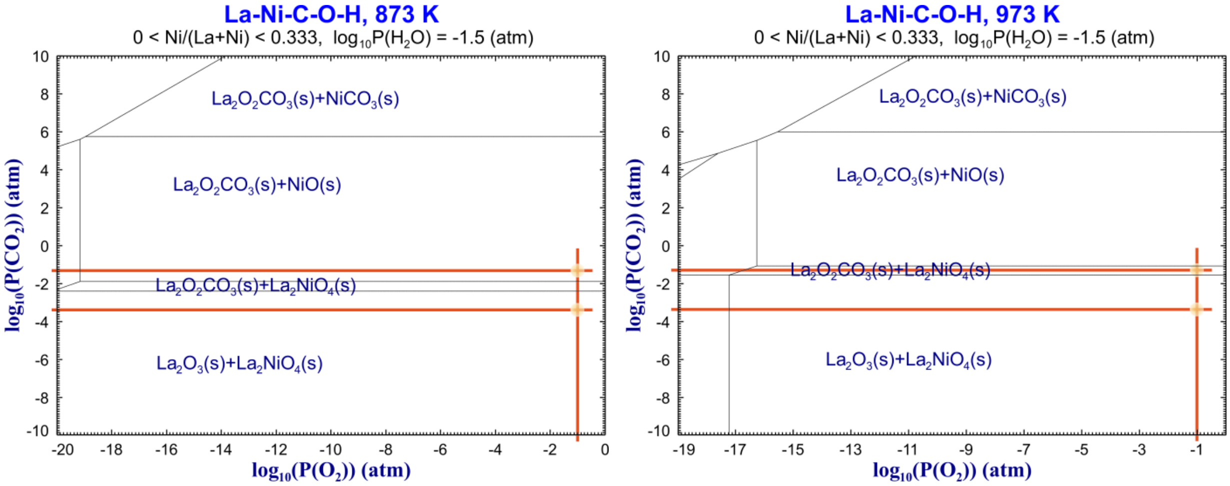

Fig. 4.36 Predominance diagrams for $La_2NiO_{4+\delta}$ in an O_2/CO_2-atmosphere at 600°C (left) and 700°C (right). The water partial pressure was set to 0.032 atm. A secondary phase of La_2O_3 is included in the diagrams due to requirements of the FactSage® software. Partial pressures corresponding to 0.04 and 5 vol% CO_2 as well as a pO_2 of 0.1 bar are marked by orange lines.

4.3.4 Sulfur tolerance of $La_2NiO_{4+\delta}$

Ambient air contains between 1 and 100 ppbv SO_2. High SO_2-concentrations can be found in world regions with strong air pollution such as industrial areas in countries with low environmental standards or ocean lanes with heavy shipping traffic. Despite the small SO_2-concentrations, SOFC-air electrodes can accumulate sulfur on the surface which may gradually deteriorate cathode performance. For perovskite-type cathode materials like $(La,Sr)CoO_{3-\delta}$, $(La,Sr)(Co,Fe)O_{3-\delta}$ and $(Sm,Sr)CoO_{3-\delta}$ the deteriorating effect of sulfur has been demonstrated by several authors and has been ascribed to the formation of $SrSO_4$ [39,40,253-255]. Nickelate compounds may thus offer higher sulfur tolerance due to the absence of alkaline earths. On the other hand the well-known affinity of nickel to sulfur might make nickelate compounds susceptible to sulfur poisoning. Engels et al. [248] investigated the effect of SO_2 on the oxygen flux rate through $La_2NiO_{4+\delta}$-membranes and found an almost complete break-down of oxygen permeation after adding 360 ppm SO_2 to the sweep gas. Sulfur-containing compounds were detected on the nickelate surface by EDX but the phase composition could not be identified.

In this work the effect of sulfur on the surface exchange coefficient of $La_2NiO_{4+\delta}$ was studied at 700°C by adding 50 ppm SO_2 to the gas stream. Reference measurements in sulfur-free atmospheres at 700°C and $pO_2 = 0.1$ bar showed excellent stabilities of the electronic conductivity and surface exchange rate over 1000 hours. However, after switching to a SO_2-containing gas flow, the contact resistances of the $La_2NiO_{4+\delta}$-sample drastically increased from sub-ohmic range to several MΩ which rendered electrical measurements impossible. After 1000 hours in SO_2-containing atmospheres the sample surface was investigated by XPS and a high level of sulfur was found extending to depths of around 400 nm (Fig. 4.37, left). Surprisingly, the topmost 50 nm were found to be completely free of any nickel, thus contradicting assumptions about the formation of Ni-S compounds (Fig. 4.37, right). XPS-measurements were complicated by surface charging due to the insulating surface layer of the sulfur-degraded sample consisting mainly of lanthanum, oxygen and sulfur.

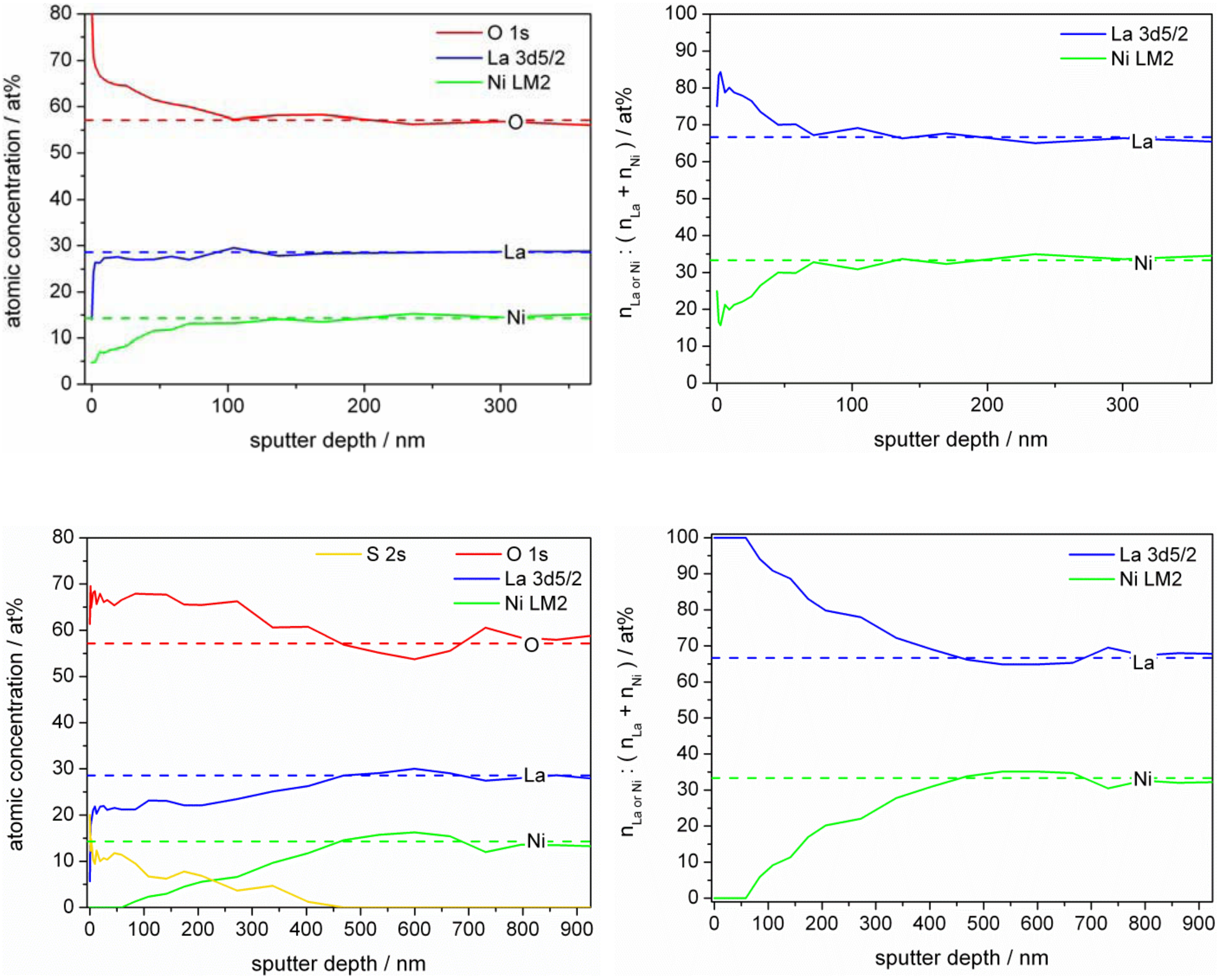

Fig. 4.37 XPS-depth profiles of La$_2$NiO$_{4+\delta}$ of the main components (left) and cation fractions (right) after 1000 hours in a pure O$_2$-Ar gas flow (10 vol% O$_2$, top row) and after additional 1000 hours in an SO$_2$-containing atmosphere (50 ppm SO$_2$, bottom row) at 700°C. Dashed lines indicate nominal compositions.

Elemental distribution maps of the SO$_2$-degraded compound have been recorded by SEM/EDX and confirm the presence of sulfur as a continuous layer on the sample surface (Fig. 4.38). Despite the complete absence of nickel in the topmost 50 nm (Fig. 4.37), Ni is identified by elemental mapping since the penetration depth of the electron beam is ca. 1 µm at 20 kV acceleration voltage.

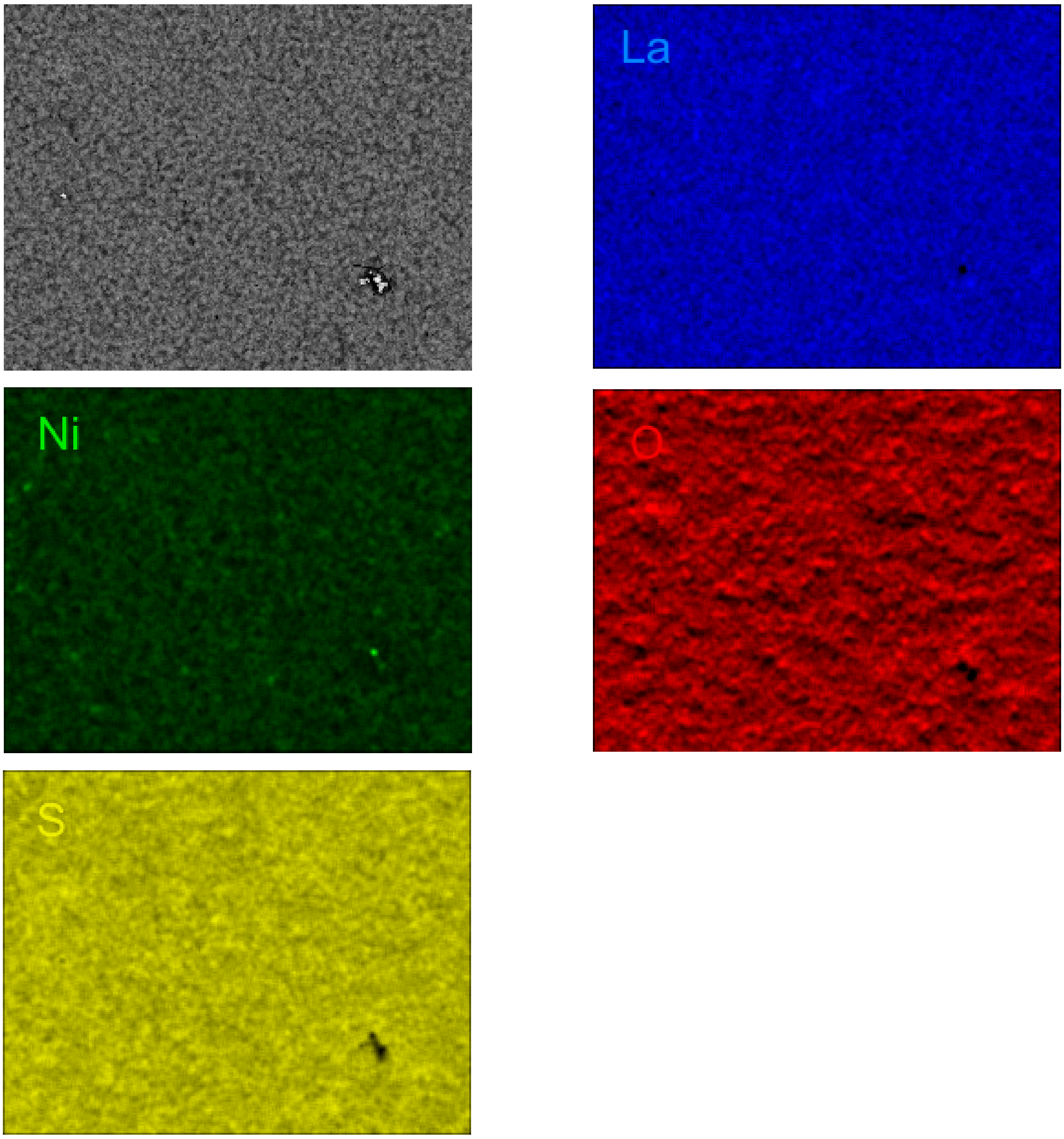

Fig. 4.38 EDX-elemental distribution maps of sulfur-exposed $La_2NiO_{4+\delta}$ annealed at 700°C and $pO_2 = 0.1$ bar for 1000 hours in atmospheres with 50 ppm SO_2. The top left picture shows a backscatter SEM-image of the selected surface region (width 108.8 µm, magnification 1000×).

Further details of the surface modification were obtained from TEM/EDX measurements. Fig. 4.39 (left) shows the TEM-picture of a FIB-lamella cut from the surface of the SO_2-degraded sample. Below the Pt-layer (sputtered for preparation purposes) a rather dense degradation layer of approx. 1 µm thickness is visible, followed by a more dispersed degradation zone where individual particles can be discerned. A magnified view of the marked region is presented in the right picture of Fig. 4.39 which shows the formation of crystals embedded in the light-gray $La_2NiO_{4+\delta}$ parent phase. Judging from differences in the material contrast the dark-grey inclusions have a lower average atomic number than the nickelate matrix.

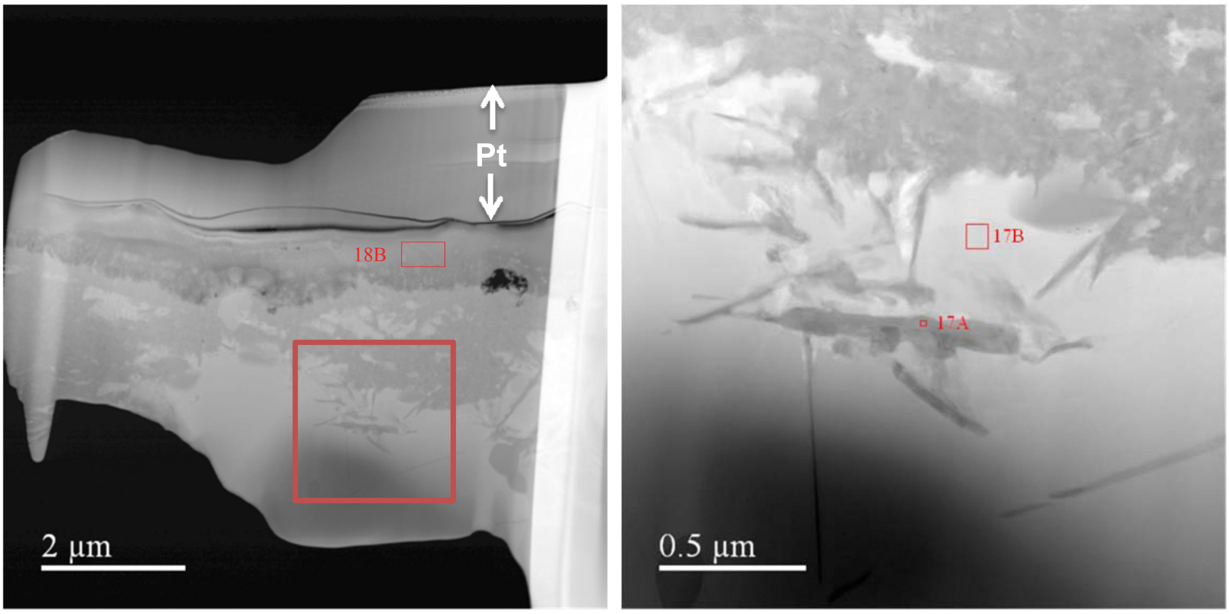

Fig. 4.39 STEM-HAADF-pictures of a $La_2NiO_{4+\delta}$-surface after 1000 hours in 50 ppm SO_2 at 700°C. A protection layer of Pt has been deposited on the sample surface for preparation of the FIB-lamella. The region marked by a red square in the left picture is reproduced on the right. Areas labeled 17A, 17B and 18B have been analyzed by EDX (see below).

EDX-analyses have been performed on positions labeled 17A, 17B and 18B in Fig. 4.39. The EDX-spectrum of the light-gray phase (17B) is given in Fig. 4.40 and corresponds to the nickelate compound (La:Ni:O ≈ 2:1:4). Additional peaks of Fe and Co originate from the interior lining of the microscope, while the Cu-signal is caused by the sample holder. No sulfur can be detected in the $La_2NiO_{4+\delta}$-phase.

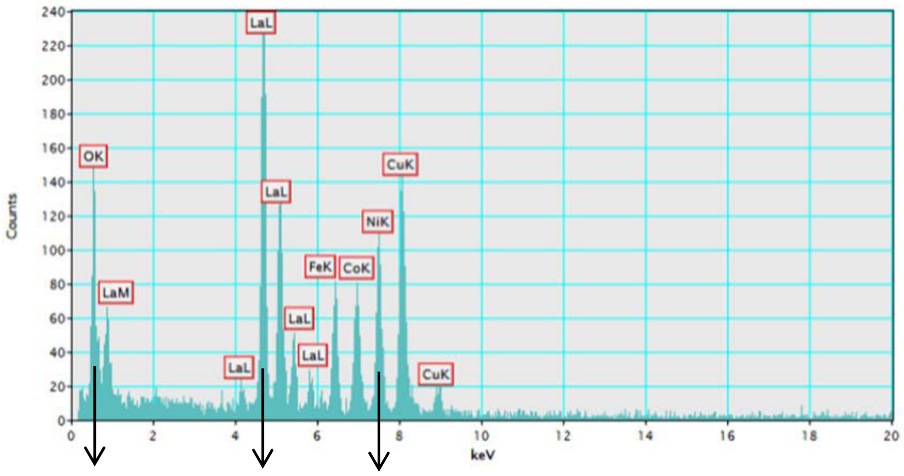

17B	net counts	k-factor (Si)	wt%	at%	rel. at%
La-L	2165	3.671	69.87	28.78	1.00
Ni-K	1048	1.525	14.05	13.70	0.48
O-K	859	2.13	16.08	57.52	2.00

Fig. 4.40 EDX-spectrum of point 17B in Fig. 4.39. Quantitative analysis is in good agreement with the nominal composition of La$_2$NiO$_{4+\delta}$. Fe/Co-peaks and Cu-signals are caused by the microscope interior and sample holder, respectively.

According to EDX-spectra of the immediate surface layer and ~2 µm below the sample surface (areas 18B and 17A in Fig. 4.39) the degradation phases consist of La, S and O with appreciable amounts of sulfur while nickel is practically absent, in agreement with results obtained from XPS-analysis. Quantitative evaluation of the La- and S-signals shows the surface layer to contain a sulfur-rich compound with equimolar contents of lanthanum and sulfur (Fig. 4.41, left). Further down below the sample surface the decomposed phase appears to be less rich in sulfur and a La:S-ratio of roughly 2:1 is obtained (Fig. 4.41, right). This is to be expected considering that sulfur is supplied from the gas phase and has to diffuse into the material. There appears to be a rather sharp boundary between the sulfur-rich and the sulfur-poor degradation phases as can be appreciated from the material contrast in Fig. 4.39 (left) where the darker shading of the surface layer indicates lower content of the heavy element lanthanum.

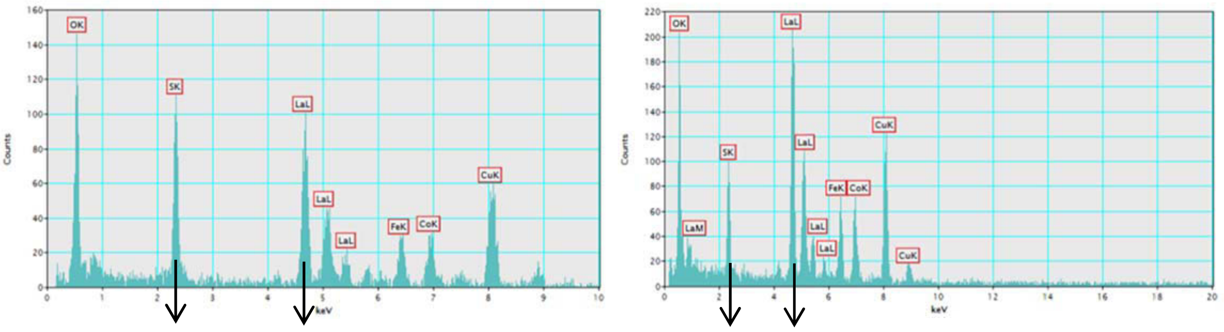

18B	net counts	k-factor (Si)	wt%	at%	rel. at%
La-L	794	3.671	81.35	50.18	1.00
S-K	653	1.023	18.65	49.82	0.99

17A	net counts	k-factor (Si)	wt%	at%	rel. at%
La-L	1988	3.671	90.86	69.64	1.00
S-K	718	1.023	9.14	30.36	0.44

Fig. 4.41 EDX-spectra of points 18B (left) and 17A (right) in Fig. 4.39. Signals of La, S and O have been identified while Ni-K peaks around 7.5 keV are practically absent. Fe/Co-peaks and Cu-signals are caused by the microscope interior and sample holder, respectively.

Further insight into possible reaction products was gained from calculated predominance diagrams of the system La-Ni-S-O-H based on partial pressures of O_2 and SO_2 at 600 and 700°C. Thermodynamic data for the sulfate and oxysulfate of lanthanum have been added to the FactSage database based on results reported by Kellogg [256] and Grizik et al. [257].

Fig. 4.42 shows that even at very low partial pressures of SO_2 the formation of thermodynamically stable degradation products is to be expected. Although the exact position of phase boundaries in the diagram may be inaccurate due to poor data quality for the La-sulfate phases, the main features are supposed to be correct. Consistent with findings from XPS- and TEM/EDX-analyses, SO_2 reacts preferentially with the La-component, forming $La_2O_2SO_4$ and $La_2(SO_4)_3$ at lower pSO_2. Ni appears to be involved only at higher sulfur contents forming $NiSO_4$. Hence, sulfur poisoning is to be taken into account for long-term operation of an IT-SOFC when using untreated ambient air as oxidation gas.

Establishing a correlation between thermodynamics and quantitative EDX-results is difficult because it is unclear whether the degradation products correspond to equilibrium phases. The identity of the compound in the surface layer (18B in Fig. 4.39) with a roughly equimolar La-S-ratio is unknown, it might be a mixture of different compounds or an intermediate phase on the transformation path to $La_2(SO_4)_3$, which is the expected reaction product according to the predominance diagram at 700°C. The sulfur-containing phase further down below the surface

(17A in Fig. 4.39) shows a La:S-ratio of 2:1 and might thus correspond to the oxysulfate $La_2O_2SO_4$.

A comparison of both predominance diagrams in Fig. 4.42 shows that by increasing the temperature from 600°C to 700°C the stability region of $La_2NiO_{4+\delta}$ is expanded and the onset of La-oxysulfate formation is shifted to higher pSO$_2$. A similar observation has been made with respect to carbonate formation, though to a somewhat smaller extent (Fig. 4.36). Thus, from a thermodynamic viewpoint, the decrease in operating temperature for IT-SOFCs favors the formation of reaction products with minor constituents in ambient air. Of course, besides such purely thermodynamic considerations kinetic aspects have to be taken into account as well.

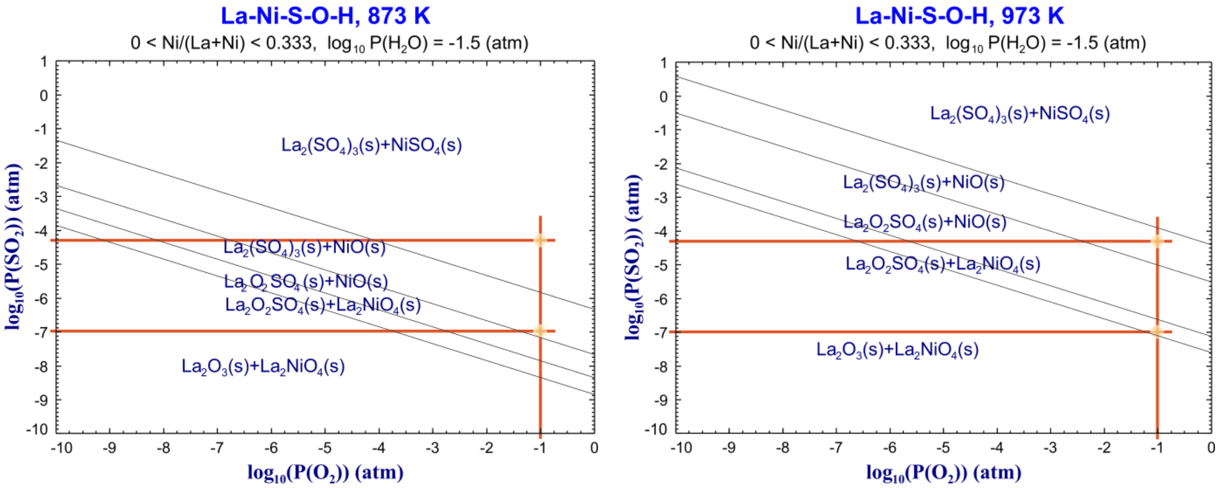

Fig. 4.42 Predominance diagrams for $La_2NiO_{4+\delta}$ in an SO_2-containing atmosphere at 600°C (left) and 700°C (right). A water partial pressure of 0.032 atm was assumed. Secondary phases of La_2O_3 are included in the diagrams due to requirements of the FactSage® software. Partial pressures corresponding to 100 ppb and 50 ppm SO_2 as well as a pO_2 of 0.1 bar are marked by orange lines.

Calculating the La-Ni-S-O-H predominance diagram for 800°C indicates that at this temperature a SO_2-degraded cathode might be regenerated or sulfur poisoning may be prevented altogether assuming SOFC-operation with highly polluted ambient air containing 100 ppb SO_2 (Fig. 4.43).

Although the focus is put on SOFC-applications in this work, the above findings might also be relevant for membrane applications as for example in oxycoal combustion processes where the ceramic membrane may be in contact with recirculated flue gas containing elevated levels of SO_2.

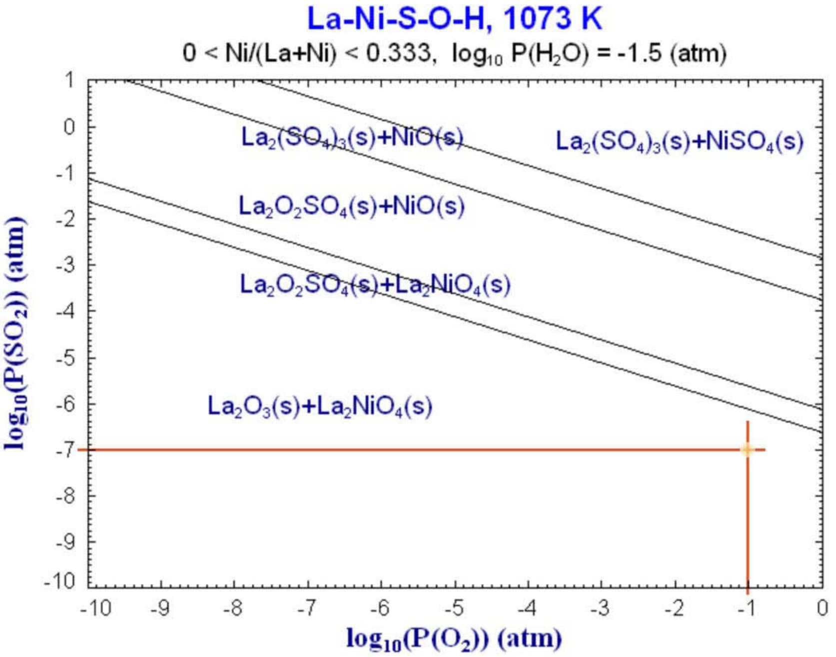

Fig. 4.43 Predominance diagram for $La_2NiO_{4+\delta}$ in SO_2-containing atmospherea at 800°C assuming a water partial pressure of 0.032 atm. Secondary phases of La_2O_3 are included in the diagrams due to requirements of the FactSage® software. A SO_2-partial pressure corresponding to 100 ppb SO_2 as well as a pO_2 of 0.1 bar are marked by orange lines.

5 Summary and conclusions

Within this work unsubstituted rare-earth nickelates have been investigated with respect to fundamental material properties and long-term stability relevant for application as SOFC-cathodes. External parameters such as temperature, oxygen partial pressure and gas phase impurities were adjusted to represent conditions expected in real intermediate temperature SOFCs. Long-term degradation experiments have been performed for at least 1000 hours to allow a reliable interpretation and a meaningful extrapolation to longer periods of operation. Although emphasis was put on the application of nickelates as SOFC-cathodes, the results may also be transferred to other applications as for example ceramic membranes used for oxygen separation. As a working hypothesis of this thesis it was assumed that the absence of alkaline earth elements in the investigated materials might be beneficial with respect to long-term stability under realistic IT-SOFC operating conditions. Thus, investigations were limited to $La_2NiO_{4+\delta}$, $Pr_2NiO_{4+\delta}$ and $Nd_2NiO_{4+\delta}$ as these compounds do not require partial substitution with alkaline earths or other elements to obtain phase-pure structures. Despite showing very promising results with respect to oxygen exchange kinetics, $Pr_2NiO_{4+\delta}$ was not further investigated in long-term degradation experiments due to its poor phase stability under IT-SOFC operating conditions.

The conductivity relaxation method has been proven as a useful method for determining oxygen transport parameters as well as for monitoring degradation phenomena occurring on the sample surface in various atmospheres. Two sample geometries with different contacting schemes have been employed in relaxation measurements, where appropriate sample and contact designs are necessary to ensure specific diffusion patterns within the sample required for a correct modeling of the oxygen exchange process. Particular caution was necessary when transferring models developed for weight relaxation measurements to conductivity relaxation experiments. Ag-coated samples of $La_2NiO_{4+\delta}$ and $Nd_2NiO_{4+\delta}$ were used to obtain reliable values for chemical diffusion coefficients. The conductivity relaxation method was also successfully employed for the investigation of long-term degradation phenomena. In this case, diffusion coefficients are assumed to be of less importance for characterizing degradation processes, which are expected to affect primarily the immediate sample surface.

The investigated materials showed excellent stability against carbonate formation in CO_2-rich atmospheres. Detrimental effects of water on the oxygen exchange kinetics of $La_2NiO_{4+\delta}$ turned out to be caused by silicon poisoning, where the quartz reactor is assumed to act as silicon source. The observed partial reversibility of H_2O-degradation after switching to dry atmospheres shows that it is probably not solely a Si-effect, which is expected to be completely irreversible under dry conditions. Separating the effects of H_2O-degradation from silicon-poisoning would require reactors made from inert materials like alumina. However, combined H_2O/Si-poisoning does quite accurately represent the conditions expected on the cathode side of a SOFC operated with undried ambient air, since stack components such as glass sealings or special alloys may act as silicon sources as well. The oxygen exchange performance of $La_2NiO_{4+\delta}$ was found to be strongly affected by SO_2 in the surrounding gas atmosphere. Analytical investigations showed the formation of a rather dense and electrically insulating sulfate reaction layer covering the sample surface after prolonged SO_2-exposition.

Degradation investigations were complemented by thermodynamic modeling based on available literature data. In all cases thermodynamic calculations clearly showed that a decrease in temperature also reduces the extent of the stability regions of the investigated materials against minor constituents in the atmosphere. Thus, the current trend in SOFC-development to lower operating temperatures – offering significant advantages with respect to metallic interconnects – appears to rather favor the formation of reaction products with contaminants at the cathode side when using ambient air as oxidant.

6 References

[1] M.A. Laguna-Bercero, J. Power Sources 203 (2012) 4-16.

[2] M. Zahid, J. Schefold, A. Brisse, *High-Temperature Water Electrolysis Using Planar Solid Oxide Fuel Cell Technology: a Review*, in Hydrogen Energy, D. Stolten, Editor, p. 227-242, WILEY-VCH, Weinheim (2010).

[3] G.P.G. Corre, J.T.S. Irvine, *High-Temperature Fuel Cell Technology*, in Hydrogen and Fuel Cells, D. Stolten, Editor, p. 61-87, Wiley-VCH, Weinheim (2010).

[4] M. Gasik, *Materials for fuel cells*, CRC Press, Boca Raton (2008).

[5] K.V. Kordesch, J. Electrochem. Soc. 125 (1978) 77C-88C.

[6] EG&G Technical Services Inc., *Fuel Cell Handbook*, 7th edition, U.S. Department of Energy, Office of Fossil Energy, National Energy Technology Laboratory, Morgantown, West Virginia (2004).

[7] E. Baur, H. Preis, Z. Elektrochem. 43 (1937) 727-732.

[8] H.H. Mobius, J. Solid State Electrochem. 1 (1997) 2-16.

[9] S.C. Singhal, Solid State Ionics 135 (2000) 305-313.

[10] M. Stanislowski, E. Wessel, K. Hilpert, T. Markus, L. Singheiser, J. Electrochem. Soc. 154 (2007) A295-A306.

[11] T.H. Etsell, S.N. Flengas, Chem. Rev. 70 (1970) 339-376.

[12] F.J. Gardner, M.J. Day, N.P. Brandon, M.N. Pashley, M. Cassidy, J. Power Sources 86 (2000) 122-129.

[13] F.G.E. Jones, P.A. Connor, A.J. Feighery, J. Nairn, J. Rennie, J.T.S. Irvine, J. Fuel Cell Sci. Technol. 4 (2007) 138-142.

[14] B.C.H. Steele, A. Heinzel, Nature 414 (2001) 345-352.

[15] B.C.H. Steele, Solid State Ionics 134 (2000) 3-20.

[16] S.C. Singhal, Solid State Ionics 152–153 (2002) 405-410.

[17] S.C. Singhal, K. Kendall, *High temperature solid oxide fuel cells: fundamentals, design and applications*, Elsevier Advanced Technology, The Boulevard, Langford lane, Kidlington, Oxford, UK, (2004).

[18] R. Barfod, A. Hagen, S. Ramousse, P.V. Hendriksen, M. Mogensen, Fuel Cells 6 (2006) 141-145.

[19] S. de Souza, S.J. Visco, L.C. De Jonghe, Solid State Ionics 98 (1997) 57-61.

[20] C. Sun, R. Hui, J. Roller, J. Solid State Electrochem. 14 (2010) 1125-1144.

[21] Y. Takeda, R. Kanno, M. Noda, Y. Tomida, O. Yamamoto, J. Electrochem. Soc. 134 (1987) 2656-2661.

[22] A. Weber, E. Ivers-Tiffée, J. Power Sources 127 (2004) 273-283.

[23] D.E. Vladikova, Z.B. Stoynov, A. Barbucci, M. Viviani, P. Carpanese, J.A. Kilner, S.J. Skinner, R. Rudkin, Electrochim. Acta 53 (2008) 7491-7499.

[24] S.B. Adler, Solid State Ionics 111 (1998) 125-134.

[25] S.B. Adler, J.A. Lane, B.C.H. Steele, J. Electrochem. Soc. 143 (1996) 3554-3564.

[26] E. Boehm, J.M. Bassat, P. Dordor, F. Mauvy, J.C. Grenier, P. Stevens, Solid State Ionics 176 (2005) 2717-2725.

[27] L.P. Sun, Q. Li, H. Zhao, L.H. Huo, J.C. Grenier, J. Power Sources 183 (2008) 43-48.

[28] F. Mauvy, C. Lalanne, J.M. Bassat, J.C. Grenier, H. Zhao, P. Dordor, P. Stevens, J. Eur. Ceram. Soc. 25 (2005) 2669-2672.

[29] V.V. Kharton, A.V. Kovalevsky, M. Avdeev, E.V. Tsipis, M.V. Patrakeev, A.A. Yaremchenko, E.N. Naumovich, J.R. Frade, Chem. Mater. 19 (2007) 2027-2033.

[30] M. Al Daroukh, V.V. Vashook, H. Ullmann, F. Tietz, I. Arual Raj, Solid State Ionics 158 (2003) 141-150.

[31] S.P. Simner, M.D. Anderson, M.H. Engelhard, J.W. Stevenson, Electrochem. Solid-State Lett. 9 (2006) A478-A481.

[32] M. Kubicek, A. Limbeck, T. Fromling, H. Hutter, J. Fleig, J. Electrochem. Soc. 158 (2011) B727-B734.

[33] O. Yamamoto, Y. Takeda, R. Kanno, M. Noda, Solid State Ionics 22 (1987) 241-246.

[34] A. Mai, V.A.C. Haanappel, S. Uhlenbruck, F. Tietz, D. Stöver, Solid State Ionics 176 (2005) 1341-1350.

[35] E. Bucher, A. Egger, G.B. Caraman, W. Sitte, J. Electrochem. Soc. 155 (2008) B1218-B1224.

[36] E. Bucher, W. Sitte, F. Klauser, E. Bertel, Solid State Ionics 208 (2012) 43-51.

[37] Z. Wuillemin, A. Nakajo, A. Müller, A.J. Schuler, S. Diethelm, J. Van Herle, D. Favrat, in 11th Intern. Symp. Solid Oxide Fuel Cells (SOFC-XI), S.C. Singhal, (Ed.), Vienna, Austria, 2009, p. 457-466.

[38] J.A. Schuler, H. Yokokawa, C.F. Calderone, Q. Jeangros, Z. Wuillemin, A. Hessler-Wyser, J. Van Herle, J. Power Sources 201 (2012) 112-120.

[39] Y. Xiong, K. Yamaji, H. Teruhisa, H. Yokokawa, J. Akikusa, H. Eto, T. Inagaki, J. Electrochem. Soc. 156 (2009) B588-B592.

[40] F. Wang, K. Yamaji, D.-H. Cho, T. Shimonosono, H. Kishimoto, M.E. Brito, T. Horita, H. Yokokawa, J. Electrochem. Soc. 158 (2011) B1391-B1397.

[41] I. Kaus, K. Wiik, M. Dahle, M. Brustad, S. Aasland, J. Eur. Ceram. Soc. 27 (2007) 4509-4514.

[42] E. Bucher, W. Sitte, F. Klauser, E. Bertel, Solid State Ionics 191 (2011) 61-67.

[43] F. Mauvy, C. Lalanne, J.M. Bassat, J.C. Grenier, H. Zhao, L.H. Huo, P. Stevens, J. Electrochem. Soc. 153 (2006) A1547-A1553.

[44] R. Sayers, J. Liu, B. Rustumji, S.J. Skinner, Fuel Cells 8 (2008) 338-343.

[45] H. Zhao, F. Mauvy, C. Lalanne, J.M. Bassat, S. Fourcade, J.C. Grenier, Solid State Ionics 179 (2008) 2000-2005.

[46] A.M. Hernández, L. Mogni, A. Caneiro, Int. J. Hydrogen Energy 35 (2010) 6031-6036.

[47] A. Montenegro-Hernández, J. Vega-Castillo, L. Mogni, A. Caneiro, Int. J. Hydrogen Energy 36 (2011) 15704-15714.

[48] L. Fawcett, J.A. Kilner, S.J. Skinner, in 10th European SOFC Forum, F. Lefebvre-Joud, (Ed.), Luzern, Switzerland, 2012, p. B0409.

[49] A. Montenegro-Hernández, L. Mogni, A. Caneiro, Int. J. Hydrogen Energy 37 (2012) 18290-18301.

[50] J.A. Schuler, H. Lübbe, A. Hessler-Wyser, J. Van Herle, J. Power Sources 213 (2012) 223-228.

[51] J.A. Schuler, H. Lübbe, A. Hessler-Wyser, J. Van Herle, in Proc. of the 15th European Solid Oxide Fuel Cell Forum, O. Bucheli and M. Spirig, (Eds.), Lucerne, Switzerland, 2011, p. B0503.

[52] C. Laberty, F. Zhao, K.E. Swider-Lyons, A.V. Virkar, Electrochem. Solid-State Lett. 10 (2007) B170-B174.

[53] C. Lalanne, G. Prosperi, J.M. Bassat, F. Mauvy, S. Fourcade, P. Stevens, M. Zahid, S. Diethelm, J. Van herle, J.C. Grenier, J. Power Sources 185 (2008) 1218-1224.

[54] M. Rieu, R. Sayers, M.A. Laguna-Bercero, S.J. Skinner, P. Lenormand, F. Ansart, J. Electrochem. Soc. 157 (2010) B477-B480.

[55] T. Ogier, F. Chauveau, J.-M. Bassat, F. Mauvy, J.-C. Grenier, J. Mougin, M. Petitjean, ECS Trans. 35 (2011) 1817-1822.

[56] C. Ferchaud, J.-C. Grenier, Y. Zhang-Steenwinkel, M.M.A. van Tuel, F.P.F. van Berkel, J.-M. Bassat, J. Power Sources 196 (2011) 1872-1879.

[57] E.V. Tsipis, V.V. Kharton, J. Solid State Electrochem. 12 (2008) 1367-1391.

[58] Y. Shen, H. Zhao, X. Liu, N. Xu, Phys. Chem. Chem. Phys. 12 (2010) 15124-15131.

[59] T. Inprasit, P. Limthongkul, S. Wongkasemjit, J. Electrochem. Soc. 157 (2010) B1726-B1730.

[60] T. Nakamura, K. Yashiro, K. Sato, J. Mizusaki, Phys. Chem. Chem. Phys. 11 (2009) 3055-3062.

[61] T. Inprasit, P. Limthongkul, S. Wongkasemjit, ECS Trans. 25(2) (2009) 2581-2588.

[62] V.V. Kharton, A.P. Viskup, E.N. Naumovich, F.M.B. Marques, J. Mater. Chem. 9 (1999) 2623-2629.

[63] A. Aguadero, M.J. Escudero, M. Perez, J.A. Alonso, V. Pomjakushin, L. Daza, Dalton Trans. (2006) 4377-4383.

[64] A. Aguadero, M.J. Escudero, M. Perez, J.A. Alonso, L. Daza, J. Fuel Cell Sci. Technol. 4 (2007) 294-298.

[65] T. Nakamura, K. Yashiro, K. Sato, J. Mizusaki, Mater. Chem. Phys. 122 (2010) 250-258.

[66] V. Vashook, E. Girdauskaite, J. Zosel, T.L. Wen, H. Ullmann, U. Guth, Solid State Ionics 177 (2006) 1163-1171.

[67] Z. Li, R. Haugsrud, T. Norby, Solid State Ionics 184 (2011) 42-46.

[68] J. DiCarlo, A. Mehta, D. Banschick, A. Navrotsky, J. Solid State Chem. 103 (1993) 186-192.

[69] Z. Li, T. Norby, R. Haugsrud, J. Am. Ceram. Soc. 95 (2012) 2065-2073.

[70] E. Boehm, J.M. Bassat, M.C. Steil, P. Dordor, F. Mauvy, J.C. Grenier, Solid State Sci. 5 (2003) 973-981.

[71] V.V. Kharton, E.V. Tsipis, A.A. Yaremchenko, J.R. Frade, Solid State Ionics 166 (2004) 327-337.

[72] G. Amow, S.J. Skinner, J. Solid State Electrochem. 10 (2006) 538-546.

[73] J.A. Kilner, C.K.M. Shaw, Solid State Ionics 154 (2002) 523-527.

[74] C.N. Munnings, S.J. Skinner, G. Amow, P.S. Whitfield, I.J. Davidson, Solid State Ionics 176 (2005) 1895-1901.

[75] D. Balz, K. Plieth, Z. Elektrochem. 59 (1955) 545-551.

[76] S.N. Ruddlesden, P. Popper, Acta Crystallogr. 10 (1957) 538-539.

[77] S.N. Ruddlesden, P. Popper, Acta Crystallogr. 11 (1958) 54-55.

[78] J.D. Jorgensen, B. Dabrowski, S. Pei, D.R. Richards, D.G. Hinks, Physical Review B 40 (1989) 2187.

[79] J. Choisnet, J. Solid State Chem. 147 (1999) 379-389.

[80] K.K. Singh, P. Ganguly, J.B. Goodenough, J. Solid State Chem. 52 (1984) 254-273.

[81] M. Greenblatt, Current Opinion in Solid State & Materials Science 2 (1997) 174-183.

[82] R.D. Shannon, Acta Crystallogr. A 32 (1976) 751-767.

[83] D.J. Buttrey, P. Ganguly, J.M. Honig, C.N.R. Rao, R.R. Schartman, G.N. Subbanna, J. Solid State Chem. 74 (1988) 233-238.

[84] E.N. Naumovich, M.V. Patrakeev, V.V. Kharton, A.A. Yaremchenko, D.I. Logvinovich, F.M.B. Marques, Solid State Sci. 7 (2005) 1353-1362.

[85] R.R. Schartman, J.M. Honig, Mater. Res. Bull. 24 (1989) 1375-1383.

[86] S.J. Skinner, Solid State Sci. 5 (2003) 419-426.

[87] C. Frayret, A. Villesuzanne, M. Pouchard, Chem. Mater. 17 (2005) 6538-6544.

[88] C. Allançon, J. Rodríguez-Carvajal, M.T. Fernández-Díaz, P. Odier, J.M. Bassat, J.P. Loup, J.L. Martínez, Z. Phys. B: Condens. Matter 100 (1996) 85-90.

[89] M.S.D. Read, M.S. Islam, F. King, F.E. Hancock, J. Phys. Chem. B 103 (1999) 1558-1562.

[90] J.C. Grenier, A. Wattiaux, J.P. Doumerc, P. Dordor, L. Fournes, J.P. Chaminade, M. Pouchard, J. Solid State Chem. 96 (1992) 20-30.

[91] A. Demourgues, F. Weill, B. Darriet, A. Wattiaux, J.C. Grenier, P. Gravereau, M. Pouchard, J. Solid State Chem. 106 (1993) 317-329.

[92] A. Demourgues, A. Wattiaux, J.C. Grenier, M. Pouchard, J.L. Soubeyroux, J.M. Dance, P. Hagenmuller, J. Solid State Chem. 105 (1993) 458-468.

[93] J.C. Grenier, J.M. Bassat, J.P. Doumerc, J. Etourneau, Z. Fang, L. Fournes, S. Petit, M. Pouchard, A. Wattiaux, J. Mater. Chem. 9 (1999) 25-33.

[94] M.T. Fernandez-Diaz, J.L. Martinez, J. Rodriguez-Carvajal, Solid State Ionics 63-65 (1993) 902-906.

[95] J.G. Bednorz, K.A. Müller, Reviews of Modern Physics 60 (1988) 585-600.

[96] S.A. Hoffman, C. Venkatraman, S.N. Ehrlich, S.M. Durbin, G.L. Liedl, Physical Review B 43 (1991) 7852-7858.

[97] A. Rabenau, P. Eckerlin, Acta Crystallogr. 11 (1958) 304-306.

[98] P. Odier, Y. Nigara, J. Coutures, M. Sayer, J. Solid State Chem. 56 (1985) 32-40.

[99] R.S. Puche, J.L. Rodriguez, F. Fernández, Inorganica Chimica Acta 140 (1987) 151-153.

[100] J. Choisnet, J.M. Bassat, H. Pilliere, P. Odier, M. Leblanc, Solid State Communications 66 (1988) 1245-1249.

[101] Z. Hiroi, T. Obata, M. Takano, Y. Bando, Y. Takeda, O. Yamamoto, Physical Review B 41 (1990) 11665-11668.

[102] T. Kajitani, Y. Kitagaki, K. Hiraga, S. Hosoya, T. Fukuda, Y. Yamaguchi, S. Wada, S. Sugai, Y. Morii, K. Fuchizaki, S. Funahashi, Physica C: Superconductivity 185-189, Part 1 (1991) 579-580.

[103] J. Rodriguez-Carvajal, M.T. Fernandez-Diaz, J.L. Martinez, J. Phys.-Condens. Matter 3 (1991) 3215.

[104] D.E. Rice, D.J. Buttrey, J. Solid State Chem. 105 (1993) 197-210.

[105] H. Tamura, A. Hayashi, Y. Ueda, Physica C: Superconductivity 216 (1993) 83-88.

[106] A. Mehta, P.J. Heaney, Physical Review B 49 (1994) 563.

[107] J.M. Tranquada, Y. Kong, J.E. Lorenzo, D.J. Buttrey, D.E. Rice, V. Sachan, Physical Review B 50 (1994) 6340.

[108] H. Tamura, A. Hayashi, Y. Ueda, Physica C 258 (1996) 61-71.

[109] A. Aguadero, J.A. Alonso, M.J. Martinez-Lope, M.T. Fernandez-Diaz, M.J. Escudero, L. Daza, J. Mater. Chem. 16 (2006) 3402-3408.

[110] D.J. Buttrey, J.D. Sullivan, G. Shirane, K. Yamada, Physical Review B 42 (1990) 3944.

[111] M.T. Fernandez-Diaz, J. Rodriguez-Carvajal, J.L. Martinez, G. Fillion, F. Fernandez, R. Saez-Puche, Z. Phys. B: Condens. Matter 82 (1991) 275-282.

[112] J.L. Martinez, M.T. Fernandez-Daz, J. Rodriguez-Carvajal, P. Odier, Physical Review B 43 (1991) 13766.

[113] J.D. Sullivan, D.J. Buttrey, D.E. Cox, J. Hriljac, J. Solid State Chem. 94 (1991) 337-351.

[114] C. Allançon, A. Gonthier-Vassal, J.M. Bassat, J.P. Loup, P. Odier, Solid State Ionics 74 (1994) 239-248.

[115] J. Rodríguez-Carvajal, M.T. Fernández-Diaz, J.L. Martinez, F. Fernández, R. Saez-Puche, Europhysics Letters 11 (1990) 261.

[116] Y. Toyosumi, H. Ishikawa, K. Ishikawa, J. Alloys Compd. 408-412 (2006) 1200-1204.

[117] S. Bhavaraju, J.F. DiCarlo, D.P. Scarfe, I. Yazdi, A.J. Jacobson, Chem. Mater. 6 (1994) 2172-2176.

[118] R.A.M. Ram, L. Ganapathi, P. Ganguly, C.N.R. Rao, J. Solid State Chem. 63 (1986) 139-147.

[119] P. Lacorre, J. Solid State Chem. 97 (1992) 495-500.

[120] Z. Zhang, M. Greenblatt, J.B. Goodenough, J. Solid State Chem. 108 (1994) 402-409.

[121] Z. Zhang, M. Greenblatt, J. Solid State Chem. 117 (1995) 236-246.

[122] M.D. Carvalho, F.M.A. Costa, I.S. Pereira, A. Wattiaux, J.M. Bassat, J.C. Grenier, M. Pouchard, J. Mater. Chem. 7 (1997) 2107-2111.

[123] J.M. Bassat, C. Allançon, P. Odier, J.P. Loup, M.D. Carvalho, A. Wattiaux, Eur. J. Solid State Inorg. Chem. 35 (1998) 173-188.

[124] A. Manthiram, J.P. Tang, V. Manivannan, J. Solid State Chem. 148 (1999) 499-507.

[125] M.D. Carvalho, M.M. Cruz, A. Wattiaux, J.M. Bassat, F.M.A. Costa, M. Godinho, J. Appl. Phys. 88 (2000) 544-549.

[126] V.I. Voronin, I.F. Berger, V.A. Cherepanov, L.Y. Gavrilova, A.N. Petrov, A.I. Ancharov, B.P. Tolochko, S.G. Nikitenko, Nuclear Instruments and Methods in Physics Research A 470 (2001) 202-209.

[127] G. Amow, J. Au, I. Davidson, Solid State Ionics 177 (2006) 1837-1841.

[128] G. Amow, I.J. Davidson, S.J. Skinner, Solid State Ionics 177 (2006) 1205-1210.

[129] M. Zinkevich, N. Solak, H. Nitsche, M. Ahrens, F. Aldinger, J. Alloys Compd. 438 (2007) 92-99.

[130] D.O. Bannikov, A.P. Safronov, V.A. Cherepanov, Thermochim. Acta 451 (2006) 22-26.

[131] D.O. Bannikov, V.A. Cherepanov, J. Solid State Chem. 179 (2006) 2721-2727.

[132] M. Zinkevich, F. Aldinger, J. Alloys Compd. 375 (2004) 147-161.

[133] A.N. Petrov, V.A. Cherepanov, A.Y. Zuyev, V.M. Zhukovsky, J. Solid State Chem. 77 (1988) 1-14.

[134] M.D. Carvalho, A. Wattiaux, L.P. Ferreira, J.M. Bassat, J. Solid State Chem. 182 (2009) 60-64.

[135] D. Pérez-Coll, A. Aguadero, M.J. Escudero, L. Daza, J. Power Sources 192 (2009) 2-13.

[136] S. Takahashi, S. Nishimoto, M. Matsuda, M. Miyake, J. Am. Ceram. Soc. 93 (2010) 2329-2333.

[137] R.J. Woolley, B.N. Illy, M.P. Ryan, S.J. Skinner, J. Mater. Chem. 21 (2011) 18592-18596.

[138] J.M. Bassat, P. Odier, A. Villesuzanne, C. Marin, M. Pouchard, Solid State Ionics 167 (2004) 341-347.

[139] M. Burriel, G. Garcia, J. Santiso, J.A. Kilner, J.C.C. Richard, S.J. Skinner, J. Mater. Chem. 18 (2008) 416-422.

[140] E.J. Opila, H.L. Tuller, B.J. Wuensch, J. Maier, J. Am. Ceram. Soc. 76 (1993) 2363-2369.

[141] L. Minervini, R.W. Grimes, J.A. Kilner, K.E. Sickafus, J. Mater. Chem. 10 (2000) 2349-2354.

[142] A.R. Cleave, J.A. Kilner, S.J. Skinner, S.T. Murphy, R.W. Grimes, Solid State Ionics 179 (2008) 823-826.

[143] A. Chroneos, D. Parfitt, J.A. Kilner, R.W. Grimes, J. Mater. Chem. 20 (2010) 266–270.

[144] D. Parfitt, A. Chroneos, J.A. Kilner, R.W. Grimes, Phys. Chem. Chem. Phys. 12 (2010) 6834-6836.

[145] H. Rickert, *Electrochemistry of Solids*, Springer Verlag, Berlin - Heidelberg - New York (1982).

[146] L. Onsager, Phys. Rev. 37 (1931) 405.

[147] L. Onsager, Phys. Rev. 38 (1931) 2265.

[148] P. Glansdorff, I. Prigogine, *Thermodynamic Theory of Structure, Stability and Fluctuations*, John Wiley & Sons, London - New York - Sydney - Toronto (1971).

[149] H.S. Kim, H.I. Yoo, Phys. Chem. Chem. Phys. 12 (2010) 15145-15145.

[150] J. Maier, J. Am. Ceram. Soc. 76 (1993) 1212-1217.

[151] J. Maier, *Festkörper - Fehler und Funktion*, Teubner Studienbücher Chemie, Stuttgart - Leipzig (2000).

[152] M.W. Barsoum, *Fundamentals of ceramics*, Institute of Physics Publishing, Bristol - Philadelphia (2003).

[153] F.A. Kröger, F.H. Stieltjes, H.J. Vink, Philips Res. Rep. 14 (1959) 557-601.

[154] J. Philibert, *Atom Movements, Diffusion and Mass Transport in Solids*, Les Editions de Physique, Les Ulis, France (1991).

[155] T. Ishigaki, S. Yamauchi, K. Kishio, J. Mizusaki, K. Fueki, J. Solid State Chem. 73 (1988) 179-187.

[156] P. Kofstad, *Nonstoichiometry, Diffusion, and Electrical Conductivity in Binary Metal Oxides*, John Wiley & Sons, New York - London - Sydney - Toronto (1972).

[157] G.E. Murch, Solid State Ionics 7 (1982) 177-198.

[158] R. Merkle, J. Maier, J. Fleig, *Mechanistic understanding and electrochemical modeling of mixed conducting (SOFC) electrodes*, in Handbook of Fuel Cells - Fundamentals, Technology and Applications, W. Vielstich, H. Yokokawa, and H.A. Gasteiger, Editors, p. 425-440, John Wiley & Sons, (2009).

[159] J. Maier, G. Schwitzgebel, physica status solidi (b) 113 (1982) 535-547.

[160] J. Maier, J. Am. Ceram. Soc. 76 (1993) 1218-1222.

[161] J. Maier, J. Am. Ceram. Soc. 76 (1993) 1223-1227.

[162] J. Maier, J. Am. Ceram. Soc. 76 (1993) 1228-1232.

[163] G.J. Dudley, B.C.H. Steele, J. Solid State Chem. 31 (1980) 233-247.

[164] L.J. van der Pauw, Philips Res. Rep. 13 (1958) 1-9.

[165] D. Grientschnig, W. Sitte, Z. Phys. Chem. 168 (1990) 143-159.

[166] I. Riess, D.S. Tannhauser, Solid State Ionics 7 (1982) 307-315.

[167] W. Preis, W. Sitte, Solid State Ionics 76 (1995) 5-14.

[168] W. Preis, M. Holzinger, W. Sitte, Monatsh. Chem. 132 (2001) 499-508.

[169] W. Preis, private communication.

[170] L. Råde, B. Westergren, *Mathematics Handbook*, 4th Edition, Springer-Verlag, Berlin - Heidelberg - New York (1999).

[171] R. Chwang, B.J. Smith, C.R. Crowell, Solid-State Electronics 17 (1974) 1217-1227.

[172] J.A. Lane, S.J. Benson, D. Waller, J.A. Kilner, Solid State Ionics 121 (1999) 201-208.

[173] J.A. Lane, J.A. Kilner, Solid State Ionics 136-137 (2000) 997-1001.

[174] S. Wang, A. Verma, Y.L. Yang, A.J. Jacobson, B. Abeles, Solid State Ionics 140 (2001) 125-133.

[175] J.E. ten Elshof, M.H.R. Lankhorst, H.J.M. Bouwmeester, J. Electrochem. Soc. 144 (1997) 1060-1067.

[176] L.M. van der Haar, M.W. den Otter, M. Morskate, H.J.M. Bouwmeester, H. Verweij, J. Electrochem. Soc. 149 (2002) J41-J46.

[177] H.J.M. Bouwmeester, M.W. Den Otter, B.A. Boukamp, J. Solid State Electrochem. 8 (2004) 599-605.

[178] M.W. den Otter, H.J.M. Bouwmeester, B.A. Boukamp, H. Verweij, J. Electrochem. Soc. 148 (2001) J1-J6.

[179] R.A. Cox-Galhotra, S. McIntosh, Solid State Ionics 181 (2010) 1429-1436.

[180] I. Yasuda, M. Hishinuma, J. Solid State Chem. 123 (1996) 382-390.

[181] S. Kim, S. Wang, X. Chen, Y.L. Yang, N. Wu, A. Ingnatiev, A.J. Jacobson, B. Abeles, J. Electrochem. Soc. 147 (2000) 2398-2406.

[182] I. Yasuda, T. Hikita, J. Electrochem. Soc. 141 (1994) 1268-1273.

[183] C.-R. Song, H.-I. Yoo, Solid State Ionics 120 (1999) 141-153.

[184] Y. Li, K. Gerdes, H. Diamond, X. Liu, Solid State Ionics 204–205 (2011) 104-110.

[185] E. Fischer, J.L. Hertz, Solid State Ionics 218 (2012) 18-24.

[186] Z. Li, R. Haugsrud, Solid State Ionics 206 (2012) 67-71.

[187] C. Elschner, M. Kusnezoff, S. Ziesche, A. Paepcke, A. Michaelis, J. Membr. Sci. 362 (2010) 545-549.

[188] M. Kusnezoff, S. Ziesche, C. Elschner, J. Membr. Sci. 360 (2010) 9-16.

[189] H. Dünwald, C. Wagner, Z. Physik. Chem. B 24 (1934) 53-58.

[190] M. Mosleh, M. Søgaard, P.V. Hendriksen, J. Electrochem. Soc. 156 (2009) B441-B457.

[191] S.B. Adler, Chem. Rev. 104 (2004) 4791-4844.

[192] H.J.M. Bouwmeester, H. Kruidhof, A.J. Burggraaf, Solid State Ionics 72 (1994) 185-194.

[193] J. Crank, *The mathematics of diffusion*, 2nd ed., Oxford University Press, Oxford, UK (1995).

[194] H.S. Carslaw, J.C. Jaeger, *Conduction of heat in solids*, 2nd ed., Oxford University Press, Oxford, UK (1988).

[195] M.W. den Otter, L.M. van der Haar, H.J.M. Bouwmeester, Solid State Ionics 134 (2000) 259-264.

[196] I. Denk, F. Noll, J. Maier, J. Am. Ceram. Soc. 80 (1997) 279-285.

[197] M. Katsuki, S. Wang, M. Dokiya, T. Hashimoto, Solid State Ionics 156 (2003) 453-461.

[198] B. Ma, J.H. Park, U. Balachandran, J. Electrochem. Soc. 144 (1997) 2816-2823.

[199] H. Kanai, T. Hashimoto, H. Tagawa, J. Mizusaki, Solid State Ionics 99 (1997) 193-199.

[200] W. Preis, E. Bucher, W. Sitte, Solid State Ionics 175 (2004) 393-397.

[201] M.H.R. Lankhorst, H.J.M. Bouwmeester, H. Verweij, J. Solid State Chem. 133 (1997) 555-567.

[202] V. Vashook, J. Zosel, U. Guth, J. Solid State Electrochem. 16 (2012) 3401-3421.

[203] C.-R. Song, H.-I. Yoo, Solid State Ionics 124 (1999) 289-299.

[204] D.C. Meeker, Finite Element Method Magnetics (FEMM), v4.2, http://www.femm.info.

[205] J.H. Scofield, J. Electron Spectrosc. Relat. Phenom. 8 (1976) 129-137.

[206] F.S. Brugner, R.N. Blumenthal, J. Am. Ceram. Soc. 54 (1971) 57-57.

[207] R. Landauer, J. Appl. Phys. 23 (1952) 779-784.

[208] W.D. Kingery, H.K. Bowen, D.R. Uhlmann, *Introduction to Ceramics*, second ed., John Wiley & Sons, New York (1976).

[209] M.N. Rahaman, *Sintering of Ceramics*, CRC Press, Boca Raton, London, New York (2008).

[210] E. Bucher, *Defect chemistry, transport properties, and microstructure of perovskite-type oxides (La,Sr)(Fe,Co)O_3*, Thesis, University of Leoben, Austria, Department of General, Analytical and Physical Chemistry, (2003).

[211] M. Søgaard, P.V. Hendriksen, M. Mogensen, F.W. Poulsen, E. Skou, Solid State Ionics 177 (2006) 3285-3296.

[212] J. Mizusaki, J. Tabuchi, T. Matsuura, S. Yamauchi, K. Fueki, J. Electrochem. Soc. 136 (1989) 2082-2088.

[213] S. Wang, P.A.W. van der Heide, C. Chavez, A.J. Jacobson, S.B. Adler, Solid State Ionics 156 (2003) 201-208.

[214] A. Egger, E. Bucher, W. Sitte, J. Electrochem. Soc. 158 (2011) B573-B579.

[215] P.F. Haworth, S. Smart, J.M. Serra, J.C. Diniz da Costa, Phys. Chem. Chem. Phys. 14 (2012) 9104-9111.

[216] H. Schäfer, W. Kluy, Z. Anorg. Allg. Chem. 536 (1986) 53-64.

[217] F. Tietz, Ionics 5 (1999) 129-139.

[218] A.V. Kovalevsky, V.V. Kharton, A.A. Yaremchenko, Y.V. Pivak, E.V. Tsipis, S.O. Yakovlev, A.A. Markov, E.N. Naumovich, J.R. Frade, J. Electroceram. 18 (2007) 205-218.

[219] H. Ishikawa, Y. Toyosumi, K. Ishikawa, J. Alloys Compd. 408-412 (2006) 1196-1199.

[220] A. Egger, E. Bucher, W. Sitte, C. Lalanne, J.M. Bassat, ECS Trans. 25(2) (2009) 2547-2556.

[221] P. Odier, C. Allançon, J.M. Bassat, J. Solid State Chem. 153 (2000) 381-385.

[222] A.V. Kovalevsky, V.V. Kharton, A.A. Yaremchenko, Y.V. Pivak, E.N. Naumovich, J.R. Frade, J. Eur. Ceram. Soc. 27 (2007) 4269-4272.

[223] J. Han, K. Zheng, K. Swierczek, Funct. Mater. Lett. 4 (2011) 151-155.

[224] B.G. Hyde, D.J.M. Bevan, L. Eyring, Philos. Trans. R. Soc. A 259 (1966) 583-614.

[225] M. Søgaard, P.V. Hendriksen, T. Jacobsen, M. Mogensen, in 7th European SOFC Forum, U. Bossel, (Ed.), Lucerne, Switzerland, 2006, p. B064.

[226] C. Laberty-Robert, K. Swider-Lyons, in Solid Oxide Fuel Cells IX (SOFC-IX), S.C. Singhal and J. Mizusaki, (Eds.), Quebec, 2005, p. 1751-1757.

[227] H. Ullmann, N. Trofimenko, F. Tietz, D. Stöver, A. Ahmad-Khanlou, Solid State Ionics 138 (2000) 79-90.

[228] V. Thangadurai, R. Huggins, W. Weppner, J. Solid State Electrochem. 5 (2001) 531-537-537.

[229] P.-N. Huang, A. Petric, W. Gong, in Proc. of the 3rd International Symposium on Ionic and Mixed Conducting Ceramics, 1998, p. 396-403.

[230] J. Maier, Solid State Ionics 112 (1998) 197-228.

[231] T. Nakamura, K. Yashiro, K. Sato, J. Mizusaki, Solid State Ionics 181 (2010) 402-411.

[232] A.L. Shaula, E.N. Naumovich, A.P. Viskup, V.V. Pankov, A.V. Kovalevsky, V.V. Kharton, Solid State Ionics 180 (2009) 812-816.

[233] F. Mauvy, J.M. Bassat, E. Boehm, J.P. Manaud, P. Dordor, J.C. Grenier, Solid State Ionics 158 (2003) 17-28.

[234] E. Bucher, A. Egger, M. Yang, W. Sitte, F. Klauser, E. Bertel, in Proc. of the 9th European Solid Oxide Fuel Cell Forum, P. Connor, (Ed.), Lucerne, Switzerland, 2010, p. 7/11-18.

[235] J.H. Joo, R. Merkle, J. Maier, J. Power Sources 196 (2011) 7495-7499.

[236] J. Choisnet, N. Abadzhieva, P. Stefanov, D. Klissurski, J.M. Bassat, V. Rives, L. Minchev, J. Chem. Soc. - Faraday Trans. 90 (1994) 1987-1991.

[237] I. Barin, *Thermochemical Data of Pure Substances*, VCH, Weinheim (1993).

[238] A. Egger, W. Sitte, F. Klauser, E. Bertel, J. Electrochem. Soc. 157 (2010) B1537-B1541.

[239] M. Backhaus-Ricoult, Solid State Sci. 10 (2008) 670-688.

[240] M.M. Viitanen, R.G. v. Welzenis, H.H. Brongersma, F.P.F. van Berkel, Solid State Ionics 150 (2002) 223-228.

[241] J.A. Schuler, Z. Wuillemin, A. Hessler-Wyser, J. Van herle, Electrochem. Solid-State Lett. 14 (2011) B20-B22.

[242] E.J. Opila, N.S. Jacobson, D.L. Myers, E.H. Copland, JOM 58 (2006) 22-28.

[243] E.J. Opila, D.S. Fox, N.S. Jacobson, J. Am. Ceram. Soc. 80 (1997) 1009-1012.

[244] N.S. Jacobson, E.J. Opila, D.L. Myers, E.H. Copland, J. Chem. Thermodyn. 37 (2005) 1130-1137.

[245] J.A. Schuler, C. Gehrig, Z. Wuillemin, A.J. Schuler, J. Wochele, C. Ludwig, A. Hessler-Wyser, J. Van Herle, in Proc. of the 9th European Solid Oxide Fuel Cell Forum, P. Connor, (Ed.), Lucerne, Switzerland, 2010, p. 7111-7127.

[246] T. Horita, H. Kishimoto, K. Yamaji, M.E. Brito, Y. Xiong, H. Yokokawa, Y. Hori, I. Miyachi, J. Power Sources 193 (2009) 194-198.

[247] T. Klande, K. Efimov, S. Cusenza, K.-D. Becker, A. Feldhoff, J. Solid State Chem. 184 (2011) 3310-3318.

[248] S. Engels, T. Markus, M. Modigell, L. Singheiser, J. Membr. Sci. 370 (2011) 58-69.

[249] Z. Shao, S.M. Haile, Nature 431 (2004) 170-173.

[250] M. Arnold, H. Wang, A. Feldhoff, J. Membr. Sci. 293 (2007) 44-52.

[251] C.W. Bale, A.D. Pelton, W.T. Thompson, G. Eriksson, K. Hack, P. Chartrand, S. Decterov, I.-H. Jung, J. Melancon, S. Peterson, FactSage© 6.2, 1976-2010 Thermfact and GTT Technologies.

[252] A.N. Shirsat, M. Ali, K.N.G. Kaimal, S.R. Bharadwaj, D. Das, Thermochim. Acta 399 (2003) 167-170.

[253] A.J. Schuler, Z. Wuillemin, A. Hessler-Wyser, J. Van Herle, in 11th Intern. Symp. Solid Oxide Fuel Cells (SOFC-XI) S.C. Singhal, (Ed.), Vienna, Austria, 2009, p. 2845-2852.

[254] E. Bucher, W. Preis, W. Sitte, C. Gspan, F. Hofer, in 10th European Solid Oxide Fuel Cell Forum, F. Lefebvre-Joud, (Ed.), Lucerne, Switzerland, 2012, p. B0543-B0552.

[255] E. Bucher, C. Gspan, F. Hofer, W. Sitte, Solid State Ionics 238 (2013) 15-23.

[256] H.H. Kellogg, Transactions of the Metallurgical Society of AIME 230 (1964) 1622-1634.

[257] A.A. Grizik, I.G. Abdullina, N.M. Garifdzhanova, Zh. Neorg. Khim. 19 (1974) 2586-2588.

Journal of The Electrochemical Society, **155** (11) B1218-B1224 (2008)
0013-4651/2008/155(11)/B1218/7/$23.00 © The Electrochemical Society

Stability of the SOFC Cathode Material $(Ba,Sr)(Co,Fe)O_{3-\delta}$ in CO_2-Containing Atmospheres

E. Bucher,[z] A. Egger, G. B. Caraman, and W. Sitte*

Chair of Physical Chemistry, University of Leoben, 8700 Leoben, Austria

The stability of the solid oxide fuel cell (SOFC) cathode material $Ba_{0.5}Sr_{0.5}Co_{0.8}Fe_{0.2}O_{3-\delta}$ in CO_2-containing atmospheres ($4 \times 10^{-4} \leqslant pCO_2/\text{bar} \leqslant 5 \times 10^{-2}$) is investigated by precision thermogravimetry (TG) and mass spectrometry (MS) as a function of temperature ($20 \leqslant T/°C \leqslant 950$). The desorption of O_2 and CO_2 from samples with different pretreatments is compared. Oxygen exchange at $300 < T/°C < 700$ is significantly impaired by CO_2-containing atmospheres. At 600°C the kinetics of carbonate formation in CO_2-rich atmosphere is described by a linear-parabolic rate law. A pronounced dependence of the rate constant on the CO_2 content is suggested. Temperature cycles at $0 \leqslant pCO_2/\text{bar} \leqslant 5 \times 10^{-2}$ and $pO_2 = 0.2$ bar, which show effects due to oxygen exchange of the perovskite and due to CO_2, are analyzed based on reference experiments in a CO_2-free atmosphere, and under consideration of the TG-MS results. The decomposition temperature of the carbonate in contact with an atmosphere of $pCO_2 = 5 \times 10^{-2}$ bar amounts to 807°C. Complementary, the impact of carbonate formation on the oxygen exchange kinetics is investigated by conductivity relaxation measurements. A severe degradation of the surface oxygen exchange coefficient is observed after 3–10 days of exposure to ambient air. Regeneration and activation of the oxygen exchange kinetics is demonstrated after treatment in a CO_2-free atmosphere at 825°C.

[DOI: 10.1149/1.2981024]

Manuscript submitted July 9, 2008; revised manuscript received August 14, 2008. Published September 25, 2008.

The lack of cathodes with excellent efficiency for oxygen reduction at intermediate temperatures (IT), i.e., 600–750°C, still represents a major obstacle toward lowering the operating temperatures of solid oxide fuel cells (SOFCs). In this regard, $Ba_{0.5}Sr_{0.5}Co_{0.8}Fe_{0.2}O_{3-\delta}$ (BSCF) was recently suggested as a highly promising candidate.[1-3] However, the successful implementation of BSCF will strongly depend on sufficiently low degradation rates under real operating conditions.

Initially developed for oxygen permeable membranes,[4-6] BSCF is a mixed ionic-electronic conducting perovskite-type oxide with an exceptionally high oxygen nonstoichiometry.[7-12] A stable cubic perovskite structure was reported from room temperature up to 700–1000°C at $10^{-5} < pO_2/\text{bar} < 0.2$.[10,13,14] However, a recent study indicated that a kinetically slow transformation from the cubic to the hexagonal modification may occur during cooling from high temperatures in air.[15]

Under CO_2-free laboratory conditions, excellent oxygen exchange properties of BSCF in the IT range have been reported.[7,16,17] Nevertheless, the long-term stability and robustness of the material, especially in CO_2-containing oxidants such as ambient air, is questionable. Investigations performed on oxygen permeable BSCF membranes indicated a degradation of BSCF in atmospheres containing CO_2 or both CO_2 and H_2O.[4,18] Early studies on the performance of IT-SOFC cells with integrated BSCF cathodes at 450–750°C showed that the presence of relatively small quantities of CO_2 ($\leqslant 3$ vol %) are sufficient to negatively affect the cell performance.[1,19] Regarding the nature of the products formed during exposure of BSCF to CO_2, a surface layer of $Ba_{1-x}Sr_xCO_3$[20,21] was suggested. The carbonate layer is presumably separated from the intact perovskite bulk by an intermediate phase of Co/Fe-enriched perovskite or a complex oxide $(Ba,Sr)_x(Co,Fe)_yO_z$ with minor amounts of CoO.[18,22]

Summarizing, indications of the degradation of BSCF in CO_2-containing atmospheres are evident throughout the literature. However, the results are mostly derived from parameters obtained from devices including components other than BSCF or operating under nonequilibrium conditions (SOFC single cells, oxygen permeable membranes). The following study is dedicated to the systematic thermoanalytic investigation of the effects of different CO_2 concentrations and pretreatments on BSCF. Complementarily, the impact of CO_2 on the oxygen exchange kinetics will be unambiguously demonstrated by conductivity relaxation measurements.

Experimental

Powder preparation.— BSCF powder was prepared by spray-pyrolysis from an aqueous solution of stoichiometric amounts of the metal nitrates at 500°C. After calcination at 950°C for 4 h in air, the powder was milled 10 h in a planetary ball mill in isopropanol, yielding an average particle size of $d_{50} = 0.42$ μm. The product was characterized with regard to phase purity and elemental composition by X-ray diffraction (XRD) and inductively coupled plasma-atomic emission spectroscopy, respectively, as described elsewhere.[23]

Thermoanalysis.— Calcined BSCF powders were fired at 1130°C for 4 h in ambient air. Thermogravimetry (TG) was performed using a symmetric precision thermobalance (Setaram, TAG 2416) with an in situ zirconia-based oxygen microsensor (Setnag). Simultaneous thermogravimetry-mass spectrometry (TG-MS) was conducted via coupling to a quadrupole mass spectrometer (Pfeiffer Vacuum, ThermoStar GSD 301 T1, maximum 100 amu) with a Faraday detector operated in multiple ion detection mode, scanning the predefined m/z channels with a rate of 1 s channel^{-1}. Oxygen partial pressures were controlled by mass flow controllers (Mykrolis, FC2700) via gas mixtures of O_2 4.5 N (purity $\geqslant$99.995%), Ar 5.0 N (purity $\geqslant$99.999%), and a commercial gas mixture of 1 vol % O_2, the rest Ar. Commercial gas mixtures of (*i*) 20 vol % O_2 + 5 vol % CO_2, the rest Ar and (*ii*) 20 vol % O_2 + 0.04 vol % CO_2, the rest Ar were used for investigating the stability of the powders vs CO_2. The usual sample mass was 30–40 mg. Experimental errors are estimated to $\Delta T = \pm 0.5$ K, $\Delta pO_2 = \pm 2$ rel %, $\Delta(\Delta m) = \pm 0.01$ mass %.

Conductivity relaxation measurements.— Calcined BSCF powder was isostatically pressed at 300 MPa, fired at 900°C for 1 h in ambient air, and ground with a ball mill. The resulting powder was uniaxially pressed (~8 mm diameter, ~1 mm thickness) at 400 MPa and sintered 80 h in ambient air at 1000°C. Heating and cooling rates were 2 and 1 K min^{-1}, respectively. The sample thus obtained had 93% of the theoretical density, $\rho_{\text{theor}} = 5.75$ g/cm^3 (determined by XRD, assuming the stoichiometric composition of oxygen). For dc conductivity relaxation (CR) measurements a thin square ($A \sim 0.5$ cm × 0.5 cm) was cut from the sintered tablet using a precision diamond saw. Subsequently, the thickness was reduced to 200 μm by grinding down to 1 μm on diamond laps. Four electrical contacts were mounted in van der Pauw geometry[24] using Au wires (Oegussa) and Au paste (Metalor).

---

* Electrochemical Society Active Member.

[z] E-mail: edith.bucher@mu-leoben.at

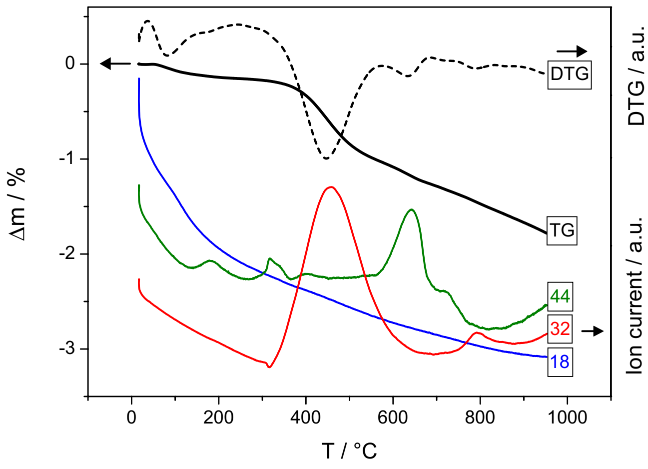

Figure 1. (Color online) TG-MS of BSCF powder in Ar 5.0 N after PT 1 (cooling from 1130°C in ambient air); relative mass loss (TG) and its first derivative (DTG), and MS signals of H_2O ($m/z = 18$), CO_2 ($m/z = 44$), and O_2 ($m/z = 32$) as a function of temperature (heating rate 5 K min^{-1}).

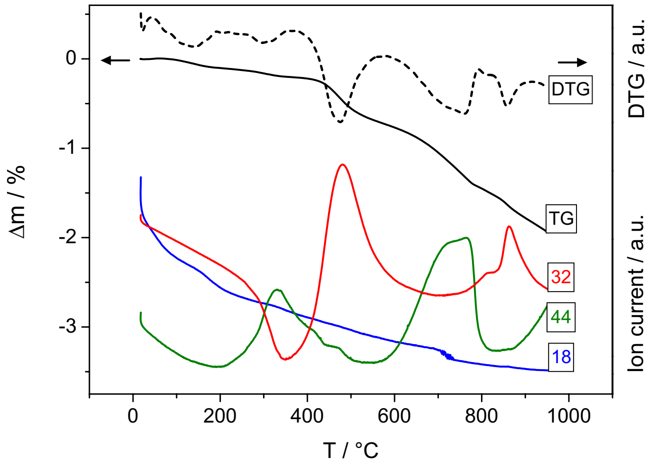

Figure 2. (Color online) TG-MS of BSCF powder in Ar 5.0 N after PT 2 (T-cycles in CO_2-rich atmosphere), relative mass loss (TG) and its first derivative (DTG), and MS signals of H_2O ($m/z = 18$), CO_2 ($m/z = 44$), and O_2 ($m/z = 32$) as a function of temperature (heating rate 5 K min^{-1}).

The kinetic parameters, i.e., the chemical diffusion coefficient of oxygen D_{chem} and the surface oxygen exchange coefficient k_{chem}, were investigated by CR experiments at 600°C. Small oxidation and reduction steps in the interval $0.01 < pO_2/bar < 0.02$ (estimated error $\Delta pO_2 = \pm 2$ rel %) were applied to study the oxygen exchange kinetics close to equilibrium. Oxygen partial pressures were adjusted by mixtures of O_2 4.5 N (purity $\geqslant$99.995%) and 1 vol % O_2, the rest Ar, using mass flow controllers (Hastings, HFC 302). Fast pO_2 steps were realized by switching between two continuous gas streams with flow rates of 2.0 L h^{-1}, respectively. The transient relaxation of the sample was monitored via the voltage response at a constant dc current of 10 mA using a sensitive digital voltmeter (Keithley, 182) and a precision current source (Keithley, 2400). A zirconia-based oxygen microsensor (Setnag) was used for the in situ measurement of the pO_2 in close vicinity to the sample. For data acquisition and instrument control, the software LabView 8.0 (National Instruments, USA) was used. The finite flush time of the empty quartz reactor was separately determined to $\tau_R = 3.1 \pm 0.5$ s using an in situ oxygen microsensor (Setnag). For the evaluation of conductivity relaxation experiments a constant τ_R of 3 s was assumed. The normalized electronic conductivity was analyzed by nonlinear least-squares fits to the solution function of the appropriate diffusion equations, taking into account the finite flush time of the reactor.[25,26] The errors of the kinetic parameters were estimated to $\Delta k_{chem} = \pm 3$ rel % and $\Delta D_{chem} = \pm 3$ rel %.

Results and Discussion

Thermoanalysis.— BSCF powders were studied as a function of pretreatment (PT) by simultaneous TG-MS in Ar 5.0 N at $20 \leqslant T/°C \leqslant 950$ (Fig. 1-3). This method provides a qualitative analysis of the desorbed gas species and sensitive detection of their relative intensities as a function of temperature (MS), as well as a precise quantitative detection of the corresponding mass changes (TG). The first derivative of the Δm vs T curves, that is differential thermogravimetric analyses (DTG), allow separation of the superimposed effects and (at constant heating rates) are direct indicators of the relative desorption rates.

PT 1: Powder cooled from 1130°C in static ambient air.— TG-MS in Ar 5.0 N acquired on powder after PT 1, i.e., cooling with 5 K min^{-1} from 1130°C in static ambient air, shows the desorption of O_2 from the perovskite at $300 < T/°C < 950$ (Fig. 1). The oxygen signal shows a low-temperature (LT) peak at $T \sim 450°C$ and an additional high-temperature (HT) peak at $T \sim 800°C$. These characteristic features of BSCF have also been observed in oxygen temperature-programmed desorption experiments, and are sometimes referred to as α- and β-O_2 at LT and HT, respectively.[4,5,9,10] The initial mass loss at $60 < T/°C < 200$ can be ascribed to the desorption of H_2O. Various peaks of CO_2 are observed at $130 < T/°C < 950$, with the most pronounced CO_2 desorption in the range 550–820°C. The significance of the latter effect is indicated by a distinct peak in the DTG signal, superimposing the oxygen desorption of the perovskite in this T-range. Further increase of the CO_2 desorption is observed at $T > 800°C$.

PT 2: Thermal cycling in dynamic CO_2-rich atmosphere.— TG-MS in Ar 5.0 N was performed after PT 1 and subsequent PT 2, i.e., two heating/cooling cycles $20 < T/°C < 900$ with 5 K min^{-1} in a CO_2-rich atmosphere of 20 vol % O_2 + 5 vol % CO_2, the rest Ar (as described later). The results are presented in Fig. 2. At $50 < T/°C < 200$ the desorption of H_2O occurs. Release of oxygen from the perovskite lattice is observed at $350 < T/°C < 950$. A pronounced LT-CO_2 peak occurs with a maximum at $T \sim 330°C$, coupled to a decrease of the O_2 signal. This indicates that after desorption of CO_2 from the surface, the sample becomes active in consuming traces of oxygen from the carrier gas. The same effect,

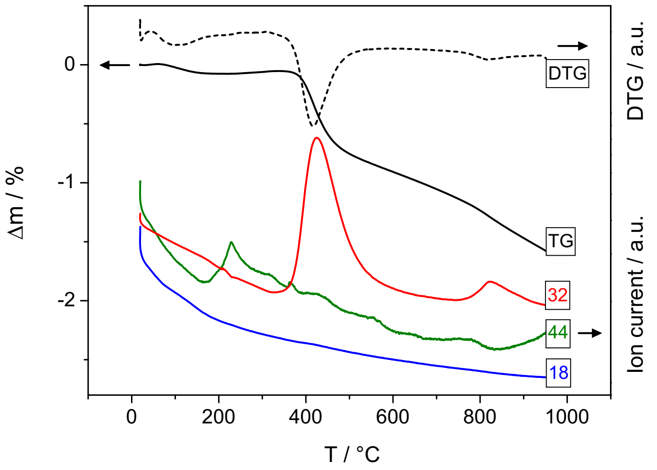

Figure 3. (Color online) TG-MS of BSCF powder in Ar 5.0 N after PT 3 (T-cycles in synthetic air), relative mass loss (TG) and its first derivative (DTG), and MS signals of H_2O ($m/z = 18$), CO_2 ($m/z = 44$), and O_2 ($m/z = 32$) as a function of temperature (heating rate 5 K min^{-1}).

Table I. Summary of TG-MS in Ar 5.0 N as a function of PT: Initial mass loss due to H_2O desorption, total mass loss during heating ($20 \leqslant T/°C \leqslant 950$); ratio of maximum intensities of LT- and HT-O_2 peaks, *T*-ranges, and characteristics of LT- and HT-CO_2 peaks.

PT	$\Delta m(H_2O)$ (mass %)	Δm(total) (mass %)	LT/HT-O_2 (—)	LT-CO_2 (°C)	HT-CO_2 (°C)
PT 1: Cooled from 1130°C in static ambient air	-0.15 ± 0.01	1.78 ± 0.01	2.4	(130–50)[a]	(550–820)[b]
PT 2: *T* cycles in dynamic CO_2-rich atmosphere	-0.10 ± 0.01	1.94 ± 0.01	1.5	(200–575)[b]	(575–835)[b]
PT 3: *T* cycles in dynamic synthetic air	-0.08 ± 0.01	1.58 ± 0.01	2.8	(170–600)[a]	(—)[c]

[a] Significant peak in MS, but not in differential thermoanalysis (DTA) signal.
[b] Significant peaks in MS and DTA signals.
[c] Peaks insignificant in MS and DTA signals.

but much less pronounced, is perceptible with the sample after PT 1 at $T \sim 320°C$ (Fig. 1). After PT 2, a HT-CO_2 peak is observed with the maximum at $T \sim 765°C$, and a further increase of CO_2 desorption occurs at $T > 835°C$. The DTG signal indicates that the magnitude of HT-CO_2 desorption is almost on the order of the oxygen desorption from the perovskite, that is, of the LT-O_2 peak at $T \sim 475°C$.

PT 3: Thermal cycling in dynamic synthetic air.— BSCF powder was subjected to PT 1 followed by PT 3, that is, two heating/cooling cycles $20 < T/°C < 900$ with 5 K min^{-1} in dynamic synthetic air of 20 vol % O_2 + 0.04 vol % CO_2, the rest Ar (as described below). Figure 3 shows the TG-MS in Ar 5.0 N obtained after PT 3. Oxygen is released from the perovskite at $300 < T/°C < 950$, with the peaks of LT- and HT-O_2 at $T \sim 420$ and 820°C, respectively. The mass loss in the LT range $50 < T/°C < 200$ can again be ascribed to the desorption of H_2O. Various minor peaks of LT-CO_2 are evident, whereas no pronounced HT-CO_2 peak is observed. Further increase of the CO_2 desorption rate does not start until $T > 850°C$. The DTG signal shows that (apart from the minor release of H_2O at $T < 200°C$) the mass loss of the sample is determined almost exclusively by O_2 desorption.

Discussion of different PTs.— The characteristics of all three experiments are compared in Table I. The initial release of H_2O at $50 < T/°C < 200$ is observed with a mean magnitude of $\Delta m = -0.15 \pm 0.03$ mass %, irrespective of the PT. This may be due to traces of superficially adsorbed H_2O, as well as hydrates/hydroxides of the cations, which can be formed from minor amounts of second phases during storage at room temperature. SrO and BaO were reported to be susceptible for the formation of hydroxides,[5] but also more complex compounds such as $Sr_3Co_2O_5(OH)_x \cdot xH_2O$ were described.[27,28] However, the small magnitude of the effect makes an identification of the presumably small quantity of this second phase difficult.

The total mass loss upon heating from 20 to 950°C after PT 1 (Fig. 1) is mainly determined by the increase of the oxygen nonstoichiometry in the perovskite, but with noticeable superposition by the decomposition of carbonates at HT. This indicates that carbonates form during cooling from sinter temperatures in static ambient air, and that even in a CO_2- and O_2-free atmosphere (Ar 5.0 N) temperatures higher than 800°C may be required for complete desorption of CO_2 within reasonable time scales.

In comparison to PT 1, the sample subjected to high CO_2 contents during PT 2 (Fig. 2) shows a higher total mass loss upon heating to 950°C. Compared to PT 1 and PT 3 (Fig. 3), the relative intensity of the LT-O_2 peak ($T \sim 475°C$) with respect to the HT-O_2 peak ($T \sim 850°C$) decreases significantly after PT 2. Presumably due to a significant surface degradation, less oxygen is released from the perovskite during heating at $300 < T/°C < 700$, after the exposure to the CO_2-rich atmosphere.

The pronounced HT-CO_2 peak observed with the powders after PT 1 and PT 2 (Fig. 1 and 2) is not observed after PT 3 (Fig. 3). The DTG signal of PT 3 indicates that the mass loss at $T > 200°C$ is almost exclusively determined by O_2 release. While CO_2 desorption can still be detected, its magnitude is comparatively small. Supposedly, the dwell times of 2 h at 900°C applied during PT 3 (as later described) lead to the decomposition of residual carbonates remaining after PT 1 (Fig. 1). The reversible formation of carbonate during cooling with 5 K min^{-1} in the relatively CO_2-lean atmosphere is below the detection limit. Nevertheless, as will be discussed later, the effect can be detected after several days of exposure at 600°C. In direct comparison of the different PTs, the highest LT/HT-O_2 peak ratio, due to almost uninhibited oxygen exchange at LT ($300 < T/°C < 700$), is observed after PT 3 (Table I). In close correlation, PT 3 exhibits the lowest total mass loss, due to negligible CO_2 desorption.

Isotherms in a CO_2-rich atmosphere.— A CO_2-enriched test gas with the nominal O_2 content of ambient air (20 vol % O_2 + 5 vol % CO_2, the rest Ar) was used to test the stability of the powders at constant temperatures of 600–900°C. During 72 h of exposure at $600 \leqslant T/°C \leqslant 800$, BSCF shows a pronounced mass increase due to CO_2 (Fig. 4). The single isotherms are characterized by initial stages of mass loss, due to the increase of oxygen nonstoichiometry of the perovskite with increasing *T*, followed by a progressive mass increase due to carbonate formation. The increments of mass increase due to CO_2 are 1.19 ± 0.01 mass % (24 h, 600°C), 3.18 ± 0.01 mass % (24 h, 700°C), and 2.33 ± 0.01 mass % (24 h, 800°C). Figure 5 shows that the isotherm at 600°C, which was acquired starting from the fresh sample, is well described by a linear-parabolic rate law, $\Delta m/l + \Delta m^2/k = t$, indicating that the kinetics of carbonate formation is controlled simultaneously by the solid–gas interface reaction and by diffusion through the surface (carbonate) layer.[29] A fit to a parabolic rate law, $\Delta m^2 = k \times t$, assuming exclusively the diffusion through the surface (carbonate) layer to be rate-determining,[29] is given for comparison. The difference plots between the experimental data and the two models clearly state that the linear-parabolic rate law is more appropriate (Fig. 5).

During heating to $T > 800°C$ a sharp onset of mass loss due to the thermal decomposition of the carbonate occurs. The estimated decomposition temperature in CO_2-rich atmosphere is $T_d = 807°C$ (Fig. 6). Similarly, studies on BSCF-based devices reported that CO_2-induced degradation occurred at $T < 800°C$,[4] and that regeneration of the performance is possible at 800°C.[19]

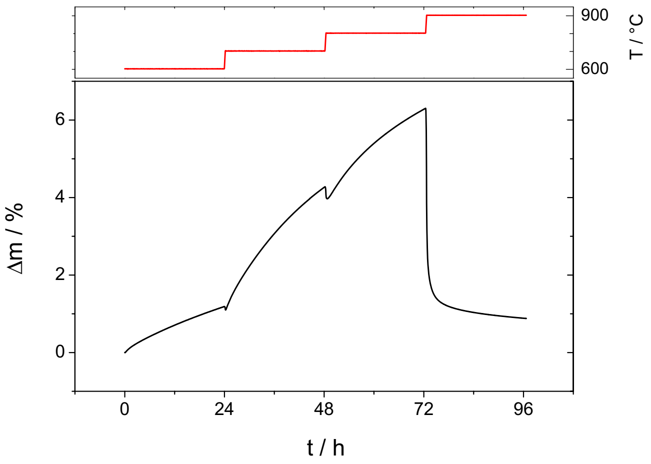

Figure 4. (Color online) Mass increase of BSCF in CO_2-rich atmosphere (20 vol % O_2 + 5 vol % CO_2, the rest Ar) during isotherms at 600–800°C and decomposition of carbonate upon heating to 900°C (compare detail in Fig. 6).

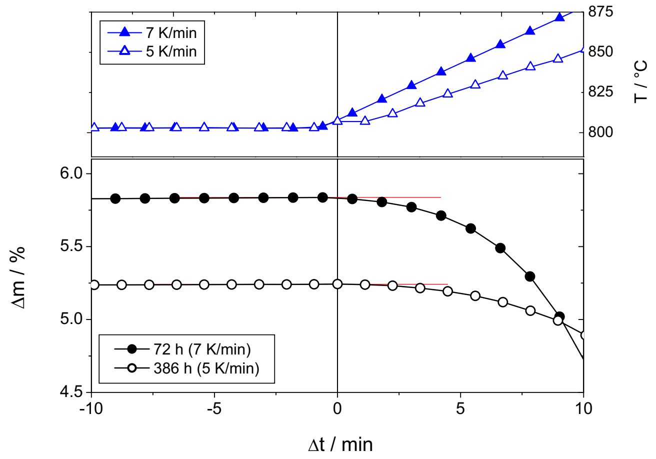

Figure 6. (Color online) Thermal decomposition of carbonate in CO_2-rich atmosphere (20 vol % O_2 + 5 vol % CO_2, the rest Ar) upon heating with 7 and 5 K min^{-1}; times of exposure at $T \leqslant 800°C$ were 72 and 386 h, respectively. The estimated decomposition temperature $T_d = 807°C$ is indicated by the vertical line.

Dynamic heating/cooling in a CO_2-rich atmosphere.— Figures 7 and 8 show the relative mass changes of BSCF powder samples during two consecutive heating/cooling cycles in a CO_2-rich atmosphere (20 vol % O_2 + 5 vol % CO_2, the rest Ar), where contributions of mass changes due to O_2 and CO_2 superimpose. For further analysis, comparison with the analogous reference experiments in CO_2-free atmosphere (20 vol % O_2, the rest Ar), showing exclusively the effects due to the T-dependence of the oxygen nonstoichiometry, is essential. During the first temperature cycle the initial mass of the reference sample (CO_2-free atmosphere) is by 0.18 ± 0.01 mass % smaller than the final mass (Fig. 7). The starting material, that is, powder cooled from 1130°C in ambient air, contains minor amounts of H_2O and LT-CO_2 which are lost at $T < 200°C$ (compare TG-MS in Fig. 1). The perovskite then becomes active for oxygen uptake in the range 250–350°C, compensating the oxygen deficiency which was created during cooling. Upon further heating the typical reversible oxygen exchange characteristics of the perovskite are observed at 350–900°C. During the cooling sequence in CO_2-free atmosphere oxygen uptake occurs down to 250°C.

The initial mass loss, due to H_2O desorption at $T < 200°C$ during the first heating sequence in CO_2-rich atmosphere, is identical to the reference experiment (Fig. 7). However, contrary to the CO_2-free atmosphere, the onset of oxygen uptake is shifted from $T \sim 250°C$ to higher temperatures, indicating that the decomposition of LT-CO_2 is inhibited in the CO_2-rich atmosphere. Mass loss due to oxygen vacancy formation in the perovskite is observed at 475–600°C, which is superimposed by mass increase due to CO_2 starting at 550–600°C (compare Fig. 9). The most prominent difference to the reference sample is the pronounced mass uptake in the interval 600–800°C, which is also observed under isothermal conditions (Fig. 4). During further heating, decomposition of the carbonate (superimposed by oxygen loss from the perovskite) is observed at $T \sim 810°C$. Upon cooling, reversible mass increase due to carbonate formation is starting at $T \sim 810°C$ (superimposed by oxygen uptake of the perovskite). In the CO_2-rich atmosphere, the sample mass saturates at $T < 350°C$.

During the second heating/cooling cycle (as recently discussed in more detail in Ref. 30), the reference experiment is almost exclusively determined by the highly reversible T-dependence of the oxygen nonstoichiometry at $T > 350°C$. The small thermal hysteresis of the reference curve at $T \sim 300°C$ is likely due to a minor oxygen

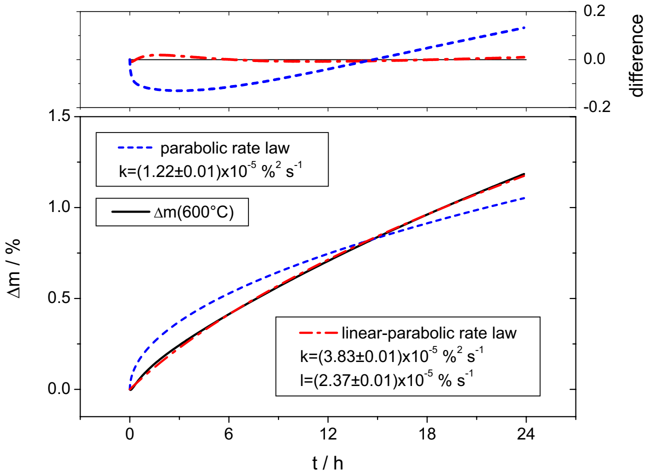

Figure 5. (Color online) Mass increase of BSCF in CO_2-rich atmosphere at 600°C (compare Fig. 4) with fits to different rate laws. Deviations between the experimental data and the fits are given for both models in the difference plot.

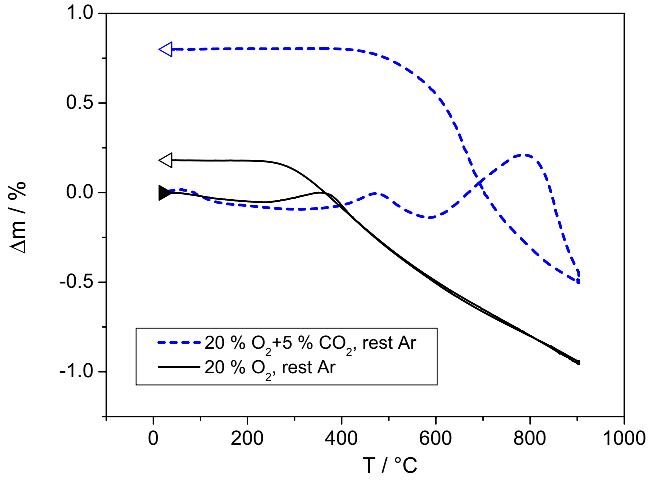

Figure 7. (Color online) First heating/cooling cycles of BSCF in CO_2-rich atmosphere compared to CO_2-free atmosphere. The cooling curves were recorded after 2 h dwell times at 900°C. Heating/cooling rates were 5 K min^{-1}.

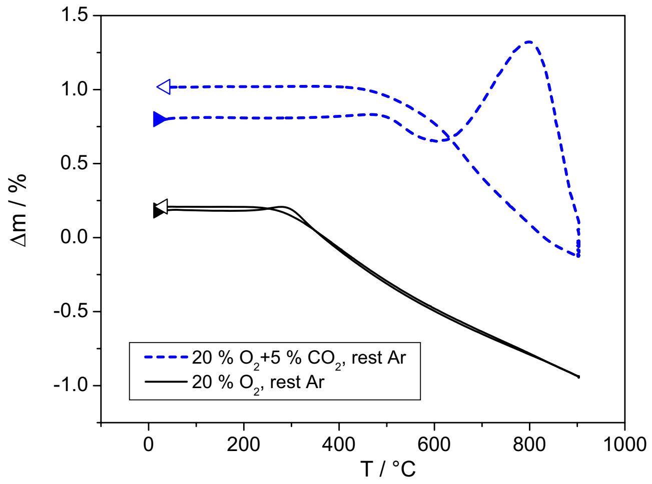

Figure 8. (Color online) Second heating/cooling cycles of BSCF in CO_2-rich atmosphere compared to CO_2-free atmosphere.[30] The cooling curves were recorded after 2 h dwell times at 900°C. Heating/cooling rates were 5 K min^{-1}.

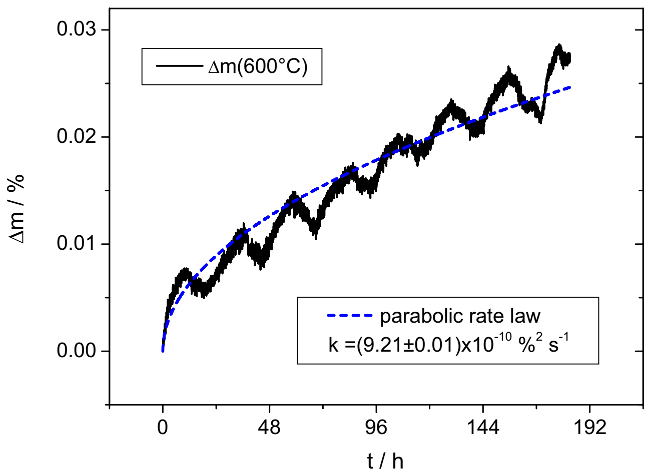

Figure 10. (Color online) Mass increase of BSCF in synthetic air at 600°C and tentative fit to a parabolic rate law.

deficiency, as observed much more pronouncedly in the first temperature cycle. During the second temperature cycle in the CO_2-rich atmosphere, the effects observed in the first sequence are qualitatively reproduced, quantitatively leading to a further increase of the final sample mass due to progressive CO_2 uptake (Fig. 8 and 9). As recently discussed,[30] the mass changes, which can mainly be ascribed to the reversible oxygen nonstoichiometry changes in the perovskite, are indicated by the parallel slopes in the Δm vs T plots during heating and cooling in both CO_2-free and CO_2-rich atmospheres (Fig. 7 and 8), and consequently by the horizontal sections in the difference plot (Fig. 9). Thus, the superposition of effects due to CO_2 can be detected at LT (300–500°C) and at HT (550–900°C), while the IT range (450–600°C) is mainly determined by oxygen exchange of the perovskite. Post-test analysis of the powder by TG-MS confirms the desorption of LT- and HT-CO_2, while the IT region is dominated by oxygen desorption (Fig. 2 and Table I).

Isotherm in synthetic air.— A test gas with the nominal O_2 and CO_2 content of ambient air, but with no further reactive components (20 vol % O_2 + 0.04 vol % CO_2, the rest Ar) was used to test the stability of BSCF powder in a CO_2-lean atmosphere at 600°C. The mass changes during exposure to synthetic air are close to the detection limit of the method. Nevertheless, a progressive increase of the sample mass is observed within 7.5 days (Fig. 10). The TG signal is superimposed by a 24 h periodic drift, due to minor changes of room temperature. However, as will be discussed later with electrical conductivity relaxation measurements, this apparently small CO_2 uptake is correlated to a significant degradation of the oxygen exchange kinetics at 600°C. A tentative fit to the parabolic rate law provides a rough estimate of the pCO_2-dependence of the carbonate formation kinetics. At constant $pO_2 = 0.20$ bar, mass increase at 600°C in CO_2-rich atmosphere ($pCO_2 = 5 \times 10^{-2}$ bar; Fig. 5) occurs with a parabolic rate constant $k \sim 10^{-5}$ mass $\%^2$ s^{-1}. In comparison, $k \sim 10^{-9}$ mass $\%^2$ s^{-1} is observed in synthetic air ($pCO_2 = 4 \times 10^{-4}$ bar) at 600°C (Fig. 10). The indicated pronounced dependence of the rate constants on pCO_2 is in agreement with earlier studies on oxygen permeable BSCF membranes which showed a pronounced increase of the degradation rate with increasing CO_2 concentration.[18]

Dynamic heating/cooling in synthetic air.— During the first heating step in synthetic air, mass loss due to the desorption of H_2O at $T < 200$°C occurs, as observed under various experimental conditions (e.g., Fig. 1-3 and 7). Figure 11 shows the second temperature cycle of BSCF in synthetic air, compared to the reference experiment in a

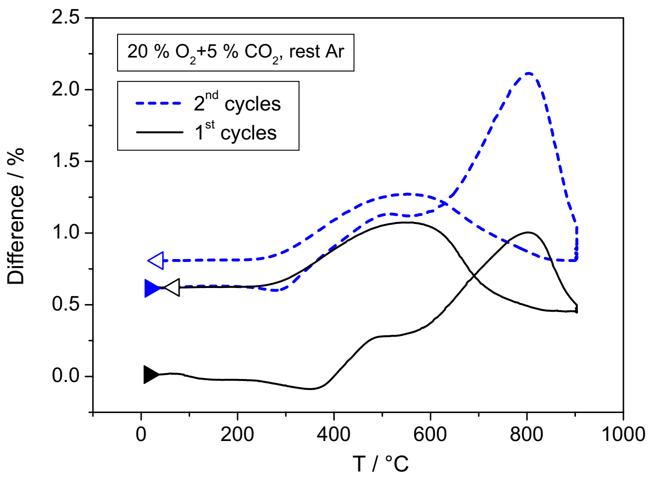

Figure 9. (Color online) Difference plots of mass changes in CO_2-rich and CO_2-free atmospheres for two consecutive heating/cooling cycles of BSCF (compare Fig. 7 and 8).

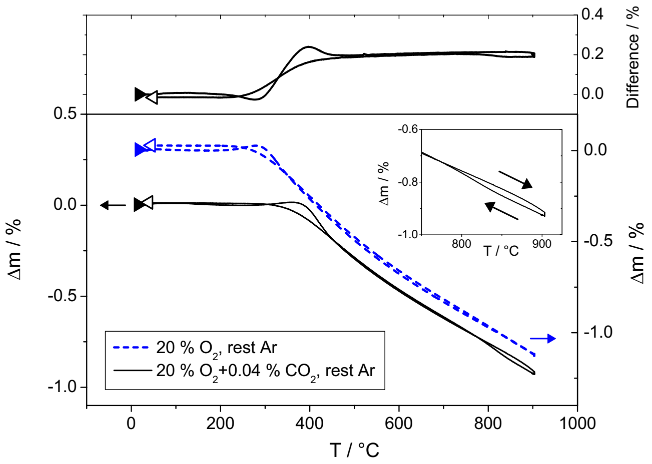

Figure 11. (Color online) Second heating/cooling cycles of BSCF in synthetic air compared to CO_2-free atmosphere and difference plot. The cooling curves were recorded after 2 h dwell times at 900°C. Heating/cooling rates were 5 K min^{-1}. The detail shows the HT hysteresis in synthetic air.

Table II. Surface oxygen exchange coefficients k_{chem}, chemical diffusion coefficients D_{chem}, and characteristic lengths $L_c = D_{chem}/k_{chem}$ of BSCF (L_s = 0.020 cm) at 600°C as a function of PT in comparison with literature data (L_s = 0.076 cm). The errors of the kinetic parameters are estimated to $\Delta k_{chem} = \pm 3\%$ and $\Delta D_{chem} = \pm 3\%$.

	Oxidation			Reduction		
PT	k^{ox}_{chem}/cm s^{-1}	D^{ox}_{chem}/cm^2 s^{-1}	L^{ox}_c/cm	k^{red}_{chem}/cm s^{-1}	D^{red}_{chem}/cm^2 s^{-1}	L^{red}_c/cm
As-prepared	5×10^{-5}	—	—	7.3×10^{-5}	2.1×10^{-7}	2.8×10^{-3}
3 days ambient air	2.4×10^{-5}	—	—	1.6×10^{-5}	—	—
7 days ambient air	2×10^{-5}	—	—	1.3×10^{-5}	—	—
7 days O_2–Ar at 600°C	2×10^{-5}	—	—	1.4×10^{-5}	—	—
7 days O_2–Ar at 825°C	5.9×10^{-4}	8.1×10^{-7}	1.4×10^{-3}	6.6×10^{-4}	6×10^{-7}	9×10^{-4}
O_2–Ar at 550–800°C[7]	4.7×10^{-4}	3.5×10^{-6}	7.6×10^{-3}	4.2×10^{-4}	2.1×10^{-6}	5×10^{-3}

CO_2-free atmosphere. Similar to the experiment in a CO_2-rich atmosphere, the onset of oxygen vacancy formation is shifted toward higher temperatures in synthetic air, indicating a CO_2-induced passivation of the surface. The effect is confirmed by the desorption of LT-CO_2 in post-test analysis by TG-MS (Fig. 3). Narrow thermal hystereses, as previously discussed, occur in both curves at the onsets of oxygen release at 300 and 400°C, respectively.

Due to the relatively small mass changes induced by CO_2, which are close to the detection limit even during long-term exposure (Fig. 10), the characteristics of both curves are mainly determined by the comparatively high mass changes originating in the reversible oxygen exchange of the perovskite (compare also the post-test analysis by TG-MS in Fig. 3). Nevertheless, characteristic features such as the additional narrow hysteresis at $T \sim 800°C$, due to decomposition and reversible formation of HT-CO_2, can be observed during the experiment in synthetic air.

Conductivity relaxation measurements.— Conductivity relaxation was studied on a thin, densely sintered BSCF sample (L_s = 0.0200 cm) at 600°C as a function of PT. The kinetic parameters, k_{chem} and D_{chem}, as well as the characteristic length $L_c = D_{chem}/k_{chem}$,[31] are summarized in Table II. The fresh sample was heated to 700°C and cooled back to 600°C in a dynamic CO_2-free atmosphere with 2 K min^{-1}. The kinetic parameters of the first measurements performed on the as-prepared sample at 600°C in a defined O_2–Ar atmosphere (curves 1 in Fig. 12) indicate that the oxygen exchange kinetics is on the borderline between the mixed-controlled and the surface-controlled regime. Both k_{chem} and D_{chem} can be determined with the reduction process, but the small ratio $L_s/L_c \sim 7$ indicates that the kinetics is close to the surface-controlled regime (Table II). From the corresponding oxidation process, which occurs slightly faster than the reduction process, only the parameter k_{chem} can be reliably determined at the given L_s. To assess the influence of CO_2-containing atmospheres on the oxygen exchange kinetics at 600°C, the sample was exposed to ambient air for 3 days. Afterward, CR indicates a decrease of k_{chem} for both oxidation and reduction by a factor of 2–5 (Table II). As a consequence, the surface exchange becomes rate-determining in both processes.

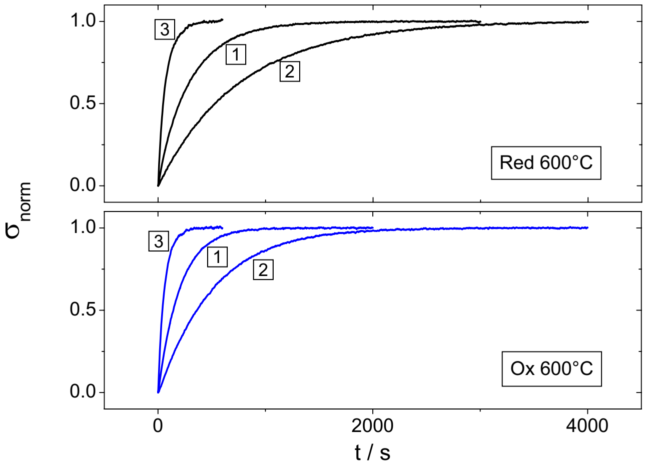

Figure 12. (Color online) Oxidation and reduction kinetics of BSCF at 600°C; the normalized electrical conductivities of (1) as-prepared sample, (2) degraded sample (after 7 days in ambient air), and (3) regenerated sample (after 7 days at 825°C in CO_2-free atmosphere) are compared. The corresponding kinetic parameters are given in Table II.

According to thermoanalysis, this degeneration can be ascribed to the adsorption of CO_2 and progressive carbonate formation of BSCF in CO_2-containing atmospheres, which can be expected to strongly reduce the activity of the surface for oxygen reduction. Another 7 days of exposure to ambient air at 600°C led to a further, but less-pronounced decrease of the k_{chem} values (curves 2 in Fig. 12 and Table II). Similarly, electrochemical impedance spectroscopy studies on a BSCF-based SOFC cell indicated a significant increase of the interface resistance with CO_2-containing oxidants at 600°C.[19]

Regeneration attempted at 600°C in a dynamic CO_2-free atmosphere (1 vol % O_2, the rest Ar) resulted only in an insignificant increase of the surface exchange coefficients (Table II). This is in agreement with our previous TG studies, providing evidence that regeneration in a CO_2-free atmosphere (20 vol % O_2, the rest Ar) at 600°C is kinetically slow and that higher temperatures are required for full recovery within reasonable time scales.[30] Sensitive TG-MS in a CO_2- and O_2-free atmosphere (Ar 5.0 N; Fig. 1 and 2) shows the onset of HT-CO_2 desorption at 550–575°C, with the rate of regeneration increasing at $T > 600°C$. For complete regeneration, the sample was annealed for 7 days at 825°C, that is, well above the onset of carbonate decomposition at 807°C determined by TG (Fig. 6). After cooling back to 600°C, the sample showed strongly activated kinetics (curves 3 in Fig. 12), which exceeded the initial values of the as-prepared state. The kinetic parameters of the regenerated sample are in good agreement with previous results on the oxygen exchange kinetics of a macroscopic BSCF sample ($L_s \sim 0.0760$ cm) obtained at 600°C in a CO_2-free atmosphere[7] (Table II). Obviously, the parameters obtained with the as-prepared sample (sintered and stored in ambient air; conditioned at T_{max} = 700°C and cooled to 600°C) during the first measurement series represent an intermediate between the degraded and the fully regenerated state (after T_{max} = 825°C). Consistently, the kinetics of the as-prepared sample is found between the mixed and the surface controlled regime, the degraded sample shows unambiguously surface controlled kinetics, and a mixed controlled regime is evident after regeneration. Thus, in agreement with thermoanalysis, CR measurements show that carbonates, which form during cooling and storage in ambient air, may remain stable up to 700°C for considerable time scales, inhibiting the surface oxygen exchange.

Conclusions

Significant carbonate formation of BSCF powders in CO_2-containing atmospheres is confirmed by precision TG. At

300–400°C the surface of BSCF is passivated with respect to oxygen exchange at $4 \times 10^{-4} \leqslant pCO_2/\text{bar} \leqslant 5 \times 10^{-2}$. A pronounced mass increase at 600–800°C is observed in CO_2-rich atmospheres (20 vol % O_2 + 5 vol % CO_2, the rest Ar). With decreasing pCO_2, the effect is still evident but less easily detected by TG. Complementary CR measurements can be regarded as a highly sensitive probe, because the surface exchange kinetics of a dense sample shows a significant decrease after exposure to small amounts of CO_2 in ambient air at 600°C. Both TG and CR indicate consistently that regeneration via decomposition of the carbonate is possible. Nevertheless, temperatures higher than 800°C are required for the process to occur within reasonable time scales. The present results imply a severe long-term degradation of the performance of BSCF cathodes operated at IT (600–750°C) in ambient air. Because small amounts of carbonate result in a substantial decrease of the activity of BSCF for oxygen reduction, the application of these cathodes with CO_2-containing oxidants at $T < 800°C$ cannot be recommended.

Acknowledgments

This work was supported by the EC within the integrated project SOFC600 under contract no. 020089. The authors thank P. Ried (EMPA/Switzerland) for preparation of the BSCF powders, and G. Moser (University of Leoben/Austria) for assistance with preparation of CR samples.

University of Leoben assisted in meeting the publication costs of this article.

References

1. Z. Shao and S. M. Haile, *Nature (London)*, **431**, 170 (2004).
2. Z. Duan, M. Yang, A. Yan, Z. Hou, Y. Dong, Y. Chong, M. Cheng, and W. Yang, *J. Power Sources*, **160**, 57 (2006).
3. W. Zhou, R. Ran, Z. Shao, W. Jin, and N. Xu, *J. Power Sources*, **182**, 24 (2008).
4. Z. Shao, W. Yang, Y. Cong, H. Dong, J. Tong, and G. Xiong, *J. Membr. Sci.*, **172**, 177 (2000).
5. Z. Shao, G. Xiong, J. Tong, H. Dong, and W. Yang, *Sep. Purif. Technol.*, **25**, 419 (2001).
6. H. Wang, Y. Cong, and W. S. Yang, *J. Membr. Sci.*, **210**, 259 (2002).
7. E. Bucher, A. Egger, P. Ried, W. Sitte, and P. Holtappels, *Solid State Ionics*, **179**, 1032 (2008).
8. E. Girdauskaite, H. Ullmann, M. Al Daroukh, V. Vashook, M. Bülow, and U. Guth, *J. Solid State Electrochem.*, **11**, 469 (2007).
9. J. F. Vente, S. McIntosh, W. G. Haije, and H. J. M. Bouwmeester, *J. Solid State Electrochem.*, **10**, 581 (2006).
10. S. McIntosh, J. F. Vente, W. G. Haije, D. H. A. Blank, and H. J. M. Bouwmeester, *Solid State Ionics*, **177**, 1737 (2006).
11. B. Wei, Z. Lu, X. Huang, J. Miao, X. Sha, X. Xin, and W. Su, *J. Eur. Ceram. Soc.*, **26**, 2827 (2006).
12. P. Zeng, Z. Chen, W. Zhou, H. Gu, Z. Shao, and S. Liu, *J. Membr. Sci.*, **291**, 148 (2007).
13. H. Wang, C. Tablet, A. Feldhoff, and J. Caro, *J. Membr. Sci.*, **262**, 20 (2005).
14. H. Lu, Y. Cong, and W. S. Yang, *Solid State Ionics*, **177**, 595 (2006).
15. S. Svarcova, K. Wiik, J. Tolchard, H. J. M. Bouwmeester, and T. Grande, *Solid State Ionics*, **178**, 1787 (2008).
16. F. S. Baumann, J. Fleig, H.-U. Habermeier, and J. Maier, *Solid State Ionics*, **177**, 3187 (2006).
17. F. S. Baumann, J. Maier, and J. Fleig, *Solid State Ionics*, **179**, 1198 (2008).
18. M. Arnold, H. Wang, and A. Feldhoff, *J. Membr. Sci.*, **293**, 44 (2007).
19. A. Yan, M. Cheng, Y. Dong, W. Yang, V. Maragou, S. Song, and P. Tsiakaras, *Appl. Catal., B*, **66**, 64 (2006).
20. J. M. Criado, M. J. Dianez, M. Macias, and M. C. Paradas, *Thermochim. Acta*, **171**, 229 (1990).
21. I. A. Kiseleva, A. R. Kotelnikov, K. V. Martynov, L. P. Ogorodova, and J. K. Kabalov, *Phys. Chem. Miner.*, **21**, 392 (1994).
22. A. Yan, V. Maragou, A. Arico, M. Cheng, and P. Tsiakaras, *Appl. Catal., B*, **76**, 320 (2007).
23. P. Ried, E. Bucher, W. Preis, W. Sitte, and P. Holtappels, *ECS Trans.*, **7**(1), 1217 (2007).
24. L. J. van der Pauw, *Philips Res. Rep.*, **13**, 1 (1958).
25. W. Preis, E. Bucher, and W. Sitte, *Solid State Ionics*, **175**, 393 (2004).
26. M. W. den Otter, H. J. M. Bouwmeester, B. A. Boukamp, and H. Verweij, *J. Electrochem. Soc.*, **148**, J1 (2001).
27. L. Viciu, H. W. Zandbergen, Q. Xu, Q. Huang, M. Lee, and R. J. Cava, *J. Solid State Chem.*, **179**, 500 (2006).
28. D. Pelloquin, N. Barrier, A. Maignan, and V. Caignaert, *Solid State Sci.*, **7**, 853 (2005).
29. C. Wagner and K. Grünewald, *Z. Phys. Chem. Abt. B*, **40**, 455 (1938).
30. E. Bucher, G. B. Caraman, and W. Sitte, in *8th European SOFC Forum*, R. Steinberger-Wilckens, Editor, p. A0603, Lucerne, Switzerland (2008).
31. P. J. Gellings and H. J. M. Bouwmeester, *The CRC Handbook of Solid State Electrochemistry*, p. 506, CRC Press, Boca Raton (1997).

Available online at www.sciencedirect.com

ScienceDirect

Solid State Ionics 179 (2008) 1032 – 1035

SOLID STATE IONICS

www.elsevier.com/locate/ssi

Oxygen nonstoichiometry and exchange kinetics of $Ba_{0.5}Sr_{0.5}Co_{0.8}Fe_{0.2}O_{3-\delta}$

Edith Bucher [a],*, Andreas Egger [a], Peter Ried [b], Werner Sitte [a], Peter Holtappels [b]

[a] *Chair of Physical Chemistry, University of Leoben, Franz-Josef-Strasse 18, A-8700 Leoben, Austria*
[b] *Empa, Laboratory for High Performance Ceramics, Ueberlandstrasse 129, CH-8600 Duebendorf, Switzerland*

Received 18 June 2007; received in revised form 18 January 2008; accepted 24 January 2008

Abstract

The oxygen nonstoichiometry of $Ba_{0.5}Sr_{0.5}Co_{0.8}Fe_{0.2}O_{3-\delta}$ (BSCF5582) was investigated by thermogravimetry resulting in values of $2.40<(3-\delta)<2.57$ for the equilibrium oxygen content in the range $600 \leq T/°C \leq 900$ and $1E-4<pO_2/bar<0.4$. The oxygen exchange kinetics was studied by electrical conductivity relaxation as a function of temperature in the range $550 \leq T/°C \leq 725$ with chemical diffusion coefficients $1E-6<D_{chem}/cm^2\ s^{-1}<3E-5$ and surface exchange coefficients $2E-4<k_{chem}/cm\ s^{-1}<3E-3$. The activation energies of the kinetic parameters amount to $E_a(D_{chem})=86\pm8$ kJ mol^{-1} and $E_a(k_{chem})=64\pm12$ kJ mol^{-1}. Self-diffusion and surface exchange coefficients, as well as ionic conductivities are estimated.

Keywords: Perovskite oxide; BSCF; Oxygen nonstoichiometry; Oxygen exchange; Conductivity relaxation

---

1. Introduction

The mixed conducting perovskite-type oxides (La,Sr)(Co,Fe)$O_{3-\delta}$ have been widely investigated with respect to basic mass and charge transport properties as well as for application in solid oxide fuel cells (SOFCs) and oxygen permeable membranes. While $SrCo_{0.8}Fe_{0.2}O_{3-\delta}$ exhibits the highest oxygen permeability in this series [1], it has the disadvantage of undergoing a transition to the oxygen vacancy ordered brownmillerite structure at $T<800$ °C [2,3]. The perovskite phase can be stabilised by Ba-substitution leading to the composition of $Ba_{0.5}Sr_{0.5}Co_{0.8}Fe_{0.2}O_{3-\delta}$ (BSCF5582), which was proposed as a superior SOFC cathode material [4,5] and as a high-performance oxygen permeable membrane [6–9]. The cubic perovskite structure with disordered oxygen vacancies is maintained in BSCF5582 even at exceptionally high oxygen deficit ($0.3<\delta<0.8$ at $600<T/°C<900$) [7,9,10]. This clearly exceeds typical values of comparable perovskites, e.g. $La_{0.6}Sr_{0.4}Co_{0.8}Fe_{0.2}O_{3-\delta}$ with $0.15<\delta<0.40$ at 700–900 °C and $1E-4<pO_2/bar<1$ [11].

So far, the oxygen exchange properties of BSCF5582 have mainly been investigated by the permeation method [6–9], studying the steady-state oxygen permeation flux in a high pO_2 gradient, while investigations by non-steady-state methods close to equilibrium are scarce [12]. For potential application in intermediate temperature SOFC cathodes the dependence of the oxygen exchange properties on temperature and on oxygen partial pressure under operating conditions of the SOFC are of special interest. In a recent study we applied the conductivity relaxation method to investigate the oxygen partial pressure dependence of the chemical surface exchange coefficients (k_{chem}) and the chemical diffusion coefficients (D_{chem}) at 600 and 700 °C [13]. The present work will focus on the kinetic parameters as a function of T between 550 and 725 °C. In combination with thermogravimetric investigations of the oxygen nonstoichiometry as a function of T and pO_2 self-diffusion coefficients and oxygen exchange coefficients as well as ionic conductivities will be estimated.

2. Experimental

BSCF5582 powder was prepared by spray pyrolysis and characterised with regard to phase purity and elemental composition by XRD and ICP-AES, respectively [13].

The oxygen nonstoichiometry δ was investigated by use of a precision thermobalance (Setaram, TAG 2416) as a function of

---

* Corresponding author.
E-mail address: Edith.Bucher@mu-leoben.at (E. Bucher).

doi:10.1016/j.ssi.2008.01.089

temperature and oxygen partial pressure. During isobaric experiments two temperature cycles were performed, heating from 20 to 900 °C and cooling back to 20 °C with rates of 1.3–5 K min^{-1}. Temperature ramps were chosen sufficiently low to obtain negligible thermal hystereses of δ (below ±0.004 in the range $600 \leq T/°\text{C} \leq 900$). Dynamic sequences were followed by dwell times of 1–2 h, where mass changes were usually below ±1 µg. Isothermal experiments were performed by equilibration of the sample at various oxygen partial pressures $1\text{E}-4 < pO_2/\text{bar} < 0.4$ until the corresponding mass signal was constant within ±1 µg. Sequentially, the pO_2 steps were performed from oxidising towards reducing atmospheres. Depending on T and pO_2, the required equilibration times between successive pO_2 steps were 1–24 h. Defined gas atmospheres were obtained by mixing Ar (5.0), O_2 (4.5), and Ar + 1 vol.% O_2 using mass flow controllers (Mycrolis, FC2700). As a reference point the absolute oxygen nonstoichiometry was determined by equilibration of a sample at 700 °C and $pO_2 = 0.37$ bar and subsequent total reduction in a mixture of Ar (5.0) and Ar + 3 vol.% H_2 at 900 °C. The oxygen partial pressure of the reducing Ar/H_2 atmosphere amounted to $pO_2 = 2.6\text{E}-21$ bar. The mass loss during reduction at 900 °C was monitored until the sample mass remained constant within ±1 µg for 24 h. XRD of the residue confirmed the total decomposition of the perovskite phase and showed characteristic reflections of Co/Fe.

The temperature dependences of the kinetic parameters (D_{chem} and k_{chem}) were investigated by dc conductivity relaxation experiments as a function of temperature ($550 \leq T/°\text{C} \leq 725$). During cooling from 700 to 550 °C experiments were performed at constant temperatures in intervals of 50 K. Subsequently, a heating run was performed with experiments in intervals of 25 K, from 550 up to 725 °C. Results obtained upon cooling were in good agreement with those obtained upon heating. Small oxidation and reduction steps between $pO_{2,\text{Hi}} = 2.1\text{E}-2$ bar and $pO_{2,\text{Lo}} = 9.0\text{E}-3$ bar were alternately applied to study the oxygen exchange kinetics close to equilibrium. Usually, a sequence of 2–3 reduction/oxidation cycles was performed at each T. Intermittent to successive pO_2 steps, the sample signal was monitored to ensure that complete equilibrium with the gas phase was obtained. The minimum factor of equilibration time relative to the duration of the experiment was 3. During the equilibration intervals between successive experiments the normalised electronic conductivity remained constant within ±1%. Oxygen partial pressures were adjusted by mixtures of O_2 (4.5) and Ar + 1 vol.%O_2 using mass flow controllers (Hastings, HFC 302). Fast pO_2 steps were realised by switching between two continuous gas streams with flow rates of 1.6 l h^{-1}. The experimental relaxation curves of a dense disc shaped sample (thickness 0.760 mm) with 4 point-contacts in van der Pauw geometry [14] were monitored via the voltage response at constant dc current with a combined high-impedance multimeter and power source (Keithley, 2400). The transient response of the gas phase (finite flush time of the reactor) was separately determined in a series of experiments with the empty reactor using the *in-situ* oxygen sensor described below. An average flush time $\tau = 4.8 \pm 0.5$ s was obtained, where reduction experiments were usually slightly faster than oxidation experiments with a difference of approximately 0.5 s. The normalised electronic conductivity was analysed by nonlinear least squares fits to the solution function of the appropriate diffusion equations, taking into account the finite flush time of the reactor [15,16], using a constant $\tau = 5$ s.

For *in-situ* measurements of the oxygen partial pressure in both thermogravimetry and conductivity relaxation experiments potentiometric oxygen sensors with Ir/IrO_2 reference (Setnag) were applied. Estimated experimental errors $\Delta T = \pm 0.5$ K, $\Delta pO_2 = \pm 2\%$, and $\Delta\delta = \pm 0.007$, and propagated errors are given as one standard deviation.

3. Results and discussion

3.1. Oxygen nonstoichiometry

The oxygen deficit of $Ba_{0.5}Sr_{0.5}Co_{0.8}Fe_{0.2}O_{3-\delta}$ is given as a function of T and pO_2 in Fig. 1. Isothermal experiments at 700–900 °C and intersections of isobaric experiments at 600–900 °C are in good agreement with each other. The oxygen nonstoichiometry increases continuously with increasing temperature and decreasing pO_2. No evidence for a transition to an ordered brownmillerite structure ($ABO_{2.5}$) at $\delta \to 0.5$ was observed.

In literature few studies on the oxygen nonstoichiometry of BSCF5582 are available. While trends in δ vs. pO_2 and vs. T are similar, discrepancies on the absolute values of δ are found. For example, data obtained at 700 °C by thermogravimetry range from $\delta = 0.26$ ($pO_2 = 0.21$ bar) [7] and $\delta = 0.34$ ($pO_2 = 1.0$ bar) [10] to $\delta = 0.68$ (0.21 bar) [9]. Vente et al. [9] also reported values determined by *in-situ* neutron diffraction at 700 °C, e.g. $\delta = 0.69$ ($pO_2 = 1.0$ bar). The oxygen nonstoichiometry as determined in the present study at 700 °C, $\delta = 0.46$ ($pO_2 = 0.21$ bar), Fig. 1, is between the upper and lower limits of currently available literature data.

The thermodynamic factor of oxygen γ_O [17] was obtained according to

$$\gamma_O = \frac{1}{2}\left(\frac{\partial \ln pO_2}{\partial \ln(3-\delta)}\right)_T \tag{1}$$

by linear regression. With good linear correlation of ln pO_2 vs. ln $(3-\delta)$ ($R^2 > 0.98$), γ_O was assumed constant over the pO_2

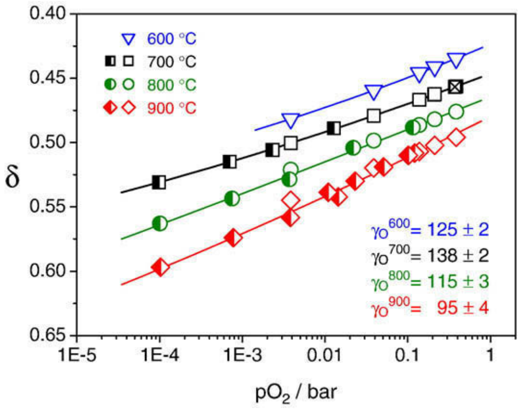

Fig. 1. Oxygen nonstoichiometry δ and thermodynamic factor of oxygen γ_O (Eq. (1)) of BSCF5582 at 600–900 °C. Results from isotherms (half filled symbols) are compared with isobars (open symbols). The reference point (☒) was obtained by total reduction in Ar–H_2. The experimental error is estimated to $\delta \pm 0.007$. Lines are a guide to the eye.

range under investigation. Values obtained at 600–900 °C are given in Fig. 1.

Fig. 2 shows derivatives of cooling curves obtained after equilibration at 900 °C and different oxygen partial pressures $4E-2 < pO_2/\text{bar} < 4E-1$. The high temperature region 600–900 °C is characterised by a continuous mass loss. The pronounced high temperature maximum with subsequent relaxation $d\delta/dT \rightarrow 0$ which is characteristic for the perovskite–brownmillerite transition of $SrCo_{0.8}Fe_{0.2}O_{3-\delta}$ [6,18] is absent. The low temperature maximum at approximately 380 °C coincides with a change in the thermal expansion coefficient and a maximum in the electronic conductivity vs. T [13]. At $T < 175$ °C the oxygen exchange is frozen in due to kinetic reasons and $d\delta/dT \rightarrow 0$. Oxygen nonstoichiometries at room temperature vary between $\delta_{RT} = 0.33$ ($pO_2 = 3.8E-1$ bar) and $\delta_{RT} = 0.37$ ($pO_2 = 3.9E-2$ bar).

3.2. Oxygen exchange kinetics

The activation energies of D_{chem} and k_{chem} were determined from the temperature dependences of both parameters in the range $550 \leq T/°C \leq 725$, Figs. 3 and 4, to 86±8 and 64±12 kJ mol^{-1}, respectively. With increasingly fast kinetics the accessible upper temperature was limited by the finite flush time of the reactor. Towards lower temperatures the deviations between experimental data and the present diffusion model increased. Possible reasons are kinetic limitations, or a change in the diffusion mechanism, e.g. grain boundary limited diffusion [19].

At constant T, the surface exchange coefficient is by approximately 2 orders of magnitude higher than the chemical diffusion coefficient. Both parameters exceed those of state-of-the-art IT-SOFC cathode materials, e.g. $La_{0.6}Sr_{0.4}Co_{0.2}Fe_{0.8}O_{3-\delta}$ with $2E-6 < k_{chem}/\text{cm s}^{-1} < 1E-3$ and $5E-8 < D_{chem}/\text{cm}^2\text{ s}^{-1} < 2E-6$ at 700 °C [20], or $(La_{0.6}Sr_{0.4})_{0.99}Co_{0.2}Fe_{0.8}O_{3-\delta}$ with $6E-5 < k_{chem}/\text{cm s}^{-1} < 4E-4$ and $2E-6 < D_{chem}/\text{cm}^2\text{ s}^{-1} < 6E-6$ at 800 °C [21].

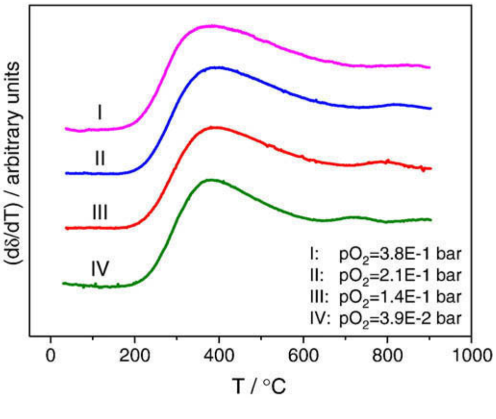

Fig. 2. Numerical derivatives of the oxygen nonstoichiometry δ of BSCF5582 vs. temperature. Curves were obtained upon cooling after equilibration at 900 °C and various oxygen partial pressures (I–IV). Cooling rates were 5 K min^{-1} (I–III) and 2.5 K min^{-1} (IV).

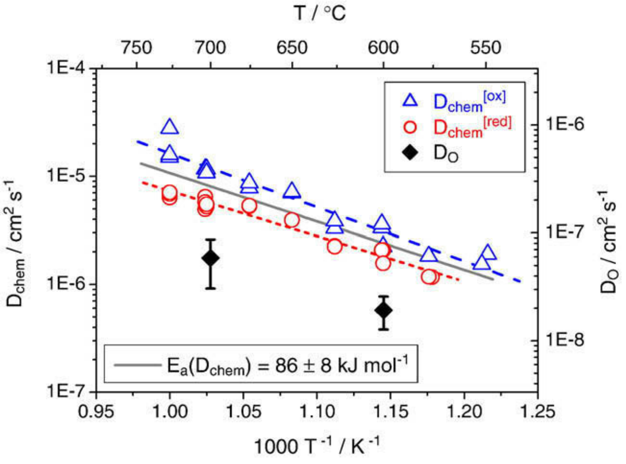

Fig. 3. Arrhenius plot with calculated mean activation energy (solid line) for chemical diffusion coefficients of BSCF5582. Oxidation and reduction steps between $pO_{2,Hi} = 2.1E-2$ bar and $pO_{2,Lo} = 9.0E-3$ bar are compared. Dashed lines represent $E_a(D_{chem}^{[ox]}) = 95 \pm 6$ kJ mol^{-1} and $E_a(D_{chem}^{[red]}) = 80 \pm 8$ kJ mol^{-1}. Self-diffusion coefficients are estimated via the thermodynamic factor, error bars indicate one standard deviation.

In Fig. 3 an offset between D_{chem} obtained from oxidation and reduction steps is observed. The same effect is perceptible with k_{chem} at 600–725 °C in Fig. 4. Similar discrepancies for conductivity relaxation experiments on $La_{0.5}Sr_{0.5}CoO_{3-\delta}$, $La_{0.6}Sr_{0.4}Co_{1-y}Fe_yO_{3-\delta}$, and $La_{0.5}Sr_{0.5}Fe_{0.8}Ga_{0.2}O_{3-\delta}$ were attributed to the determining influence of the target pO_2 and limitations of the experimental setup [20,22–25]. Since in our study systematically $D_{chem}^{[ox]} > D_{chem}^{[red]}$ and mostly $k_{chem}^{[ox]} > k_{chem}^{[red]}$, the offset could originate in the pronounced positive pO_2 dependences of the parameters, e.g. $D_{chem} \propto pO_2^{(0.6 \pm 0.1)}$ and $k_{chem} \propto pO_2^{(0.6 \pm 0.1)}$ at 700 °C [13]. Further studies with systematic variation of the magnitude and direction of the pO_2 step would be required to investigate this effect.

Within the limits of error, no explicit temperature dependence of L_c in the range $550 \leq T/°C \leq 725$ can be given. The mean critical length resulting from the ratio D_{chem}/k_{chem} of experimental data in Figs. 3 and 4 is $L_c = 0.055 \pm 0.027$ mm. Comparison of L_c with half the sample thickness $L_s/2 = 0.380$ mm confirms that the oxygen exchange kinetics in the T and pO_2 ranges under investigation is determined by both D_{chem} and k_{chem} (mixed regime).

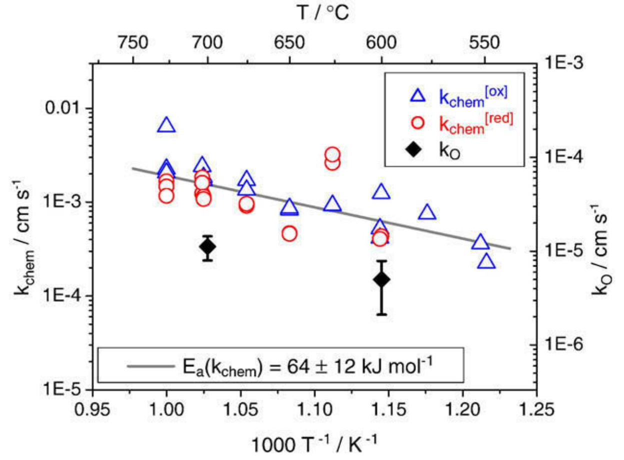

Fig. 4. Arrhenius plot with calculated activation energy for chemical surface exchange coefficients of BSCF5582. Oxidation and reduction steps between $pO_{2,Hi} = 2.1E-2$ bar and $pO_{2,Lo} = 9.0E-3$ bar are compared. Self surface exchange coefficients are estimated via the thermodynamic factor, error bars indicate one standard deviation.

Via the thermodynamic factor, Fig. 1, self-diffusion coefficients D_O and surface exchange coefficients k_O at 600 and 700 °C (Figs. 3 and 4) were estimated from $D_{chem}=D_O\gamma_O$ and $k_{chem}\approx k_O\gamma_O$ [26,27]. Further, the ionic conductivity was obtained from D_O according to the Nernst–Einstein relation [17]

$$\sigma_O = \frac{4F^2(3-\delta)D_O}{RTV_m} \tag{2}$$

where $V_m=38.3\pm0.3$ cm^3 mol^{-1} was used as the mean molar volume based on available XRD data in air and argon [8,10]. The calculated ionic conductivities amount to $\sigma_O=0.006\pm0.002$ S cm^{-1} (600 °C) and $\sigma_O=0.018\pm0.008$ S cm^{-1} (700 °C).

4. Conclusions

At $550\leq T/°C\leq 725$ the kinetic parameters of BSCF5582 $1E-6<D_{chem}/cm^2\ s^{-1}<3E-5$ and $2E-4<k_{chem}/cm\ s^{-1}<3E-3$ are higher than those of comparable IT-SOFC cathode materials, e.g. $La_{0.6}Sr_{0.4}Co_{0.2}Fe_{0.8}O_{3-\delta}$. BSCF5582 combines exceptionally fast oxygen exchange kinetics in the intermediate temperature range with moderate activation energies $E_a(D_{chem})=86\pm8$ kJ mol^{-1} and $E_a(k_{chem})=64\pm12$ kJ mol^{-1}. With $0.43<\delta<0.60$ at 600–900 °C and $1E-4<pO_2/bar<0.4$ bar BSCF5582 exhibits a high concentration of oxygen vacancies in a stable perovskite matrix. Estimates based on the magnitude of the oxygen nonstoichiometry and the chemical diffusion coefficients indicate high ionic conductivities of 0.01–0.02 S cm^{-1} at 600–700 °C. These features support the application of BSCF5582 in IT-SOFCs as cathodes with low polarisation resistance even with reducing the operating temperatures towards 600 °C.

Acknowledgment

Financial support by the EC within the integrated project SOFC600 (contract no. 020089) is gratefully acknowledged.

References

[1] Y. Teraoka, H.M. Zhang, H.-M. Furukawa, N. Yamazoe, Chem. Lett. 14 (1985) 1743.
[2] N. Grunbaum, L. Mogni, F. Prado, A. Caneiro, J. Solid State Chem. 177 (2004) 2350.
[3] L.M. Liu, T.H. Lee, Y.L. Qiu, Y.L. Yang, A.J. Jacobson, Mater. Res. Bull. 31 (1996) 29.
[4] Z. Shao, S.M. Haile, Nature 431 (2004) 170.
[5] Z. Duan, M. Yang, A. Yan, Z. Hou, Y. Dong, Y. Chong, M. Cheng, W. Yang, J. Power Sources 160 (2006) 57.
[6] Z. Shao, G. Xiong, J. Tong, H. Dong, W. Yang, Separ. Purif. Technol. 25 (2001) 419.
[7] H. Wang, Y. Cong, W.S. Yang, J. Membr. Sci. 210 (2002) 259.
[8] H. Lu, Y. Cong, W.S. Yang, Solid State Ionics 177 (2006) 595.
[9] J.F. Vente, S. McIntosh, W.G. Haije, H.J.M. Bouwmeester, J. Solid State Electrochem. 10 (2006) 581.
[10] E. Girdauskaite, H. Ullmann, M. Al Daroukh, V. Vashook, M. Bülow, U. Guth, J. Solid State Electrochem. 7 (2007) 469.
[11] E. Bucher, W. Sitte, G.B. Caraman, V.A. Cherepanov, T.V. Aksenova, M. V. Ananyev, Solid State Ionics 177 (2006) 3109.
[12] B. Wei, Z. Lu, X. Huang, J. Miao, X. Sha, X. Xin, W. Su, J. Eur. Ceram. Soc. 26 (2006) 2827.
[13] P. Ried, E. Bucher, W. Preis, W. Sitte, P. Holtappels, Proc. 10th International Symposium on Solid Oxide Fuel Cells (SOFC-X), Nara, Japan, 2007, p. 1217.
[14] L.J. van der Pauw, Philips Res. Rep. 13 (1958) 1.
[15] W. Preis, E. Bucher, W. Sitte, Solid State Ionics 175 (2004) 393.
[16] M.W. den Otter, H.J.M. Bouwmeester, B.A. Boukamp, H. Verweij, J. Electrochem. Soc. 148 (2001) J1.
[17] P.J. Gellings, H.J.M. Bouwmeester (Eds.), The CRC Handbook of Solid State Electrochemistry, CRC Press, 1997.
[18] S. McIntosh, J.F. Vente, W.G. Haije, D.H.A. Blank, H.J.M. Bouwmeester, Solid State Ionics 177 (2006) 1737.
[19] H. Wang, C. Tablet, A. Feldhoff, J. Caro, J. Membr. Sci. 262 (2005) 20.
[20] H.J.M. Bouwmeester, M.W. Den Otter, B.A. Boukamp, J. Solid State Electrochem. 8 (2004) 599.
[21] M. Søgard, P.V. Hendriksen, T. Jacobson, M. Mogensen, Proc. 7th European Solid Oxide Fuel Cell Forum, 2006, p. B064.
[22] S. Kim, S. Wang, X. Chen, Y.L. Yang, N. Wu, A. Ignatiev, A.J. Jacobson, B. Abeles, J. Electrochem. Soc. 147 (2000) 2398.
[23] S. Wang, A. Verma, Y.L. Yang, A.J. Jacobson, B. Abeles, Solid State Ionics 140 (2001) 125.
[24] X. Chen, S. Wang, Y.L. Yang, L. Smith, N.J. Wu, B.I. Kim, S.S. Perry, A.J. Jacobson, A. Ignatiev, Solid State Ionics 146 (2002) 405.
[25] J.A. Lane, J.A. Kilner, Solid State Ionics 136–137 (2000) 997.
[26] J.A. Lane, S.J. Benson, D. Waller, J.A. Kilner, Solid State Ionics 121 (1999) 201.
[27] J.E. ten Elshof, M.H.R. Lankhorst, H.J.M. Bouwmeester, J. Electrochem. Soc. 144 (1997) 1060.

Journal of The Electrochemical Society, **157** (11) B1537-B1541 (2010)
0013-4651/2010/157(11)/B1537/5/$28.00 © The Electrochemical Society

Long-Term Oxygen Exchange Kinetics of $Nd_2NiO_{4+\delta}$ in H_2O- and CO_2-Containing Atmospheres

A. Egger,[a,*,z] **W. Sitte,**[a,**,z] **F. Klauser,**[b] **and E. Bertel**[b]

[a] *Chair of Physical Chemistry, University of Leoben, A-8700 Leoben, Austria*
[b] *Institute of Physical Chemistry, University of Innsbruck, A-6020 Innsbruck, Austria*

The degradation of the solid oxide fuel cell cathode material $Nd_2NiO_{4+\delta}$ with respect to the oxygen exchange kinetics in H_2O- and CO_2-containing atmospheres has been investigated at 700°C. The material exhibits excellent stability in dry Ar + 1% O_2 atmosphere over 1000 h. No appreciable degradation has been observed after exposure to a CO_2-rich atmosphere, but a decrease in the chemical surface exchange coefficient of oxygen by 1 order of magnitude has been found after 1000 h under moist conditions (30% relative humidity). Post-test X-ray photoelectron spectroscopy depth analysis showed significant changes in the Nd:Ni cation ratio within the topmost 100 nm of the H_2O-degraded sample. It is concluded that the degradation mechanism involves hydroxides as intermediate species even if the predominant species in the degraded surface is $NdNiO_3$.
[DOI: 10.1149/1.3481420]

Manuscript submitted March 19, 2010; revised manuscript received July 26, 2010. Published September 7, 2010.

Long-term degradation remains an important issue of solid oxide fuel cells (SOFCs) to date and the limited lifetimes of stacks is the main barrier for a commercial introduction of the SOFC technology. The current trend is to reduce the operating temperature of SOFCs to 600–800°C, which stimulated the development of new mixed ionic electronic conducting (MIEC) cathode materials that show sufficient electrochemical performance at these reduced temperatures.[1,2]

So far, the dominating material class for MIEC cathodes are the perovskite oxides ($ABO_{3-\delta}$) and a great number of compounds with different compositions on the A- and B-site have been investigated. More recently, mixed conducting rare-earth (RE) nickelates $RE_2NiO_{4+\delta}$ have attracted interest as alternative cathode material. They adopt the perovskite-related K_2NiF_4 structure and feature fast oxygen incorporation and diffusion,[3] high electrocatalytic activity for oxygen reduction[4] and low thermal expansion coefficients[3,5,6] matching reasonably well those of current electrolytes such as yttria-stabilized zirconia or gadolinia-doped ceria.

Cathode-based degradation can be caused by the cathode material itself such as insufficient phase stability or cation segregation,[7-9] formation of detrimental phases at the interface to the electrolyte[10,11] or to the interconnect,[12,13] loss of mechanical or electrical contact between these components due to differences in thermal expansion coefficients, and reaction with trace gases in the oxidant such as water vapor or carbon dioxide.

Several investigations on perovskites deal with the formation of hydroxides and/or carbonates of SOFC cathode materials at operating conditions in humid[14,15] or CO_2-containing[15-21] atmospheres. The perovskite-related K_2NiF_4-type nickelates have been reported to be stable in moist atmosphere.[22] Egger et al.[23] investigated Nd_2NiO_4 after exposure to H_2O- and CO_2-containing gases by thermogravimetric analysis combined with mass spectrometry and found no evidence for adverse effects on oxygen exchange in the short-term range. The absence of alkaline earth metals in this material might be beneficial for the stability against hydroxide and carbonate formation. However, data about long-term stability with respect to humidity or CO_2 in the oxidant gas is scarce for this material. In this work, we present results concerning the long-term stability of $Nd_2NiO_{4+\delta}$ with respect to oxygen exchange performance at 700°C in H_2O- and CO_2-containing atmospheres.

Experimental

Sample preparation.— Nd_2NiO_4 was synthesized by the polyacrylamide gel route as given in more detail by Egger et al.[23] The final sintering step at 1350°C for 4 h gave a cylindrical pellet of 1.5 cm diameter and 7 mm thickness with a relative density of 98% based on a theoretical density of 7.53 g/cm^3 as determined from XRD. The K_2NiF_4 structure of the material was verified by XRD with a small amount of Nd_2O_3 present. Square slabs of 7 × 7 × 1 mm were cut from the center part of the sintered pellet with a diamond wire saw, ground with a SiC paper (240 grit), and polished with polymer-embedded diamond lapping films of 30, 6, and 1 μm particle size. Two samples for investigating the degradation effect of water and carbon dioxide were prepared with a thickness of 467 and 415 μm, respectively. The samples were contacted at the corners using gold wires attached with gold paste (Metalor) because gold is rather inactive in the oxygen exchange process.

Experimental setup.— Samples were mounted in a quartz reactor with a zirconia-based oxygen sensor with an integrated S-thermocouple (MicroPoas, Setnag) placed close to the sample. Conductivity and conductivity relaxation measurements[24,25] were performed in the van der Pauw geometry at 700°C and 0.01–0.02 bar oxygen partial pressure (pO_2) in a tube furnace with a total gas flow of 5 L/h adjusted by mass flow controllers (Hastings HFC-302). Within the H_2O degradation experiments, the gases were passed through water flasks containing deionized water at a constant temperature of 6°C, which corresponds to a pH_2O of 0.9 kPa or 30% relative humidity at 25°C under equilibrium conditions.[26] CO_2 degradation was investigated by flushing the reactor with a mixture of 5% CO_2 + 20% O_2 in Ar at a flow rate of 1 L/h.

Conductivity relaxation.— High temperature electrical conductivity measurements were performed by the four-point van der Pauw technique using a Keithley 2400 current/voltage source. Conductivity relaxation transients were recorded using a Keithley 182 sensitive voltmeter and a Keithley 2400 current source. Switching between gas flows with different oxygen partial pressures was done manually by a four-way valve. Chemical surface exchange coefficients (k_{chem}) and chemical diffusion coefficients (D_{chem}) of oxygen were obtained by nonlinear least-squares fitting of the appropriate solution of the diffusion equation to the relaxation profile, taking into account the finite flushtime of the quartz reactor as determined from a separate measurement of the empty reactor. Analytic expressions used in the nonlinear regression analysis are given in Eq. 1 for the case of surface controlled oxygen exchange kinetics and in Eq. 2 for a mixed surface exchange/diffusion controlled oxygen exchange process[27,28]

$$\sigma_n = 1 - \frac{1}{1 - \frac{2k_{chem}\tau_r}{L}}\left[\exp\left(-\frac{2k_{chem}}{L}t\right) - \frac{2k_{chem}\tau_r}{L}\exp\left(-\frac{t}{\tau_r}\right)\right] \qquad [1]$$

---

[*] Electrochemical Society Student Member.
[**] Electrochemical Society Active Member.
[z] E-mail: andreas.egger@unileoben.ac.at; sitte@unileoben.ac.at

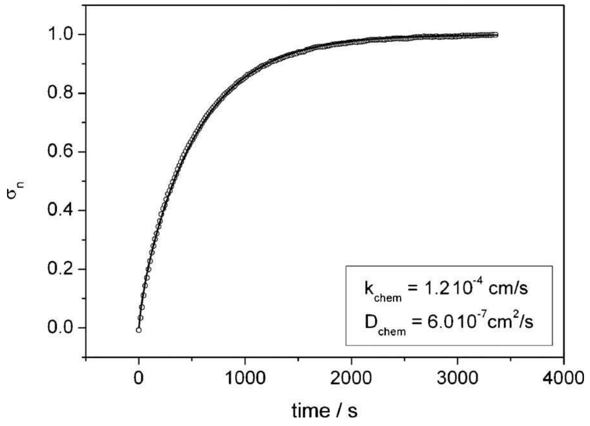

Figure 1. Relaxation data of the normalized conductivity σ_n as a response to an abrupt change in the oxygen partial pressure in the ambient atmosphere from 0.01 to 0.02 bar at 700°C. Data points are plotted as circles and the fitting curve obtained from fitting Eq. 2a to the data is drawn as solid line. Not all data points are shown for reasons of clarity.

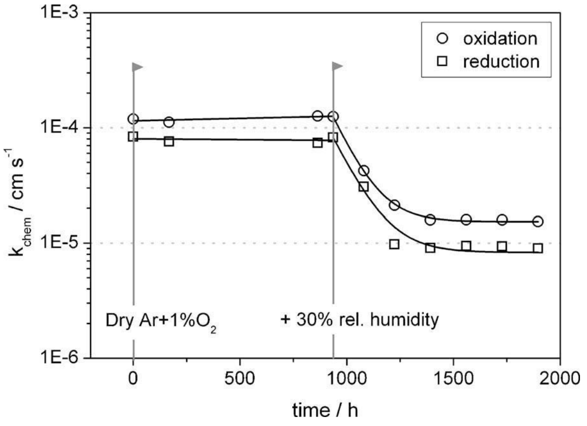

Figure 2. Decrease in the chemical surface exchange coefficient k_{chem} of oxygen for $\mathrm{Nd_2NiO_{4+\delta}}$ as a function of time due to humidification of the ambient atmosphere (30% relative humidity at 25°C) at $T = 700°\mathrm{C}$ and $p\mathrm{O_2} = 0.01–0.02$ bar. Lines are linear and exponential fits to data obtained from measurements in dry and wet atmospheres, respectively.

$$\sigma_{\mathrm{n}} = 1 - \exp\left(-\frac{t}{\tau_{\mathrm{r}}}\right) - \sum_{n=1}^{\infty} \frac{2L_{\alpha}^2}{\alpha_{\mathrm{n}}^2(\alpha_{\mathrm{n}}^2 + L_{\alpha}^2 + L_{\alpha})} \frac{1}{1 - \frac{4D_{\mathrm{chem}}\alpha_{\mathrm{n}}^2\tau_{\mathrm{r}}}{L^2}} \times \left[\exp\left(-\frac{4D_{\mathrm{chem}}\alpha_{\mathrm{n}}^2}{L^2}t\right) - \exp\left(-\frac{t}{\tau_{\mathrm{r}}}\right)\right] \qquad [2a]$$

$$\alpha_{\mathrm{n}} \tan \alpha_{\mathrm{n}} = L_{\alpha} \equiv \frac{Lk_{\mathrm{chem}}}{2D_{\mathrm{chem}}} \qquad [2b]$$

where σ_n is the electrical conductivity normalized with respect to the equilibrium conductivities before and after the $p\mathrm{O_2}$ step $\sigma_n = (\sigma_t - \sigma_0)/(\sigma_\infty - \sigma_0)$, τ_r is the flushtime of the reactor volume assuming continuous ideally stirred tank reactor behavior,[27] L is the sample thickness, and t is time. The infinite sum in Eq. 2a runs over all positive roots α_n of Eq. 2b. The Levenberg–Marquardt algorithm was employed for adjusting the fitting parameters k_{chem} and D_{chem} by minimization of the unweighted sum of squared residuals between calculated and measured data points. A typical example of experimental relaxation data together with the fitting curve of Eq. 2a is presented in Fig. 1.

XPS.— The chemical composition of the sample surface was quantified by X-ray photoelectron spectroscopy (XPS). The measurements were carried out at room temperature in ultrahigh vacuum (UHV) at a base pressure of 2×10^{-10} mbar utilizing a Thermo MultiLab 2000 spectrometer equipped with an alpha 110 hemispherical analyzer from Thermo Electron, operated in the constant analyzer energy mode at a pass energy of 100 eV corresponding to 2.5 eV overall resolution. All spectra were collected using Al Kα radiation (1486.6 eV) monochromatized by a twin crystal monochromator yielding a focused X-ray spot with a diameter of 500 μm. The chemical composition was obtained from the areas of the detected XPS peaks in survey scans, performing a linear-background subtraction and taking into account Scofield sensitivity factors for each constituent.[29] Depth profiles were realized by an EX05 Ion Gun from Thermo Electron providing a 3 keV Ar ion beam, irradiating a 2 × 2 mm surface area at an ion current of 2.5 μA.

Results and Discussion

Phase purity.— XRD confirmed the presence of the $\mathrm{K_2NiF_4}$ type main phase, additional peaks in the XRD pattern could be ascribed to a minor amount of $\mathrm{Nd_2O_3}$ secondary phase. The Nd:Ni ratio was determined as 2.0 ± 0.1 (2σ) by inductively coupled plasma-mass spectometry (ICP-MS) after dissolving the sample in 6 M HCl.

Oxygen exchange kinetics in wet atmosphere.— Figures 2 and 3 show the chemical surface exchange coefficient k_{chem} and the chemical diffusion coefficient D_{chem} of oxygen for $\mathrm{Nd_2NiO_{4+\delta}}$ over a period of about 2000 h. During the first ~1000 h the sample was kept at 700°C in dry Ar + 1% $\mathrm{O_2}$ atmosphere with a permanent gas flow of 1 L/h. No decrease in the kinetic parameters k_{chem} and D_{chem} was observed under dry conditions. Due to technical reasons, an intermittent shutdown of the furnace for 2 weeks was necessary, which had no detrimental effect on both parameters. Values for k_{chem} and D_{chem} obtained from oxidation experiments ($p\mathrm{O_2}$ 0.01 → 0.02 bar) were found to be systematically larger than those extracted from reduction runs ($p\mathrm{O_2}$ 0.02 → 0.01 bar) over the entire series of measurements.

For the investigation of the effect of water on oxygen exchange properties, the sample was kept in a humidified gas stream over a period of 1000 h. The degradation process was monitored in weekly intervals by conductivity relaxation and electrical conductivity mea-

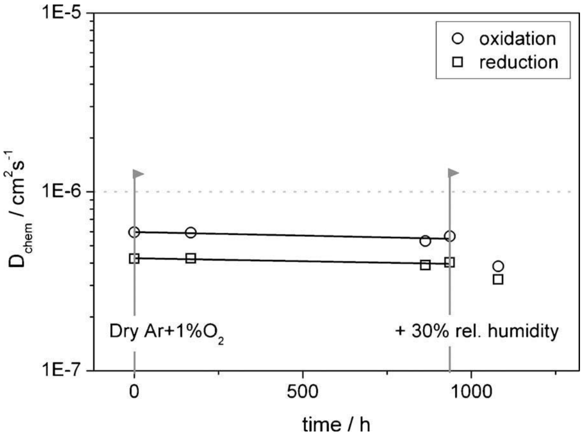

Figure 3. Chemical diffusion coefficient D_{chem} of oxygen for $\mathrm{Nd_2NiO_{4+\delta}}$ as a function of time due to humidification of the ambient atmosphere (30% relative humidity at 25°C) at $T = 700°\mathrm{C}$ and $p\mathrm{O_2} = 0.01–0.02$ bar. Only limited data is available for D_{chem} due to a change in the oxygen exchange mode from mixed control to surface control shortly after changing to wet atmosphere. Lines are linear fits to data obtained from measurements in dry atmosphere.

surements. A decrease by factor of 3 for k_{chem} and (less pronounced) by factor of 1.5 for D_{chem} was observed after 1 week as a result of the humidified atmosphere (Fig. 2 and 3). The slight decrease in the diffusivity is unlikely to be caused by the degradation itself because the thickness of the affected surface layer is below 300 nm (see XPS results below) but is rather an indication that because degradation also proceeds during the relaxation measurement, fitting of the equation for mixed control does not afford a perfect separation of the contribution of k_{chem} and D_{chem} to the overall relaxation process.

After another week, the relaxation process was found to be limited solely by the surface exchange of oxygen and only values for k_{chem} could be determined from that point on. After 3 weeks, the decrease in the surface exchange coefficient ceased and k_{chem} remained constant for the rest of the investigated period, resulting in an overall decrease in k_{chem} by 1 order of magnitude from about 1×10^{-4} to 1×10^{-5} cm s^{-1} over ~1000 h in humid atmosphere (30% relative humidity).

Before each conductivity relaxation measurement, the electronic conductivity σ was determined, yielding $\sigma = 101–102$ S cm^{-1} for $pO_2 = 0.01$ bar and $\sigma = 104–105$ S cm^{-1} for $pO_2 = 0.02$ bar at 700°C. No systematic change in the conductivity was observed during H_2O degradation, which is to be expected because a thin poorly conducting surface layer should have no appreciable effect in parallel with the largely unaffected bulk.

Although a deteriorating effect of water on the oxygen exchange in $Nd_2NiO_{4+\delta}$ has been verified, the degradation is less severe than for the perovskite-type SOFC cathode material $La_{0.58}Sr_{0.4}Co_{0.2}Fe_{0.8}O_{3-\delta}$, where a much more pronounced decrease in k_{chem} of a factor of ~200 has been observed at 700°C after exposure to wet atmospheres.[30] This difference in oxygen exchange deactivation may be related to the absence of Sr in the investigated nickelate compound. The comparison should be regarded with some caution because the water content differed in both studies (74% relative humidity vs 30% in this work). However, results in Bucher and Sitte[30] suggest that the H_2O-induced degradation in $La_{0.58}Sr_{0.4}Co_{0.2}Fe_{0.8}O_{3-\delta}$ is rather insensitive to the precise amount of water content in the surrounding atmosphere.

XPS analysis before and after H_2O degradation.— Depth profiles of the elemental composition of the sample surface were recorded by XPS up to approximately 350 nm sputtering depth for both the degraded and nondegraded sample (Fig. 4 and 5). The nondegraded sample was annealed for 1000 h under flowing dry Ar + 1% O_2 before XPS analysis to unambiguously ascribe any difference in the composition profiles to the degradation process in humid atmosphere.

Small amounts of bismuth and cadmium have been identified by XPS in the topmost surface layer. The source of this contamination is most likely the gold paste used for contacting the sample, as minor amounts of Bi, Cd, and Pb were detected in fresh unsintered gold paste by X-ray fluorescence analysis. No silicon peaks have been found in any of the XPS spectra.

The XPS depth profile of nondegraded $Nd_2NiO_{4+\delta}$ kept in pure Ar–O_2 atmosphere is shown in Fig. 4a. The rather large deviation of the measured elemental composition from the nominal one is caused by a preferential loss of oxygen from the reducible oxides due to sputtering in UHV as has been noted earlier.[31] The composition is quite homogeneous throughout the profile except within the topmost ~20 nm of the surface, where strong oxygen enrichment is observed, presumably due to partially reversible H_2O adsorption from the ambient atmosphere.

In Fig. 4b the concentration profile has been renormalized to the cations to reveal changes in the Nd:Ni ratio more clearly. Beyond a depth of 50 nm, the cation ratio agrees well with that of the nominal composition. At the immediate surface a ~50 nm thick layer is present where Nd is enriched with respect to Ni. A similar RE enrichment after oxygen exposure has been reported for polycrystalline $La_2NiO_{4+\delta}$ by Choisnet et al.[32] and for $LaNi_5$ by Schlapbach and Brundle.[33] The chemically driven RE enrichment results from the higher thermodynamic stability of the RE oxides ($\Delta_f H^{\Theta}(Nd_2O_3) = -1808$ kJ/mol) in comparison to NiO ($\Delta_f H^{\Theta}(NiO) = -240$ kJ/mol).[34]

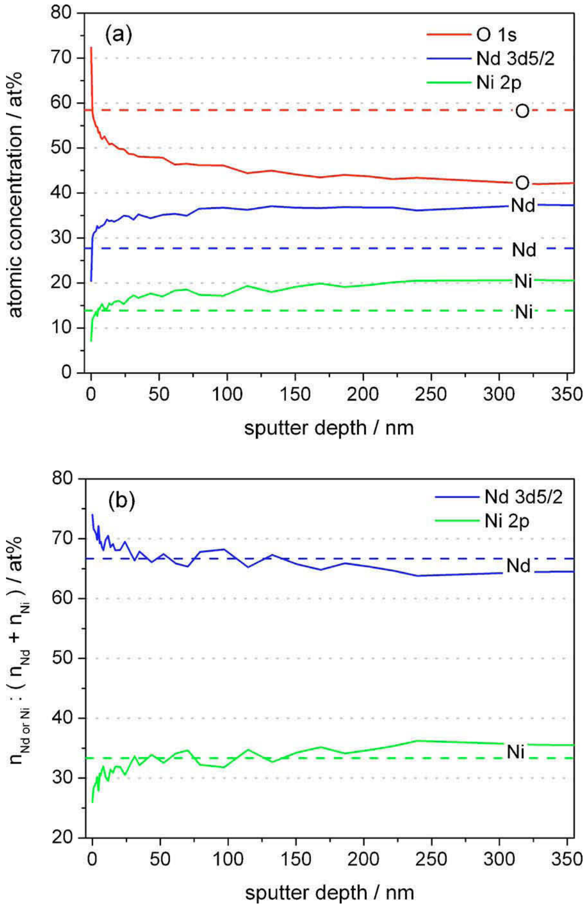

Figure 4. (Color online) XPS depth profile of (a) the overall composition and (b) the cation composition from the surface layer of nondegraded $Nd_2NiO_{4+\delta}$ (solid lines). The sample was kept 1000 h under dry Ar + 1% O_2 at 700°C before XPS analysis. Dashed lines mark nominal compositions.

XPS depth profiles of degraded $Nd_2NiO_{4+\delta}$ after 1000 h at 700°C in wet atmosphere (30% relative humidity) are presented in Fig. 5a for the overall composition and in Fig. 5b for cations only. As mentioned above, deviations from the nominal composition in the bulk shown in Fig. 5a arise from measuring a too low oxygen concentration caused by the sputtering process. The elemental distribution in the degraded surface appears to be less homogeneous than for the nondegraded sample (see Fig. 5a and 4a). The most striking feature is a drastic decrease in the Nd:Ni ratio from 2:1 in nondegraded $Nd_2NiO_{4+\delta}$ (Fig. 4) to 1:1 in the near-surface region of the degraded sample. Figure 5b shows the change in the cation distribution even more clearly. Beyond 300 nm depth, the nominal bulk composition is found. As one approaches the surface, a Ni depletion zone is crossed between 300 and 100 nm depth, while in the topmost 50 nm the Nd:Ni ratio approaches unity.

The present observations provide an important clue about the degradation mechanism of $Nd_2NiO_{4+\delta}$ in wet atmosphere. Degradation of the related material La_2NiO_4 has been attributed earlier to conversion Ni^{2+} to Ni^{3+}, the latter being more stable at moderate temperatures.[35] This is indeed consistent with the present finding of a nearly balanced Nd:Ni concentration at the degraded sample surface and suggests the presence of a $NdNiO_3$ perovskite phase. In fact, Nd_2NiO_4 and $NdNiO_3$ can be considered as the respective endpoints of a Ruddlesden–Popper type series $NdO(NdNiO_3)_n$ of ox-

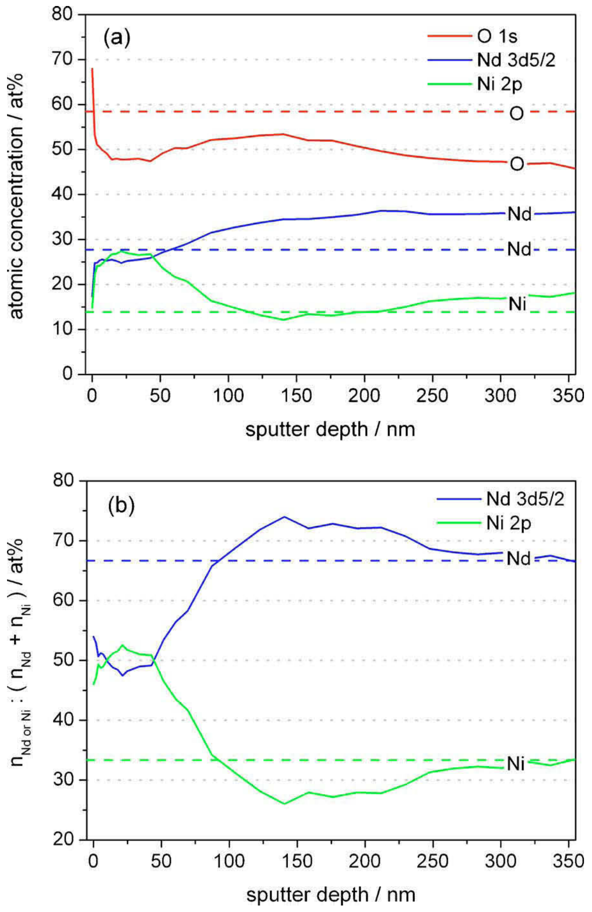

Figure 5. (Color online) XPS depth profiles of (a) the overall composition and (b) the cation composition from the surface layer of $Nd_2NiO_{4+\delta}$ after degradation (solid lines). The sample was first kept 1000 h at 700°C under dry Ar + 1% O_2 and subsequently exposed to humid atmospheres for another 1000 h at 700°C before XPS analysis. Dashed lines mark nominal compositions.

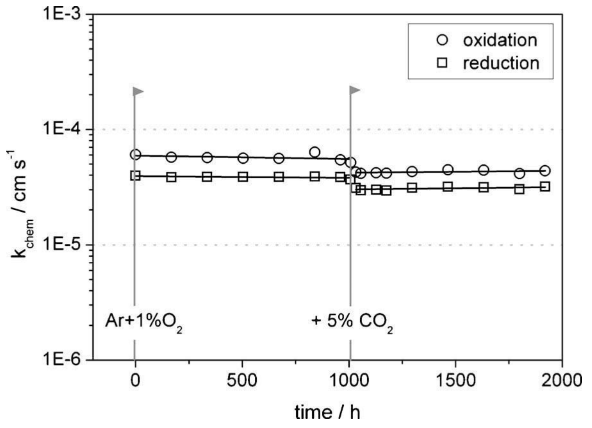

Figure 6. Effect of CO_2 on the chemical surface exchange coefficient k_{chem} of oxygen for $Nd_2NiO_{4+\delta}$ at 700°C as a function of time. CO_2 sensitivity of the material was assessed by exposing the sample for 1000 h to a gas flow of 5% CO_2 + 20% O_2 in Ar with intermittent measurements of k_{chem} at pO_2 = 0.01–0.02 bar. Lines are linear fits to the data before and after introduction of CO_2.

ides. Gauquelin et al.[36] identified intermediate-order Ruddlesden–Popper phases $La_3Ni_2O_7$ and $La_4Ni_3O_{10}$ by transmission electron microscopy on the surface of single crystal $La_2NiO_{4+\delta}$ after annealing at 1000°C for 13 days in ambient air. However, our results are at variance with a degradation taking place via successive transformation through such oxides. This clearly points to a pivotal role of the water content in the ambient atmosphere. Alonso et al.[37] demonstrated the growth of $NdNiO_3$ crystals at 4 GPa from hydroxides as starting reactants. The use of hydroxides seemed to be essential, which led the authors to postulate a water vapor transport driven growth mechanism. These results and the present observations indicate a degradation route, which proceeds via hydroxide formation as an intermediate stage rather than involving merely a gradual conversion to Ni^{3+} by increasing *n* in the Ruddlesden–Popper series.

Of course, elucidation of the precise mechanism would require a detailed, locally resolved structure analysis of the surface phases, but the XPS results provide at least some hints about the conversion of the original surface layer toward the $NdNiO_3$ phase. The native surface before H_2O exposure exhibits a Nd- and O-rich termination, indicating the presence of a thin Nd_2O_3 layer as is common for RE compounds.[32,33] RE oxide surfaces dissociate water readily, which results in at least partial conversion of the Nd_2O_3 layer into a hydroxide as the H_2O partial pressure in the ambient atmosphere is increased. According to the observations reported by Alonso et al.,[37] $NdNiO_3$ may then be nucleated at the interface between the surface hydroxide and the $Nd_2NiO_{4+\delta}$ bulk phase. Because $NdNiO_3$ is thermodynamically more stable, this is a down-hill process. As the degradation continues, the $NdNiO_3$ nucleation is followed by three-dimensional growth, which consumes Ni from the underlying Nd_2NiO_4 lattice. In this way a Ni-rich surface layer grows, while a Ni depletion zone is formed in the underlying bulk. In principle, this process should be kinetically forbidden because the transfer of Ni from the bulk to the growing $NdNiO_3$ phase requires the destruction of the Nd_2NiO_4 lattice. However, this is very likely the point where the catalyzing action of water steps in. The water dissociation on the surface provides a supply of protons, which readily diffuse into the bulk.[33] Here, they may convert oxygen into OH groups, thus destabilizing the Nd_2NiO_4 lattice. Of course the proposed mechanism is just a plausible speculation at the present state of knowledge. Local structure sensitive probes are required to decide on the validity of this hypothesis. Interestingly, in the present case, the reaction proceeds even at normal pressure although at a slow pace.

Oxygen exchange kinetics in CO_2-containing atmosphere.— Figure 6 shows the effect of CO_2 on the surface exchange coefficient k_{chem} of oxygen at 700°C. Contrary to experiments in wet atmospheres, the oxygen exchange was found to be controlled by the surface exchange process over the entire measurement period due to a smaller sample thickness.[24,27] Similar to the sample used for H_2O degradation excellent stability in dry Ar + 1% O_2 over 1000 h was observed. Changing the gas flow to 5% CO_2 + 20% O_2 in Ar had a rather minor effect on oxygen exchange, reducing k_{chem} by factor 1.3 within 1 day and having no further effect afterwards over another 1000 h. Electronic conductivities showed the same values as given above and were not affected by CO_2 exposure.

Post-test surface investigations of the CO_2-treated sample by XPS (Fig. 7) evidence a rather small influence of CO_2 on the elemental distribution in the topmost ~200 nm when compared to the nondegraded sample in Fig. 4. However, in the immediate surface layer (~20 nm) there seems to be a slight local enrichment of Ni over Nd in contrast to the oxygen-exposed specimen (Fig. 4). The small variation in composition is not directly related to a reaction with CO_2 because the carbon level drops below the detection limit within the first 2 nm of the surface.

Conclusions

$Nd_2NiO_{4+\delta}$ exhibits excellent stability in dry O_2–Ar atmospheres over 1000 h at 700°C. A decrease of 1 order of magnitude for the chemical surface coefficient k_{chem} of oxygen has been observed after exposing the material to a humidified Ar + 1% O_2 atmosphere at 700°C. k_{chem} dropped from $\sim 1 \times 10^{-4}$ cm s^{-1} down to ~1

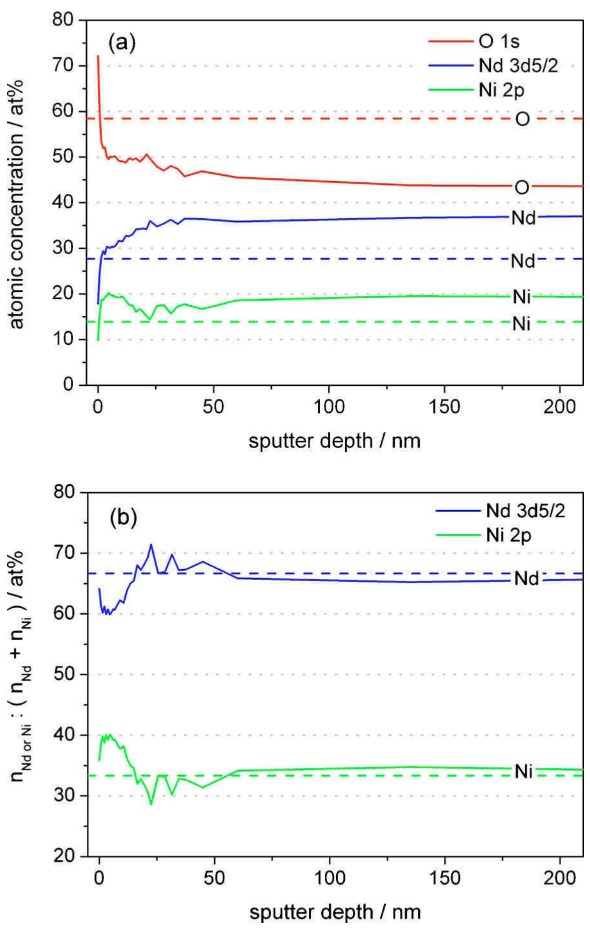

Figure 7. (Color online) XPS depth profiles of (a) the overall composition and (b) the cation composition from the surface layer of $Nd_2NiO_{4+\delta}$ after exposure to CO_2 (solid lines). The sample was first kept for 1000 h at 700°C under dry Ar + 1% O_2 followed by a 1000 h exposure to 5% CO_2 + 20% O_2 in Ar at 700°C and subsequent XPS analysis. Nominal compositions are plotted as dashed lines.

$\times 10^{-5}$ cm s^{-1} over a period of 450 h and then remained constant for another 500 h. Shortly after switching to a wet atmosphere, the surface exchange of oxygen has been found to be limiting the rate of oxygen exchange for the sample. This, together with the observation that the electronic conductivity remained unchanged, suggests that it is the surface that is mainly affected during degradation. XPS depth profiles showed that the oxygen exchange deactivation is accompanied by a significant decrease in the Nd:Ni ratio, changing from a 2:1 ratio in the bulk to 1:1 within the topmost ~100 nm of the sample. Exposure to CO_2 for 1000 h had only a minor effect on the oxygen surface exchange kinetics and XPS-depth profiling consistently demonstrated the elemental surface composition to be much less affected by CO_2 than by water.

The cation composition of the nickelate surface changes significantly during exposure to oxygen and in wet atmosphere. Exposure to oxygen causes a Nd enrichment, presumably due to Nd_2O_3 formation at the surface, but this has little effect on the oxygen exchange performance of the $Nd_2NiO_{4+\delta}$ sample. In contrast, a surface excess of Ni is observed after degradation in wet atmosphere. In this case, the degradation is tentatively attributed to partial conversion of the surface layer into $NdNiO_3$ with much more serious consequences for the performance of the material. Water plays an essential role in this conversion, suggesting the formation of hydroxides as reaction intermediates.

Acknowledgment

Financial support from the EC within the integrated project SOFC600 (contract no. 020089) is gratefully acknowledged. The authors thank Jean-Marc Bassat and Cécile Lalanne from ICMCB-CNRS (France) for providing the sample within the EC project SOFC600 as well as Thomas Meisel of the University of Leoben (Austria) for ICP-MS measurements and Edith Bucher of the University of Leoben (Austria) for helpful suggestions.

University of Leoben assisted in meeting the publication costs of this article.

References

1. Y. Takeda, R. Kanno, M. Noda, Y. Tomida, and O. Yamamoto, *J. Electrochem. Soc.*, **134**, 2656 (1987).
2. J. Richter, P. Holtappels, T. Graule, T. Nakamura, and L.J. Gauckler, *Monatshefte für Chemie/Chemical Monthly*, **140**, 985 (2009).
3. L. P. Sun, Q. Li, H. Zhao, L. H. Huo, and J. C. Grenier, *J. Power Sources*, **183**, 43 (2008).
4. F. Mauvy, J. M. Bassat, E. Boehm, J. P. Manaud, P. Dordor, and J. C. Grenier, *Solid State Ionics*, **158**, 17 (2003).
5. E. Boehm, J. M. Bassat, P. Dordor, F. Mauvy, J. C. Grenier, and P. Stevens, *Solid State Ionics*, **176**, 2717 (2005).
6. M. Al Daroukh, V. V. Vashook, H. Ullmann, F. Tietz, and I. A. Raj, *Solid State Ionics*, **158**, 141 (2003).
7. G. Amow and S. J. Skinner, *J. Solid State Electrochem.*, **10**, 538 (2006).
8. F. Tietz, A. Mai, and D. Stöver, *Solid State Ionics*, **179**, 1509 (2008).
9. S. P. Simner, M. D. Anderson, M. H. Engelhard, and J. W. Stevenson, *Electrochem. Solid-State Lett.*, **9**, A478 (2006).
10. O. Yamamoto, Y. Takeda, R. Kanno, and M. Noda, *Solid State Ionics*, **22**, 241 (1987).
11. H. Y. Tu, Y. Takeda, N. Imanishi, and O. Yamamoto, *Solid State Ionics*, **117**, 277 (1999).
12. J. Y. Kim, V. L. Sprenkle, N. L. Canfield, K. D. Meinhardt, and L. A. Chick, *J. Electrochem. Soc.*, **153**, A880 (2006).
13. H. Yokokawa, T. Horita, N. Sakai, K. Yamaji, M. E. Brito, Y. P. Xiong, and H. Kishimoto, *Solid State Ionics*, **177**, 3193 (2006).
14. P. Hjalmarsson, M. Søgaard, and M. Mogensen, *Solid State Ionics*, **179**, 1422 (2008).
15. S. J. Benson, D. Waller, and J. A. Kilner, *J. Electrochem. Soc.*, **146**, 1305 (1999).
16. E. Bucher, A. Egger, G. B. Caraman, and W. Sitte, *J. Electrochem. Soc.*, **155**, B1218 (2008).
17. E. Bucher, G. B. Caraman, and W. Sitte, in Proc. of the 8th European SOFC Forum, R. Steinberger-Wilckens, Editor, p. A0603 (2008).
18. M. Arnold, H. Wang, and A. Feldhoff, *J. Membr. Sci.*, **293**, 44 (2007).
19. A. Yan, M. Cheng, Y. Dong, W. Yang, V. Maragou, S. Song, and P. Tsiakaras, *Appl. Catal., B*, **66**, 64 (2006).
20. A. Yan, V. Maragou, A. Arico, M. Cheng, and P. Tsiakaras, *Appl. Catal., B*, **76**, 320 (2007).
21. I. V. Khromushin, T. I. Aksenova, and Z. R. Zhotabaev, *Solid State Ionics*, **162–163**, 37 (2003).
22. J. C. Grenier, F. Mauvy, C. Lalanne, J. M. Bassat, F. Chauveau, J. Mougin, J. Dailly, and M. Marrony, *ECS Trans.*, **25**(2), 2537 (2009).
23. A. Egger, E. Bucher, W. Sitte, C. Lalanne, and J. M. Bassat, *ECS Trans.*, **25**(2), 2547 (2009).
24. L. M. van der Haar, M. W. den Otter, M. Morskate, H. J. M. Bouwmeester, and H. Verweij, *J. Electrochem. Soc.*, **149**, J41 (2002).
25. W. Preis, E. Bucher, and W. Sitte, *Solid State Ionics*, **175**, 393 (2004).
26. *CRC Handbook of Chemistry and Physics*, 76th ed., D. R. Lide, Editor, pp. 1995–1996, CRC Press, Boca Raton, FL.
27. M. W. den Otter, H. J. M. Bouwmeester, B. A. Boukamp, and H. Verweij, *J. Electrochem. Soc.*, **148**, J1 (2001).
28. W. Preis, E. Bucher, and W. Sitte, *J. Power Sources*, **106**, 116 (2002).
29. J. H. Scofield, *J. Electron Spectrosc. Relat. Phenom.*, **8**, 129 (1976).
30. E. Bucher and W. Sitte, *Solid State Ionics*, In press.
31. C. Morant, J. M. Sanz, and L. Galán, *Phys. Rev. B*, **45**, 1391 (1992).
32. J. Choisnet, N. Abadzhieva, P. Stefanov, D. Klissurski, J. M. Bassat, V. Rives, and L. Minchev, *J. Chem. Soc., Faraday Trans.*, **90**, 1987 (1994).
33. L. Schlapbach and C. R. Brundle, *Helv. Phys. Acta*, **52**, 352 (1979).
34. I. Barin, *Thermochemical Data of Pure Substances*, VCH, Weinheim (1993).
35. G. Amow, I. J. Davidson, and S. J. Skinner, *Solid State Ionics*, **177**, 1205 (2006).
36. N. Gauquelin, T.E. Weirich, M. Ceretti, W. Paulus, and M. Schroeder, *Monatshefte für Chemie/Chemical Monthly*, **140**, 1095 (2009).
37. J. A. Alonso, A. Muñoz, A. Largeteau, and G. Demazeau, *J. Phys.: Condens. Matter*, **16**, S1277 (2004).

Journal of The Electrochemical Society, **158** (5) B573-B579 (2011)
0013-4651/2011/158(5)/B573/7/$28.00 © The Electrochemical Society

Oxygen Exchange Kinetics of the IT-SOFC Cathode Material $Nd_2NiO_{4+\delta}$ and Comparison with $La_{0.6}Sr_{0.4}CoO_{3-\delta}$

A. Egger,[*] E. Bucher,[**] and W. Sitte[,z]**

Department of Physical Chemistry, University of Leoben, A 8700 Leoben, Austria

---

For the promising intermediate temperature solid oxide fuel cell (IT-SOFC) cathode material $Nd_2NiO_{4+\delta}$, chemical surface exchange coefficients k_{chem} and chemical diffusion coefficients D_{chem} of oxygen have been determined by conductivity relaxation measurements and compared with results for $La_{0.6}Sr_{0.4}CoO_{3-\delta}$ between 575 and 725°C. At 725°C and an oxygen partial pressure of 0.1 bar, k_{chem} and D_{chem} of $Nd_2NiO_{4+\delta}$ amount to 1×10^{-3} cm s^{-1} and 2×10^{-6} cm^2 s^{-1}, respectively, which are higher than those for $La_{0.6}Sr_{0.4}CoO_{3-\delta}$. However, due to high activation energies, a strong decrease of both kinetic parameters is observed for $Nd_2NiO_{4+\delta}$ upon temperature reduction. Activation energies of k_{chem} and D_{chem} are lower for $La_{0.6}Sr_{0.4}CoO_{3-\delta}$, leading to faster oxygen exchange compared to $Nd_2NiO_{4+\delta}$ at 600°C. Electronic conductivities of $Nd_2NiO_{4+\delta}$ amount to 100–125 S cm^{-1} while those of $La_{0.6}Sr_{0.4}CoO_{3-\delta}$ are between 1600 and 2200 S cm^{-1} in the investigated temperature and oxygen partial pressure range. Ionic conductivities and surface exchange resistances, which were calculated from the kinetic parameters, further show superior oxygen transport properties of $La_{0.6}Sr_{0.4}CoO_{3-\delta}$ compared to $Nd_2NiO_{4+\delta}$ in pure O_2–Ar atmospheres.
[DOI: 10.1149/1.3569697]

Manuscript submitted November 15, 2010; revised manuscript received March 1, 2011. Published March 28, 2011.

The current effort of lowering the operating temperature of solid oxide fuel cells (SOFCs) to intermediate temperatures (IT) of 600–800°C has drawn special attention to the cathode polarization resistance as a limiting factor for efficiency.[1] One approach for reducing the overpotential at the air electrode involves employing mixed ionic electronic conducting (MIEC) ceramics, where the reaction zone for oxygen reduction, dissociation and incorporation is extended from the immediate three-phase boundary to part of the two-phase gas-cathode surface region.

So far, the dominating structure type of mixed-conducting SOFC-cathode materials has been the perovskite structure $ABO_{3-\delta}$ with oxygen deficiency introduced by substitution with acceptor ions on the A-site. Within the perovskite family the Sr-doped lanthanum cobaltites are of special interest, in particular $La_{0.6}Sr_{0.4}CoO_{3-\delta}$, which is one of the best electrical conductors in the $La_{1-x}Sr_xCoO_{3-\delta}$ series.[2,3] The cobaltites feature fast oxygen surface exchange and diffusion kinetics,[4–7] high electrocatalytic activity for oxygen reduction[8,9] as well as high electronic[2,3,10–13] and ionic[14–16] conductivities. Disadvantages are their high thermal expansion coefficients resulting from their large Co-content,[3,15] formation of resistive interlayers with YSZ at high temperatures,[17,18] segregation of Sr to the surface[19,20] and limited stability against H_2O, possibly due to the presence of Sr.[21]

Oxygen hyperstoichiometric compounds $Ln_2NiO_{4+\delta}$ (Ln = La, Pr, Nd) have been proposed as alternative cathode materials. They adopt the K_2NiF_4-type structure,[22] which is the first member of the perovskite-related Ruddlesden-Popper series $A_{n+1}B_nO_{3n+1}$.[23] Its structure consists of alternating perovskite NiO_2-layers and Ln_2O_2-rock salt double-layers. Based on the values of the respective ionic radii, the layers do not match perfectly because the Ln-O distance in the rock salt layer is too small with respect to the NiO_2-layer. Due to the lanthanide contraction, this mismatch increases for lanthanides with higher atomic numbers, Sm already being too small to give a stable structure, as undoped $Sm_2NiO_{4+\delta}$ does not exist.[24]

The most significant feature of the nickelates is their ability to accommodate additional oxygen on interstitial positions located inside the rock salt double layers. The tendency towards oxygen incorporation can be explained by a reduction of the mismatch between perovskite and rock salt layers due to (i) a decrease of the average Ni-O bond distance caused by partial oxidation of Ni^{2+} to Ni^{3+} and (ii) an increase of the average Ln-O distance due to a higher average coordination number of the lanthanide ions.[25] Oxygen hyperstoichiometries δ of $Pr_2NiO_{4+\delta}$ and $Nd_2NiO_{4+\delta}$ are generally higher than those of $La_2NiO_{4+\delta}$, due to the smaller ionic radii of Pr and Nd, which results in a stronger driving force to relieve the interlayer-strain by oxygen incorporation.[24]

Thermal expansion coefficients of $Ln_2NiO_{4+\delta}$ are lower than those of perovskite-type cathode materials (and far below those of cobaltites),[26] giving a better match with common electrolyte materials such as yttria-stabilized zirconia or gadolinia-doped ceria.[27] Furthermore, the absence of Sr in undoped $Ln_2NiO_{4+\delta}$ might be beneficial with respect to long term stability, as the detrimental formation of strontium carbonates or hydroxides cannot occur when the cathode is in contact with humid atmospheres or atmospheres containing CO_2.[21,28]

$Nd_2NiO_{4+\delta}$ has been reported to exhibit high electrocatalytic activity for oxygen reduction.[29] In this study, we compare results for the chemical surface exchange and diffusion coefficients of oxygen as well as ionic conductivities and surface exchange resistances of $Nd_2NiO_{4+\delta}$ with those of $La_{0.6}Sr_{0.4}CoO_{3-\delta}$ with respect to IT-SOFC cathode applications.

Experimental

Sample preparation.—$Nd_2NiO_{4+\delta}$ was synthesized by means of the polyacrylamide gel route.[30] Individual aqueous solutions of each cation were prepared from nitrate salts. The cations were then chelated by triammonium citrate (*p*H controlled via NH_4OH). Solutions of chelated cations were mixed in a stoichiometric ratio. The organic gels were made using monomers of acrylamide to form chains and the cross-linker *N*,*N*′-methylene-bis-acrylamide α,α'-Azoisobutyronitrile dissolved in a few ml of acetone was used as a polymerization initiator. The gel was transferred to a porcelain bowl and heated in a ventilated furnace at 3 K min^{-1} up to 800°C with 1 h dwell. A final annealing at 1100°C was required to obtain the single phase $Nd_2NiO_{4+\delta}$. The particle size was approximately 0.8 μm after an attrition stage. Uniaxial pressing at 1.5 MPa and sintering at 1350°C for 4 h gave a cylindrical sample of ca. 15 mm diameter and 7 mm thickness with a relative density of 98%, based on a theoretical density of 7.53 g cm^{-3}, as determined from XRD-measurements. From this tablet, a thin slice of $7 \times 7 \times 1$ mm^3 was cut with a diamond wire saw, which was then ground with SiC-paper (240 grit) and polished to a thickness of 0.467 mm on polymer-embedded diamond lapping films with 30, 6, and 1 μm particle size. Electrical contacts were established by attaching four gold wires to the corners of the sample with gold paste (Metalor).

A single-phase pellet of $La_{0.6}Sr_{0.4}CoO_{3-\delta}$ was obtained from commercial powder (Praxair Specialty Ceramics) after pressing and sintering at 1200°C for 4 h in air with heating and cooling rates of 5 K min^{-1}. The geometric density of the pellet was above 95% of the

---

[*] Electrochemical Society Student Member.
[**] Electrochemical Society Active Member.
[z] E-mail: sitte@unileoben.ac.at

theoretical density. A sample with dimensions of $5 \times 5 \times 0.204$ mm^3 was prepared and electrically contacted according to the procedure described above.

X-ray diffraction (XRD).—XRD-spectra were recorded with a Bruker AXS (model D8 Advance) employing Cu-Kα radiation in the range $10° \leq 2\theta \leq 100°$ with a resolution of 0.020° per step (2θ).

Thermoanalysis.—Changes in oxygen content and chemical stability of $Nd_2NiO_{4+\delta}$ were investigated by precision thermogravimetry (TG) with a symmetric thermobalance (Setaram, model TAG 2416). Heating and cooling segments (5 K min^{-1}) of each thermal cycle were interrupted by a 2 h equilibration time. Powder for thermogravimetric measurements was obtained by crushing a sintered tablet in an agate mortar. As a rule, 30–40 mg were used for each experiment. Oxygen partial pressures were adjusted by mixing O_2 (purity ≥ 99.995%) and Ar (purity ≥ 99.999%) in appropriate ratios using mass flow controllers (Mykrolis, FC2700). For investigations of the stability of the nickelate powder vs. CO_2, a commercial gas mixture of 20 vol. % $O_2 + 5$ vol. % CO_2 in Ar was used. A moist atmosphere with $pH_2O = 9 \times 10^{-3}$ bar (∼30% relative humidity at 25°C) was prepared by humidification of the O_2-Ar mixture.

Electrical conductivity relaxation (CR).—Electrical conductivity and conductivity relaxation measurements were performed in a quartz reactor placed in a tube furnace. During each measurement, the reactor was flushed with appropriate gas mixtures of 1 vol. % O_2 in Ar and 20 vol. % O_2 in Ar using mass flow controllers (Teledyne Hastings 302) at a total flow of 5 l h^{-1} (STP). Sample temperature and oxygen partial pressure (pO_2) were measured with a potentiometric oxygen sensor with integrated S-thermocouple (MicroPoas, Setnag) placed close to the sample. The dc electrical conductivity was measured in the van der Pauw geometry[31,32] at pO_2 of 0.01, 0.02, 0.1, and 0.2 bar. Four-point dc conductivity relaxation measurements[33] were conducted by oxygen partial pressure steps of 0.01–0.02 bar and 0.1–0.2 bar while recording the transient voltage signal as a function of time. Current was applied with a precision current source (Keithley, model 2400) and the voltage was measured with a sensitive digital voltmeter (Keithley, model 182). A four-way valve was used for manually switching between different gas mixtures. Chemical surface exchange coefficients k_{chem} and diffusion coefficients D_{chem} of oxygen were obtained by fitting the appropriate solution of the diffusion equation to the normalized conductivity values, taking into account the flush time of the reactor.[34,35] Standard errors from non-linear regression analysis were about 1% for both parameters. Standard deviations calculated from repeated measurements at constant temperature (disregarding the systematic differences between oxidation and reduction steps) were usually below 20% for both k_{chem} and D_{chem}.

Results and Discussion

Phase purity.—Crystal structure and phase purity were verified by XRD at room temperature on sintered disks of $Nd_2NiO_{4+\delta}$ and $La_{0.6}Sr_{0.4}CoO_{3-\delta}$. XRD-patterns confirm the presence of a distorted K_2NiF_4-type main phase for $Nd_2NiO_{4+\delta}$, additional reflections can be ascribed to a minor amount of Nd_2O_3 secondary phase. The Nd:Ni-ratio was determined as 2.0 ± 0.1 by ICP-MS after dissolving the nickelate in 6 M HCl. $La_{0.6}Sr_{0.4}CoO_{3-\delta}$ was found to crystallize in the rhombohedrally distorted perovskite structure, and no secondary phases were detected by XRD.

Thermoanalysis.—Powders of $Nd_2NiO_{4+\delta}$ were characterized by thermogravimetric analyses under dry conditions as well as in humidified and CO_2-enriched atmospheres. Typically, the first heating cycle contains anomalies due to non-equilibrium effects resulting from high cooling rates after sintering and adsorbed gas species.[28] Consequently, only the second or third thermal cycles, which show good reproducibility of mass changes during heating and cooling, are used for evaluation.

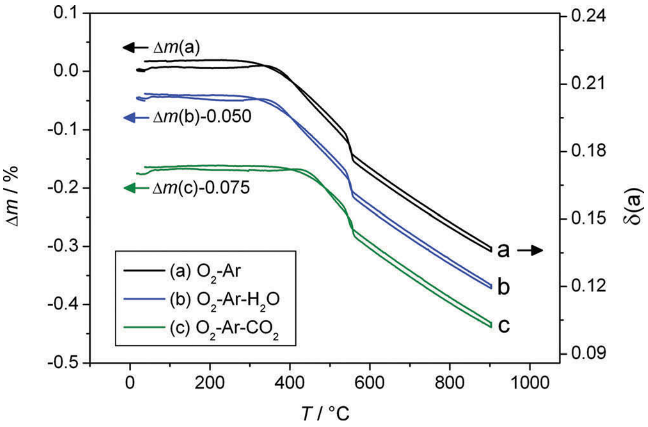

Figure 1. (Color online) Relative mass changes of $Nd_2NiO_{4+\delta}$ during heating/cooling cycles (rates 5 K min^{-1}) in different atmospheres of 20 vol. % O_2 and (a) rest Ar, (b) 30% relative humidity, rest Ar, (c) 5 vol. % CO_2, rest Ar. The oxygen excess δ was calculated for curve (a). For reasons of clarity, curves (b) and (c) are shifted on the relative mass scale by increments of $\Delta m = -0.050$ and -0.075, respectively.

The relative mass changes of $Nd_2NiO_{4+\delta}$ in dry, CO_2-free atmosphere are shown in Fig. 1, line (a). The oxygen excess δ was calculated based on the reference point δ∼0.22 at room temperature.[27,36] Oxygen exchange starts at around 350°C and occurs in two defined regions, which are separated by a reversible transition at ∼550°C. In the LT range (low temperatures, 350–550°C), oxygen release is ∼1.5 times faster than at HT (high temperatures, 550–900°C). Boehm et al.[27] describe the same transition at δ_{trans} ∼0.18, which is in good agreement with our results. The effect was shown to be related to the transition between orthorhombic (LT) and pseudo-tetragonal (HT) modifications by Ishikawa et al.,[36] who report a slightly different transition point of δ_{trans} ∼0.15. It is likely that discrepancies between transition points found in the literature originate in the uncertainty of the determination of the reference point for δ. As discussed below, an additional source of error may be introduced by small deviations from A-site stoichiometry, since δ_{trans} of $Nd_{2-x}NiO_{4+\delta}$ is dependent on x.[27]

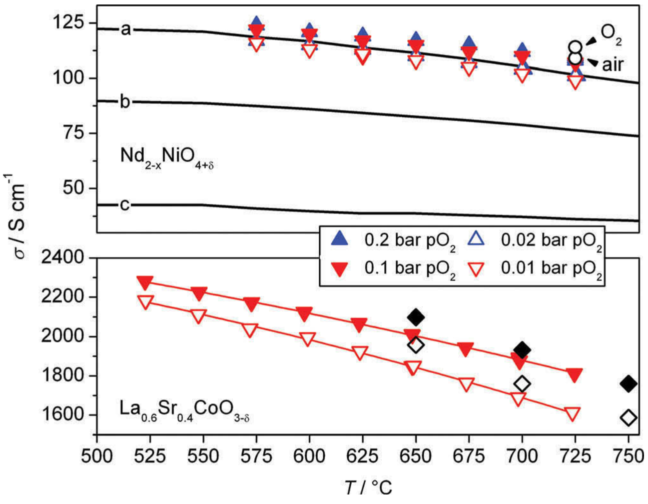

Figure 2. (Color online) Electronic conductivity of $Nd_{2-x}NiO_{4+\delta}$ (top) vs. temperature at different oxygen partial pressures. Lines represent data from Boehm et al.[27] for (a) $Nd_{1.95}NiO_{4+\delta}$, (b) $Nd_{1.90}NiO_{4+\delta}$ and (c) $Nd_2NiO_{4+\delta}$ in air. The electronic conductivity of $La_{0.6}Sr_{0.4}CoO_{3-\delta}$ (bottom) is more than 1 order of magnitude larger than for the nickelate. Data from Søgaard et al.[41] of $(La_{0.6}Sr_{0.4})_{0.99}CoO_{3-\delta}$ are given for $pO_2 = 0.1$ bar (solid diamonds) and $pO_2 = 0.01$ bar (open diamonds). Lines in the bottom diagram are guides for the eye.

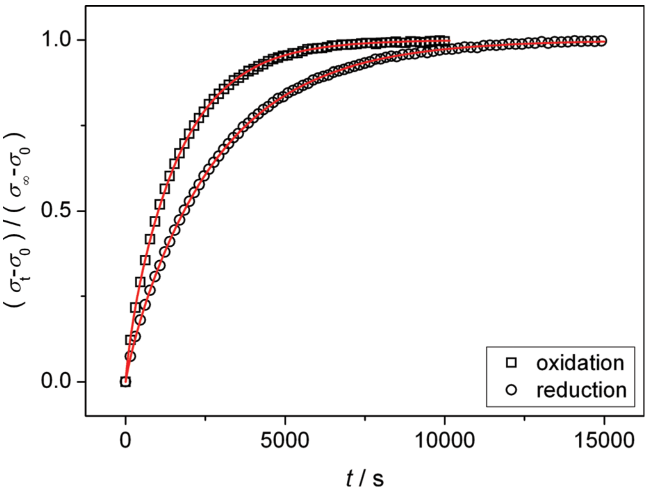

Figure 3. (Color online) Relaxation data of $Nd_2NiO_{4+\delta}$ given as normalized conductivity vs. time for pO_2-steps between 1×10^{-2} and 2×10^{-2} bar at 650°C. For reasons of clarity not all data points are shown. Solid lines are non-linear least squares fits of the model for mixed control to the data with k_{chem} and D_{chem} as fitting parameters, taking into account a reactor flush time of 1 s. Values extracted from the fits are $k_{chem} = 3.4 \times 10^{-5}$ cm s^{-1}, $D_{chem} = 2.1 \times 10^{-7}$ cm^2 s^{-1} for oxidation and $k_{chem} = 1.5 \times 10^{-5}$ cm s^{-1}, $D_{chem} = 1.6 \times 10^{-7}$ cm^2 s^{-1} for reduction.

The oxygen exchange characteristics of $Nd_2NiO_{4+\delta}$ in humid atmosphere (Fig. 1b) show no difference from the analogous experiment under dry conditions. With the presence of carbon dioxide, the onset of mass loss is shifted to a higher temperature of ~400°C (Fig. 1c). Oxygen exchange seems to be suppressed by adsorbed CO_2 at lower temperatures and starts after the CO_2 has been removed from the sample surface during heating. This has been previously investigated in more detail by coupled TG-mass spectrometry.[37] Apart from this effect CO_2 appears to have no significant impact up to 900°C. In particular, there is no indication of any carbonate formation as was found, for example, for $Ba_{0.5}Sr_{0.5}Co_{0.8}Fe_{0.2}O_{3\text{-}\delta}$ by TG measurements.[28,38]

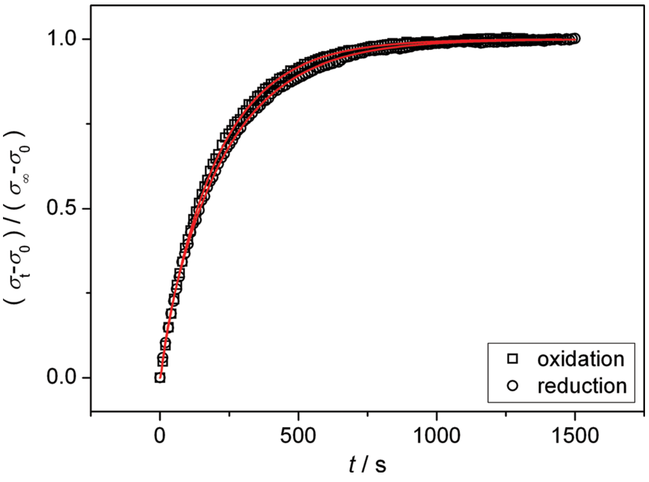

Figure 4. (Color online) Relaxation data of $La_{0.6}Sr_{0.4}CoO_{3\text{-}\delta}$ given as normalized conductivity vs. time for pO_2-steps between 0.1 and 0.15 bar at 650°C. For reasons of clarity not all data points are shown. Solid lines are non-linear least squares fits of the model for mixed control to the data using k_{chem} and D_{chem} as fitting parameters and taking into account a reactor flush time of 3 s. Values obtained from regression analysis are $k_{chem} = 8.8 \times 10^{-5}$ cm s^{-1}, $D_{chem} = 4.4 \times 10^{-7}$ cm^2 s^{-1} for oxidation and $k_{chem} = 1.1 \times 10^{-4}$ cm s^{-1}, $D_{chem} = 2.8 \times 10^{-7}$ cm^2 s^{-1} for reduction.

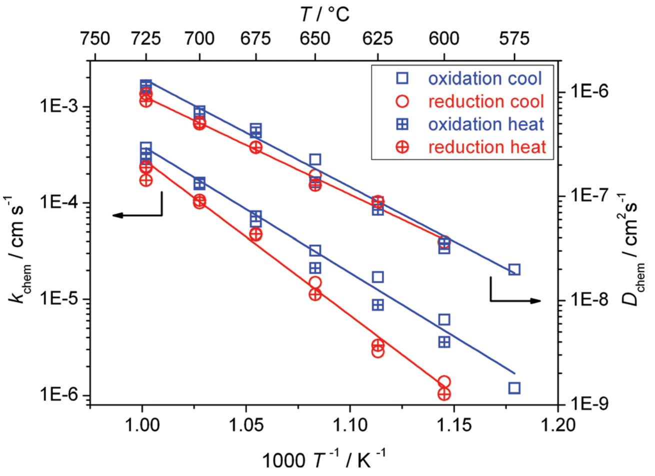

Figure 5. (Color online) Arrhenius plot of the chemical surface exchange coefficient k_{chem} and chemical diffusion coefficient D_{chem} of oxygen for $Nd_2NiO_{4+\delta}$. The square and circle symbols denote results obtained from pO_2-steps of $1 \times 10^{-2} \rightarrow 2 \times 10^{-2}$ bar and $2 \times 10^{-2} \rightarrow 1 \times 10^{-2}$ bar, respectively. Empty and crossed symbols mark results determined from cooling and heating runs, respectively. Activation energies were obtained from linear fits shown as solid lines (see Table I).

Electronic conductivity.—Figure 2 (top) shows the electronic conductivity of $Nd_2NiO_{4+\delta}$ as a function of temperature between 575 and 725°C at oxygen partial pressures of 0.01, 0.02, 0.1, and 0.2 bar. At 725°C, additional measurements in air and pure oxygen were carried out to show the effect of pO_2-variation on the conductivity more clearly. Within the investigated ranges of temperature and pO_2, the following trends can be observed: (i) the conductivity decreases for increasing temperature and (ii) the conductivity increases for higher oxygen partial pressures. As described below, both effects are ultimately a consequence of the *p*-type electronic conduction in $Nd_2NiO_{4+\delta}$.[39,40] Since the electric current is mainly carried by electronic charge carriers (see below), a discussion of the observed changes in conductivity can be based on the fundamental equation

$$\sigma \cong \sigma_e = e c_h \, \mu_h \qquad [1]$$

where σ is the total electrical conductivity, σ_e the electronic conductivity, e the elementary charge, c_h is the number density of electron holes and μ_h is their mobility. Equation 1 states that any change in σ is a consequence of changes in c_h or μ_h or both.

Rationalizing the pO_2-dependence of σ is straightforward for $Nd_2NiO_{4+\delta}$. It has been established by Nakamura et al.[40] that the hole mobility μ_h of $Nd_2NiO_{4+\delta}$ does not change with oxygen partial pressure between 1×10^{-4} and 1 bar in the temperature range of 600–900°C. Hence the pO_2-dependence of σ can be assumed to be solely a result of the change in the hole concentration c_h. Raising

Table I. Activation energies E_a of k_{chem} and D_{chem} for $Nd_2NiO_{4+\delta}$. Results obtained at $pO_2 = 0.1$ bar are separated into two temperature regions $575 \leq T/°C \leq 650$ (LT) and $675 \leq T/°C \leq 725$ (HT) (see text for details).

	0.01 bar ↔ 0.02 bar		0.1 bar ↔ 0.2 bar	
	Oxidation	Reduction	Oxidation	Reduction
E_a (k_{chem})/kJ mol^{-1}	253	312	225 (LT) 315 (HT)	220 (LT) 454 (HT)
E_a (D_{chem})/kJ mol^{-1}	200	182	220 (HT)	236 (HT)

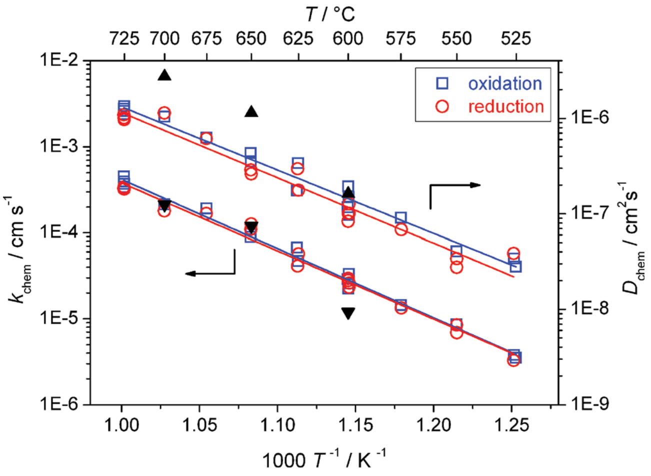

Figure 6. (Color online) Arrhenius plot of the chemical surface exchange coefficient k_{chem} and chemical diffusion coefficient D_{chem} of oxygen for $La_{0.6}Sr_{0.4}CoO_{3-\delta}$. Square and circle symbols denote results obtained from pO_2-steps of 0.1 → 0.15 bar and 0.15 → 0.1 bar, respectively. Activation energies were obtained from linear fits shown as solid lines (see Table II). Data from van der Haar et al.[47] of $La_{0.5}Sr_{0.5}CoO_{3-\delta}$ at $pO_2 = 0.1$ bar are given for D_{chem} (solid triangles tip up) and k_{chem} (solid triangles tip down).

the oxygen partial pressure leads to interstitial incorporation of oxygen into the material, which is compensated by the creation of electron holes, according to the defect equation

$$1/2O_2 + V_i^\times \leftrightarrow O_i'' + 2h^\bullet \qquad [2]$$

The temperature dependence of σ in $Nd_2NiO_{4+\delta}$ is more complex, since a change in temperature affects both hole concentration c_h and mobility μ_h simultaneously. Firstly, as reported by Nakamura et al.[40] for undoped Nd-nickelate, μ_h increases with temperature between 300 and 600°C and starts to decrease at temperatures above. Secondly, raising the temperature also leads to oxygen being released from the sample, which lowers the concentration of electron holes according to Reaction 2.

Of course, changes in oxygen stoichiometry are only relevant for temperatures where oxygen exchange with the gas phase is kinetically possible. As oxygen exchange kinetics for $Nd_2NiO_{4+\delta}$ is frozen in below ~350°C (Fig. 1), σ increases with increasing T below this temperature as is typical for a p-type semiconductor. Once the rate of oxygen exchange becomes significant upon heating above 350°C, σ will increasingly be affected and finally dominated by the decrease in hole concentration due to oxygen release, i.e. σ decreases with increasing T. Based on these competing contributions, a maximum is to be expected in the conductivity vs. temperature graph.

Boehm et al.[27] have measured electronic conductivities of $Nd_{2-x}NiO_{4+\delta}$ (x = 0, 0.05, and 0.1) between 100 and 800°C in air and indeed found an increase in conductivity below 400°C, broad maxima between 400 and 550°C and a decrease in conductivity above 550°C, which is also in agreement with our TG results.

Table II. Activation energies E_a of k_{chem} and D_{chem} for $La_{0.6}Sr_{0.4}CoO_{3-\delta}$ in the temperature region $525 \leq T/°C \leq 725$. For D_{chem} at $pO_2 = 0.01$ bar, too few data points are available for a reliable determination of E_a (see Fig. 8).

	0.01 bar ↔ 0.015 bar		0.1 bar ↔ 0.15 bar	
	Oxidation	Reduction	Oxidation	Reduction
E_a (k_{chem})/kJ mol^{-1}	147	160	154	152
E_a (D_{chem}) / kJ mol^{-1}	—	—	127	131

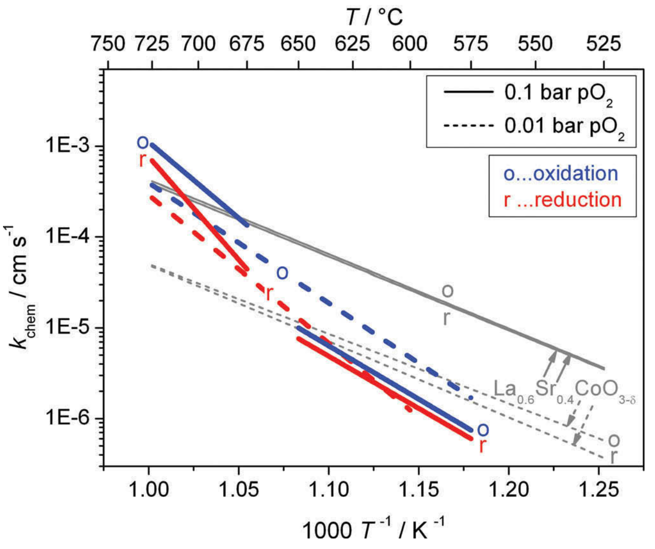

Figure 7. (Color online) Arrhenius plot of the chemical surface exchange coefficient of oxygen for $Nd_2NiO_{4+\delta}$ at different oxygen partial pressures. Data of $La_{0.6}Sr_{0.4}CoO_{3-\delta}$ are given for comparison (marked with arrows). For clarity, only linear fits to the data are shown. Solid and dashed lines represent data at 0.1 and 0.01 bar pO_2, respectively. Results obtained from oxidation and reduction steps are labeled with letters 'o' and 'r', respectively.

A significant difference is observed between the absolute values of electronic conductivities of $Nd_2NiO_{4+\delta}$ determined in this work and in Boehm et al.[27] Differences in oxygen partial pressures can be excluded as a source of the discrepancy, because the effect of pO_2-variation on the conductivity is not sufficiently pronounced to explain such a large deviation (Fig. 2). However, Boehm et al.[27] showed in their work that a small substoichiometry of Nd on the A-site has a strong impact on conductivity. For instance, changing A-site deficiency x from 0 to 0.05 in $Nd_{2-x}NiO_{4+\delta}$ increased the conductivity by a factor of ~3 (Fig. 2). This may be due to an increase in electron hole concentration as one possible mechanism for charge compensation of Nd-vacancies (another compensation mechanism being the decrease of oxygen stoichiometry in the sample). A similar increase in the electronic conductivity for small deviations from the stoichiometric A/B-ratio was also observed for various perovskite oxides by Ullmann et al.[15]

It is therefore proposed that the difference between electronic conductivities given in Boehm et al.[27] and this work is due to a small Nd-deficiency in the nickelate, resulting from either the use of a Nd-substoichiometric starting mixture for synthesis or from the presence of a small amount of Nd_2O_3 secondary phase and the corresponding formation of a Nd-deficient main phase $Nd_{2-x}NiO_{4+\delta}$. It is difficult to obtain a reliable estimation of the Nd-deficiency based on a comparison of electronic conductivities in this study with those given in Boehm et al.[27] because the conductivity-deficiency correlation is not monotonic (see Fig. 2).

The electronic conductivity of $La_{0.6}Sr_{0.4}CoO_{3-\delta}$ is shown in Fig. 2 (bottom) between 525°C and 725°C at $pO_2 = 0.01$ and 0.1 bar. It is well known that high Co-content in perovskite oxides leads to high electronic conductivity (as well as large thermal expansion coefficients). The observed dependence of the conductivity on temperature and oxygen partial pressure in Fig. 2 can be rationalized along similar lines as for the nickelate. However, the defect chemistry associated with oxygen exchange is different for $La_{0.6}Sr_{0.4}CoO_{3-\delta}$, as deviations from oxygen stoichiometry are realized by oxygen vacancies, according to

$$1/2O_2 + V_O^{\bullet\bullet} \leftrightarrow O_O^x + 2h^\bullet \qquad [3]$$

$La_{0.6}Sr_{0.4}CoO_{3-\delta}$ is a p-type conductor[10,41] whose hole mobility is not appreciably affected by changes in δ and shows a metallic-like

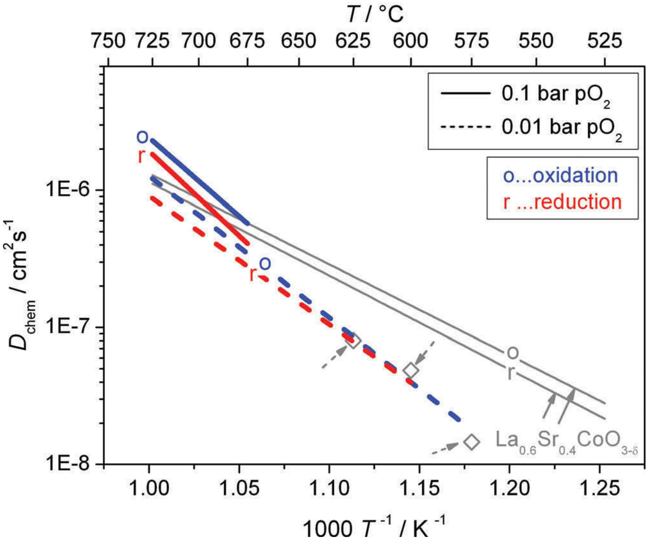

Figure 8. (Color online) Arrhenius plot of the chemical diffusion coefficient of oxygen for $Nd_2NiO_{4+\delta}$ at different oxygen partial pressures, compared to data of $La_{0.6}Sr_{0.4}CoO_{3-\delta}$ (marked with arrows). For clarity, only linear fits to the data are shown, with the exception of data points for $La_{0.6}Sr_{0.4}CoO_{3-\delta}$ at $pO_2 = 0.01$ bar (open diamonds). Solid and dashed lines represent data at 0.1 and 0.01 bar pO_2, respectively. Results obtained from oxidation and reduction steps are labeled with letters 'o' and 'r', respectively.

inversely proportional T-dependence at elevated temperatures.[41] Since oxygen release in $La_{0.6}Sr_{0.4}CoO_{3-\delta}$ starts above ~400°C,[7] the observed decrease in conductivity is caused by a decrease in hole concentration upon lowering pO_2 and by a decrease in both concentration and mobility of holes with increasing temperatures.

Oxygen exchange kinetics.—Kinetic parameters for $Nd_2NiO_{4+\delta}$ and $La_{0.6}Sr_{0.4}CoO_{3-\delta}$ were determined at pO_2-values of 0.1 and 0.01 bar. This pO_2-range represents the expected operating conditions in an actual SOFC cathode, where the equilibrium oxygen partial pressure (with respect to the oxygen stoichiometry of the cathode material, see Eqs. 2 and 3 above) decreases from the cathode-gas (air) interface to the cathode-solid electrolyte interface due to polarization under electrical load.[42]

Representative examples of conductivity relaxation curves including the corresponding fitting lines from non-linear regression analyses are displayed in Figs. 3 and 4 for $Nd_2NiO_{4+\delta}$ and $La_{0.6}Sr_{0.4}CoO_{3-\delta}$, respectively. Relaxation processes for oxidizing steps were consistently found to be faster than those in the reducing direction, the effect being more pronounced for the nickelate and less significant in the cobaltite. Systematically faster oxidation kinetics has also been reported by other authors,[33,43–46] who proposed various explanations, such as experimental difficulties or a non-linear pO_2-dependence of k_{chem} and D_{chem}. However, the frequent occurrence of this phenomenon even for small oxygen pressure steps rather suggests a mechanism which has not been clarified so far.

Results for k_{chem} and D_{chem} for $Nd_2NiO_{4+\delta}$ as obtained from CR-measurements with pO_2-steps between 0.01 and 0.02 bar are shown in Fig. 5 as an Arrhenius-type plot. The oxygen exchange process was in most cases in the regime of mixed-controlled exchange kinetics, allowing for the simultaneous determination of both k_{chem} and D_{chem}. The measurement series was started at 725°C and a complete thermal cycle with a minimum temperature of 575°C was performed to assess the reproducibility of the kinetic parameters. As can be seen from Fig. 5, little to no thermal hysteresis was found between cooling and heating runs. Activation energies obtained from linear fits are collected in Table I.

Results for k_{chem} and D_{chem} of $La_{0.6}Sr_{0.4}CoO_{3-\delta}$ obtained from conductivity relaxation measurements between $pO_2 = 0.1$ and 0.15 bar are presented in detail in Fig. 6. Data points were recorded in steps of 25°C down to 525°C, after which the sample was reheated to check the thermal reversibility of the oxygen exchange performance. Again, the values obtained after reheating to 700 and 725°C were identical to those in the cooling run. The data show good linearity in the Arrhenius plot, activation energies derived from linear regression analysis are listed in Table II. Results for $La_{0.5}Sr_{0.5}CoO_{3-\delta}$ from van der Haar et al.[47] are given in Fig. 6 for comparison.

The complete set of kinetic parameters for $Nd_2NiO_{4+\delta}$ and $La_{0.6}Sr_{0.4}CoO_{3-\delta}$ is presented in Fig. 7 (k_{chem}) and Fig. 8 (D_{chem}). For reasons of clarity, only regression lines obtained from linear fits to the data points are shown.

For the nickelate, D_{chem} could not be extracted by regression analysis below 675°C at 0.1 bar pO_2 because the chemical diffusion coefficient was too high in order to be reliably determined for the given sample thickness. This is a consequence of the very high activation energy for k_{chem} (Table I), which leads to a faster decrease in the oxygen surface exchange rate as compared to oxygen diffusion and finally renders the relaxation rate completely determined by the surface exchange process. This transition is accompanied by a significant change in the activation energy for k_{chem} (Fig. 7). The origin of this effect is currently unclear. A reversible phase transition in $Nd_2NiO_{4+\delta}$ has been reported in the literature based on XRD and thermogravimetric investigations,[27,36,48] and was confirmed by TG-analysis in this work, as discussed above. However, this phase transition takes place well below 650°C, although the precise transition temperature depends on the Nd-stoichiometry,[27] oxygen partial pressure[48] and the thermal history of the sample.[36] Phase transition temperatures of $Nd_2NiO_{4+\delta}$, as determined by thermogravimetry in this work and in Egger et al.[37] were 550 and 500°C in Ar + 20% O_2 and pure Ar, respectively, 550°C in Boehm et al.[27] (TG in air), 570°C in Ishikawa et al.[36] (TG-DTA in air), 610°C in Toyosumi et al.[48] (XRD in air) and 620°C in Boehm et al.[27] (XRD in air). It is interesting to note that XRD measurements consistently yield transition temperatures higher than those obtained from TG-analysis. Nd-deficient compounds $Nd_{2-x}NiO_{4+\delta}$ were investigated by Boehm et al.,[27] where TG-data gave transition temperatures of 550°C for x = 0, 555°C for x = 0.05 and 600°C for x = 0.1 in air. All in all, even though there appears to be some variability in the temperature data, it seems unlikely that the phase transition is the reason for the change in activation energy of k_{chem} around 650°C.

In Figs. 7 and 8 k_{chem} and D_{chem} of $La_{0.6}Sr_{0.4}CoO_{3-\delta}$ and $Nd_2NiO_{4+\delta}$ are directly compared. Above 700°C, the surface exchange coefficients and chemical diffusivities of $Nd_2NiO_{4+\delta}$ are higher than those of $La_{0.6}Sr_{0.4}CoO_{3-\delta}$. However, due to the very

Table III. Data for $Nd_2NiO_{4+\delta}$ obtained from conductivity relaxation measurements at 0.01 bar oxygen partial pressure. Oxygen non-stoichiometry data were taken from Nakamura et al.[50]

T / °C	δ	γ_o	D_{chem} / cm^2s^{-1}	D_o / cm^2s^{-1}	σ_i / S cm^{-1}	k_{chem} / cm s^{-1}	k_o / cm s^{-1}	r_p / Ω cm^2
575	0.129	518	1.99×10^{-8}	3.84×10^{-11}	1.50×10^{-5}	1.19×10^{-6}	2.29×10^{-9}	1115
600	0.126	488	3.44×10^{-8}	7.05×10^{-11}	2.68×10^{-5}	3.03×10^{-6}	6.21×10^{-9}	424
625	0.122	479	8.37×10^{-8}	1.75×10^{-10}	6.44×10^{-5}	7.97×10^{-6}	1.66×10^{-8}	163
650	0.119	471	1.76×10^{-7}	3.74×10^{-10}	1.34×10^{-4}	2.25×10^{-5}	4.77×10^{-8}	59
675	0.116	449	3.62×10^{-7}	8.06×10^{-10}	2.81×10^{-4}	5.76×10^{-5}	1.28×10^{-7}	22
700	0.112	439	5.73×10^{-7}	1.31×10^{-9}	4.44×10^{-4}	1.31×10^{-4}	2.99×10^{-7}	10
725	0.109	426	9.96×10^{-7}	2.34×10^{-9}	7.73×10^{-4}	2.67×10^{-4}	6.26×10^{-7}	5

Table IV. Data for $La_{0.6}Sr_{0.4}CoO_{3\text{-}\delta}$ obtained from conductivity relaxation measurements at 0.1 bar oxygen partial pressure. Oxygen non-stoichiometry data were taken from Sitte et al.[7]

T / °C	δ	γ_o	D_{chem} / cm^2 s^{-1}	D_o / cm^2 s^{-1}	σ_i / S cm^{-1}	k_{chem} / cm s^{-1}	k_o / cm s^{-1}	r_p / Ω cm^2
525	0.023	206	3.35×10^{-8}	1.62×10^{-10}	7.75×10^{-5}	3.27×10^{-6}	1.59×10^{-8}	132
550	0.024	181	3.40×10^{-8}	1.87×10^{-10}	8.67×10^{-5}	7.98×10^{-6}	4.40×10^{-8}	49
575	0.026	161	7.95×10^{-8}	4.94×10^{-10}	2.21×10^{-4}	1.39×10^{-5}	8.63×10^{-8}	26
600	0.029	145	1.21×10^{-7}	8.40×10^{-10}	3.66×10^{-4}	2.72×10^{-5}	1.88×10^{-7}	12
625	0.032	131	2.46×10^{-7}	1.88×10^{-9}	7.95×10^{-4}	5.32×10^{-5}	4.06×10^{-7}	6
650	0.036	120	3.34×10^{-7}	2.78×10^{-9}	1.14×10^{-3}	1.09×10^{-4}	9.06×10^{-7}	3
675	0.041	111	6.21×10^{-7}	5.59×10^{-9}	2.23×10^{-3}	1.79×10^{-4}	1.62×10^{-6}	2
700	0.046	104	1.09×10^{-6}	1.05×10^{-8}	4.09×10^{-3}	1.97×10^{-4}	1.90×10^{-6}	1
725	0.052	98	1.13×10^{-6}	1.16×10^{-8}	4.37×10^{-3}	3.63×10^{-4}	3.71×10^{-6}	1

high activation energies found for both k_{chem} and D_{chem} of $Nd_2NiO_{4+\delta}$, both parameters are comparable to or even below those of $La_{0.6}Sr_{0.4}CoO_{3\text{-}\delta}$ around 600°C.

For a conclusive assessment of both investigated compounds for SOFC applications, the ionic conductivity σ_i and the surface exchange resistance r_p have been calculated from D_{chem} and k_{chem}, respectively. For a predominantly electronic conductor a conversion of the diffusivity D_o into σ_i is achieved through the Nernst-Einstein equation (neglecting the Haven ratio and the correlation factor)

$$\sigma_i = \frac{4F^2 c_o D_o}{RT} \qquad [4]$$

where F is the Faraday constant, c_o the molar concentration of oxygen ions, R the ideal gas constant and D_o the self diffusion coefficient of oxygen. The surface exchange resistance r_p has been evaluated by means of Eq. 5 (Ref. 42)

$$r_p = \frac{RT}{4F^2 c_o k_o} \qquad [5]$$

where k_o is the surface exchange coefficient of oxygen.

Self diffusion coefficients and surface exchange coefficients have been obtained through the thermodynamic factor of oxygen γ_o, defined as

$$\gamma_o = \frac{1}{2}\left(\frac{\ln pO_2}{\ln c_o}\right)_T \qquad [6]$$

and using the relations $D_{chem} = D_o\gamma_o$ and $k_{chem} = k_o\gamma_o$.[49] Both c_o and γ_o were obtained from oxygen non-stoichiometry data given in Sitte et al.[7] for $La_{0.6}Sr_{0.4}CoO_{3\text{-}\delta}$ and Nakamura et al.[50] for $Nd_2NiO_{4+\delta}$, using unit cell volumes of 58.1 Å^3 and 185.2 Å^3 for $La_{0.6}Sr_{0.4}CoO_{3\text{-}\delta}$ and $Nd_2NiO_{4+\delta}$, respectively.

Results for both investigated compounds are collected in Tables III and IV for $Nd_2NiO_{4+\delta}$ and $La_{0.6}Sr_{0.4}CoO_{3\text{-}\delta}$, respectively. Figure 9 compares ionic conductivities of both compounds at temperatures between 550 and 725°C. For $La_{0.6}Sr_{0.4}CoO_{3\text{-}\delta}$, σ_i is approximately 1 order of magnitude higher than that of the nickelate, which is due to differences in D_{chem} and the thermodynamic factors. Ionic conductivities of $La_{0.6}Sr_{0.4}CoO_{3\text{-}\delta}$ determined in this work are lower than those given in the literature, for example at 700°C and 0.1 bar pO_2 σ_i is 4.1×10^{-3} S cm^{-1}, while Søgaard et al.[41] reported 1.6×10^{-2} S cm^{-1} (~0.01 bar pO_2) and Teraoka et al.[51] give 1.3×10^{-1} S cm^{-1} (air). For $Nd_2NiO_{4+\delta}$, ionic conductivities of this study are about 2 orders of magnitude below values reported by Mauvy et al.[29]

Surface exchange resistances r_p of $La_{0.6}Sr_{0.4}CoO_{3\text{-}\delta}$ and $Nd_2NiO_{4+\delta}$ are compared in Fig. 10 and show smaller resistances for the cobaltite by roughly 1 order of magnitude.

Conclusions

The electronic conductivity of $Nd_2NiO_{4+\delta}$ in the investigated temperature and pO_2-range is consistent with a p-type (electron hole) conduction mechanism. Deviation from values given in the literature may be traced to the presence of small amounts of Nd_2O_3 impurities and the formation of a slightly Nd-deficient main phase. In comparison, the electronic conductivity of $La_{0.6}Sr_{0.4}CoO_{3\text{-}\delta}$ is more than 1 order of magnitude higher than that of undoped K_2NiF_4-type nickelates.

$Nd_2NiO_{4+\delta}$ exhibits fast oxygen surface exchange kinetics and high oxygen diffusivities at temperatures around 700°C. Due to high

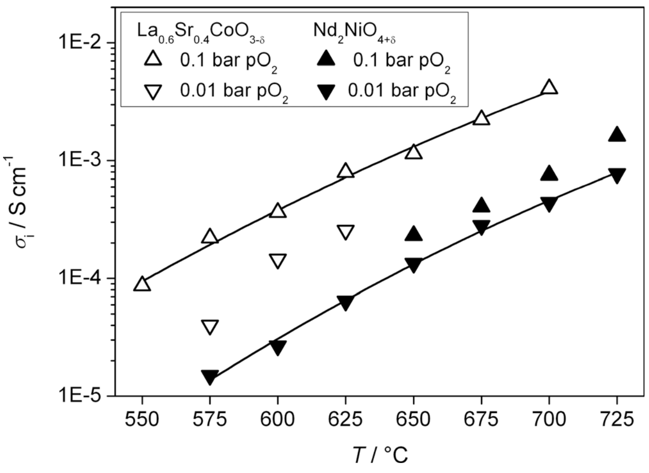

Figure 9. Ionic conductivity vs. temperature for $La_{0.6}Sr_{0.4}CoO_{3\text{-}\delta}$ (open triangles) and $Nd_2NiO_{4+\delta}$ (solid triangles) at oxygen partial pressures of 0.1 bar (triangles tip up) and 0.01 bar (triangles tip down). Lines are guides for the eye.

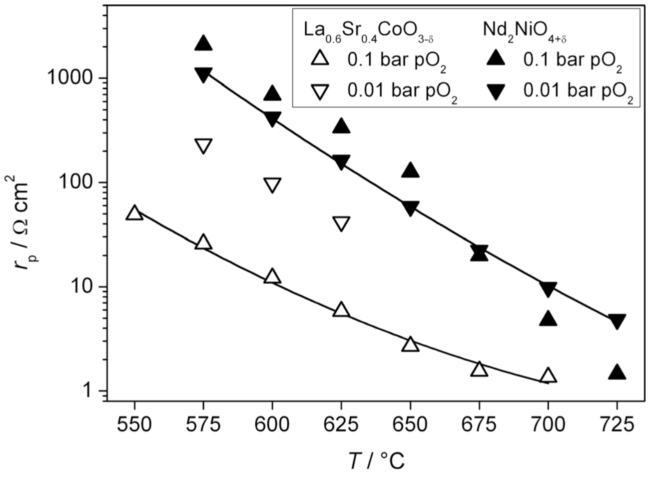

Figure 10. Surface exchange resistance vs. temperature for $La_{0.6}Sr_{0.4}CoO_{3\text{-}\delta}$ (open triangles) and $Nd_2NiO_{4+\delta}$ (solid triangles) at oxygen partial pressures of 0.1 bar (triangles tip up) and 0.01 bar (triangles tip down). Lines are guides for the eye.

activation energies for both k_{chem} and D_{chem}, a strong decrease of both parameters has been observed for decreasing temperatures. At 700°C, the oxygen exchange coefficient of $Nd_2NiO_{4+\delta}$ is higher than that of $La_{0.6}Sr_{0.4}CoO_{3-\delta}$, but it becomes comparable or lower at 600°C due to lower activation energies of k_{chem} and D_{chem} for the latter compound. Ionic conductivities and surface exchange resistances, as calculated from D_{chem} and k_{chem} of both compounds, show superior oxygen transport properties of $La_{0.6}Sr_{0.4}CoO_{3-\delta}$ compared to $Nd_2NiO_{4+\delta}$ for application as IT-SOFC cathode material in pure O_2-Ar atmospheres.

TG measurements for $Nd_2NiO_{4+\delta}$ indicate good short–term stability of the oxygen exchange properties in dry air as well as in atmospheres containing H_2O and CO_2 up to 900°C. The absence of alkaline earth metals in $Nd_2NiO_{4+\delta}$ may account for its resistance to carbonate formation. Nevertheless, it should be mentioned that an in-depth investigation of the chemical stability of $Nd_2NiO_{4+\delta}$ by Egger et al.[52] showed some impact of water on the surface chemistry of the nickelate, as detected by X-ray photoelectron spectroscopy, whereas an excellent stability of $Nd_2NiO_{4+\delta}$ in dry atmospheres both with and without CO_2 over at least 1000 h has been demonstrated. The investigation of the long-term stability of $La_{0.6}Sr_{0.4}CoO_{3-\delta}$ in dry and wet atmospheres is under progress.[53]

Acknowledgment

Financial support from the EC within the integrated project SOFC600 (contract no. 020089) is gratefully acknowledged. The authors thank Jean-Marc Bassat and Cécile Lalanne from ICMCB-CNRS (France) and Frans van Berkel from ECN (the Netherlands) for providing the sintered pellets as well as Thomas Meisel from the University of Leoben (Austria) for assistance with ICP-MS measurements.

University of Leoben assisted in meeting the publication costs of this article.

References

1. C. Sun, R. Hui, and J. Roller, *J. Solid State Electrochem.*, **14**, 1125 (2010).
2. A. N. Petrov, O. F. Kononchuk, A. V. Andreev, V. A. Cherepanov, and P. Kofstad, *Solid State Ionics*, **80**, 189 (1995).
3. A. Petric, P. Huang, and F. Tietz, *Solid State Ionics*, **135**, 719 (2000).
4. R. A. De Souza and J. A. Kilner, *Solid State Ionics*, **106**, 175 (1998).
5. R. A. De Souza and J. A. Kilner, *Solid State Ionics*, **126**, 153 (1999).
6. A. V. Berenov, A. Atkinson, J. A. Kilner, E. Bucher, and W. Sitte, *Solid State Ionics*, **181**, 819 (2010).
7. W. Sitte, E. Bucher, and W. Preis, *Solid State Ionics*, **154–155**, 517 (2002).
8. Y. Takeda, R. Kanno, M. Noda, and O. Yamamoto, *Bull. Inst. Chem. Res., Kyoto Univ.*, **64**, 157 (1986).
9. Y. Takeda, R. Kanno, M. Noda, Y. Tomida, and O. Yamamoto, *J. Electrochem. Soc.*, **134**, 2656 (1987).
10. J. Mizusaki, J. Tabuchi, T. Matsuura, S. Yamauchi, and K. Fueki, *J. Electrochem. Soc.*, **136**, 2082 (1989).
11. A. Mineshige, M. Inaba, T. Yao, Z. Ogumi, K. Kikuchi, and M. Kawase, *J. Solid State Chem.*, **121**, 423 (1996).
12. A. Mineshige, M. Kobune, S. Fujii, Z. Ogumi, M. Inaba, T. Yao, and K. Kikuchi, *J. Solid State Chem.*, **142**, 374 (1999).
13. E. B. Mitberg, M. V. Patrakeev, I. A. Leonidov, V. L. Kozhevnikov, and K. R. Poeppelmeier, *Solid State Ionics*, **130**, 325 (2000).
14. V. V. Kharton, E. N. Naumovich, A. A. Vecher, and A. V. Nikolaev, *J. Solid State Chem.*, **120**, 128 (1995).
15. H. Ullmann, N. Trofimenko, F. Tietz, D. Stöver, and A. Ahmad-Khanlou, *Solid State Ionics*, **138**, 79 (2000).
16. W. Zipprich and H.-D. Wiemhöfer, *Solid State Ionics*, **135**, 699 (2000).
17. O. Yamamoto, Y. Takeda, R. Kanno, and M. Noda, *Solid State Ionics*, **22**, 241 (1987).
18. M. Backhaus-Ricoult, *Solid State Sci.*, **10**, 670 (2008).
19. J. P. Kemp, D. J. Beal, and P. A. Cox, *J. Solid State Chem.*, **86**, 50 (1990).
20. P. A. W. van der Heide, *Surf. Interface Anal.*, **33**, 414 (2002).
21. P. Hjalmarsson, M. Søgaard, and M. Mogensen, *Solid State Ionics*, **179**, 1422 (2008).
22. D. Balz and K. Plieth, *Z. Elektrochem.*, **59**, 545 (1955).
23. S. N. Ruddlesden and P. Popper, *Acta Crystallogr.*, **11**, 54 (1958).
24. G. Amow and S. J. Skinner, *J. Solid State Electrochem.*, **10**, 538 (2006).
25. M. T. Fernandez-Diaz, J. L. Martinez, and J. Rodriguez-Carvajal, *Solid State Ionics*, **63–65**, 902 (1993).
26. M. Al Daroukh, V. V. Vashook, H. Ullmann, F. Tietz, and I. Arual Raj, *Solid State Ionics*, **158**, 141 (2003).
27. E. Boehm, J. M. Bassat, P. Dordor, F. Mauvy, J. C. Grenier, and P. Stevens, *Solid State Ionics*, **176**, 2717 (2005).
28. E. Bucher, A. Egger, G. B. Caraman, and W. Sitte, *J. Electrochem. Soc.*, **155**, B1218 (2008).
29. F. Mauvy, J. M. Bassat, E. Boehm, J. P. Manaud, P. Dordor, and J. C. Grenier, *Solid State Ionics*, **158**, 17 (2003).
30. A. Douy, *Int. J. Inorg. Mater.*, **3**, 699 (2001).
31. L. J. van der Pauw, *Philips Res. Rep.*, **13**, 1 (1958).
32. D. Grientschnig and W. Sitte, *Z. Phys. Chem.*, **168**, 143 (1990).
33. W. Preis, E. Bucher, and W. Sitte, *Solid State Ionics*, **175**, 393 (2004).
34. M. W. den Otter, H. J. M. Bouwmeester, B. A. Boukamp, and H. Verweij, *J. Electrochem. Soc.*, **148**, J1 (2001).
35. W. Preis, E. Bucher, and W. Sitte, *J. Power Sources*, **106**, 116 (2002).
36. H. Ishikawa, Y. Toyosumi, and K. Ishikawa, *J. Alloys Compd.*, **408–412**, 1196 (2006).
37. A. Egger, E. Bucher, W. Sitte, C. Lalanne, and J. M. Bassat, *ECS Trans.*, **25**(2), 2547 (2009).
38. E. Bucher, G. B. Caraman, and W. Sitte, in *Proceedings of the Eighth European SOFC Forum*, R. Steinberger-Wilckens, Editor, p. A0603, Lucerne, Switzerland (2008).
39. C. Laberty-Robert and K. Swider-Lyons, in *Solid Oxide Fuel Cells (SOFC IX)*, S. C. Singhal and J. Mizusaki, Editors, PV 2005-07, p. 1751, The Electrochemical Society, Proceedings Series, Pennington, NJ (2005).
40. T. Nakamura, K. Yashiro, K. Sato, and J. Mizusaki, *Mater. Chem. Phys.*, **122**, 250 (2010).
41. M. Søgaard, P. V. Hendriksen, M. Mogensen, F. W. Poulsen, and E. Skou, *Solid State Ionics*, **177**, 3285 (2006).
42. M. Søgaard, P. V. Hendriksen, T. Jacobsen, and M. Mogensen, in *Proceedings of the Seventh European SOFC Forum*, U. Bossel, Editor, p. B064, Lucerne, Switzerland (2006).
43. S. Kim, S. Wang, X. Chen, Y. L. Yang, N. Wu, A. Ingnatiev, A. J. Jacobson, and B. Abeles, *J. Electrochem. Soc.*, **147**, 2398 (2000).
44. S. Wang, A. Verma, Y. L. Yang, A. J. Jacobson, and B. Abeles, *Solid State Ionics*, **140**, 125 (2001).
45. J. A. Lane and J. A. Kilner, *Solid State Ionics*, **136–137**, 997 (2000).
46. S. Wang, P. A. W. van der Heide, C. Chavez, A. J. Jacobson, and S. B. Adler, *Solid State Ionics*, **156**, 201 (2003).
47. L. M. van der Haar, M. W. den Otter, M. Morskate, H. J. M. Bouwmeester, and H. Verweij, *J. Electrochem. Soc.*, **149**, J41 (2002).
48. Y. Toyosumi, H. Ishikawa, and K. Ishikawa, *J. Alloys Compd.*, **408–412**, 1200 (2006).
49. J. E. ten Elshof, M. H. R. Lankhorst, and H. J. M. Bouwmeester, *J. Electrochem. Soc.*, **144**, 1060 (1997).
50. T. Nakamura, K. Yashiro, K. Sato, and J. Mizusaki, *Solid State Ionics*, **181**, 402 (2010).
51. Y. Teraoka, H. M. Zhang, K. Okamoto, and N. Yamazoe, *Mater. Res. Bull.*, **23**, 51 (1988).
52. A. Egger, W. Sitte, F. Klauser, and E. Bertel, *J. Electrochem. Soc.*, **157**, B1537 (2010).
53. E. Bucher, F. Klauser, E. Bertel, and W. Sitte, To be published.

Solid State Ionics 192 (2011) 148–152

Contents lists available at ScienceDirect

Solid State Ionics

journal homepage: www.elsevier.com/locate/ssi

Electrical properties of bulk and grain boundaries of scandia-stabilized zirconia co-doped with yttria and ceria

W. Preis [a],*, J. Waldhäusl [a], A. Egger [a], W. Sitte [a], E. de Carvalho [b], J.T.S. Irvine [b]

[a] Chair of Physical Chemistry, University of Leoben, A-8700 Leoben, Austria
[b] School of Chemistry, University of St. Andrews, St. Andrews, KY16 9ST, Scotland, UK

ARTICLE INFO

Article history:
Received 13 August 2009
Received in revised form 14 May 2010
Accepted 14 June 2010
Available online 13 July 2010

Keywords:
Solid electrolyte
Oxide ion conductor
Impedance spectroscopy
Scandia-stabilized zirconia
IT-SOFC

ABSTRACT

The electrical properties of bulk and grain boundaries of scandia-stabilized zirconia co-doped with yttria and ceria have been determined as a function of temperature ($300<T/°C<700$) and oxygen partial pressure [$10^{-24} \leq p(O_2)/\text{bar} \leq 1$, $T = 700$ °C] by application of impedance spectroscopy. The yttria and ceria contents of $Ce_xY_{0.2-x}Sc_{0.6}Zr_{3.2}O_{8-\delta}$ ($0 \leq x \leq 0.2$) have been varied systematically. Homogeneous samples have been prepared by means of a sol–gel (glycine-nitrate) combustion process. The ionic conductivity in air is almost independent of composition with typical values around 0.03–0.04 S cm^{-1} for the bulk at 700 °C. A significant decrease of the ionic conductivities of bulk and grain boundaries is found for samples co-doped with ceria at low oxygen partial pressures [$p(O_2)<10^{-15}$ bar, $T = 700$ °C]. Activation energies for the ionic transport in oxidizing (air) and reducing (1%-H_2/Ar) atmospheres have been extracted from Arrhenius-plots. The oxygen nonstoichiometry in 1%-H_2/Ar has been investigated by employing thermogravimetry. The decrease of the ionic conductivity under reducing conditions is accompanied by an increase of the corresponding high temperature activation energy of the bulk, which is interpreted in terms of defect association or clustering.

1. Introduction

Intermediate temperature solid oxide fuel cells (IT-SOFCs) are usually operated at temperatures between 600 and 800 °C. The reduction of the operation temperature requires the development of new solid electrolytes with high ionic conductivity and negligible electronic conduction under reducing conditions. Yttria-stabilized zirconia (YSZ) shows high phase stability and negligible low electronic conductivity in both oxidizing and reducing atmospheres [1,2]. While a much higher ionic conductivity is found for gadolinia-doped ceria (GDC) compared to YSZ at 700 °C, the electronic conductivity of GDC increases considerably under reducing conditions, such that ceria-based electrolytes become mixed conductors at low oxygen partial pressures [3,4]. The cubic fluorite-type phase of scandia-stabilized zirconia (ScSZ) meets both requirements for application in IT-SOFCs [5–7]. However, co-doping with yttria and/or ceria is necessary to avoid detrimental phase transformations and to stabilize the cubic modification [8,9].

Oxygen vacancies are created in zirconia-based electrolyte materials by doping with aliovalent cations. The ionic conductivity of the system ZrO_2–Ln_2O_3 (Ln = lanthanides) shows a maximum between 8 and 11 mol% Ln_2O_3 depending on the dopant [10]. This behaviour may be caused by the formation of defect associates or clusters between the trivalent dopant cations and oxygen vacancies [11,12]. A detailed understanding of the defect chemistry of doped fluorite-based oxides is crucial for the development of novel electrolyte materials with improved transport properties.

It is the aim of this contribution to present a systematic study of the electrical properties of bulk and grain boundaries of $Ce_xY_{0.2-x}Sc_{0.6}Zr_{3.2}O_{8-\delta}$ ($0 \leq x \leq 0.2$) as a function of temperature ($300<T/°C<700$) and oxygen partial pressure, ranging from 1 to 10^{-24} bar at 700 °C, by application of impedance spectroscopy. In contrast to microcrystalline bulk samples, nanocrystalline thin films of scandia-stabilized zirconia exhibit high electronic conductivities under reducing conditions [7]. The variation of the oxygen partial pressure, $p(O_2)$, will elucidate in how far the electronic conductivity of microcrystalline samples, co-doped with ceria, is increased at low $p(O_2)$ values. The experimental results for the ionic transport properties are interpreted in terms of defect association or clustering.

2. Experimental

Powders of $Ce_xY_{0.2-x}Sc_{0.6}Zr_{3.2}O_{8-\delta}$ ($0 \leq x \leq 0.2$) were prepared by means of a sol–gel (glycine-nitrate) combustion process and disc-shaped samples were obtained by sintering at 1500 °C. The sintered pellets (diameter: ca. 9.5 mm, thickness: 0.5–1.5 mm) were removed from the furnace at 1000 °C and cooled down to room temperature. Details of sample preparation can be found elsewhere [13]. The crystal

---

* Corresponding author. Tel.: +43 3842 402 4805; fax: +43 3842 402 4802.
E-mail address: wolfgang.preis@mu-leoben.at (W. Preis).

0167-2738/$ – see front matter © 2010 Elsevier B.V. All rights reserved.
doi:10.1016/j.ssi.2010.06.013

structure of calcined powders was analyzed by X-ray diffraction (Phillips Diffractometer, 20–90° 2θ, step size 0.02° 2θ, CuKα radiation). The microstructure of sintered samples was investigated in a JEOL JSM-5600 scanning electron microscope (SEM). The average grain size was estimated from SEM micrographs of polished and thermally etched samples.

The conductivities of the bulk and grain boundaries were characterized by application of impedance spectroscopy (Alpha-A Analyzer, Novocontrol). The effective voltage was $V_{rms} = 20$ mV at frequencies ranging from 3 MHz to 100 mHz. Platinum paste, burned-in at 1000 °C for 2 h, served as electrodes at both faces of the disc-shaped specimens (symmetrical two-electrode cell). The stray inductance of the leads of the sample holder amounted to 0.02–0.04 μH, which was determined on the empty (short-circuited) measurement rig. All impedance measurements were performed in four-wire mode, resulting in negligible stray resistances of the sample holder. The temperature was varied from 300 to 700 °C under oxidizing (air) as well as reducing conditions (1%-H_2/Ar). The furnace temperature was held constant within ±1 °C by employing a precision temperature controller (Eurotherm 2416). The temperature and the oxygen partial pressure were determined close to the sample by using type-S thermocouples and a zirconia-based potentiometric oxygen sensor (Setnag), respectively. In addition, the oxygen partial pressure dependence of the electrical conductivity was studied from 1 to 10^{-24} bar at 700 °C by employing a zirconia-based electrochemical oxygen pump which allows the precise and continuous variation of $p(O_2)$ [14].

Furthermore, the oxygen nonstoichiometry was investigated on powdered samples by thermogravimetry (precision thermobalance, Setaram TAG 2416) in 1%-H_2/Ar at 700 °C. The heating and cooling rates amounted to 8 °C/min and 1 °C/min. The samples were isothermally equilibrated at 700 °C in reducing atmosphere [1%-H_2/Ar, $p(O_2) \approx 10^{-24}$ bar] until the mass signal was constant within ±1 μg. Re-oxidation experiments were performed on selected samples in a O_2/Ar-gas mixture [$p(O_2) = 0.2$ bar] at 700 °C.

3. Results and discussion

The average grain size of the sintered pellets amounts to approximately 5 μm as obtained from SEM micrographs. In some cases small "sub-grains" of 10–100 nm were observed inside larger grains (5 μm), especially for samples containing ceria. XRD-pattern confirmed that all compositions of the system $Ce_xY_{0.2-x}Sc_{0.6}Zr_{3.2}O_{8-\delta}$ ($0 \leq x \leq 0.2$) are single phase and show cubic fluorite-type structure.

The bulk and grain boundary conductivities of $Y_{0.2}Sc_{0.6}Zr_{3.2}O_{7.60}$ and $Ce_{0.12}Y_{0.08}Sc_{0.6}Zr_{3.2}O_{7.66}$ as determined by application of impedance spectroscopy are depicted as a function of temperature (Arrhenius-plots) in Fig. 1. First, a temperature (heating) run has been carried out in air [$p(O_2) = 0.21$ bar] from 300 to 700 °C. Then the specimens have been equilibrated under reducing conditions (1%-H_2/Ar, 700 °C) for

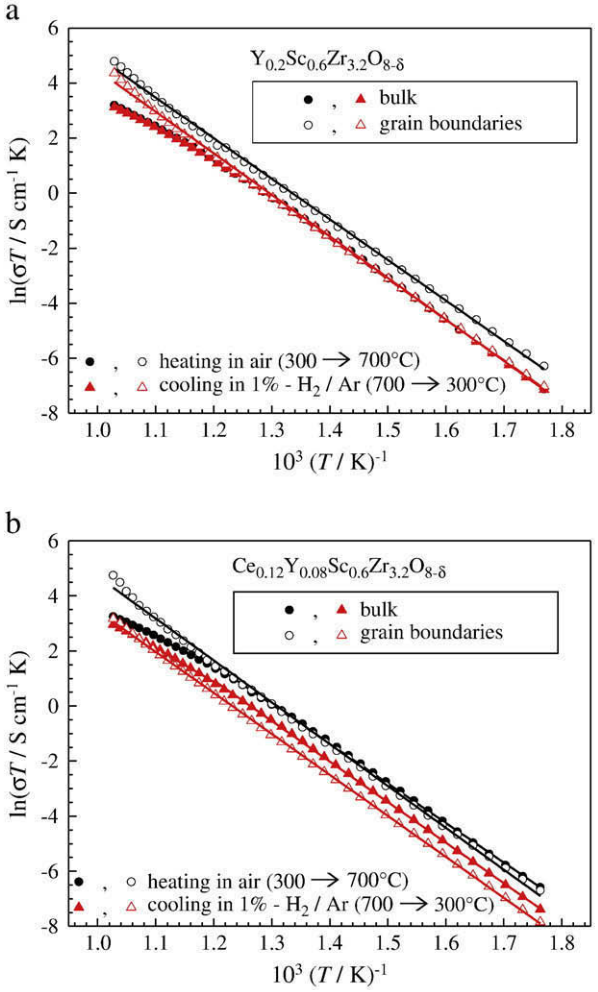

Fig. 1. Temperature dependence of the ionic conductivity in oxidizing (air) and reducing (1%-H_2/Ar) atmospheres. The data in 1%-H_2/Ar were obtained after reduction at 700 °C for approximately four days. Filled and open symbols refer to the bulk and grain boundaries, respectively. (a) $Y_{0.2}Sc_{0.6}Zr_{3.2}O_{8-\delta}$, sample with no ceria. (b) $Ce_{0.12}Y_{0.08}Sc_{0.6}Zr_{3.2}O_{8-\delta}$, typical example for a sample co-doped with ceria.

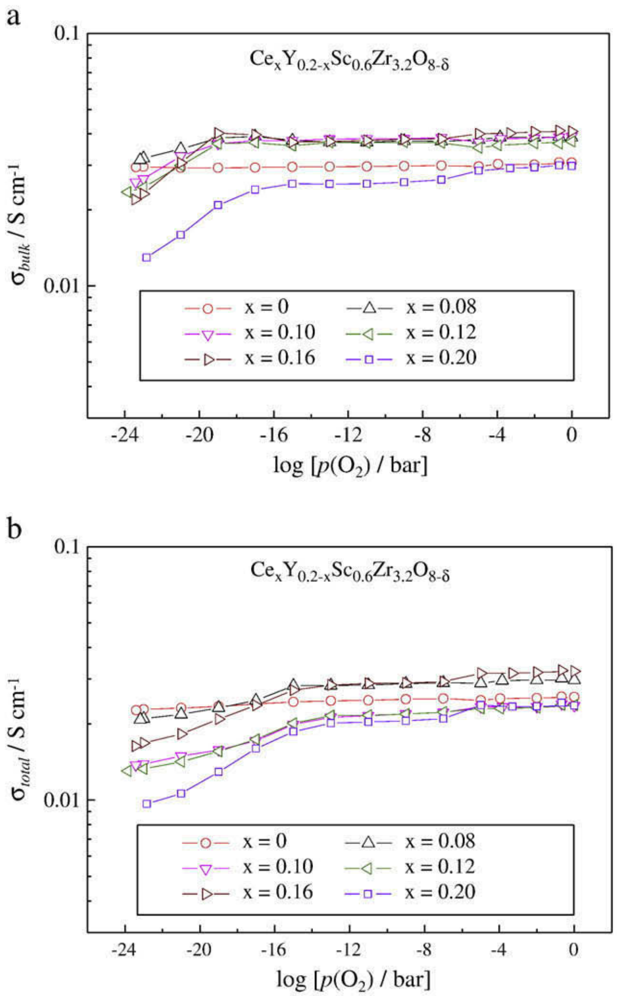

Fig. 2. Electrical conductivities of $Ce_xY_{0.2-x}Sc_{0.6}Zr_{3.2}O_{8-\delta}$ ($0 \leq x \leq 0.2$) at 700 °C plotted as a function of oxygen partial pressure. (a) Bulk conductivity. (b) Total (bulk + grain boundary) conductivity.

approximately four days (until the conductivity values remained constant). Finally, a temperature (cooling) run has been performed from 700 to 300 °C in 1%-H_2/Ar. In the case of $Ce_{0.12}Y_{0.08}Sc_{0.6}Zr_{3.2}O_{7.66}$ (typical example for a ceria containing sample) both the bulk and grain boundary conductivities decreased significantly during reduction in 1%-H_2/Ar at 700 °C. On the contrary, no significant change of the bulk conductivities was observed for the sample with no ceria ($Y_{0.2}Sc_{0.6}Zr_{3.2}O_{7.60}$), see Fig. 1a. The grain boundary conductivities of $Y_{0.2}Sc_{0.6}Zr_{3.2}O_{7.60}$ were diminished somewhat upon reduction (Fig. 1a). The extent of this effect, however, is less pronounced than in the case of $Ce_{0.12}Y_{0.08}Sc_{0.6}Zr_{3.2}O_{7.66}$ (Fig. 1b). It is worth mentioning that the initial bulk and grain boundary conductivities were almost fully recovered by re-oxidation in air at 700 °C, indicating that the increase of resistivities in reducing atmospheres is reversible.

The variation of the bulk and grain boundary conductivities of $Ce_xY_{0.2-x}Sc_{0.6}Zr_{3.2}O_{8-\delta}$ $(0 \leq x \leq 0.2)$ with oxygen partial pressure at 700 °C is illustrated in Fig. 2. In contrast to $Y_{0.2}Sc_{0.6}Zr_{3.2}O_{7.60}$, all samples co-doped with ceria show a remarkable decrease of both bulk and grain boundary conductivities at $p(O_2) < 10^{-15}$ bar. An enhancement of the total conductivity under reducing conditions owing to a possible increase of the amount of electronic charge carriers was not found. It can be concluded that the diminished conductivities at low $p(O_2)$ values are consistent with a decrease of the mobility and/or concentration of free (mobile) oxygen vacancies (ionic charge carriers).

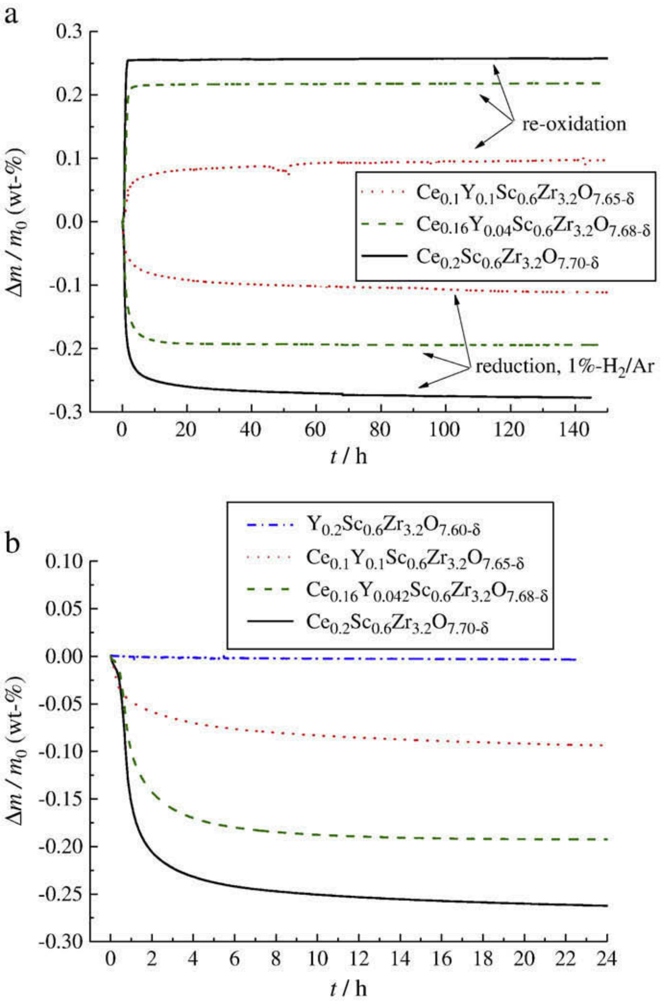

Fig. 3. (a) Relative mass change, $\Delta m/m_0$, of various samples of the system $Ce_xY_{0.2-x}Sc_{0.6}Zr_{3.2}O_{8-\delta}$ $(0 \leq x \leq 0.2)$ during reduction in 1%-H_2/Ar and subsequent re-oxidation in a O_2/Ar-gas mixture [$p(O_2) = 0.2$ bar] at 700 °C. (b) Comparison of relative mass loss, $\Delta m/m_0$, between $Y_{0.2}Sc_{0.6}Zr_{3.2}O_{7.60-\delta}$ (sample with no ceria) and various samples co-doped with ceria in reducing atmosphere (1%-H_2/Ar) at 700 °C.

Table 1
Oxygen nonstoichiometry δ and ratio $[Ce^{3+}]/([Ce^{3+}]+[Ce^{4+}])$ of $Ce_xY_{0.2-x}Sc_{0.6}Zr_{3.2}O_{7.6+x/2-\delta}$ $(0 \leq x \leq 0.2)$ at $p(O_2) \approx 10^{-24}$ bar (700 °C).

x	δ	$[Ce^{3+}]/([Ce^{3+}]+[Ce^{4+}])$
0	0.0009	–
0.10	0.033	0.66
0.16	0.057	0.71
0.20	0.081	0.81

The relative mass changes due to the release of oxygen during reduction in 1%-H_2/Ar and the reversible uptake of oxygen during re-oxidation [$p(O_2) = 0.2$ bar] at 700 °C are depicted for various samples of the system $Ce_xY_{0.2-x}Sc_{0.6}Zr_{3.2}O_{8-\delta}$ $(0 \leq x \leq 0.2)$ in Fig. 3a. The onset of mass loss occurred at approximately 500 °C for the heating period (8 °C/min) in 1%-H_2/Ar. No mass loss was detected for $Y_{0.2}Sc_{0.6}Zr_{3.2}O_{7.60}$ within the limits of experimental error, when equilibrated in 1%-H_2/Ar at 700 °C, see Fig. 3b. The oxygen nonstoichiometry at $p(O_2) \approx 10^{-24}$ bar (700 °C) is clearly correlated with the ceria content. The corresponding oxygen nonstoichiometries δ of $Ce_xY_{0.2-x}Sc_{0.6}Zr_{3.2}O_{7.6+x/2-\delta}$ as well as ratios between Ce^{3+} and the total amount of Ce, i.e. $[Ce^{3+}]/([Ce^{3+}]+[Ce^{4+}])$, are listed in Table 1.

The ionic conductivities of the bulk of $Ce_xY_{0.2-x}Sc_{0.6}Zr_{3.2}O_{8-\delta}$ $(0 \leq x \leq 0.2)$ are plotted versus ceria content at various temperatures in Fig. 4. The data are obtained from temperature runs in oxidizing and reducing atmospheres. While the ionic conductivity in air (oxidizing conditions) is almost independent of composition with typical values around 0.03–0.04 S cm^{-1} at 700 °C, the decrease of the bulk conductivities under reducing conditions is more evident at a higher ceria content. Although oxygen vacancies are created during reduction in 1%-H_2/Ar at 700 °C as confirmed by thermogravimetry, which corresponds to $2Ce_{Zr}^{\times} + O_O^{\times} \rightarrow 2Ce'_{Zr} + V_O^{\bullet\bullet} + 1/2O_2(g)$, the concentration of free (mobile) ionic charge carriers is rather decreased. This behaviour can be attributed to vacancy association, $Ce'_{Zr} + V_O^{\bullet\bullet} \rightarrow (Ce'_{Zr}V_O^{\bullet\bullet})^{\bullet}$ or the formation of more complex defect clusters, which seems to be more pronounced with increasing ceria content. It should be noted that according to atomistic modelling using a Born-like model [15], the binding energy for next-nearest neighbour associates increases considerably with increasing ion radius of the trivalent dopant cation in the sequence $Sc^{3+} < Y^{3+} < Ce^{3+}$ [16]. In a fluorite-type lattice the oxygen ions are coordinated tetrahedrally by the cations. Oxygen ion transport is accomplished by jumps of oxygen vacancies through the common edge of two adjacent tetrahedra. Recent density functional theory (DFT) calculations [17,18] indicate that the migration energy for

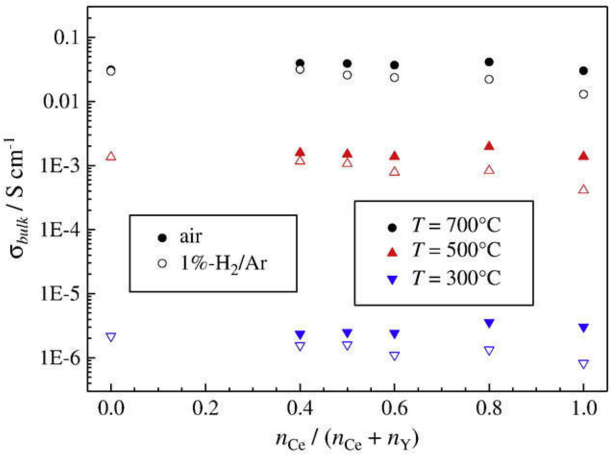

Fig. 4. Bulk conductivities in oxidizing (air) and reducing (1%-H_2/Ar) atmospheres plotted versus ceria content of $Ce_xY_{0.2-x}Sc_{0.6}Zr_{3.2}O_{8-\delta}$ $(0 \leq x \leq 0.2)$ at various temperatures.

oxygen ion transport is enhanced when dopant cations with a significantly higher ion radius than Zr^{4+} occupy a site at the common cation edge. If cerium is reduced from Ce^{4+} to Ce^{3+}, the ion radius is considerably increased [19]. Thus, it might be concluded that reduction of ceria in scandia-stabilized zirconia gives rise to an increase of both the association energy and the migration energy. This rise of the binding and migration energies should lead to lower conductivities and higher activation energies, when the samples are reduced.

The activation energy for ionic transport through the bulk decreases with increasing temperature above approximately 560 °C (see Fig. 1). A low temperature activation energy valid between 300 and 560 °C as well as a high temperature activation energy for the range $700<T/°C<560$ can be extracted from the pertinent Arrhenius-plots. In contrast to the bulk, the activation energy for ionic transport across the grain boundaries is almost independent of temperature with typical values around 1.3 eV. Fig. 5a shows a plot of the activation energies of the bulk as a function of ceria content for oxidizing as well reducing atmospheres. Fig. 5b reveals that the change of the high temperature activation energy due to reduction in 1%-H_2/Ar (700 °C) increases significantly with increasing ceria content. The change of the low temperature activation energies due to reduction seems to be unaffected by the ceria content. It is worthwhile mentioning that the mass change (increase of oxygen content) upon cooling in 1%-H_2/Ar, recorded by thermogravimetry at the same conditions as for impedance measurements, was typically less than 2% of the total mass loss during reduction at 700 °C. From the slope d ln δ/d T^{-1} one can extract an additional contribution of less than 0.01 eV to the observed activation energy, which is smaller than the uncertainties obtained from the Arrhenius-plots of Fig. 1 indicated by the error bars in Fig. 5b. Moreover, the variation of the oxygen nonstoichiometry with temperature observed by thermogravimetry is certainly an upper limit, since these measurements have been performed on powdered samples, while the electrical characterization has been carried out on disc-shaped specimens where the kinetics for oxygen incorporation can be expected to be more sluggish compared to the thermogravimetric experiments. Hence, the variation of the oxygen nonstoichiometry with temperature during the impedance measurements (temperature runs under reducing conditions) can be neglected, which corresponds to a constant (frozen-in) ratio $[Ce^{3+}]/([Ce^{3+}]+[Ce^{4+}])$.

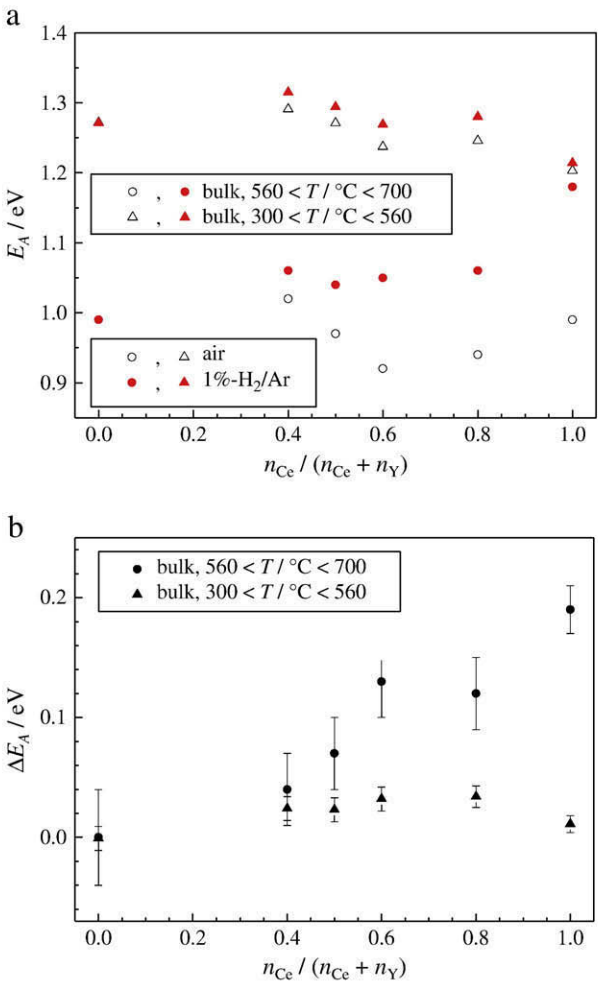

Fig. 5. (a) Activation energies for ionic transport in the bulk plotted versus ceria content of $Ce_xY_{0.2-x}Sc_{0.6}Zr_{3.2}O_{8-\delta}$ $(0\leq x\leq 0.2)$. Open and filled symbols refer to oxidizing (air) and reducing (1%-H_2/Ar) atmospheres, respectively. (b) Change of activation energy due to reduction $[\Delta E_A=E_A(\text{red.})-E_A(\text{ox.})]$ plotted versus ceria content of $Ce_xY_{0.2-x}Sc_{0.6}Zr_{3.2}O_{8-\delta}$ $(0\leq x\leq 0.2)$. Error bars correspond to 2σ.

In accordance with Ref. [9] the high temperature activation energy is composed of the migration and association energy, especially when the highest value of the temperature range is restricted to 700 °C. Therefore, the increase of the high temperature activation energy after equilibration in reducing atmospheres can be interpreted in terms of enhanced values for both migration and association energy as predicted by atomistic modelling. The low temperature activation energy may contain an additional contribution originating from vacancy ordering at low temperatures [9,20]. It should be mentioned that the tendency for ordering is diminished, when the size of the dopants is increased, e.g., because of reduction of Ce^{4+} to Ce^{3+}.

4. Conclusions

The bulk and grain boundary conductivities of disc-shaped samples of scandia-stabilized zirconia co-doped with yttria and ceria have been investigated by application of impedance spectroscopy as a function of temperature and oxygen partial pressure. The yttria and ceria contents of $Ce_xY_{0.2-x}Sc_{0.6}Zr_{3.2}O_{8-\delta}$ $(0\leq x\leq 0.2)$ have been varied systematically. The oxygen partial pressure dependence of the electrical conductivity has been studied in the range from 1 to 10^{-24} bar at 700 °C. The formation of oxygen vacancies due to reduction of Ce^{4+} to Ce^{3+} has been confirmed by thermogravimetry. Whereas the ionic conductivity of $Y_{0.2}Sc_{0.6}Zr_{3.2}O_{8-\delta}$ is almost independent of $p(O_2)$, both the bulk and grain boundary conductivities decrease remarkably at $p(O_2)<10^{-15}$ bar (700 °C) in the case of samples co-doped with ceria. No enhancement of the total conductivity owing to the creation of electronic charge carriers under reducing conditions has been detected. Temperature runs between 300 and 700 °C in oxidizing (air) and reducing (1%-H_2/Ar) atmospheres have been performed. Activation energies for the bulk and grain boundaries have been extracted from Arrhenius-plots. The decrease of the ionic conductivity for bulk regions of ceria containing samples is accompanied by an increase of the high temperature activation energy due to reduction in 1%-H_2/Ar (700 °C), which is interpreted in terms of defect association or clustering.

Acknowledgements

Financial support from the EC within the integrated project SOFC600 (contract no. 020089) and from EPSRC (UK) is gratefully acknowledged.

References

[1] N.Q. Minh, J. Am. Ceram. Soc. 76 (1993) 563.
[2] J.-H. Park, R.N. Blumenthal, J. Electrochem. Soc. 136 (1989) 2867.
[3] B.C.H. Steele, Solid State Ionics 129 (2000) 95.
[4] C.M. Kleinlogel, L.J. Gauckler, J. Electroceram. 5 (2000) 231.
[5] S.P.S. Badwal, F.T. Ciacchi, D. Milosevic, Solid State Ionics 136–137 (2000) 91.
[6] Y. Arachi, T. Asai, O. Yamamoto, Y. Takeda, N. Imanishi, K. Kawate, C. Tamakoshi, J. Electrochem. Soc. 148 (2001) A520.
[7] I. Kosacki, H.U. Anderson, Y. Mizutani, K. Ukai, Solid State Ionics 152–153 (2002) 431.

[8] T.I. Politova, J.T.S. Irvine, Solid State Ionics 168 (2004) 153.

[9] J.T.S. Irvine, J.W.L. Dobson, T. Politova, S.G. Martin, A. Shenouda, Faraday Discuss. 134 (2007) 41.

[10] Y. Arachi, H. Sakai, O. Yamamoto, Y. Takeda, N. Imanishai, Solid State Ionics 121 (1999) 133.

[11] J.A. Kilner, C.D. Waters, Solid State Ionics 6 (1982) 253.

[12] J.A. Kilner, Solid State Ionics 129 (2000) 13.

[13] E. de Carvalho, W. Preis, W. Sitte, J.T.S. Irvine, “Investigation of conductivity of $(Ce_xY_{0.2-x}Sc_{0.6})Zr_{3.2}O_{8-\delta}$ system and its dependence upon oxygen partial pressure”, Solid State Ionics (in press).

[14] A. Bürgermeister, A. Benisek, W. Sitte, Solid State Ionics 170 (2004) 99.

[15] A. Dwivedi, A.N. Cormack, Phil. Mag. A 61 (1990) 1.

[16] M.O. Zacate, L. Minervini, D.J. Bradfield, R.W. Grimes, K.E. Sickafus, Solid State Ionics 128 (2000) 243.

[17] R. Krishnamurthy, Y.-G. Yoon, D.J. Srolovitz, R. Car, J. Am. Ceram. Soc. 87 (2004) 1821.

[18] R. Pornprasertsuk, P. Ramanarayanan, C.B. Musgrave, F.B. Prinz, J. Appl. Phys. 98 (2005) 103513.

[19] R.D. Shannon, C.T. Prewitt, Acta Cryst. B 25 (1969) 925.

[20] I.R. Gibson, J.T.S. Irvine, J. Mater. Chem. 6 (1996) 895.

Solid State Ionics 225 (2012) 55–60

Contents lists available at SciVerse ScienceDirect

Solid State Ionics

journal homepage: www.elsevier.com/locate/ssi

Comparison of oxygen exchange kinetics of the IT-SOFC cathode materials $La_{0.5}Sr_{0.5}CoO_{3-\delta}$ and $La_{0.6}Sr_{0.4}CoO_{3-\delta}$

Andreas Egger, Edith Bucher, Min Yang, Werner Sitte *

Chair of Physical Chemistry, Montanuniversität Leoben, Franz-Josef-Strasse 18, 8700 Leoben, Austria

ARTICLE INFO

Article history:
Received 9 September 2011
Received in revised form 8 December 2011
Accepted 28 February 2012
Available online 23 March 2012

Keywords:
LSC
Cathode
SOFC
Electrical conductivity
Oxygen exchange kinetics

ABSTRACT

$La_{0.5}Sr_{0.5}CoO_{3-\delta}$ and $La_{0.6}Sr_{0.4}CoO_{3-\delta}$ are characterized with respect to application as cathode materials in intermediate temperature solid oxide fuel cells (IT-SOFCs). Surface exchange and transport parameters of oxygen are determined by the conductivity relaxation technique between 525 °C and 725 °C at oxygen partial pressures of 0.1, 0.01 and 0.001 bar. Electrical conductivities of both compounds range between 1000 and 2400 S cm^{-1} and are slightly higher for $La_{0.6}Sr_{0.4}CoO_{3-\delta}$. However, $La_{0.5}Sr_{0.5}CoO_{3-\delta}$ shows superior performance with regard to oxygen diffusion, ionic conductivity and oxygen surface exchange within the investigated range of temperatures and oxygen partial pressures. At 725 °C the chemical surface exchange coefficient of oxygen is 2×10^{-3} cm s^{-1} for $La_{0.5}Sr_{0.5}CoO_{3-\delta}$ and 4×10^{-4} cm s^{-1} for $La_{0.6}Sr_{0.4}CoO_{3-\delta}$. At lower oxygen partial pressures a strong decrease in the surface exchange coefficient is observed and diffusion data cannot be obtained from relaxation measurements. Oxygen vacancy diffusion coefficients are similar for both compounds and range between 10^{-6} and 10^{-8} cm^2 s^{-1} with activation energies around 100 $kJmol^{-1}$. At 725 °C and 0.1 bar oxygen partial pressure, the ionic conductivity of $La_{0.5}Sr_{0.5}CoO_{3-\delta}$ is 1×10^{-2} S cm^{-1} with an activation energy of 118 $kJmol^{-1}$. The results show that both compositions meet the requirements for the application as IT-SOFC cathodes in the short-term range.

1. Introduction

Strontium doped lanthanum cobalt oxides (LSCs) are promising materials for several technical applications such as cathodes for solid oxide fuel cells (SOFCs), high-temperature permeation membranes for oxygen separation or partial oxidation of hydrocarbons, and oxygen gas sensors. LSCs are perovskite-type mixed ionic electronic conductors (MIEC) with high electronic conductivity and relatively high oxygen ionic conductivities close to or even exceeding those of solid electrolytes such as yttria stabilized zirconia (YSZ). LSC received much attention as a promising material for SOFC cathodes due to the current trend in SOFC-research to reduce operating temperatures from the high-temperature region above 800 °C to intermediate temperatures (IT) of 500-750 °C. At such reduced temperatures the standard cathode material $(La,Sr)MnO_3$ cannot be used as it is too inactive for the oxygen reduction reaction due to its low oxygen diffusivity. However, employing MIEC materials reduces the cathodic polarization resistance by extending the active zone of the reaction from the immediate three phase boundary to part of the cathode–gas interface [1,2]. LSCs feature high catalytic activity for oxygen reduction and fast oxygen diffusion at reduced temperatures. The drawbacks of LSCs include high thermal expansion coefficients with respect to common SOFC-electrolyte materials [3,4] and chemical reactivity with YSZ [5], which makes it necessary to apply additional barrier layers or to use alternative solid electrolytes in the cell. The properties of LSCs can be tailored over wide ranges through variation of the Sr-content and partial substitution of Co by other 3d-transition metals, thereby changing their electrical, thermodynamic, thermomechanical and oxygen transport properties. $La_{1-x}Sr_xCoO_{3-\delta}$ compounds with compositions of x = 0.2–0.5 show the highest electronic conductivities in the LSC series [6,7]. In the present work two promising compositions of $La_{1-x}Sr_xCoO_{3-\delta}$, where x = 0.4 (LSC64) and x = 0.5 (LSC55), are compared in terms of parameters important to SOFC-cathode materials. Experimental studies are carried out at temperatures and oxygen partial pressures of relevance for IT-SOFCs.

2. Experimental

2.1. Sample preparation

LSC55 was synthesized by a modified Pechini process starting from aqueous solutions of $La(NO_3)_3$, $Sr(NO_3)_2$ and $Co(NO_3)_2$. After mixing the solutions in the appropriate ratio, ethylene glycol and citric acid were added adjusting the citric acid to total cation molar ratio to 10:1. The solution was stirred at 140 °C until a gel was formed. After aging the gel for 2 days at 180 °C and calcination at 400 °C and 700 °C with intermediate grinding steps the powder was

---

* Corresponding author. Tel.: +43 3842 402 4800; fax: +43 3842 402 4802.
E-mail address: sitte@unileoben.ac.at (W. Sitte).

0167-2738/$ – see front matter © 2012 Elsevier B.V. All rights reserved.
doi:10.1016/j.ssi.2012.02.050

isostatically pressed and sintered at 900 °C for 6 h, yielding a sample with 94% relative density. Resintering for 2 h at 1100 °C was performed to increase the grain size to 0.5–1 μm. A pellet of LSC64 with a relative density above 95% was obtained from commercial powder (Praxair) after pressing and sintering at 1200 °C for 4 h in air. Samples with relative densities around 95% or higher can be assumed to show no open porosity [8] and are expected to yield reliable results in diffusion measurements [9].

Thin slabs were cut from the pellets with a diamond wire saw and polished on polymer embedded diamond lapping films with increasing fineness up to 1 μm diamond particle size for the final polishing step. The dimensions of the specimens were ca. $5 \times 5\ \mathrm{mm}^2$ with a thickness of 0.229 mm and 0.204 mm for LSC55 and LSC64, respectively. Both samples were contacted with gold wires and gold paste (Metalor) for measurements in the four-point van der Pauw geometry.

2.2. Chemical and structural analysis

The chemical composition of each sample was examined by X-ray fluorescence spectroscopy (XRF; PANalytical, model Axios) and scanning electron microscopy (Stereoscan 250 MK3, Cambridge) with energy dispersive X-ray spectroscopy (SEM-EDX; Oxford Instruments, model 6272). X-ray diffraction (XRD) patterns were recorded with a Bruker AXS (model D8 Advance) using Cu-Kα radiation in the range $10° \leq 2\theta \leq 100°$ with a step size of 0.020° and acquisition time of 2–3 s per step.

2.3. Electrical conductivity (EC) and conductivity relaxation (CR) measurements

The samples were placed in a quartz reactor inside a tube furnace. Oxygen partial pressures (pO_2) were adjusted by flushing the reactor with appropriate mixtures of O_2 in argon by means of mass flow controllers at a total gas flow of 2 L/h. Temperature and pO_2 were monitored with a potentiometric oxygen sensor with an integrated S-thermocouple (MicroPoas, Setnag) placed close to the sample. The electrical conductivity was measured by the van der Pauw method [10,11] using a Keithley 2400 combined current source and voltmeter. Chemical diffusion coefficients and chemical surface exchange coefficients of oxygen were determined by the conductivity relaxation method [12–14]. Current was applied with a Keithley 2400 and the voltage was measured with a sensitive digital voltmeter Keithley 182. A manual four-way valve was used for switching between different gas mixtures corresponding to pO_2-steps of 0.1/0.15, 0.01/0.015 and 0.001/0.0015 bar/bar. Kinetic parameters for oxygen exchange were obtained by fitting the appropriate solutions of the diffusion equation to the conductivity transients by least squares nonlinear regression analysis [13].

3. Results and discussion

3.1. Phase purity

The compositions of both compounds were checked by XRF and SEM-EDX analyses and cation ratios close to the nominal values were found. Perovskite phases were confirmed by room temperature XRD measurements and no secondary phases were detected in either case. For LSC64 a rhombohedral distortion of the perovskite structure was verified.

3.2. Electrical conductivity

Electrical conductivities of LSC55 and LSC64 are compared in Fig. 1. Results are in good agreement with data from Søgaard et al. [15] and Petrov et al. [16] for LSC64 and LSC55, respectively. As is well known from the literature, Sr-doped lanthanum cobaltites exhibit high electrical conductivity, which is essentially *p*-type electronic. Trends with respect to changes in temperature, oxygen partial pressure and Sr-content are evident in Fig. 1. An increase in conductivity is found for decreasing temperatures, increasing pO_2 and decreasing Sr-content.

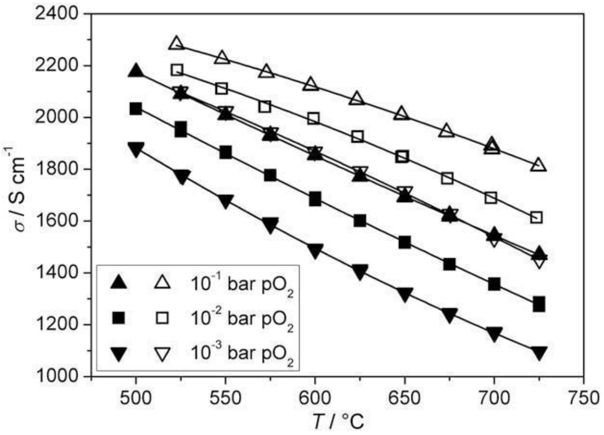

Fig. 1. Electronic conductivity of $La_{0.5}Sr_{0.5}CoO_{3-\delta}$ (solid symbols) and $La_{0.6}Sr_{0.4}CoO_{3-\delta}$ (open symbols) as a function of temperature at different oxygen partial pressures. Lines are drawn for visual clarity.

Numerous studies concerning the electronic conductivity and its dependence on temperature, pO_2 and Sr-content have been reported for LSC. An interpretation of these relationships is complicated by the fact that there are (at least) two contributions to the conductivity of LSC: (i) the specifics of the crystal structure, i.e. interatomic distances and angles and (ii) the charge carrier concentration, which is – in the *p*-type regime – the concentration of electron holes. Care must be taken to draw meaningful conclusions from experiments in which both contributions are changed at the same time.

3.2.1. pO_2-dependence of the electronic conductivity

The observed decrease in conductivity for lower pO_2 is clearly a consequence of the decrease in hole concentration due to the removal of oxygen from the structure, according to the defect equation (Kröger–Vink notation)

$$O_O^x + 2h^{\bullet} \rightleftarrows V_O^{\bullet\bullet} + 1/2O_2 \qquad (1)$$

Such correlation between pO_2 and conductivity has been consistently reported for Sr-doped lanthanum cobaltites. It is convenient that in this case detailed knowledge about the electronic structure of the *p*-type conductor (e.g. itinerant versus localized electronic defects [17,18]) is not necessary. However, changes in oxygen stoichiometry inevitably also have an effect on the crystal structure, so that varying pO_2 alone can, in principle, lead to changes in the electronic structure of the compound [19].

3.2.2. Temperature dependence of the electronic conductivity

A discussion of the temperature dependence of the conductivity is less straightforward, as both crystal structure and hole concentration are simultaneously affected by changes in temperature. LSC crystallizes in two main modifications, rhombohedral (*R*- 3c) and cubic (*P*m –3m). The rhombohedral structure is the low-temperature phase, which transforms to the cubic modification at higher temperatures. The temperature of the rhombohedral–cubic phase transition depends on the Sr-content and decreases with increasing Sr-substitution, so that for $x \geq 0.55$, $La_{1-x}Sr_xCoO_{3-\delta}$ is cubic even at room temperature [6,20–22]. Transition temperatures reported in the literature vary, Petrov et al. state 291 °C and 93 °C for LSC64 and LSC55 [6], respectively, Søgaard et al. estimate 475 °C for $(La_{0.6}Sr_{0.4})_{0.99}CoO_{3-\delta}$ [15]. The discussion above gives only a broad picture based on results from conventional XRD technique. Several in-depth investigations of Sr-rich LSC by X-ray, neutron and electron diffraction measurements suggest that the structural details are more intricate and include the formation of microdomains with superstructures due to ordering of oxygen vacancies [20,23–26].

Several authors have reported that the electronic structure of LSC is very sensitive to slight changes in the crystal structure. Mizusaki et al. reported a transition from semiconducting to metallic conduction when the rhombohedral lattice angle falls below 60.3–60.4° [22]. Mineshige et al. proposed the Co–O–Co angle as the relevant structural parameter and found the transition from semiconducting to metallic when the Co–O–Co angles increases above ~165° [19].

For conductivity measurements in the cubic phase region the rhombohedral angle and the Co-O-Co angle are fixed at 60° and 180°, respectively, and the electronic conduction mechanism is therefore expected to be metallic. Indeed, decreasing conductivity with increasing temperature at constant oxygen vacancy concentration has been reported for LSC [15,27]. However, there is another effect of increasing temperature on the electronic conductivity, which is a decrease in the hole concentration due to a temperature-induced oxygen release as a consequence of the endothermic nature of reaction (1). Assuming that all measurements in this study were conducted in the cubic phase region of LSC64 and LSC55, the observed decrease in conductivity upon heating is a combined effect of the metallic conduction mechanism and the decrease in hole concentration due to oxygen release.

3.2.3. Influence of Sr-content on the electronic conductivity

The lower conductivity of LSC55 compared to LSC64 appears to be inconsistent with the trend expected for higher acceptor levels in a *p*-type conductor. Since conductivity measurements in this study were performed at temperatures where LSC55 and LSC64 are expected to adopt the cubic symmetry, it seems unlikely that subtle modification in the crystal structure and corresponding changes in the electron band structure are responsible for the observed decrease in electronic conductivity for increased acceptor content. Instead, the current discussion is based on changes in hole concentration. For lanthanum cobaltites, changes in Sr-content can be charge-compensated by both electronic and ionic mechanisms, i.e. by changes in the concentrations of electron holes and oxygen vacancies, respectively. Mizusaki et al. showed by thermogravimetric analysis that electronic and ionic contributions to charge compensation in $La_{1-x}Sr_xCoO_{3-\delta}$ at 800 °C strongly depend on Sr-content and oxygen partial pressure [28]. At lower Sr-content ($x \leq 0.2$) electroneutrality is maintained predominantly by electronic compensation and indeed electronic conductivity rises with Sr-content [22]. However, in the intermediate doping regime $0.2 \leq x \leq 0.5$ ionic charge compensation becomes increasingly important and can, at elevated temperatures, even overcompensate the charge induced by acceptor doping, thus leading to a net decrease in hole concentration upon increase in acceptor content [6,28]. This effect of ionic overcompensation at high temperatures is more pronounced at lower pO_2, consistent with the current data where the difference in conductivity between LSC55 and LSC64 increases slightly with decreasing pO_2.

3.3. Oxygen exchange kinetics

Chemical surface exchange coefficients k_{chem} and chemical diffusion coefficients D_{chem} of oxygen for LSC55 and LSC64 are plotted in Figs. 2 and 3 for different temperatures and oxygen partial pressures. Relaxation measurements were performed by abrupt changes of the oxygen partial pressure within a factor of 1.5. A good agreement between results for oxidation steps (low to high pO_2) and reduction steps (high to low pO_2) was observed. For both compounds the surface exchange process was rate-limiting at 0.01 bar and 0.001 bar pO_2 and thus diffusion coefficients could not be derived. Values of k_{chem} and D_{chem} for LSC55 were consistently larger than those of LSC64 in the whole temperature and pO_2-range under investigation. Activation energies obtained by linear regression in Arrhenius plots are listed in Table 1. As can be seen in Fig. 2, k_{chem} decreased at lower oxygen partial pressures for both compounds. Assuming a $k_{chem} \sim pO_2^n$ relationship, linear regression of data points in a log-log plot of k_{chem} vs. pO_2 yields values of n between 0.5 and 1.

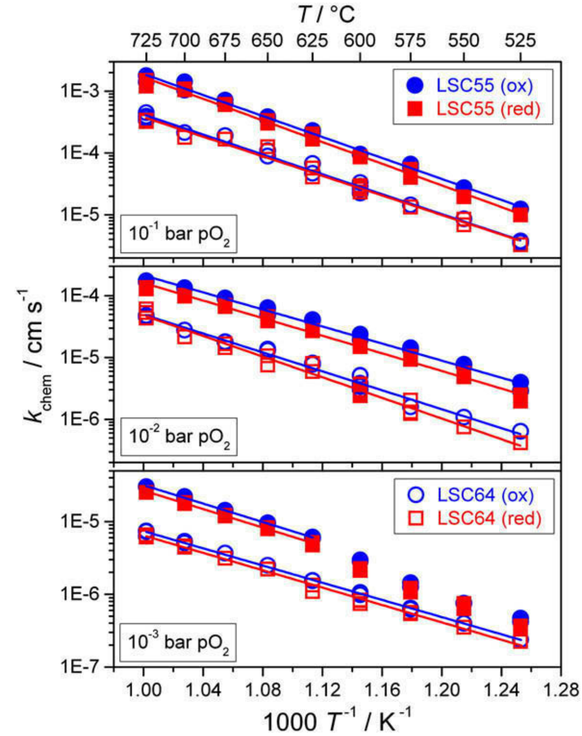

Fig. 2. Arrhenius plots of the chemical surface exchange coefficient of oxygen for $La_{0.5}Sr_{0.5}CoO_{3-\delta}$ (solid symbols) and $La_{0.6}Sr_{0.4}CoO_{3-\delta}$ (open symbols) at different oxygen partial pressures. Circle and square symbols denote results obtained from pO_2-steps in oxidizing (low to high pO_2) and reducing (high to low pO_2) directions, respectively. Activation energies were obtained from linear regression shown as solid lines (see Table 1).

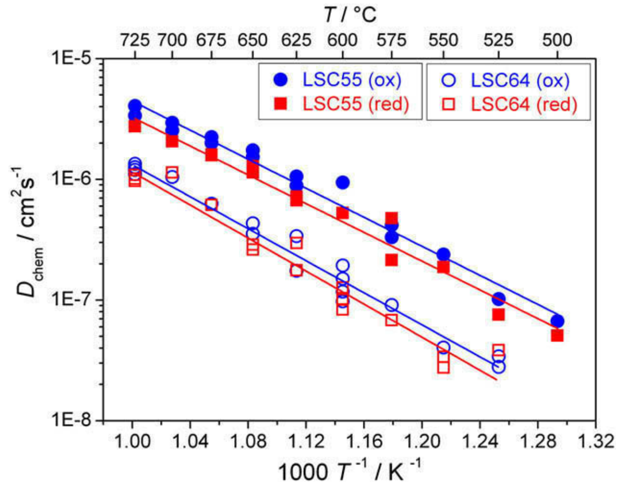

Fig. 3. Arrhenius plot of the chemical diffusion coefficient of oxygen for $La_{0.5}Sr_{0.5}CoO_{3-\delta}$ (solid symbols) and $La_{0.6}Sr_{0.4}CoO_{3-\delta}$ (open symbols) at 0.1 bar oxygen partial pressure. Circle and square symbols denote results obtained from pO_2-steps of 0.1 → 0.15 bar and 0.15 → 0.1 bar, respectively. Activation energies were obtained from linear regression shown as solid lines (see Table 1).

Table 1
Activation energies E_a of surface exchange and transport parameters of oxygen for $La_{0.5}Sr_{0.5}CoO_{3-\delta}$ and $La_{0.6}Sr_{0.4}CoO_{3-\delta}$ in the temperature range $525 \leq T/°C \leq 725$.

	LSC55			LSC64		
	0.1 bar	0.01 bar	0.001 bar	0.1 bar	0.01 bar	0.001 bar
E_a (k_{chem})/kJ mol^{-1}	165	134	122	153	155	114
E_a (D_{chem})/kJ mol^{-1}	112			129		
E_a (k_o)/kJ mol^{-1}	172	140	154	178	180	139
E_a (D_o)/kJ mol^{-1}	119			154		
E_a (D_v)/kJ mol^{-1}	101			123		
E_a (σ_{ion})/kJ mol^{-1}	118			154		

Slower oxygen surface exchange kinetics at lower oxygen partial pressures have been reported frequently for Sr-doped lanthanum cobaltites [15,29,30]. Wang et al. found the same trend for LSC55 when plotting k_{chem} against the final oxygen partial pressure of the pO_2-step [31]. This is in general a consequence of the rate laws for the elementary reactions governing the surface exchange where oxygen from the gas-phase is involved in the rate determining step or in quasi-equilibrium reactions preceding or succeeding the rate determining step [30,31]. Moreover, vacancy ordering effects at low pO_2 due to increasing interactions at higher vacancy concentrations have been proposed in the literature [29,32]. Of course, this should mainly affect D_{chem} but may also have an impact on k_{chem} if the ordering process extends to the surface, since mobile oxygen vacancies seem to play a crucial role in the surface exchange process as evidenced by the correlation between k^* and D^* from tracer experiments for various perovskite compounds [33–36].

As a consequence of the strong decrease of k_{chem} upon pO_2-reduction the relaxation process is limited by the surface exchange process for $pO_2 \leq 0.01$ bar. Although no data for D_{chem} at lower oxygen partial pressures are available in this study, it follows from the change in the rate-limiting step that a reduction in D_{chem} with decreasing pO_2, if any, is less pronounced than for k_{chem}. Activation energies of k_{chem} were found to decrease with decreasing pO_2 for both compounds except for LSC64 between 0.1 bar and 0.01 bar pO_2 (Table 1). A clear trend with respect to Sr-content cannot be observed for the activation energies of k_{chem}.

Chemical diffusion coefficients and chemical surface exchange coefficients of oxygen were converted to self diffusion coefficients D_o and surface exchange coefficients k_o using the relations $D_{chem} = \gamma_O D_O$ and $k_{chem} \approx \gamma_O k_O$ [37–39], with the thermodynamic factor of oxygen γ_o defined by

$$\gamma_O = \frac{1}{2}\left(\frac{\partial \ln pO_2}{\partial \ln c_O}\right)_T = \frac{1}{2}\left(\frac{\partial \ln pO_2}{\partial \ln(3-\delta)}\right)_T \tag{2}$$

where c_o is the concentration of oxygen ions. Oxygen non-stoichiometry data δ as a function of temperature from Mizusaki et al. [28] and Sitte et al. [40] has been used for calculating γ_o of LSC55 and LSC64, respectively. Thermodynamic factors were assumed to be independent of oxygen partial pressure between 0.1 and 0.001 bar pO_2 [29,31]. Thermodynamic factors of both compounds range between 100 and 200 and the overall trends for D_o and k_o with temperature and pO_2 are similar to those of D_{chem} and k_{chem} (Figs. 4 and 5). The oxygen vacancy diffusion coefficient D_v can be calculated from the self diffusion coefficient and the concentrations of oxygen ions c_o and oxygen vacancies c_v according to

$$D_V = \frac{c_O}{c_V} D_O = \frac{3-\delta}{\delta} D_O \tag{3}$$

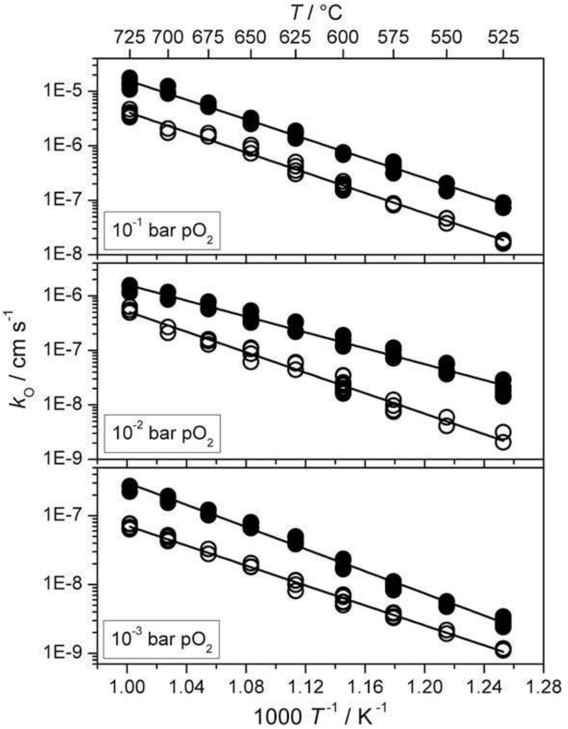

Fig. 4. Arrhenius plots of the surface exchange coefficient of oxygen for $La_{0.5}Sr_{0.5}CoO_{3-\delta}$ (solid circles) and $La_{0.6}Sr_{0.4}CoO_{3-\delta}$ (open circles) at 0.1, 0.01 and 0.001 bar oxygen partial pressure. Activation energies were obtained from linear regression shown as solid lines (see Table 1).

or, equivalently, through $D_{chem} = \gamma_V D_V$, where γ_v is defined similarly to Eq. (2)

$$\gamma_V = -\frac{1}{2}\left(\frac{\partial \ln pO_2}{\partial \ln c_V}\right)_T = -\frac{1}{2}\left(\frac{\partial \ln pO_2}{\partial \ln \delta}\right)_T \tag{4}$$

Results for D_v are plotted in Fig. 6 and are quite similar for both compositions, with activation energies of 101 kJ/mol and 123 kJ/mol for LSC55 and LSC64, respectively. Several authors have observed that there is little variation in vacancy diffusivities among lanthanum cobaltites with differing Sr-contents and even between different perovskite oxides [33,41–44].

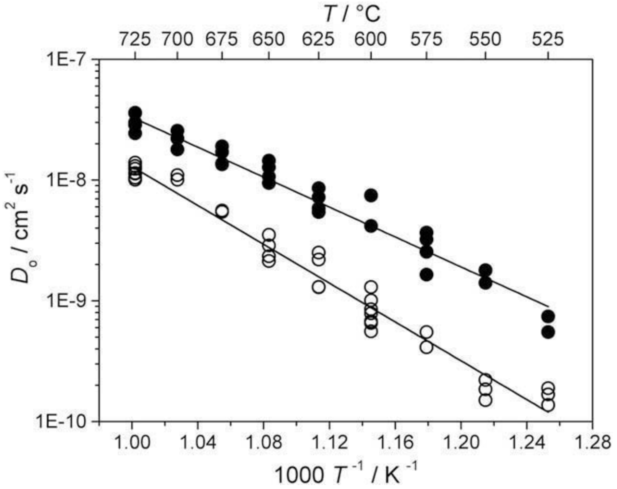

Fig. 5. Arrhenius plot of the self diffusion coefficient of oxygen for $La_{0.5}Sr_{0.5}CoO_{3-\delta}$ (solid circles) and $La_{0.6}Sr_{0.4}CoO_{3-\delta}$ (open circles) at 0.1 bar oxygen partial pressure. Activation energies were obtained from linear regression shown as solid lines (see Table 1).

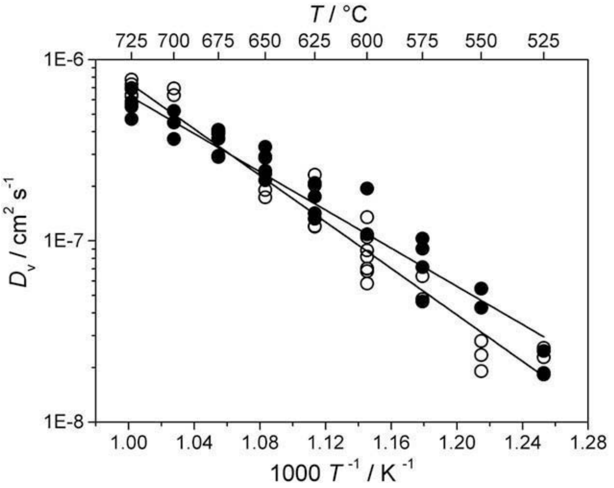

Fig. 6. Arrhenius plot of the oxygen vacancy diffusion coefficient for $La_{0.5}Sr_{0.5}CoO_{3-\delta}$ (solid circles) and $La_{0.6}Sr_{0.4}CoO_{3-\delta}$ (open circles) at 0.1 bar oxygen partial pressure. Activation energies were obtained from linear regression shown as solid lines (see Table 1).

For a further comparison of both compounds with respect to oxygen transport properties the ionic conductivity σ_{ion} has been calculated from D_o according to the Nernst-Einstein equation (neglecting contributions from the correlation factor and Haven-ratio)

$$\sigma_{ion} = \frac{4F^2 c_O D_O}{RT} = \frac{4F^2 c_V D_V}{RT} \tag{5}$$

and the surface exchange resistance r_p has been obtained from the surface exchange coefficient k_o by [45]

$$r_p = \frac{RT}{4F^2 c_O k_O} \tag{6}$$

The ionic conductivity of LSC55 at 0.1 bar pO_2 exceeds that of LSC64 by a factor of 2 to 5 (Fig. 7) and surface exchange resistances of LSC55 are lower than those of LSC64 (Fig. 8) for all temperatures and oxygen partial pressures investigated. This is consistent with the higher oxygen vacancy concentration in LSC55 resulting from the higher Sr-content (Fig. 9), since oxygen transport in LSC takes place by a vacancy mechanism [43,46] and oxygen vacancies also appear to be involved in the oxygen incorporation reaction at the surface [33–36]. Comparing ionic conductivities with the total conductivity in Fig. 1 shows the total electrical conductivity in LSC to be predominantly electronic. Activation energies of the ionic conductivity were determined by linear regression in an Arrhenius plot of $\sigma_{\text{ion}}T$ (Fig. 10) and are given in Table 1.

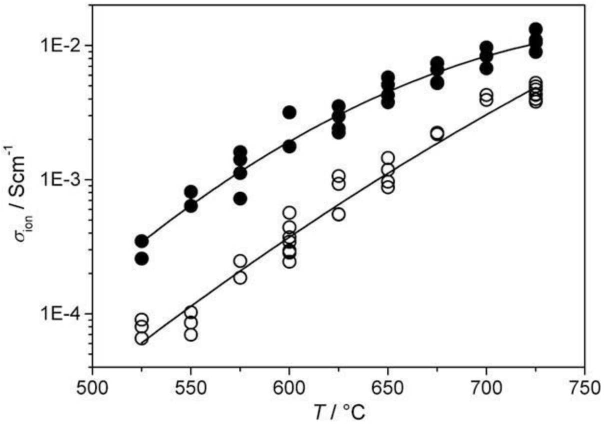

Fig. 7. Ionic conductivity for $La_{0.5}Sr_{0.5}CoO_{3-\delta}$ (solid circles) and $La_{0.6}Sr_{0.4}CoO_{3-\delta}$ (open circles) at 0.1 bar oxygen partial pressure. Lines are guides for the eye.

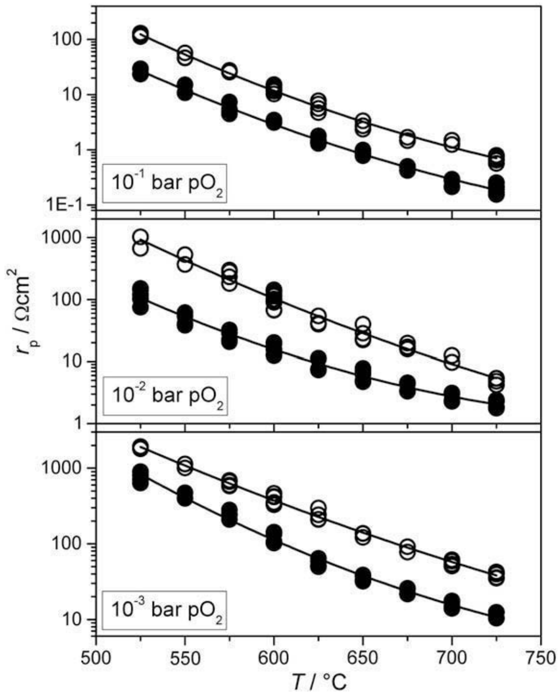

Fig. 8. Surface exchange resistance as a function of temperature for $La_{0.5}Sr_{0.5}CoO_{3-\delta}$ (solid circles) and $La_{0.6}Sr_{0.4}CoO_{3-\delta}$ (open circles) at oxygen partial pressures of 0.1 bar, 0.01 bar and 0.001 bar. Lines are drawn for visual clarity.

4. Conclusions

LSC64 and LSC55 were investigated with respect to electrical conductivity and oxygen transport and exchange parameters between 525 and 725 °C at 0.1, 0.01 and 0.001 bar pO_2. Both compounds exhibit high electrical conductivity ($>1000\ \text{S cm}^{-1}$) which is predominantly electronic. LSC55 has a lower electronic conductivity than LSC64 despite its higher content of acceptor-dopant (Sr), which has

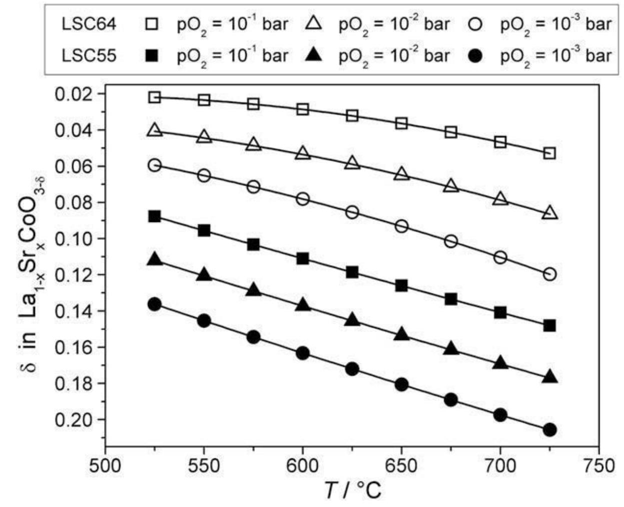

Fig. 9. Oxygen deficiency as a function of temperature for $La_{0.5}Sr_{0.5}CoO_{3-\delta}$ (solid symbols) and $La_{0.6}Sr_{0.4}CoO_{3-\delta}$ (open symbols) at oxygen partial pressures of 0.1 bar, 0.01 bar and 0.001 bar [28,40]. Lines are guides for the eye.

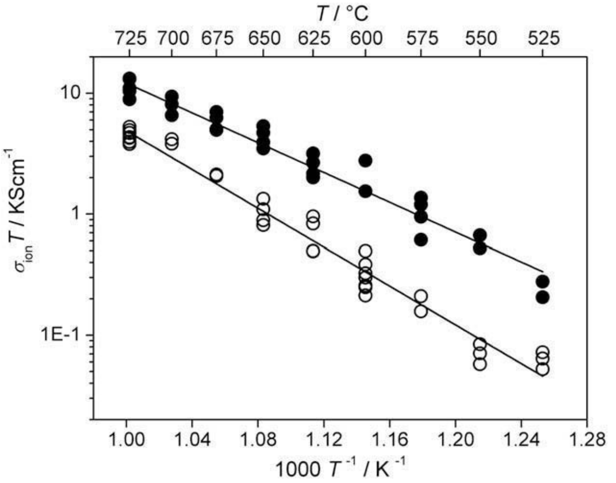

Fig. 10. Arrhenius plot of the ionic conductivity for $La_{0.5}Sr_{0.5}CoO_{3-\delta}$ (solid circles) and $La_{0.6}Sr_{0.4}CoO_{3-\delta}$ (open circles) at 0.1 bar oxygen partial pressure. Activation energies were determined by linear regression analysis shown as solid lines (see Table 1).

been ascribed to a higher degree of ionic charge compensation in LSC55. However, with respect to surface exchange (k_{chem}, k_{o}, r_{p}) and oxygen transport (D_{chem}, D_{o}, D_{v}, σ_{ion}) LSC55 was found to be superior to LSC64, which results from the higher concentration of oxygen vacancies with increasing Sr- levels. It is well known that the lanthanum cobaltite structure supports a wide range of solid solutions with SrO, from Sr-free $LaCoO_3$ to Sr-contents as high as x = 0.7–0.9, depending on the synthesis route [20,23]. Raising the Sr-doping level above x = 0.5 in $La_{1-x}Sr_xCoO_{3-\delta}$ is expected to enhance surface exchange and oxygen transport [1,3,29], however, at the expense of the electronic conductivity and thermodynamic stability as well as causing further increase in the thermal expansion coefficient [4,6,7]. It is interesting to note that there appears to be a maximum in ionic conductivity of $La_{1-x}Sr_xCoO_{3-\delta}$ around $x \approx 0.7$ [16,47]. This may be caused by the limited phase stability of highly Sr-substituted lanthanum cobaltites or by increasing interactions between point defects (e.g. $V_O^{\bullet\bullet}$ with Sr'_{La} or Co'_{Co}), which reduce the number of mobile oxygen vacancies necessary for mass transport in LSC. Several vacancy trapping effects have been reported in the literature, ranging from charged or neutral local associates like $[Co'_{Co}-V_O^{\bullet\bullet}]^{\bullet}$ and $[Sr'_{La}-V_O^{\bullet\bullet}-Sr'_{La}]^{x}$ to the formation of larger defect clusters and vacancy-ordered microdomains to the appearance of distinct crystal structures as in $SrCoO_{3-\delta}$ [6,20,23,48–51].

Finally, it should be mentioned that the results presented in this study refer to short-term investigations in pure and dry $Ar–O_2$ atmospheres. With respect e.g. to long-term stability in humid atmospheres a current investigation (for periods of more than 1000 h) showed that LSC64 undergoes a significant degradation due to Sr-enrichment and surface reconstruction as well as Si-poisoning at 600 °C [52].

Acknowledgements

Financial support from the EC within the integrated project SOFC600 (contract no. 020089) is gratefully acknowledged. The authors thank Frans van Berkel from ECN (the Netherlands) for providing one of the samples within the project SOFC600 as well as Thomas Meisel from the University of Leoben (Austria) for assistance with XRF-measurements.

References

[1] Y. Takeda, R. Kanno, M. Noda, Y. Tomida, O. Yamamoto, J. Electrochem. Soc. 134 (1987) 2656.
[2] S.B. Adler, Chem. Rev. 104 (2004) 4791.
[3] H. Ullmann, N. Trofimenko, F. Tietz, D. Stöver, A. Ahmad-Khanlou, Solid State Ionics 138 (2000) 79.
[4] E.V. Tsipis, V.V. Kharton, J. Solid State Electrochem. 12 (2008) 1039.
[5] M. Backhaus-Ricoult, Solid State Sci. 10 (2008) 670.
[6] A.N. Petrov, O.F. Kononchuk, A.V. Andreev, V.A. Cherepanov, P. Kofstad, Solid State Ionics 80 (1995) 189.
[7] A.N. Petrov, V.A. Cherepanov, A.Y. Zuev, J. Solid State Electrochem. 10 (2006) 517.
[8] W.D. Kingery, H.K. Bowen, D.R. Uhlmann (Eds.), Introduction to Ceramics, second ed, John Wiley & Sons, New York, 1976, p. 521.
[9] E. Boehm, J.M. Bassat, M.C. Steil, P. Dordor, F. Mauvy, J.C. Grenier, Solid State Sci. 5 (2003) 973.
[10] L.J. van der Pauw, Philips Res. Rep. 13 (1958) 1.
[11] D. Grientschnig, W. Sitte, Z. Phys. Chem. 168 (1990) 143.
[12] W. Preis, E. Bucher, W. Sitte, Solid State Ionics 175 (2004) 393.
[13] M.W. den Otter, H.J.M. Bouwmeester, B.A. Boukamp, H. Verweij, J. Electrochem. Soc. 148 (2001) J1.
[14] W. Preis, E. Bucher, W. Sitte, J. Power Sources 106 (2002) 116.
[15] M. Søgaard, P.V. Hendriksen, M. Mogensen, F.W. Poulsen, E. Skou, Solid State Ionics 177 (2006) 3285.
[16] V.V. Kharton, E.N. Naumovich, A.A. Vecher, A.V. Nikolaev, J. Solid State Chem. 120 (1995) 128.
[17] M.H.R. Lankhorst, H.J.M. Bouwmeester, H. Verweij, J. Solid State Chem. 133 (1997) 555.
[18] E.B. Mitberg, M.V. Patrakeev, I.A. Leonidov, V.L. Kozhevnikov, K.R. Poeppelmeier, Solid State Ionics 130 (2000) 325.
[19] A. Mineshige, M. Kobune, S. Fujii, Z. Ogumi, M. Inaba, T. Yao, K. Kikuchi, J. Solid State Chem. 142 (1999) 374.
[20] R.H.E. van Doorn, A.J. Burggraaf, Solid State Ionics 128 (2000) 65.
[21] A. Mineshige, M. Inaba, T. Yao, Z. Ogumi, K. Kikuchi, M. Kawase, J. Solid State Chem. 121 (1996) 423.
[22] J. Mizusaki, J. Tabuchi, T. Matsuura, S. Yamauchi, K. Fueki, J. Electrochem. Soc. 136 (1989) 2082.
[23] M. James, T. Tedesco, D.J. Cassidy, R.L. Withers, Mater. Res. Bull. 40 (2005) 990.
[24] M. James, D. Cassidy, D.J. Goossens, R.L. Withers, J. Solid State Chem. 177 (2004) 1886.
[25] C. Gspan, W. Grogger, B. Bitschnau, E. Bucher, W. Sitte, F. Hofer, J. Solid State Chem. 181 (2008) 2976.
[26] E. Bucher, W. Sitte, I. Rom, I. Papst, W. Grogger, F. Hofer, Solid State Ionics 152–153 (2002) 417.
[27] E. Bucher, W. Jantscher, A. Benisek, W. Sitte, W. Preis, I. Rom, F. Hofer, Solid State Ionics 141–142 (2001) 375.
[28] J. Mizusaki, Y. Mima, S. Yamauchi, K. Fueki, H. Tagawa, J. Solid State Chem. 80 (1989) 102.
[29] L.M. van der Haar, M.W. den Otter, M. Morskate, H.J.M. Bouwmeester, H. Verweij, J. Electrochem. Soc. 149 (2002) J41.
[30] R.H.E. van Doorn, I.C. Fullarton, R.A. de Souza, J.A. Kilner, H.J.M. Bouwmeester, A.J. Burggraaf, Solid State Ionics 96 (1997) 1.
[31] S. Wang, A. Verma, Y.L. Yang, A.J. Jacobson, B. Abeles, Solid State Ionics 140 (2001) 125.
[32] H.J.M. Bouwmeester, M.W. Den Otter, B.A. Boukamp, J. Solid State Electrochem. 8 (2004) 599.
[33] J.A. Kilner, R.A. De Souza, I.C. Fullarton, Solid State Ionics 86–88 (1996) 703.
[34] R.A. De Souza, J.A. Kilner, Solid State Ionics 126 (1999) 153.
[35] R. Merkle, J. Maier, Top. Catal. 38 (2006) 141.
[36] R. Merkle, J. Maier, H.J.M. Bouwmeester, Angew. Chem. Int. Ed. 43 (2004) 5069.
[37] J.E. ten Elshof, M.H.R. Lankhorst, H.J.M. Bouwmeester, J. Electrochem. Soc. 144 (1997) 1060.
[38] J.A. Lane, S.J. Benson, D. Waller, J.A. Kilner, Solid State Ionics 121 (1999) 201.
[39] R. Merkle, J. Maier, J. Fleig, in: W. Vielstich, H. Yokokawa, H.A. Gasteiger (Eds.), Handbook of Fuel Cells - Fundamentals, Technology and Applications, John Wiley & Sons, 2009, p. 425.
[40] W. Sitte, E. Bucher, W. Preis, Solid State Ionics 154–155 (2002) 517.
[41] J. Mizusaki, Solid State Ionics 52 (1992) 79.
[42] J. Mizusaki, I. Yasuda, J. Shimoyama, S. Yamauchi, K. Fueki, J. Electrochem. Soc. 140 (1993) 467.
[43] T. Ishigaki, S. Yamauchi, K. Kishio, J. Mizusaki, K. Fueki, J. Solid State Chem. 73 (1988) 179.
[44] J. Yoo, A. Verma, S. Wang, A.J. Jacobson, J. Electrochem. Soc. 152 (2005) A497.
[45] M. Søgaard, P.V. Hendriksen, T. Jacobsen, M. Mogensen, Proc. 7th European SOFC Forum, 2006, p. B064.
[46] Y. Teraoka, H.M. Zhang, K. Okamoto, N. Yamazoe, Mater. Res. Bull. 23 (1988) 51.
[47] E.V. Tsipis, V.V. Kharton, J. Solid State Electrochem. 12 (2008) 1367.
[48] A.N. Petrov, A.Y. Zuev, A.I. Vylkov, D.S. Tsvetkov, J. Mater. Sci. 42 (2007) 1909.
[49] V.L. Kozhevnikov, I.A. Leonidov, E.B. Mitberg, M.V. Patrakeev, A.N. Petrov, K.R. Poeppelmeier, J. Solid State Chem. 172 (2003) 296.
[50] J.A.M. Van Roosmalen, E.H.P. Cordfunke, J. Solid State Chem. 93 (1991) 212.
[51] R.F. Klie, Y. Ito, S. Stemmer, N.D. Browning, Ultramicroscopy 86 (2001) 289.
[52] E. Bucher, W. Sitte, F. Klauser, E. Bertel, Solid State Ionics 208 (2012) 43.